



City Research Online

City, University of London Institutional Repository

Citation: Li, K. (1998). Intelligent Adaptive Digital Distance Relaying for High Resistance Earth Faults. (Unpublished Doctoral thesis, City, University of London)

This is the accepted version of the paper.

This version of the publication may differ from the final published version.

Permanent repository link: <https://openaccess.city.ac.uk/id/eprint/31133/>

Link to published version:

Copyright: City Research Online aims to make research outputs of City, University of London available to a wider audience. Copyright and Moral Rights remain with the author(s) and/or copyright holders. URLs from City Research Online may be freely distributed and linked to.

Reuse: Copies of full items can be used for personal research or study, educational, or not-for-profit purposes without prior permission or charge. Provided that the authors, title and full bibliographic details are credited, a hyperlink and/or URL is given for the original metadata page and the content is not changed in any way.

**INTELLIGENT ADAPTIVE DIGITAL
DISTANCE RELAYING
for
HIGH RESISTANCE EARTH FAULTS**

by

Kai-Kwong Li

This thesis is submitted for the degree of

Doctor of Philosophy

at

Department of Electrical, Electronics and Information Engineering

City University

February, 1998.

TABLE OF CONTENTS

TABLE OF CONTENTS	ii
LIST OF FIGURES	vii
LIST OF TABLES	xi
ACKNOWLEDGMENTS	xii
Declaration	xiii
ABSTRACT	xiv
LIST OF ABBREVIATIONS USED IN THE THESIS	xv
Chapter I: INTRODUCTION	1
1.1 Historical background	1
1.2 Challenge of protection system	2
1.3 Transients existing in the system	3
1.4 Microprocessor based protective relay	4
1.5 Development of the digital relay algorithm	6
1.6 Adaptive relaying	8
1.7 Scope of study of this thesis	9
1.8 Organization of the thesis	11
1.9 Statement of originality	12
LIST OF PUBLICATIONS	14
Chapter II: DIGITAL DISTANCE RELAY THEORY	17
2.1 Digital distance algorithms	17
2.2 Waveform model algorithm	17
2.3 System model algorithm	19
2.4 Finite transform technique	21
2.4.1 Fault impedance measurement	23
2.4.2 Technique for discrete digital signal processing	25
2.4.3 Choice of window length	26
2.4.4 Further Development of the Finite Transform Technique	28
Chapter III: VARIABLE WINDOW LENGTH ALGORITHM	29
3.1 Introduction	29

3.2	Pre-fault processing technique	29
3.3	Variable window processing technique	30
3.4	The choice of pre-fault and post-fault window length	33
3.5	The use of moving average technique	37
3.6	Simulation results	39
3.6.1	Phase-to-ground faults	39
3.6.2	Phase-to-phase faults	44
3.6.3	Three phase faults	47
3.7	Analysis of results	49
Chapter IV:	DEVELOPMENT OF THE ADAPTIVE WINDOW LENGTH ALGORITHM	50
4.1	The need for adaptive window length for relaying algorithm	50
4.2	Theory of the adaptive window length algorithm	51
4.3	Fault detection and starting of variable window algorithm	52
4.4	Variable window processing technique	53
4.5	Final window length	54
4.6	Simulation system layout	55
4.7	Simulation results	56
4.7.1	Single phase faults in a strong system	56
4.7.2	Phase to phase faults in a strong system	69
4.7.3	Performance in a weak local system	73
4.7.4	Accuracy of the algorithm	81
4.8	Performance of the algorithm	82
Chapter V:	USE OF ARTIFICIAL INTELLIGENCE TECHNIQUE TO IDENTIFY HIGH RESISTANCE EARTH FAULT	83
5.1	Background	83
5.2	Adverse effect of fault resistance	84
5.3	Implementation of artificial intelligence technique to digital distance relaying - method 1	87
5.3.1	An ideal trip characteristic.....	87

5.3.2	Application of artificial neural network in identifying trip region	88
5.3.3	Design of artificial neural network	88
5.3.4	Prefault setting	89
5.3.5	Trip decision making	89
5.3.6	Training of neural network	90
5.3.7	Testing patterns and results	92
5.3.8	Possible sources of error	93
	A Slight change in power flow	93
	B Larger change in power flow	95
5.4	Implementation of artificial intelligence technique to digital distance relaying - method 2	97
5.4.1	A practical trip characteristic	97
5.4.2	Design of artificial neural network	98
5.4.3	Training of artificial neural network	99
5.4.4	Trip decision making	100
5.4.5	Neural network training result	100
5.4.6	Testing patterns and results	102
5.4.7	Effect of load flow changes on the output of neural network	103
	A Decrease in power flow	103
	B Increase in power flow	105
	C Slight increase in P and Q flow in the line	106
	D Slight increase in P flow and larger increase in Q flow in the line	107
5.4.8	Effect of remote end load switching	108
5.5	Analysis of result	109
Chapter VI:	IDEAL OPERATING REGION OF DIGITAL DISTANCE RELAY UNDER HIGH RESISTANCE EARTH FAULT	110
6.1	Introduction	110
6.2	System model for distance relay studies	110
6.3	Ideal operating region of distance relay	114

6.3.1	The influence of active and reactive power flow in the line	114
6.3.2	Influence of external system connections	117
6.4	Accuracy of the ideal operating region	120
6.5	Application for adaptive distance relay	121
Chapter VII:	DEVELOPMENT OF THE STAND ALONE INTELLIGENT DIGITAL DISTANCE RELAY	122
7.1	Introduction	122
7.2	Application of artificial neural network in adaptive distance relay	123
7.2.1	Design of artificial neural network	123
7.2.2	Trip boundary prediction	125
7.3	Training data	125
7.4	Training the artificial neural network	127
7.5	Neural network training result	128
7.6	Testing patterns and results	132
7.6.1	Testing pattern	132
7.6.2	Testing results	133
7.7	Proposed tripping scheme	135
7.8	Implementation of the neural network theory to digital distance protection relay	135
Chapter VIII:	CONCLUSION AND FURTHER WORKS	137
8.1	Conclusion	137
8.1.1	Development of the adaptive window length algorithm	137
8.1.2	Relationship between the distance relay ideal operating region and the active and reactive power flow in the protected line	137
8.1.3	Development of the stand alone intelligent digital distance relay	138
8.2	Further works	139
8.2.1	Development of the mathematical relationship for the line flow and ideal operating region	139
8.2.2	The possibility of using fuzzy neural network for operating region identification	142
8.2.3	Practical range of P and Q flow for ANN training	143

8.2.4	Development of a comprehensive high impedance fault detection relay	143
	Reference	145
Appendix A	Impedance Measured at the Relaying Point at the Relaying Point with the Presence of Fault Resistance	149
Appendix B	Case Study on the Application of Artificial Neural Network in Adaptive Distance Relay for High Resistance Fault Identification	152
	B.1 System Configuration	152
	B.2 Selection of Training Cases for the Training of the ANN	153
	B.3 Load Flow Studies on the Selected Cases	154
	B.4 Transient Analysis	154
	B.5 Computation of the Ideal Operating Region	158
	B.6 Inputs and Targets of ANN	158
	B.7 Training the Artificial Neural Network	161
	B.8 Testing of ANN	162
Appendix C	Load Flow Results	165
	C.1 Load Flow for Case Studies in Chapter 6	165
	C.2 Load Flow for Case Studies in Chapter 7	175

LIST OF FIGURES

<i>Number</i>	<i>Page</i>
Fig. 2.1: Frequency response of full-cycle Fourier algorithm (12 samples per cycle)	18
Fig. 2.2: Frequency response of Fourier algorithm with shortened data window (12 samples per cycle)	19
Fig. 2.3: Frequency response of Differential Equation algorithm (12 samples per cycle)	21
Fig. 2.4: Data window on waveform	22
Fig. 2.5: Voltage & current waveforms during line to earth fault on phase-A	23
Fig. 2.6: Two-source system model	27
Fig. 2.7: Impedance measurement using a fixed window length of 4 ms	27
Fig. 2.8: Impedance measurement using a fixed window length of 10 ms	28
Fig. 3.1: Impedance measurement using a variable window length from 4 to 10 ms	32
Fig. 3.2: Impedance measurement using a variable window length from 1 to 10 ms	34
Fig. 3.3: Impedance measurement using a variable window length from 2 to 10 ms	34
Fig. 3.4: Impedance measurement using a variable window length from 4 to 10 ms	35
Fig. 3.5: Impedance measurement using a variable window length from 4 to 10 ms	35
Fig. 3.6: Impedance measurement using a variable window length from 4 to 20 ms	36
Fig. 3.7: Instantaneous and average impedance measurement using a variable window length from 4 to 10 ms	38
Fig. 3.8: Impedance measurement with local SCL = 5 GVA	39
Fig. 3.9 : Impedance measurement with local SCL = 35 GVA	40
Fig. 3.10: Impedance measurement with fault inception angle = 90°	41
Fig. 3.11: Impedance measurement with fault inception angle = 0°	41
Fig. 3.12: Impedance measurement with fault inception angle = 90°	42
Fig. 3.13: Impedance measurement with fault inception angle = 0°	42
Fig. 3.14: Impedance measurement with fault inception angle = 90°	43
Fig. 3.15: Impedance measurement with fault inception angle = 0°	43
Fig. 3.16: Impedance measurement with fault inception angle = 90°	44
Fig. 3.17: Impedance measurement with fault inception angle = 0°	44
Fig. 3.18: Impedance measurement with fault inception angle = 90°	45

<i>Number</i>	<i>Page</i>
Fig. 3.19: Impedance measurement with fault inception angle = 0°	45
Fig. 3.20: Impedance measurement with fault inception angle = 90°	46
Fig. 3.21: Impedance measurement with fault inception angle = 0°	46
Fig. 3.22: Impedance measurement for fault at 90% of line length	47
Fig. 3.23: Impedance measurement for fault at 70% of line length	47
Fig. 3.24: Impedance measurement for fault at 40% of line length	48
Fig. 3.25: Impedance measurement for fault at 10% of line length	48
Fig. 4.1: Flow chart of the adaptive window length algorithm	52
Fig. 4.2: Three source system model	55
Fig. 4.3: Voltage & current at relaying point for case 4.7.1.i	57
Fig. 4.4: Measured impedance for case 4.7.1.i	57
Fig. 4.5: Fault detection and changes of window length for case 4.7.1.i	58
Fig. 4.6: Voltage & current at relaying point for case 4.7.1.ii	59
Fig. 4.7: Measured impedance for case 4.7.1.ii	59
Fig. 4.8: Fault detection and changes of window length for case 4.7.1.ii	60
Fig. 4.9: Voltage & current at relaying point for case 4.7.1.iii	61
Fig. 4.10: Measured impedance for case 4.7.1.iii	61
Fig. 4.11: Fault detection and changes of window length for case 4.7.1.iii	62
Fig. 4.12: Voltage & current at relaying point for case 4.7.1.iv	63
Fig. 4.13: Measured impedance for case 4.7.1.iv	63
Fig. 4.14: Fault detection and changes of window length for case 4.7.1.iv	64
Fig. 4.15: Voltage & current at relaying point for case 4.7.1.v	65
Fig. 4.16: Measured impedance for case 4.7.1.v	65
Fig. 4.17: Fault detection and changes of window length for case 4.7.1.v	66
Fig. 4.18: Voltage & current at relaying point for case 4.7.1.vi	67
Fig. 4.19: Measured impedance for case 4.7.1.vi	67
Fig. 4.20: Fault detection and changes of window length for case 4.7.1.vi	68
Fig. 4.21: Voltage & current at relaying point for case 4.7.2.i	69
Fig. 4.22: Measured impedance for case 4.7.2.i	69
Fig. 4.23: Fault detection and changes of window length for case 4.7.2.i	70

<i>Number</i>	<i>Page</i>
Fig. 4.24: Voltage & current at relaying point for case 4.7.2.ii	71
Fig. 4.25: Measured impedance for case 4.7.2.ii	71
Fig. 4.26: Fault detection and changes of window length for case 4.7.2.ii	72
Fig. 4.27: Voltage & current at relaying point for case 4.7.3.i	73
Fig. 4.28: Measured impedance for case 4.7.3.i	74
Fig. 4.29: Fault detection and changes of window length for case 4.7.3.i	74
Fig. 4.30: Voltage & current at relaying point for case 4.7.3.ii	75
Fig. 4.31: Measured impedance for case 4.7.3.ii	75
Fig. 4.32: Fault detection and changes of window length for case 4.7.3.ii	76
Fig. 4.33: Voltage & current at relaying point for case 4.7.3.iii	77
Fig. 4.34: Measured impedance for case 4.7.3.iii	77
Fig. 4.35: Fault detection and changes of window length for case 4.7.3.iii	78
Fig. 4.36: Voltage & current at relaying point for case 4.7.3.iv	79
Fig. 4.37: Measured impedance for case 4.7.3.iv	79
Fig. 4.38: Fault detection and changes of window length for case 4.7.3.iv	80
Fig. 5.1: Variation of measured impedance with fault resistance for different fault locations	86
Fig. 5.2: An ideal trip region	87
Fig. 5.3: Training pattern selection	91
Fig. 5.4: Testing pattern	92
Fig. 5.5: Changes in ideal trip region	94
Fig. 5.6: Variation of measured impedance with fault resistance for different power flow conditions	96
Fig. 5.7: A practical trip region	97
Fig. 5.8: ANN predicted boundary	101
Fig. 5.9: Testing pattern for the neural network	103
Fig. 5.10: Changes in relay coverage due to decrease in the power flow of the line	104
Fig. 5.11: Changes in relay coverage due to increase in the power flow of the line	105
Fig. 5.12: Changes in relay coverage due to increase in the active and reactive power flow of the line	106

<i>Number</i>	<i>Page</i>
Fig. 5.13: Changes in relay coverage due to increase in the active and reactive power flow of the line	107
Fig. 5.14: Effect of Load Switching	108
Fig. 6.1: Two-source system model	111
Fig. 6.2: Extended two-source system model	112
Fig. 6.3: Two-source system model with parallel line	112
Fig. 6.4: Three-source system model	113
Fig. 6.5: Ideal operating region of cases 1 and 2	115
Fig. 6.6: Ideal operating region of cases 3 and 4	115
Fig. 6.7: Ideal operating region of cases 5 and 6	116
Fig. 6.8: Variations in ideal operating region of cases 1, 3, and 5	116
Fig. 6.9: Ideal operating region of case 7 as compared with case 3	118
Fig. 6.10: Ideal operating region of case 8 as compared with case 3	119
Fig. 6.11: Ideal operating region of case 9 as compared with case 3	119
Fig. 6.12: Ideal operating region of case 10 as compared with case 3	120
Fig. 7.1: Relay ideal boundaries of case 1, 3, 7 & 9	127
Fig. 7.2: ANN predicted relay boundary for test case A	129
Fig. 7.3: ANN predicted relay boundary for test case B	130
Fig. 7.4: ANN predicted relay boundary for test case C	130
Fig. 7.5: ANN predicted relay boundary for test case D	131
Fig. 7.6: Testing patterns	132
Fig. 8.1: Flow chart of digital distance relay for high resistance fault detection	144

LIST OF TABLES

<i>Number</i>	<i>Page</i>
Table 4.1: Accuracy of the adaptive variable window algorithm	81
Table 5.1: Output of neural network	93
Table 5.2: Output of neural network	102
Table 5.3: Output of neural network for decrease in power flow	104
Table 5.4: Output of neural network for increase in power flow	105
Table 5.5: Output of neural network for slight increase in P and Q flow in the line	106
Table 5.6: Output of neural network for slight increase in P flow and larger increase in Q flow	107
Table 6.1: System configurations for cases 1 to 6	114
Table 6.2: Load conditions for cases 1 to 6 (contd.)	114
Table 6.3: System configurations for cases 3, 7, 8, 9 and 10	117
Table 6.4: Load conditions for cases 3, 7, 8, 9 and 10 (contd.)	118
Table 7.1 System information of the training cases	126
Table 7.2 System information of the training cases (contd.)	126
Table 7.3 System information of the test cases	128
Table 7.4 System information of the test cases (contd.)	128
Table 7.5 Output of neural network for test case A	133
Table 7.6 Output of neural network for test case B	134
Table 7.7 Output of neural network for test case C	134
Table 7.8 Output of neural network for test case D	134

ACKNOWLEDGEMENTS

The author wishes to give his sincere thanks to his supervisor Dr. L.L. Lai for his help and guidance throughout the course of this work, especially in solving the problems in the Electro Magnetic Transient Program and the artificial intelligence programming technique.

Special thanks are also to Prof. A.K. David, Head, Department of Electrical Engineering, Hong Kong Polytechnic University for his help and variable advice in the research carried out and also in reducing my normal work load so that I can concentrate in the PhD research work.

This thesis is dedicated to my wife, Betty, for her continued support over the last four years.

Declaration

The author hereby grant powers of discretion to the City University Librarian to allow this thesis to be copied in whole or in part without further reference to the author. This permission covers only single copies made for study purposes, subject to normal conditions of acknowledgement.

Abstract

Protective relays serve to detect and respond to intolerable power system conditions at high speed and with minimum impact on utility loads. Abnormalities such as short circuits must be detected and removed from the power system rapidly, while tolerable abnormalities, such as switching surges, must not cause undesired circuit disconnection. With the rapid development of microprocessor technology and the consequent decline of costs, it is now able to use a high speed and possible application of specific microcomputer for a very complicate protection function. With this target in mind, a new adaptive algorithm based on finite-transform solution of the differential equation with adaptive variable window is proposed. An improved fault detection technique which is suitable for use under high resistance earth fault is also developed. Optimum performance of both operating time and reach accuracy has been obtained. The algorithm, using fast processing techniques, involves reasonable on-line calculation so that a very high sampling frequency can be employed. This thesis will discuss the ideal operating region of distance relay under different conditions. Its relationship with the system configuration and condition is thoroughly reviewed. A method is then developed to deduce the ideal operating region of distance relays under different load conditions in the line without the need for real time computation and thus can overcome the restrictions caused by the need of communication channels. The effect caused by changes in power system configurations will also be discussed. Finally this thesis propose a method to incorporate artificial intelligence technique into the digital distance relay. The relationship between the loading conditions of the line and the corresponding ideal operating region is used to train the digital distance relay by applying the neural network technique and discriminate internal and external faults under different load conditions. The end result is an intelligent digital distance relay which can identify even high resistance earth faults within its designated operating region. This relay is fully adaptive to changes in the power system and its performance will not be degraded within a wide operating range.

List of abbreviations used in the thesis

V_s	Sine components of voltage
V_c	Cosine components of voltage
I_s	Sine components of current
I_c	Cosine components of current
v_k	Instantaneous voltage at sample k
N	Number of samples taken per fundamental cycle
$v(t)$	Instantaneous voltage at instant t
$i(t)$	Instantaneous current at instant t
$\bar{v}_r(j\omega_e, t)$	Instantaneous voltage at the relaying point in the domain of extraction frequency
$\bar{i}_r(j\omega_e, t)$	Instantaneous current at the relaying point in the domain of extraction frequency
Δt	Time interval between two successive samples
T_w	Length of sampling window in seconds
ω_e	Extraction frequency
N_{max}	Number of samples in the maximum window length in the fault-on period
n_{av}	Number of samples to be averaged over
N_{fin}	Number of samples in the post-fault final window length
R	Total resistance of the protected line
L	Total inductance of the protected line
Z_{av}	Average magnitude of measured impedance
R_{av}	Average value of resistance measured over recent n_{av} samples
X_{av}	Average value of reactance measured over recent n_{av} samples
Z_{diff}	Absolute value of per unit difference of impedance calculations over successive samples
$Z_{diff\ set}$	Setting of Z_{diff} to trigger the increase of window length
E_L	Equivalent potential at the local end
E_R	Equivalent potential at the remote end
E_E	Equivalent potential at the external end
h_{RL}	Ratio of magnitude of equivalent potential between the remote and local end
h_{EL}	Ratio of magnitude of equivalent potential between the external and local end
h_{ER}	Ratio of magnitude of equivalent potential between the external and remote end

δ_{RL}	Phase angle difference between the remote and local end
δ_{EL}	Phase angle difference between the external and local end
δ_{ER}	Phase angle difference between the external and remote end
Z_{SL}	Source impedance at the local end
Z_{SR}	Source impedance at the remote end
Z_{SE}	Source impedance at the external end
Z_L	Impedance of the protected line
p	Proportion of line length from the relaying point
R_f	Fault resistance
V_{s-l}	Corresponding sequence fault voltage at relaying point
V_{s-f}	Corresponding sequence fault voltage at fault location
z_{s-lf}	Corresponding sequence line impedance between node l and f
I_{s-lf}	Corresponding sequence fault current in the line from node l to node f
V_f	Pre-fault voltage at fault location
Z_{s-lf}	Corresponding sequence transfer impedance between node l and f
Z_{s-ff}	Corresponding sequence diagonal impedance for node f
Z_T	Driving point impedance at node $f = Z_{0-ff} + Z_{1-ff} + Z_{2-ff} + 3R_f$
Z_{0-ff}	Zero sequence diagonal impedance for node f
Z_{1-ff}	Positive sequence diagonal impedance for node f
Z_{2-ff}	Negative sequence diagonal impedance for node f
I_{0-l}	Zero sequence current at the relaying point at local end
Z_{0L}	Total zero sequence impedance of the protected line
Z_{1L}	Total positive sequence impedance of the protected line
z_{1lf}	Positive sequence line impedance of the faulted section
V_f	Pre-fault voltage at faulted location
I_{a0-f}	Total A phase zero sequence fault current at fault location
I_{a1-f}	Total A phase positive sequence fault current at fault location
I_{a2-f}	Total A phase negative sequence fault current at fault location
C_1	Positive sequence current distribution ratio at the relaying point comparing to the total positive sequence fault current

C_2	Negative sequence current distribution ratio at the relaying point comparing to the total negative sequence fault current
C_0	Zero sequence current distribution ratio at the relaying point comparing to the total zero sequence fault current
f_{tan}	Hypertangent sigmoid transfer function
f_{log}	Logistic sigmoid transfer function
$f_{purelin}$	Pure linear sigmoid transfer function
$ W_1 $	weights of the trained network for layers 1
$ W_2 $	weights of the trained network for layers 2
$ B_1 $	Biases of the trained network for layers 1
$ B_2 $	Biases of the trained network for layers 2
$ Z $	Impedance input to the neural network.
Y	Output of the neural network
ΔP	Changes of active power flow in the line from fixed reference values
ΔQ	Changes of reactive power flow in the line from fixed reference values
P_{LR}	Active power flow from local to remote end
Q_{LR}	Reactive power flow from local to remote end
V_L	Voltage at local end
I_{LR}	Current flow from local to remote end
δ_L	Phase angle of voltage at local end
δ_R	Phase angle of voltage at remote end
Z_L	Impedance of the protected line

Chapter I

INTRODUCTION

1.1 HISTORICAL BACKGROUND

Protective relays serve to detect and respond to intolerable power system conditions at high speed and with minimum impact on utility loads. In the process, relaying minimizes damage to equipment and circuits and protects people. Abnormalities such as short circuits must be detected and removed from the power system rapidly, while tolerable abnormalities, such as switching surges, must not cause undesired circuit disconnection.

As operating principles became increasingly sophisticated protection relaying hardware allows the implementation of advanced concepts that has been developed. Solenoid and induction disc relays were introduced in the first generation. These relays are still in service or in production today. Progress to solid state relaying (transistorized relays) was slow when first introduced in the sixties, partly because of conservatism and partly because of widespread problems with surges produced by the inductive coils in the DC circuits and by switching in the primary power system. When integrated circuits replaced discrete component, use of operational amplifiers, counters, oscillators and other digital circuits produced more compact, lighter and lower burden relays. However, the function and operating principles of these relays, no matter whether they are electro-mechanical or solid state, remain almost the same.

Computer based relaying development stretches back almost 30 years. It started in the era of minicomputers. Early work considered the use of a central substation computer to handle all the relaying functions in that substation [1]. Based on the hardware available and cost at that time, this was a logical and justified approach when computers are proposed for protection purposes. Most recently, with the rapid development of microprocessor technology and the consequent

decline of costs, it is now able to use a high speed and possible application of specific microcomputer for each separate protection function.

1.2 CHALLENGE OF PROTECTION SYSTEM

Utilities are facing increasing pressure to cut costs while maintaining or improving service reliability in recent years. In addition, obtaining transmission rights-of-way and construction approvals have become increasingly difficult. The widespread opposition to nuclear energy, emission constraints and environmental issues have exacerbated the utilities's problems, creating a severe financial drain and delaying generation availability. While some areas now have substantial surplus generation, load growth and plant retirements threaten to rapidly absorb this surplus. As a result the recent past has shown the following trends in the power systems field.

- (1) An overwhelming need for flexibility of power plants to switch over or to adapt quickly to a variety of "classical" or new-look type fuels or forms of primary energy;
- (2) a corresponding need to transmit the generated power through the network, no matter what "exotic" generation scheduling pattern or load management situation is at hand at that precise moment as a result of differential fuel prices or the actual general load situation;
- (3) although HV networks still show a definite tendency to become more and more meshed, the relative electrical distance between sources and load has, nevertheless, a tendency to increase; moreover new large generators are bigger in size and more economic to use, but without special precautions, they are more easily endangered, electromechanically. They also put more constraints on the general network operating stability;
- (4) simultaneous tripping or outage of several network links has become more likely due to more intensive use of limited rights of way by new multi-circuit lines often parallel and very close to each other over long distance.
- (5) finally, short-circuit power levels have, generally speaking, been growing less faster than planned; in recently added HV or EHV portions of some network, mostly in developed

countries, it has been lower for a longer period than initially foreseen, causing sustained trouble with regard to poor transient stability.

As a consequence of all this, network operation has become far more tricky and complex than in the years before while economy transfers are loading the transmission systems and reducing margins for contingencies. Therefore, protection of today's transmission lines is not as simple as in the past. Considerations of economics and operating requirements make the application of protective relays to transmission lines both an art as well as a science. On the other hand, transmission system protective relaying reliability becomes increasingly important, especially for heavily loaded transmission lines.

1.3 TRANSIENTS EXISTING IN THE SYSTEM

The voltage and current signals at the time of fault inception are usually severely distorted. A great deal of non-fundamental components will exist in the relaying signals and the waveforms are no longer sinusoidal. If these transients are ignored, a significant measuring errors will result. The transient components basically consists of three types:

- (i) A DC exponentially decaying component present in the current waveform with a time constant depending on the R/L ratio of the line. The magnitude of this DC exponential decaying component is largely dependent on the fault inception angle and it can be as large as the peak of the fundamental component of the fault current.
- (ii) Harmonics in the voltage and current waveforms produced by nonlinear power system equipments. Saturation of voltage and current transformers is also a cause of harmonics to appear in the relaying input. Capacitive voltage transformers may also be responsible for part of the DC and transient oscillations in the relay input. The non-linear fault arc will also contribute part of the harmonics in the system.

- (iii) The reflection of surges between the bus and the fault will produce high frequency components and will be superimposed on the voltage and current signals. The frequency and magnitude of these high frequency components depends on the distance of the fault from the relaying point and the capacity of the system at local and remote ends.

1.4 MICROPROCESSOR BASED PROTECTIVE RELAY

A microprocessor based relay accepts voltage, current, and other analogue and digital signals and makes trip decision after processing the data. Properly designed microprocessor relays and systems are in several ways superior to the electromechanical and solid state relays and are being increasingly accepted for general uses in industry. Based on a thorough investigation, two IEEE courses [9,13] have summarized the advantages of the microprocessor based relaying system as follows:

Improved Performance: Properly designed digital relays perform at least as well as the electromechanical and solid state relays. The performance in this context includes operating speed, security and consistency. Certain operating features are improved by using digital processors without incorporating substantial design modifications. For example, memory action is provided in a microprocessor based relay without a major design effort; a complex operating characteristic is easily programmed. Besides improved performance can be obtained due to the merits of digital technology, (i) the characteristics of digital components do not drift with temperature, supply voltage changes or ageing, (ii) the performance of digital components do not change from part to part as long as a numerical value stored in memory remains the value irrespective of where the number is stored, (iii) the resolution of the solutions provided by digital devices depends on the number of bits per word used in the arithmetic calculations, (iv) the digital devices are not required to be tuned individually to obtain consistent results, (v) a digital device can perform both logic and arithmetic functions while controlling a process and, (vi) the data recorded by a digital device is not corrupted except when equipment failure is experienced.

High Reliability: Digital equipment is perceived to fail more frequently than the components of the electromechanical and solid state relays. However, most digital relays are designed to monitor themselves at regular intervals by executing the software in conjunction with pre-specified data and comparing the results with those expected from a properly functioning device. In the event of the results differing from the expected values, the microprocessor relay alerts an operator of the equipment failure or impending failure. System reliability can be further increased by the relay monitoring its peripherals. Several self testing techniques have been used in commercially available protection systems, such the ROM, RAM, power supply, A/D conversion, as well as setting check, analog gain and offset check, CPU test and output logic confirmation.

Flexibility: Digital processor relays are more flexible than the conventional relays. They include multiple characteristics and an option to select any one of those characteristics. This would ultimately reduce the inventory required for repair and maintenance of relays as currently used relays are replaced by their digital counterparts. Another factor that affects flexibility is the possibility of replacing the software of a digital relay and changing its entire nature. Because some inputs to the relays in a substation are identical, a single transducer can provide an input to all digital relays. These features increase the hardware and software costs that must be justified by the resulting improvements in system operation.

Background Tasks: The practice of collecting data at HV and EHV substations and providing to regional control centres is quite common. Transmitting supervisory and maintenance alarms and their descriptions has been in use for over twenty years. More recently, operational data, such as, voltages, currents and power flows have been collected at dispersed locations in power systems and transmitted to regional and central control centres. Since microprocessors handle the communication functions with ease, several microprocessor based relays and systems are designed to collect data and transmit it to a pre-specified location as a background task. Another task that is performed by some microprocessor relays is the post-fault analysis of the data collected during a fault. The relay computes the distance of a fault and provides the information for use maintenance personnel immediately if the fault is of a permanent nature and for future use

if it is of temporary nature. Most digital relays also collect a sequence of event information locally, analyze it and provide the details and the results to a control computer.

Bv-products: Like the solid state relays, the microprocessor relays present low burdens to current and voltage transducers. Also, microprocessor relays can use digitized data that can be received over fibre optic links from electronic transducers installed at the HV and EHV levels. This approach results in savings in cabling costs and the high costs presently encountered in HV and EHV current and voltage transformers. It will provide an impetus for developing, in the future, unified systems of transducers and protection systems.

Identical Hardware Design: Developments in the electronic industry has lowered the cost of digital devices rapidly during the last twenty years and the trend is accelerating, whereas the cost of their electromechanical and solid state counterparts has been increasing. Equipment designs based on digital technology use fewer parts and fewer connections, which is beneficial for reducing the cost further and is able to improve reliability. Most design changes of relays can be made by changing the software only, while the hardware remains the same, which is flexible as well as economical.

1.5 DEVELOPMENT OF THE DIGITAL RELAY ALGORITHM

The performance of digital distance relays must be independent of the system waveforms. Measurements of the fault impedance must be accurate and have a high operating speed. To achieve these goals, the algorithm employed must converge rapidly and the fault impedance must be calculated precisely by processing a small window of information. To facilitate hardware implementation, the algorithm must not involve too much computation.

Since the development of digital protection by Rockefeller [1] in 1969, many alternative digital relay algorithms and techniques have been developed [2-6, 8, 9, 13]. The existing algorithms proposed for use in digital relaying can be grouped into two categories. The first type is based

on a model of the waveform itself, i.e., the voltage or current. The parameter of interest for the relaying application is contained in the waveform description. Examples would include:

- (i) The peak value of sinusoidal current for overcurrent protection [2].
- (ii) The fundamental frequency voltage and current phasors for impedance relaying [2].
- (iii) The magnitude of harmonics in current waveforms for harmonic restraint in transformer protection [5].
- (iv) The fundamental frequency of a periodic signal for a frequency relay.

The following algorithms are appropriate for the waveform models:

- (a) **Fourier Algorithms** [4]: In its simplest form a Fourier algorithm extracts the fundamental frequency phasor from samples of a periodic signal taken at equal intervals over a full period of the signal.
- (b) **Curve Fitting Algorithm** [6]: Curve fitting algorithms attempt to fit some parameterized representation of the signal to the measurements. Parameterization include polynomials, trigonometric series, and a mix of trigonometric functions and exponential.

The second type involves a model of the system rather than the waveforms. In particular a series R-L model of the faulted line implies that the terminal voltage and current must satisfy a first order linear differential equation. The parameters of interest for relaying are the values of R and L in the system model which must be estimated from the waveforms [3].

The algorithms developed in the early years usually employed a relatively low sampling rate and the fault impedance calculation was based on sinusoidal measurands. However during fault conditions, the range of system voltage and current waveforms encountered is extremely large and depend on many factors, including the plant configuration and the location of fault. The post fault waveforms are usually distorted and contain numerous harmonics and reflected travelling wave components [7]. Filters have to be used extensively to suppress these non-fundamental

components in order to achieve a stable operation. The use of filters, plus the relatively low sampling rate (600 Hz) makes the response of the relay too slow to rival conventional static distance relays.

Accurate calculation and fast convergence of an impedance measuring algorithm are essential for satisfactory relaying. Substantial research work towards better algorithms has been carried out for more than 20 years [8, 12]. The differential equation based algorithm [2] and Fourier Transform based algorithms [4], are widely accepted by the protective relaying industry because of their inherent advantages. However, disadvantages still remain to be overcome. The differential equation based algorithms exhibit poor high frequency characteristics so that significantly time delaying filters are required. The Fourier Transform algorithm possesses a good frequency characteristic but the presence of a DC component adversely affects the calculation accuracy.

1.6 ADAPTIVE RELAYING

The use of microprocessor based relays as one to one replacements for conventional relays provides an excellent foundation for evolution. The availability of communication ports will enhance the acceptance of computer relaying concepts, by allowing the relay engineer convenient access to the system for education and monitoring as well as remote setting capability. This will set the stage for implementation of more elaborate hardware and software. The design of a hierarchical structure must provide for stand alone functioning with minimum degradation in performance should the higher level be lost temporarily. In addition, sufficient monitoring must be provided to properly evaluate new adaptive functions initially in an open mode.

As defined by the IEEE Working Group K-8 of the Power System Relaying Committee, the concept of an adaptive function [23] is defined as a function within a protective relay or system that automatically adjusts the operating characteristics (setting or state change) of the relay system in response to changing power system conditions. Many existing relays are adaptive to a limited extent. An inverse-time overcurrent relay, for example, could be considered to adapt

its trip time to the current level. With the advent of microprocessor based relaying systems and the possibility of improved communication, more complicated adaptation methods can be envisaged.

The opportunities for improved relaying reliability, and hence power system reliability, offer a strong incentive for implementing adaptive concepts, particularly in the face of significantly increased economic loading of the transmission systems. As the use of computers in relaying designs becomes more acceptable and wide spread, adaptive relaying concepts will evolve naturally. Those concepts, which offer compelling economic or performance advantages and which pose limited risks during the trial period, will lead the way. The use of on-line periodic checking of coordination of adaptive and non-adaptive settings will enhance the reliability of the relaying and increase user confidence. Minimum reliance upon communication links during the fault period should also help; ideally the adaptations should occur prior to or after disturbances to avoid concerns about computer system response time. In any case the relaying must handle rapid fire multiple disturbances where the communications needed to update settings and logic may not stay in step. Transient blocking techniques are needed to update and place the relaying in its most secure state shortly after a disturbance is detected and until sufficient time has elapsed in a steady state to allow complete updating.

1.7 SCOPE OF STUDY OF THIS THESIS

The tremendous expansion in interconnected power systems, the higher voltage levels and the complexity of network configurations, present adverse conditions for the performance of protective relays [10]. On the other hand, system security and stability concerns aggravate the stringent requirement for power system relaying. Confronting the challenge, researchers and engineers are required to take the opportunity to contribute their talent and effort to bring new ingenuity to bear on these problems. This is also the general objective of the thesis.

The scope of this thesis is confined to digital distance relaying for power transmission lines, particularly under high resistance earth faults. The performance of digital distance relays, like the

conventional distance relays, refers to three measures, *speed*, *selectivity* and *reliability*. There has been an increasing awareness of the benefits of extra-high-speed clearance of faults for security and economic concerns. Both transient corruptions and uncertainties in the steady state network configurations of the power system adversely affect the clearance of faults without losing selectivity and reliability. This thesis, accordingly, is concerned with minimizing these limitations.

A new adaptive algorithm based on finite-transform solution of the differential equation with adaptive variable window is proposed. An improved fault detection technique which is suitable for use under high resistance earth fault is also developed. Optimum performance of both operating time and reach accuracy has been obtained. The algorithm, using fast processing techniques, involves reasonable on-line calculation so that a very high sampling frequency can be employed.

This thesis will discuss the ideal operating region of distance relay under different conditions. Its relationship with the system configuration and condition is thoroughly reviewed. A method is then developed to deduce the ideal operating region of distance relays under different load conditions in the line without the need for real time computation and thus can overcome the restrictions caused by the need of communication channels [26]. The effect caused by changes in power system configurations will also be discussed.

Finally this thesis proposes a method to incorporate artificial intelligence techniques into the digital distance relay. The relationship between the loading conditions of the line and the corresponding ideal operating region is used to train the digital distance relay by applying the neural network technique and discriminate internal and external faults under different load conditions. The end result is an intelligent digital distance relay which can identify even high resistance earth faults within its designated operating region. This relay is fully adaptive to changes in the power system and its performance will not be degraded within a wide operating range.

1.8 ORGANIZATION OF THE THESIS

Chapter 2 describes the background digital distance relay algorithm using finite transform theory, the use of discrete digital signal processing techniques. It also discuss the choice of window length on the performance of the algorithm.

Chapter 3 describes the development of the variable window length algorithm and how it is modified to improve performance. This chapter covers pre-fault processing techniques, and the use of a moving average technique to improve the stability in resistance and reactance calculations.

Chapter 4 describes the development of the adaptive window length feature for the variable window length algorithm developed in Chapter 3. A sensitive and reliable fault detection technique which is better than the present technique has been developed. It deals with the starting of the variable window, and the factors which decides the final window length.

Chapter 5 describes how artificial intelligence techniques are employed in distance relays. It discusses how Artificial Neural Network (ANN) is used to identify the trip region for a high resistance fault up to 200 Ω . The error caused due to changes in line loading is discussed.

Chapter 6 describes the main factors which affect the ideal operating region of distance relay and how it is related to the active and reactive power flow in the line. A wide range of system configurations had been studied. The error effect caused by changes in power system configurations will also be discussed.

Chapter 7 describes how ANN is further applied to solve the overreach and underreach problems of a distance relay caused by remote end infeed under high resistance earth fault. This chapter explains how the findings in Chapter 5 and 6 are employed to develop an intelligent digital distance relay by using neural network theory. After the ANN is successfully trained within a specified range of active and reactive power flow in the line, it is able to predict the correct

operating region in any loading condition within the specified range with a small error. The relay is thus able to adapt its operating region and can overcome the traditional overreach and underreach problems of distance relays.

Chapter 8 concludes the finding in this thesis and discusses the work that can be carried out in future. A comprehensive tripping scheme is also proposed.

1.9 STATEMENT OF ORIGINALITY

Original contributions or important developments of this thesis are given in the following statements:

1. Both the first-order differential equation based algorithms and the Fourier transform algorithms are well known. The former has an advantage of not being affected by the decaying DC component while the latter has a good high frequency characteristic. An algorithm has been developed which combines these two merits into one by solving the differential equation using a finite transform using a variable window. In the original variable window algorithm the window length starts from 1 sample from fault inception to a fixed length after inception. The new work done in the algorithm in this thesis is in improving the variable window algorithm. A fixed window length is used in the pre-fault period. Upon fault inception, the window length will be increased automatically by using a newly developed fault detection and starting technique. The final window length is adaptive to the nature of the disturbance and the most suitable post-fault window length will be used. The improved algorithm satisfies both speed, accuracy and stability requirement. A new fault detection technique is also developed. This fault detection technique is proved to be better than conventional techniques and it is used to trigger the starting of window length increase.
2. One of the major discoveries in this project is the relationship between the ideal distance relay operating region and the active and reactive power flow in the line. No such finding

has been reported so far to the knowledge of this author. It has been shown that the ideal distance relay operating region is affected mainly by the active and reactive power flow in the line. Other changes in power system configurations, for example, change in generation and load conditions in other parts of the system, do not affect the ideal operating region to the same extent as long as the load flow in the line remains unchanged. Even if there is a major switching operation in the system, the change in the relay trip region is still within a reasonable limit.

- 3 Another major part of work reported in this thesis is the development of the intelligent digital distance relay. Based on the factors which affect the ideal operating region, artificial intelligence techniques are employed to develop a distance relay which can solve the overreach and underreach problems caused by remote end infeed under high resistance earth fault. Ideal operating regions of the distance relay under a range of active and reactive power flow in the line can be determined. This information is then used to train the relay employing neural network theory. After the relay is successfully trained, it can identify the correct operating region as long as the pre-fault load flow in the line is known. As the load flow in the line normally varies slowly and continuously, the relay can also adjust adaptively to the correct operating region at the same time. This concept works even under high resistance earth faults. The traditional overreach and underreach problems under high resistance earth fault have thus been solved.

1.10 PUBLICATIONS

Two papers have been published during this period in the leading international journals, two more papers are under review. Seven conference papers have also been presented. The papers are listed below.

Refereed Journal Papers:

1. Y.Q. Xia, K.K. Li : 'Development and Implementation of a Variable Window Algorithm for High Speed and Accurate Digital Distance Protection', *IEE Proceeding, Generation Transmission and Distribution*, Vol. 141, No. 4, July 1994, pp.383-389.
2. K.K. Li : 'An Adaptive Window Length Algorithm for Accurate High Speed Digital Distance Protection', *The International Journal of Electrical Power & Energy Systems*, Volume 19, No. 6, August 1997, pp. 375-383.
3. K.K. Li, L.L. Lai : 'Ideal Operating Region of Digital Distance Relay Under High Resistance Earth Fault', *International Journal of Electric Power System Research*, Elsevier Science Ltd., Vol. 43, No.3, Dec. 1997, pp. 215-219.
4. K.K. Li, L.L. Lai, A.K. David : 'Stand Alone Intelligent Digital Distance Relay', *IEEE Transactions on Power Systems*, paper submitted for consideration.
5. K.K. Li, L.L. Lai, A.K. David : 'Application of Artificial Neural Network to Digital Distance Protection', *International Journal of Engineering Intelligent Systems*, paper submitted for consideration.

Conference Papers:

1. K.K. Li, C. Cheung, Y.Q. Xia, : 'High Speed Digital Distance Protection - Real Time Simulation and Hardware Development', *1st IEE International Conference in Advances in Power System Control, Operation, and Management (APSCOM-91)*, Hong Kong, 5-8 November 1991, pp. 95-100.
2. K.K. Li, Y.Q. Xia, : 'Operating Speed and Reach Accuracy Study for a Digital Distance Relaying Algorithm', *1993 IEEE Region 10 Conference on Computer, Communication, Control and Power Engineering (TENCON-93/BEJING)*, 19-21 October 1993, Beijing, Vol. 5, pp. 284-287.
3. K.K. Li, Y.Q. Xia, : 'Considerations for Adaptive Distance Relaying', *2nd IEE International Conference in Advances in Power System Control, Operation, and Management (APSCOM-93)*, Hong Kong, 7-10 December 1993, Vol. 1, pp. 379-384.
4. K.K. Li, Y.Q. Xia, : 'Application of Artificial Neural Network in Adaptive Distance Relaying', *Electrical Engineering Congress 94 (EEC-94)*, Sydney, 24-30 November 1994, Vol. 1, pp. 3-8.
5. K.K. Li, A.K. David, L.L. Lai, Y.Q. Xia, : 'An Adaptive Digital Distance Relay for EHV Transmission Lines", Preprints, *International Federation of Automatic Control (IFAC-95) Symposium on Large Scale Systems*, London, July 1995, Vol. 1, pp. 433-438.
6. K.K. Li, L.L. Lai, Y.Q. Xia, : 'Development in Variable Window Algorithm for High Speed and Accurate Digital Distance Protection', *3rd IEE International Conference in Advances in Power System Control, Operation, and Management (APSCOM-95)*, Hong Kong, November 1995, Vol. 1, pp.271-276.

7. K.K. Li, L.L. Lai, A.K. David : 'Intelligent Digital Distance Relay', *The International Conference on Intelligent Systems - Applications to Power Systems (ISAP'97)*, Seoul, Korea, 6 - 10 July 1997, pp. 279-283.
8. K.K. Li, L.L. Lai : 'An Adaptive Variable Window Algorithm for Digital Distance Protection', *4th IEE International Conference in Advances in Power System Control, Operation, and Management (APSCOM-97)*, Hong Kong, November 11-14, 1997, Vol. 1, pp. 83-88.
9. K.K. Li, L.L. Lai, A.K. David : 'High Speed and Stable Adaptive Variable Window Algorithm for Digital Distance Protection', *Australian Universities Power Engineering Conference / IEAust Energy Conference (AUPEC/EEC 97)*, Sydney, 29 September - 1 October, 1997, Vol. 2, pp. 383-388.

CHAPTER II

DIGITAL DISTANCE RELAY THEORY

2.1 DIGITAL DISTANCE RELAY ALGORITHMS

Since the development of digital protection by Rockefeller [1] in 1969, many alternative digital relay algorithms and techniques have been developed [2-6, 8, 9, 13]. Most of the existing algorithms proposed for use in digital relaying can be grouped into two categories. The first type is based on a model of the waveform itself, i.e., the voltage or current. The parameter of interest for the relaying application is contained in the waveform description. The second type involves a model of the system rather than the waveforms. In particular a series R-L model of the faulted line implies that the terminal voltage and current must satisfy a first order linear differential equation. The parameters of interest for relaying are the values of R and L in the system model which must be estimated from the waveforms [3].

2.2 WAVEFORM MODEL ALGORITHM

Fourier Algorithms. [4] In its simplest form a Fourier algorithm extracts the fundamental frequency phasor from samples of a periodic signal taken at equal intervals over a full period of the signal. Ramamoorthy [4] was the first of many to propose that the desired fundamental component of voltage or current be extracted from the fault transients by correlating one cycle of data samples with the stored samples of reference fundamental sine and cosine waves. The general expressions for the sine and cosine components of voltage at a sample point k are

$$V_s = \frac{1}{N} \left[2 \sum_{l=1}^{N-1} v_{k-N+l} \sin \left(\frac{2\pi}{N} l \right) \right] \quad 2.1$$

$$V_c = \frac{1}{N} \left[v_{k-N} + v_k + 2 \sum_{l=1}^{N-1} v_{k-N+l} \cos \left(\frac{2\pi}{N} l \right) \right] \quad 2.2$$

where v_i are the voltage samples and N is the number of samples taken per fundamental cycle. Similar expressions are evaluated for current components I_s and I_c . These may be converted to polar form using

$$V = \sqrt{V_s^2 + V_c^2} \tag{2.3}$$

$$\phi_V = \tan^{-1} \left(\frac{V_s}{V_c} \right) \tag{2.4}$$

The frequency response of the algorithm is shown in Fig. 2.1 with nulls at DC and at all harmonic frequencies. High frequencies above the second harmonic are all well attenuated. Digital relay employing the full cycle Fourier algorithm has an operation time of more than 1 cycle as the algorithm requires information for 1 full cycle post-fault before a correct calculation can be obtained. The operation time of the Fourier algorithm can be faster if the window length is reduced. Fig. 2.2 shows the frequency response of the algorithm when the window length is reduced to 1/2 cycle plus one sample and is less effective in rejecting DC and even harmonics. The vertical axis of Fig. 2.1 and 2.2 are normalized to show the relative response of the algorithm.

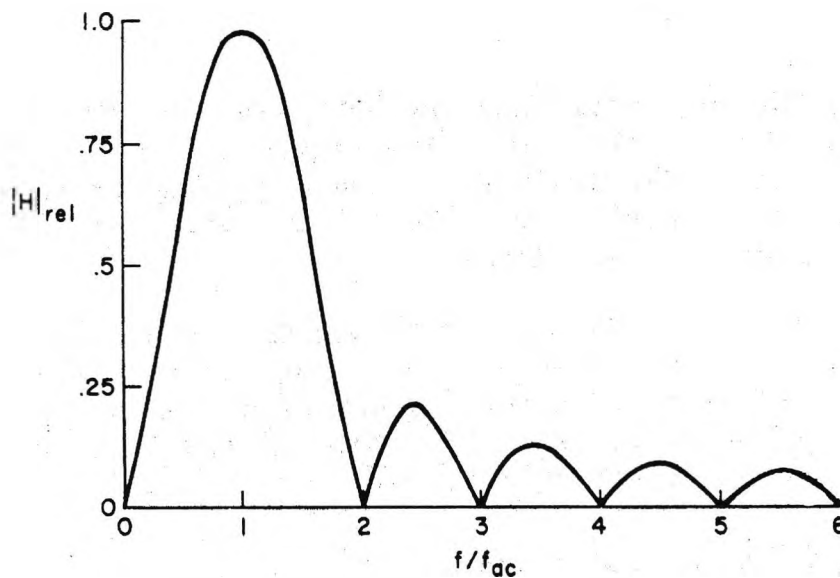


Fig. 2.1 Frequency response of full-cycle Fourier algorithm (12 samples per cycle)

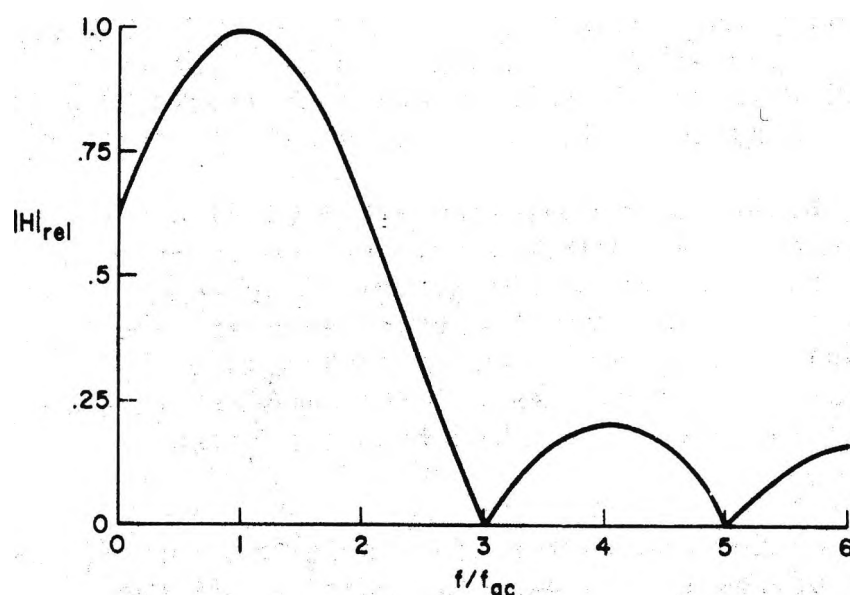


Fig. 2.2 Frequency response of Fourier algorithm with shortened data window (12 samples per cycle)

2.3 SYSTEM MODEL ALGORITHM

Differential Equation Algorithm [3] is produced if the parameters of interest are included in the system description rather than the waveform. It is widely accepted by the protective relaying engineering community and commercial products are available since McInnes and Morrison [3] first modelled a faulted line as a series R-L circuit.

$$v(t) = R i(t) + L \frac{di(t)}{dt} \quad 2.5$$

Since measurements are made of $v(t)$ and $i(t)$ a more tractable version of eqn. 2.5 is obtained by integrating over two successive time periods to form

$$\int_{t_0}^{t_1} v(t) dt = R \int_{t_0}^{t_1} i(t) dt + L [i(t_1) - i(t_0)] \quad 2.6$$

$$\int_{t_1}^{t_2} v(t) dt = R \int_{t_1}^{t_2} i(t) dt + L [i(t_2) - i(t_1)] \quad 2.7$$

If the integrals are evaluated using the trapezoidal rule with t_0 , t_1 , and t_2 corresponding to samples $k-2$, $k-1$, and k , the inductance and resistance of the line model can be evaluated as

$$L = \frac{\Delta t}{2} \left| \frac{(i_k + i_{k-1})(v_{k-1} + v_{k-2}) - (i_{k-1} + i_{k-2})(v_k + v_{k-1})}{(i_k + i_{k-1})(i_{k-1} - i_{k-2}) - (i_{k-1} + i_{k-2})(i_k - i_{k-1})} \right| \quad 2.8$$

$$R = \left| \frac{(v_k + v_{k-1})(i_{k-1} - i_{k-2}) - (v_{k-1} + v_{k-2})(i_k - i_{k-1})}{(i_k + i_{k-1})(i_{k-1} - i_{k-2}) - (i_{k-1} + i_{k-2})(i_k - i_{k-1})} \right| \quad 2.9$$

The frequency response of the algorithm is shown in Fig. 2.3. This algorithm has the advantage of recognizing DC offsets as valid components of fault currents rather than processing them as spurious signals since the lumped R-L model expects the existence of transients. Frequency response to DC and low frequencies components does not reflect unfavourably on the ability of the algorithm to deal with the exponentially decaying DC offset whose occurrence is consistent with the line model employed. Very fast response can be achieved by using a short window of as little as 3 samples. Disadvantages appear when the voltage and current signals are severely distorted. Low pass filtering with a rather low cut-off frequency is required and this causes steady state and dynamic problems. Time delay is the most commonly realised concern.

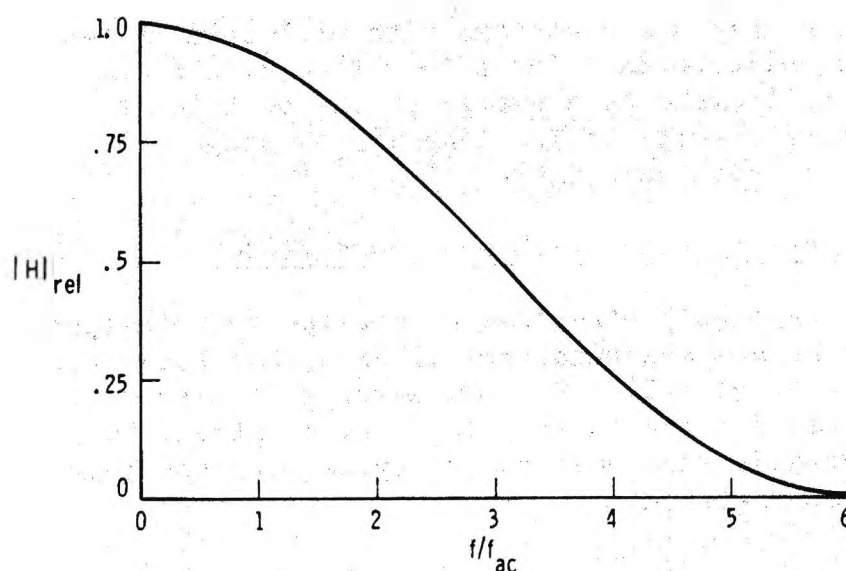


Fig. 2.3 Frequency response of Differential Equation algorithm (12 samples per cycle)

2.4 FINITE TRANSFORM TECHNIQUE [8, 12, 16, 17, 22]

The performance of a digital distance relay must be independent of the system waveform. Measurements of the fault impedance must be accurate and must be executed at high speed. Therefore the algorithm employed must converge rapidly and the fault impedance must be calculated precisely by processing a small window of information. To facilitate hardware implementation, the algorithm must not involve too much computation.

The Finite Transform algorithm is developed by combining the Fourier algorithm and the differential equation algorithm. On-line evaluation of the Fourier Transform is carried out using a data window imposed on a small section of voltage and current waveforms (Fig. 2.4) at the relaying point. As the data window progresses with time, a new transform is obtained by modifying the previous calculated values. Because most of the transform values inside the data window remain unchanged, each new transform is obtained with relatively few additional computations.

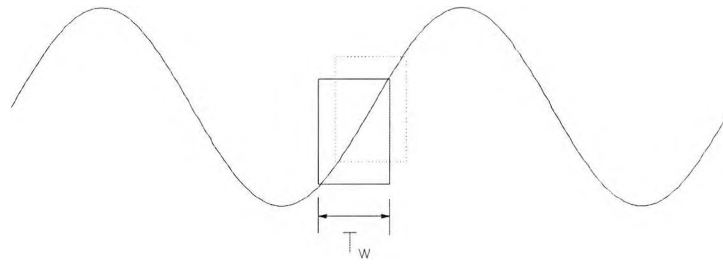


Fig. 2.4 Data window on waveform

As the digital relay is processing signals for a fixed window length T_w , transforming the system voltage v_r at the relaying point gives

$$\bar{v}_r(j\omega_e, t) = \int_{t-T_w}^t v_r(\tau) \exp(-j\omega_e \tau) d\tau \quad 2.10$$

This is the transform of the following unit step function,

$$\bar{v}_r(j\omega_e, t) = \int_{-\infty}^{\infty} [H(\tau - (t - T_w)) - H(\tau - t)] v(\tau) \exp(-j\omega_e \tau) d\tau \quad 2.11$$

Similarly,

$$\bar{i}_r(j\omega_e, t) = \int_{t-T_w}^t i_r(\tau) \exp(-j\omega_e \tau) d\tau \quad 2.12$$

The finite Fourier integral extracts the spectral component at a chosen frequency $f_e = \omega_e / 2\pi$ from the time variation of the voltage $[v_r(t)]$ and current $[i_r(t)]$ within a finite time T_w preceding any time t at which computation is implemented (Fig. 2.5) [12]. The fundamental advantage of the finite transform method is its insensitivity to transient waveform distortion [8].

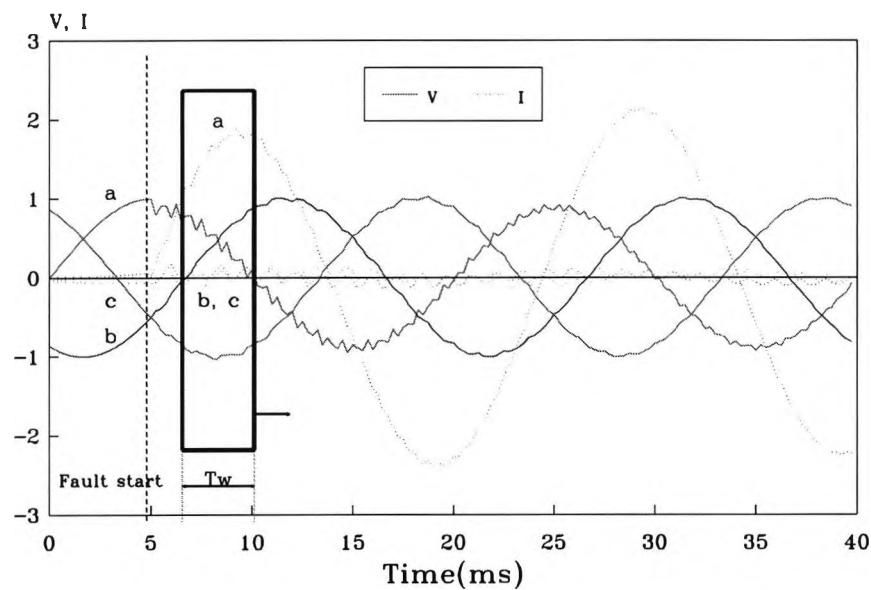


Fig. 2.5 Voltage & current waveforms during line to earth fault on phase-A

2.4.1 Fault Impedance Measurement

For both phase and ground faults, the relationship between the relaying voltage and current can be described by the first-order linear differential equation

$$v(t) = Ri(t) + L\frac{di(t)}{dt} \quad 2.13$$

based on the positive phase sequence series inductance and resistance of the line at power frequency provided high frequency components caused by fault induced travelling waves are prefiltered.

This relationship holds for both steady-state and transient components at any instant. Therefore, employing a finite transform defined by

$$X(j\omega, t) = \int_t^{t+T_w} X(\tau) \exp(-j\omega\tau) d\tau \quad 2.14$$

the following relationship will still be valid at any instant t for any finite transform duration

$$\int_t^{t+T_w} v(\tau) \exp(-j\omega\tau) d\tau = R \int_t^{t+T_w} i(\tau) \exp(-j\omega\tau) d\tau + L \int_t^{t+T_w} \frac{di(\tau)}{d\tau} \exp(-j\omega\tau) d\tau \quad 2.15$$

where T_w is a finite duration and $\omega = 2\pi f$, f being the fundamental frequency.

The finite Fourier transform of equation 2.15 gives

$$\begin{aligned} \bar{v}_r(j\omega_e, t) = & R \bar{i}_r(j\omega_e, t) + j\omega_e L \bar{i}_r(j\omega_e, t) \\ & + L \{i_r(t) \exp(-j\omega_e t) - i_r(t-T_w) \exp[-j\omega_e(t-T_w)]\} \end{aligned} \quad 2.16$$

The last term on the RHS of equation 2.16 accounts for the sudden drop to zero of the time function at the beginning and at the end of the window.

Integrating by parts and taking the real and imaginary parts separately, we can, after algebraic manipulation, obtain two linear simultaneous equations

$$\begin{aligned} I_{r1} R + I_{m2} L &= V_{r1} \\ I_{r2} R + I_{m1} L &= V_{r2} \end{aligned} \quad 2.17$$

where V_{r1} , V_{r2} , I_{r1} , I_{r2} are the four integrals given by

$$V_{r1} = \int_t^{t+T_w} v(\tau) \cos(\omega\tau) d\tau \quad 2.18$$

$$V_{r2} = \int_t^{t+T_w} v(\tau) \sin(\omega\tau) d\tau \quad 2.19$$

$$I_{r1} = \int_t^{t+T_w} i(\tau) \cos(\omega\tau) d\tau \quad 2.20$$

$$I_{r2} = \int_t^{t+T_w} i(\tau) \sin(\omega \tau) d\tau \quad 2.21$$

and I_{m1} , I_{m2} are defined by

$$I_{m1} = i(t+T_w) \sin\{\omega(t+T_w)\} - i(t) \sin(\omega t) - \omega I_{r1} \quad 2.22$$

$$I_{m2} = i(t+T_w) \cos\{\omega(t+T_w)\} - i(t) \cos(\omega t) + \omega I_{r2} \quad 2.23$$

The solution of equation 2.17 will give a measurement of the apparent resistance and inductance

$$R = \frac{I_{m1}V_{r1} - I_{m2}V_{r2}}{I_{r1}I_{m1} - I_{r2}I_{m2}} \quad L = \frac{I_{r1}V_{r2} - I_{r2}V_{r1}}{I_{r1}I_{m1} - I_{r2}I_{m2}} \quad 2.24$$

Hence a measurement of the line impedance as seen from the relaying point has been obtained.

2.4.2 Technique For Discrete Digital Signal Processing [16, 17, 22]

To achieve fast operation of the protective relay, real time calculation must be a minimum. Referring to equation 2.24, the first step is to calculate v_{r1} , v_{r2} , i_{r1} , i_{r2} . For the n-th elemental strip, the area A_n under the integral is estimated by equation 2.25 to make use of the information conveyed by $\cos(\omega_e \tau)$.

$$A_n = \frac{1}{2} \{v_r(t_{n-1}) + v_r(t_n)\} \int_{t_{n-1}}^{t_n} \cos(\omega_e \tau) d\tau \quad 2.25$$

Therefore,

$$v_{r1} = \frac{1}{2\omega_e} \sum_{n=1}^N \{[v_r(t_{n-1}) + v_r(t_n)][\sin(\omega_e t_n) - \sin(\omega_e t_{n-1})]\} \quad 2.26$$

where N is the number of samples in one data window.

To reduce the computing task, v_{r1} is calculated by modifying the previous integral as follows:

$$v_{r1}(k) = v_{r1}(k-1) + [v_r(t_k) + v_r(t_{k-1})] * C(k) - [v_r(t_{k-N}) + v_r(t_{k-1-N})] * C(k-N) \quad 2.27$$

where $v_{r1}(k-1)$ = the result calculated in last sample period and $C(k) = \sin(\omega_c t_n) - \sin(\omega_c t_{n-1})$.

In a similar way, $v_{r2}(k)$, $i_{r1}(k)$, $i_{r2}(k)$, $I_{m1}(k)$, $I_{m2}(k)$ can be calculated. The measured resistance and reactance at the sample instant k are calculated from equation 2.24 in a similar way.

2.4.3 Choice Of Window Length

Since the relaying voltage and current signals under fault conditions are distorted, it is necessary to extract the fundamental spectral component from all the existing frequency components in a finite length data window. The extraction efficiency, as expected, would depend on the length of the window and the sampling rate.

Different sampling rates and window lengths have been investigated by using the fault data derived from the well known Electro-Magnetic Transient Program (EMTP). Analysis for a single-phase-to-earth fault located at 80 % of the line length on a two-source system as shown in Fig. 2.6 has been carried out. The fault is applied at the voltage peak (fault angle = 90°) which will produce maximum high frequency transients due to reflection of travelling waves. Using a sampling rate of 4 kHz, it can be shown that the impedance calculated with a fixed window length of 4 ms (Fig. 2.7) is still oscillating at 20 ms after fault inception due to numerical instability. With the same sampling rate, but fixed window length of 10 ms (Fig. 2.8) a more stable result is obtained but the impedance did not converge until about 10 ms after fault inception, i.e. until the window has completely passed the fault inception instant.

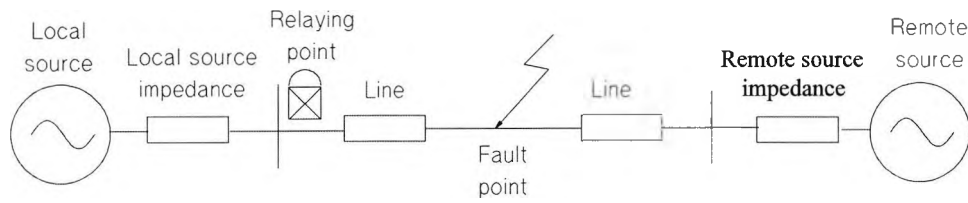


Fig. 2.6 Two-source system model

Fault level at local end = 15 GVA, Fault level at remote end = 35 GVA,
 $|V_L| / |V_R| = 1$, $MVA_{base} = 600$ MVA, $Z_{0SL}/Z_{1SL}=1$, $Z_{0SR}/Z_{1SR}=1$, Fault angle = 90° ,
 Power Flow = 500 MW (Local to Remote), Voltage = 400 kV, Line length = 128 km,
 $Z_{1L}=38.4\angle 86^\circ \Omega$, $Z_{0L}=139.9\angle 69^\circ \Omega$.

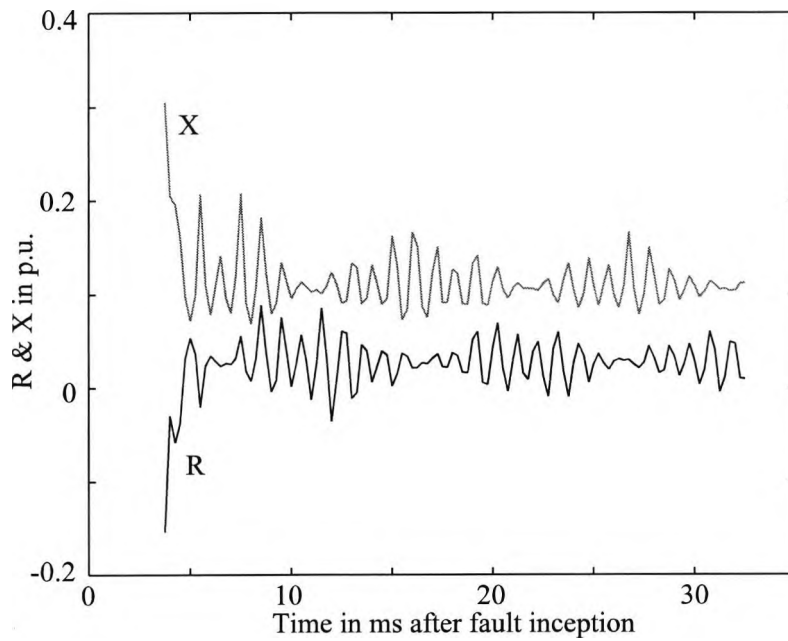


Fig. 2.7 Impedance measurement using a fixed window length of 4 ms

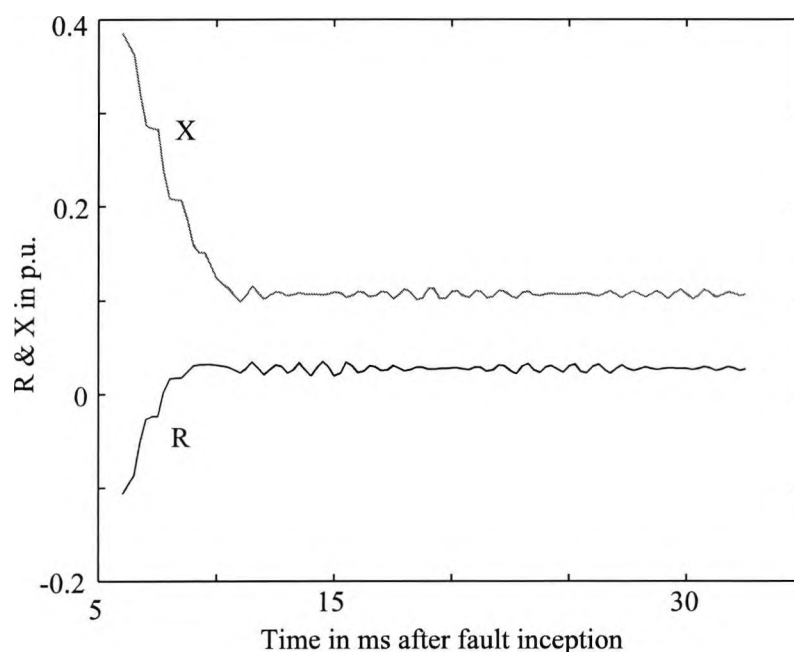


Fig. 2.8 Impedance measurement using a fixed window length of 10 ms

2.4.4 Further Development of the Finite Transform Technique

An initial investigation on the finite transform technique shows that the algorithm combines the differential equation and fourier algorithms and possesses features of both algorithms. The use of numerical integration technique in this algorithm greatly reduces the processing work required by the main processor. Even a common microprocessor can handle all the necessary computation well within the time limit.

Accurate calculation and fast convergence of an impedance measuring algorithm are essential for satisfactory relaying. The fixed window length Finite Transform algorithm has solved part of the problems. However, choice of a short window length does not satisfy the reach accuracy requirement. On the other hand, the long window length algorithm limits the operating speed. The problem caused by the decaying DC component still remains. Therefore there is still room for improvement for the algorithm in the aspects of speed and stability which will be dealt with in the next chapter.

CHAPTER III**VARIABLE WINDOW ALGORITHM****3.1 INTRODUCTION**

Accurate calculation and fast convergence of an impedance measuring algorithm are essential for satisfactory relaying. The fixed window length Finite Transform Algorithm described in Chapter Two has solved part of the problems. However, choice of a short window length does not satisfy the reach accuracy requirement. On the other hand, the long window length algorithm limits the operating speed. Transient error problems caused by constant window correlation have been discussed and a variable window technique has been proposed in Reference 28. However, the problem caused by the decaying DC component still remains.

To solve the speed and stability problems, the concept of a variable window technique [28, 32] has thus evolved. A fixed window length is used in the pre-fault period. As DC and high frequency components are absent in pre-fault conditions, a fixed data window length of say 1/5th of a cycle is adequate to provide a stable output during pre-fault. On fault inception, owing to the DC offset and induced transient, the window length has to be increased in order to provide a stable output. The following sections explain the working principle of the algorithm and its performance under various conditions.

3.2 PRE-FAULT PROCESSING TECHNIQUE

A fixed length window is used in the pre-fault period. Whenever a new sampled data set becomes available, the $(k+1)$ th evaluation can be recursively derived from the results of the k th evaluation. Taking V_{r1} as an example

$$V_{r1}(k+1) = V_{r1}(k) + v(t_{k+1})C(k+1) - v(t_{k+1-N_{pre}})C(k+1-N_{pre}) \quad 3.1$$

where $v(t_{k+1})$ is the instantaneous value of $v(t)$ at the $(k+1)$ sample point, N_{pre} is the number of samples in the pre-fault window, and

$$C(k+1) = \cos \left\{ \frac{2\pi(k+1)}{N_{ac}} \right\} \quad 3.2$$

where N_{ac} is the no. of samples per cycle.

As DC and high frequency components are almost absent in pre-fault conditions, a relatively short and fixed length data window is adequate to provide a stable output during the pre-fault period.

3.3 VARIABLE WINDOW PROCESSING TECHNIQUE

When a fault is detected, the window length will be increased in order to provide an accurate measurement. Again taking V_{r1} as an example, the $(k+1)th$ evaluation can be derived as

$$V_{r1}(k+1) = V_{r1}(k) + v(t_{k+1})C(k+1) \quad 3.3$$

As the data window length is steadily increased as new sets of sampled data become available, the filtering feature becomes more efficient. When the data window reaches a pre-selected maximum window length, the window length will be switched back to a pre-set constant. The four discrete integrals V_{r1} , V_{r2} , I_{r1} , and I_{r2} will be switched back to recursive evaluations. For example

$$V_{r1}(k+1) = V_{r1}(k) + v(t_{k+1})C(k+1) - v(t_{k+1-N_{max}})C(k+1-N_{max}) \quad 3.4$$

where N_{max} is the number of samples in the maximum window length in the fault-on period.

The switching of data window length can be initiated by a fault detection device. Based upon a signal received from the fault detection device, the window length will start to increase from the pre-fault window length. When a new sample is retrieved, the old data will not be discarded and the window length will be increased by 1 sample. More information is thus contained in the calculations when the window length increases. This process will be repeated until the window length has reached at a pre-set maximum. The window length will then stop increasing and will be switched back to the processing method for a constant window length algorithm. This processing technique is beneficial to both fast response and accurate measurement.

Analysis for a single-phase-to-earth fault at 80 % of the line length on a two-source system as shown in Fig. 2.6 has been carried out. The fault is applied at the voltage peak (fault angle = 90°) which will produce maximum high frequency transients. The sampling rate used is 4 kHz as before. Using a variable window technique with a pre-fault window length of 4 ms and a maximum window length of 10 ms shows that the impedance starts to converge at 4 ms and has completely converged 10 ms after fault inception (Fig. 3.1). Comparing Fig. 3.1 with Fig. 2.7 and 2.8, which uses a constant sampling window of 4 and 10 ms respectively, it shows that the algorithm employing a variable window from 4 to 10 ms converges faster.

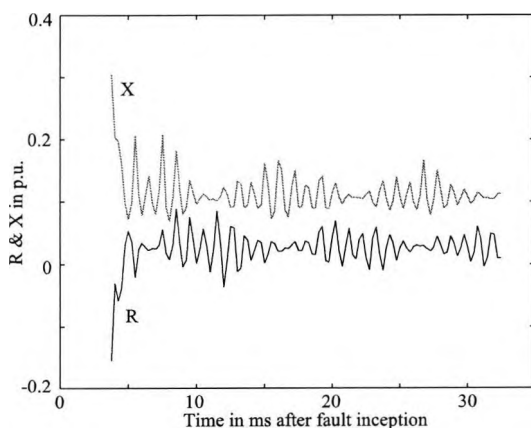


Fig. 2.7 Impedance measurement using a fixed window length of 4 ms

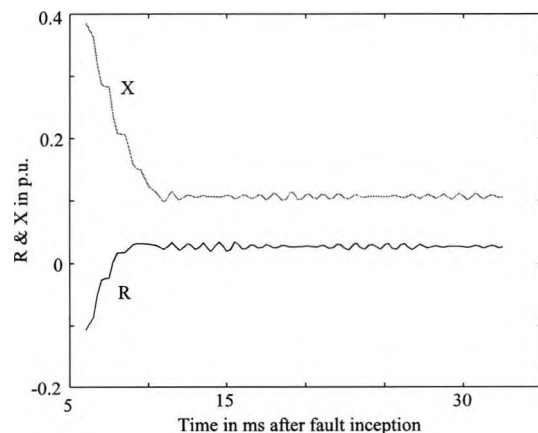


Fig. 2.8 Impedance measurement using a fixed window length of 10 ms

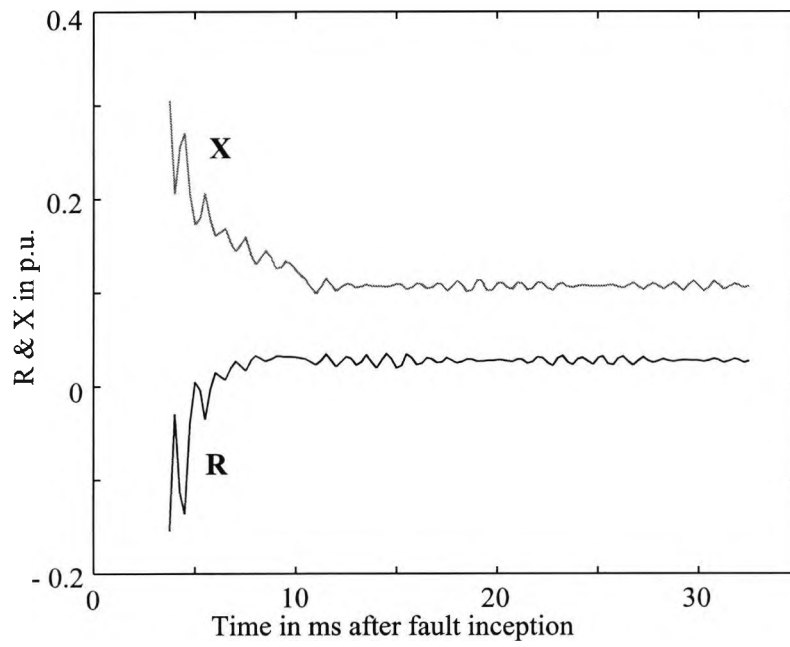


Fig. 3.1 Impedance measurement using a variable window length from 4 to 10 ms

3.4 THE CHOICE OF PRE-FAULT AND POST-FAULT WINDOW LENGTH

In the analysis carried out, a pre-fault window length of 4 ms and a maximum post-fault window length of 10 ms are used. The use of shorter pre-fault window length may result in unstable calculation during pre-fault period. This effect is illustrated in the simulation carried out on a very weak system as shown in Figs. 3.2 - 3.4. Unstable impedance calculations exist during the pre-fault period. This is because the digital relay is processing discrete data and owing to the large dynamic range between normal and fault conditions, the relay may produce some error in pre-fault calculations due to inadequate resolution and information. This will not cause the relay to mal-operate as the impedance locus is usually far away from the normal operating zone. Using a longer post-fault window length will produce more stable results and will not delay the response to a great extent (Figs. 3.5 & 3.6). It is therefore concluded that a pre-fault window length of 4 ms and a post-fault window length of 20 ms will give optimum performance even in the worst scenario.

In Figs. 3.2 - 3.6, fault level at local end is 5 GVA, fault level at remote end is 35 GVA, pre-fault power flow is 100 MW (Local to Remote). A single phase to earth fault is applied at 80% of line length at a fault inception angle of 90° . Fig. 3.5 is extracted from Fig. 3.4 to show the detail post-fault resistance and reactance measurements.

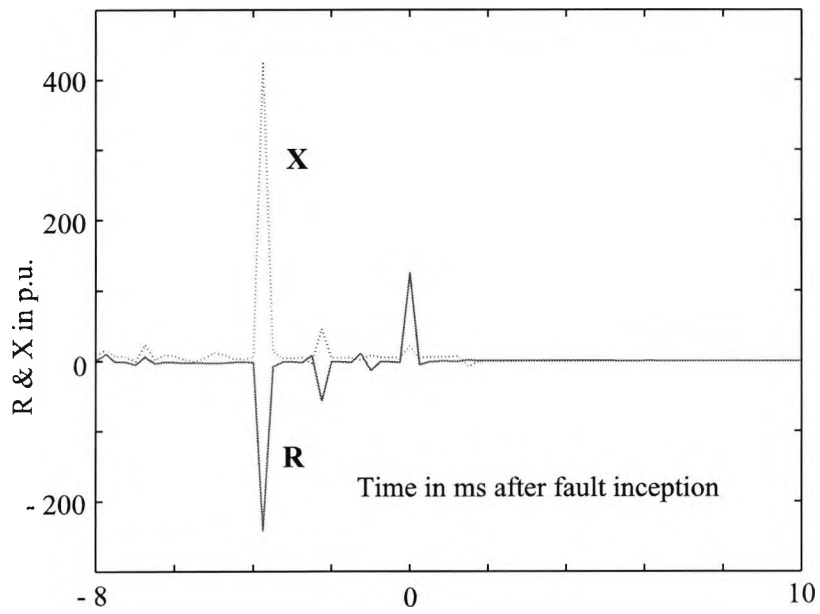


Fig. 3.2 Impedance measurement using a variable window length from 1 to 10 ms

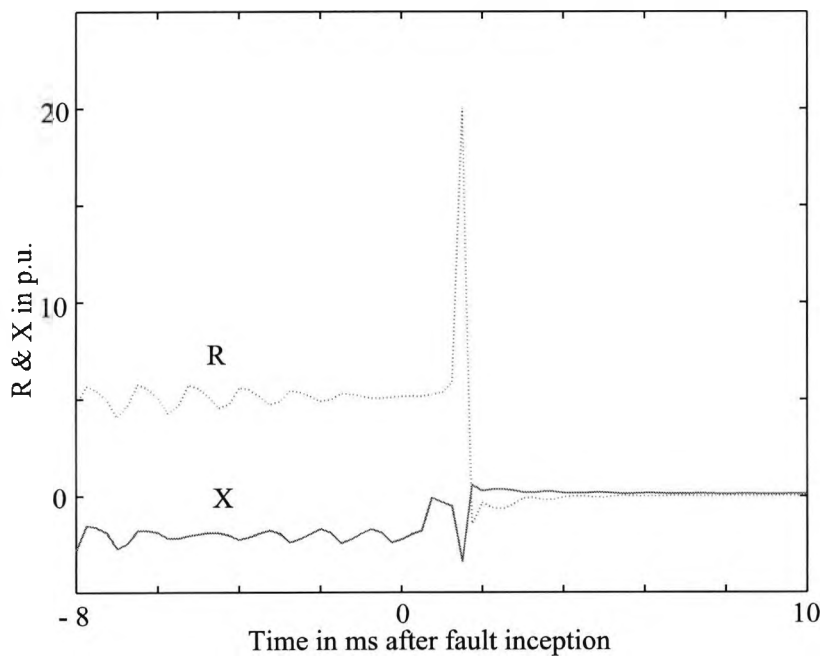


Fig. 3.3 Impedance measurement using a variable window length from 2 to 10 ms

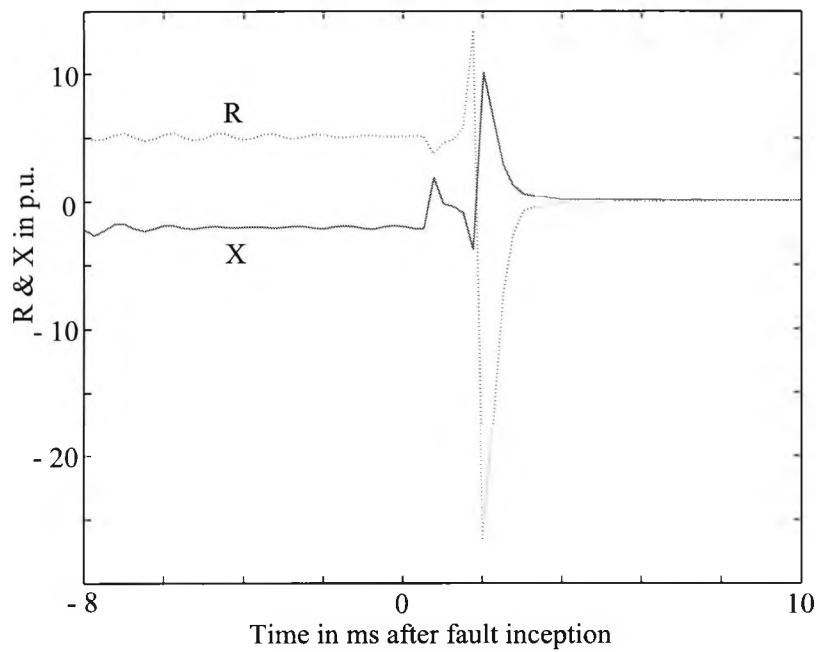


Fig. 3.4 Impedance measurement using a variable window length from 4 to 10 ms

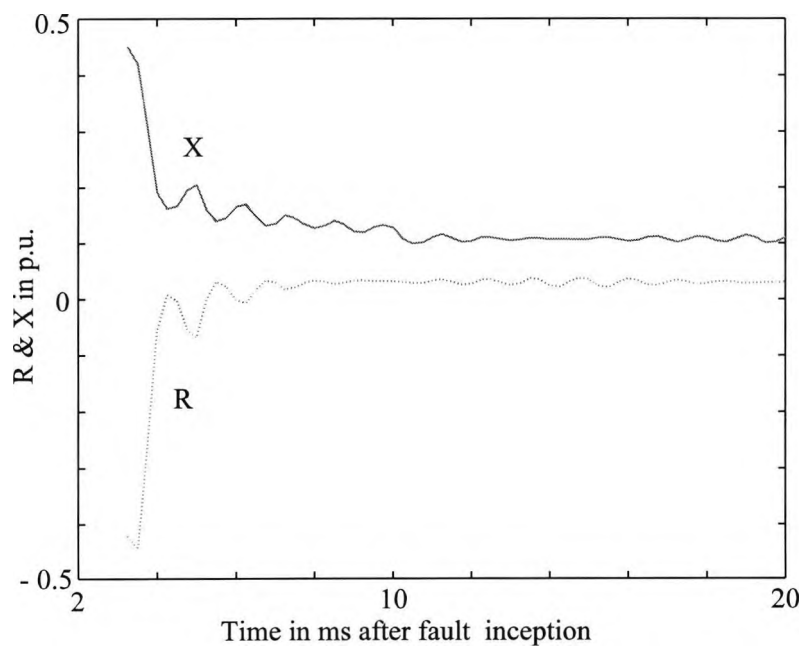


Fig. 3.5 Impedance measurement using a variable window length from 4 to 10 ms

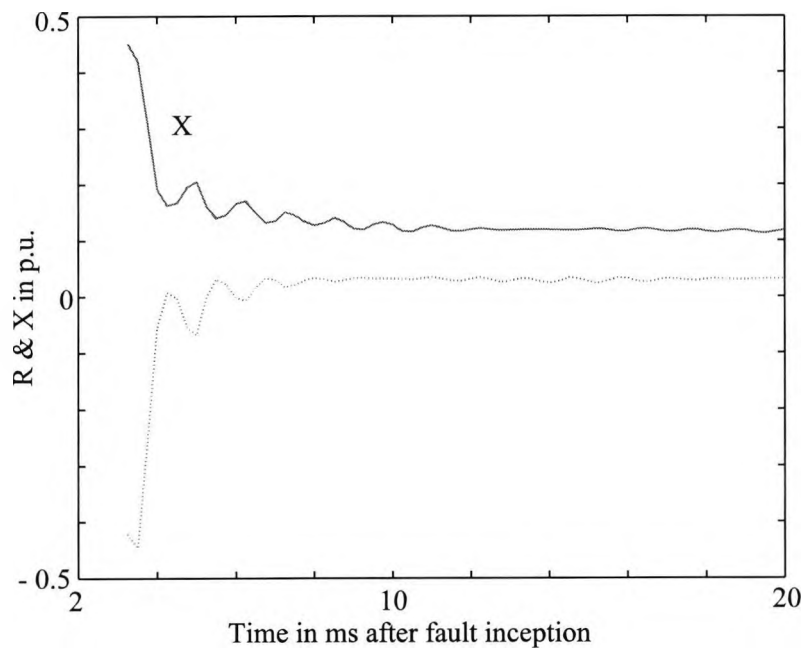


Fig. 3.6 Impedance measurement using a variable window length from 4 to 20 ms

3.5 THE USE OF MOVING AVERAGE TECHNIQUE [32]

Because of the high frequency disturbances caused by fault transients, the calculated impedance is haphazard initially. Using an algorithm with a good frequency extraction characteristic will of course reduce frequency and amplitude fluctuations, but it is well known that even an algorithm with strong filtering cannot prevent uncontrollable numerical oscillations during the initial fault inception period. These fluctuations will no doubt delay the trip decision making. From the calculated results it has been observed that if the mean value of the fluctuating impedance calculations is examined, a very stable and converging output can be obtained in a short time. The most recently calculated value is averaged with the previous calculations and for example, the average value of X at sample k can be obtained from

$$X_{av}(k) = \left\{ \sum_{i=k-n_{av}}^k X_i \right\} / n_{av} \quad 3.5$$

where n_{av} is the number of samples to be averaged over.

Eqns. (3.6) is a recursive formulation of eqn. (3.5).

$$X_{av}(k+1) = \left[\left\{ \sum_{i=k-n_{av}}^k X_i \right\} + X_{k+1} - X_{k-n_{av}} \right] / n_{av} \quad 3.6$$

Fig. 3.7 shows the measured impedance in a very weak system. A fault is simulated in a system configuration as in Fig. 2.6 so that very strong transients caused by travelling wave components are present. Pre-fault and post-fault window lengths of 4 and 10 ms respectively are chosen. Calculated impedances with and without using the averaging method are presented. The value of n_{av} used here is 4. It is found that if n_{av} is too small, the result is not significant. On the other hand, if n_{av} is too large, it will delay the response time of the relay. In general a value between 4 to 10 is satisfactory. The use of average values is a very useful technique in avoiding transient fluctuations.

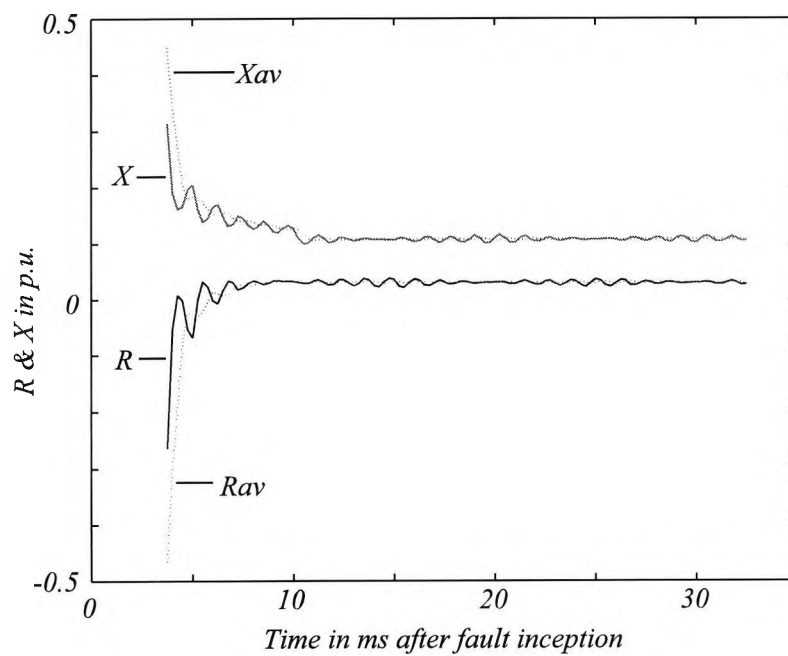


Fig. 3.7 Instantaneous and average impedance measurement using a variable window length from 4 to 10 ms
 Fault level at local end = 5 GVA,
 Fault level at remote end = 35 GVA,
 Power Flow = 100 MW (Local to Remote),
 (—) = Real time values,
 (- - - - -) = Average values.

3.6 SIMULATION RESULTS

Numerous simulations have been conducted for phase to ground, phases to phase, and three phase faults at various locations with different source capacities, fault inception angles and power transfer conditions. Some typical results are shown below. The pre-fault and maximum post-fault window lengths are 4 and 20 ms respectively. A value of 5 is used for n_{av} . The remote-end short circuit level (SCL) in all cases is 35 GVA. In the diagram below, solid lines are X_{av} , dotted lines are R_{av} , and time is in ms after fault inception.

3.6.1 Phase-to-Ground Faults

In Fig. 3.8 and 3.9, the fault is at 80% of line length from relaying point with a power flow of 500MW from the local end to the remote end. Fault inception angle is 90° .

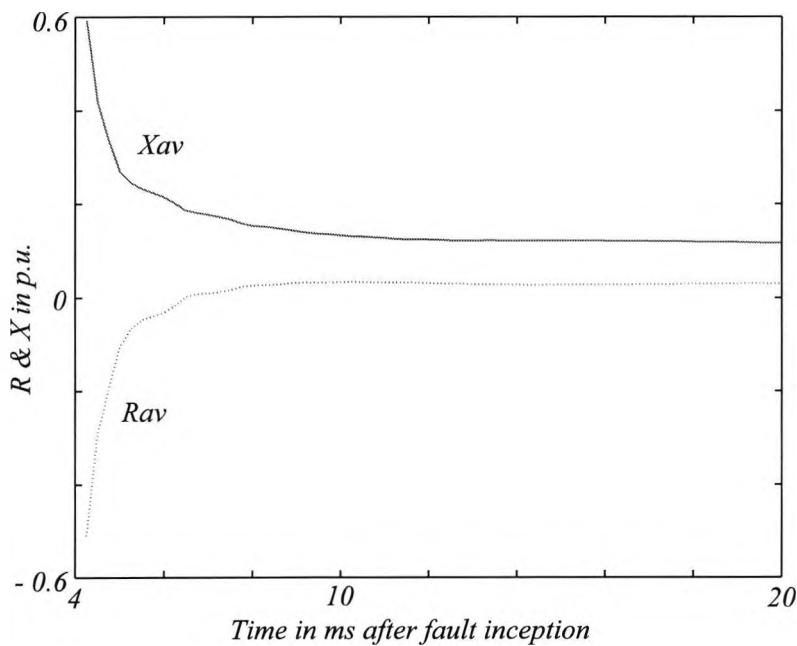


Fig. 3.8 Impedance measurement with local SCL = 5 GVA

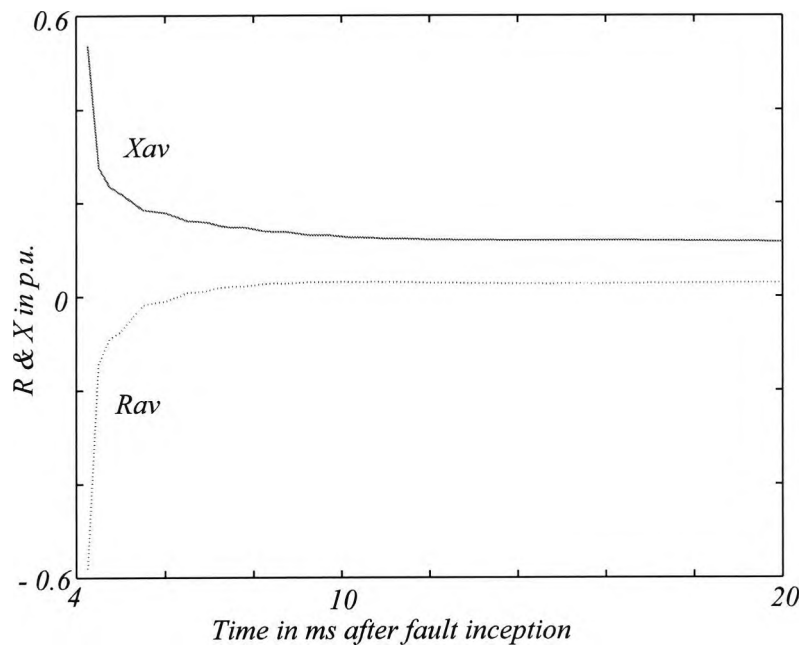


Fig. 3.9 Impedance measurement with local SCL = 35 GVA

In Fig. 3.10 and 3.11, the fault is at 90% of line length from the relaying point. The local end SCL is 5 GVA and the power flow is 100 MW from the local to remote.

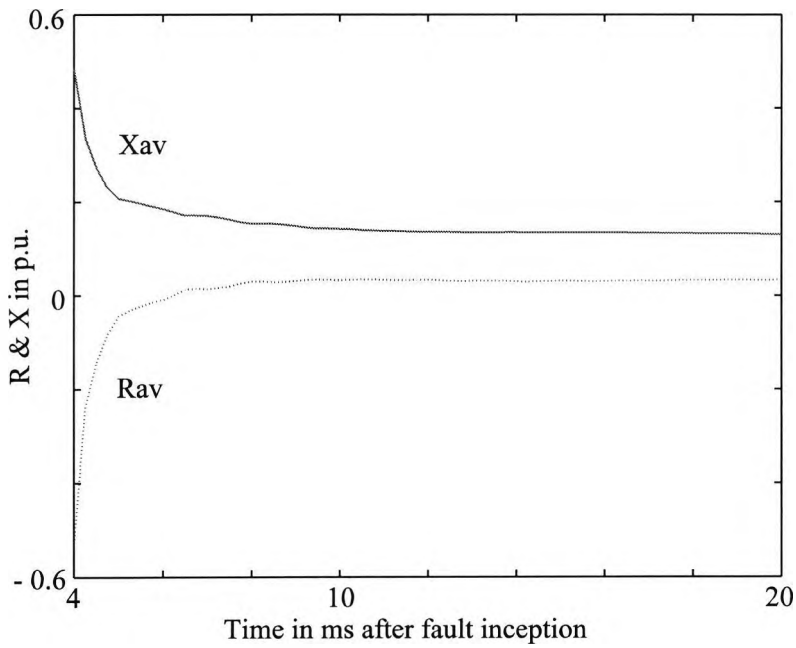


Fig. 3.10 Impedance measurement with fault inception angle = 90°

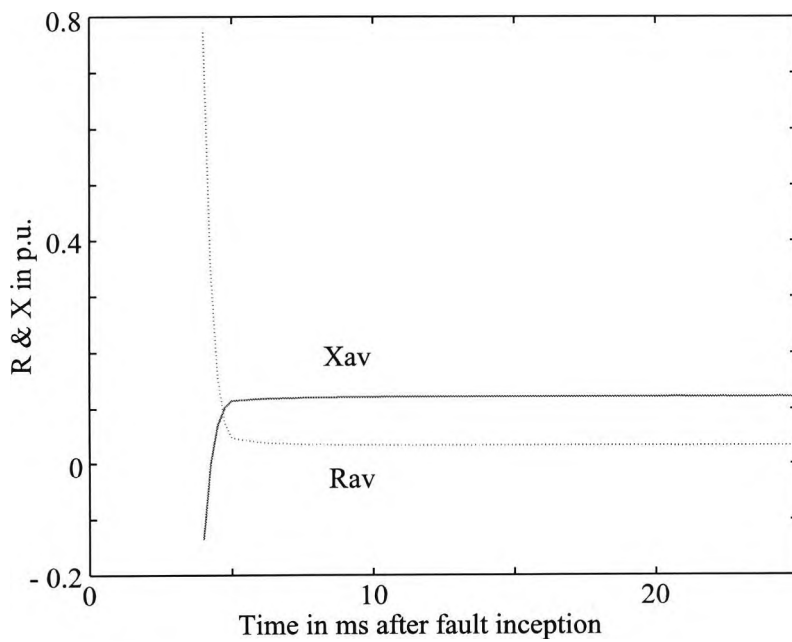


Fig. 3.11 Impedance measurement with fault inception angle = 0°

In Fig. 3.12 and 3.13, the fault is at 50% of line length. The local end SCL is 5 GVA. The power flow is 100MW from the local end to the remote end.

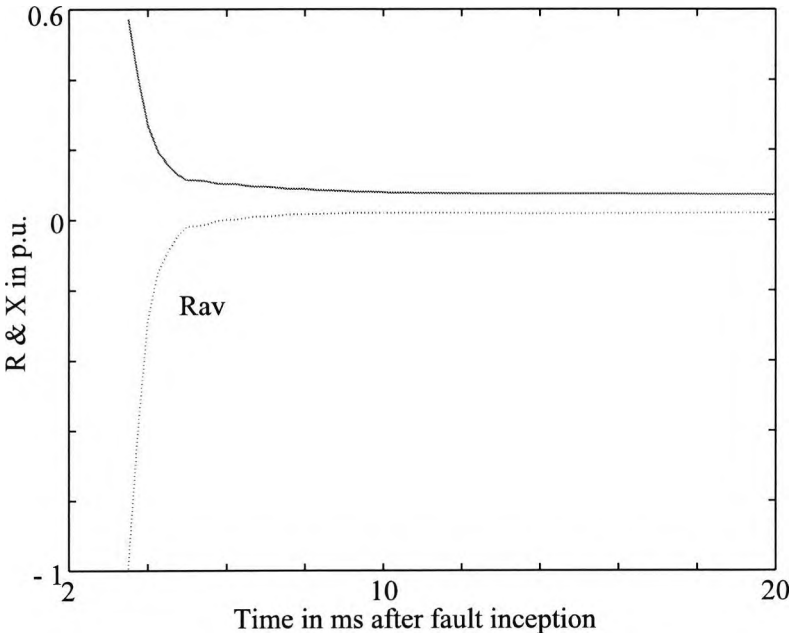


Fig. 3.12 Impedance measurement with fault inception angle = 90°

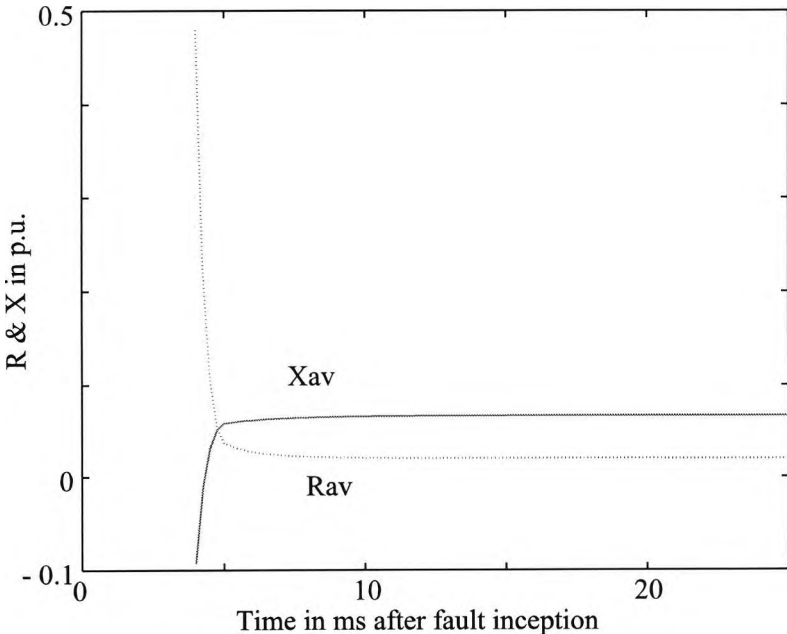


Fig. 3.13 Impedance measurement with fault inception angle = 0°

In Fig. 3.14 and 3.15, the fault is at 10% of line length. Local end SCL is 5 GVA and the power flow is 100 MW from the local end to the remote end.

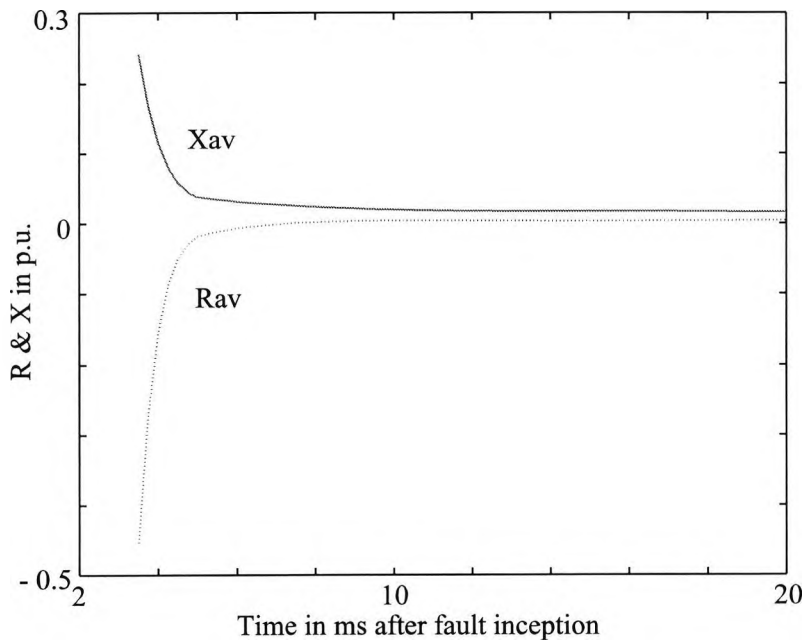


Fig. 3.14 Impedance measurement with fault inception angle = 90°

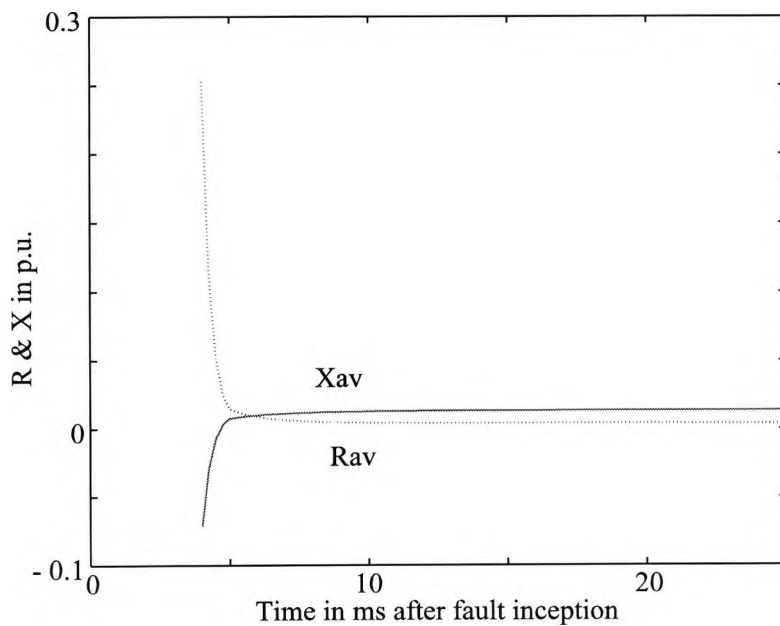


Fig. 3.15 Impedance measurement with fault inception angle = 0°

3.6.2 Phase-to-Phase Faults

In Fig. 3.16 and 3.17, the fault is at 90% of line length. Local end SCL is 5 GVA and the power flow is 100 MW from the local end to the remote end.

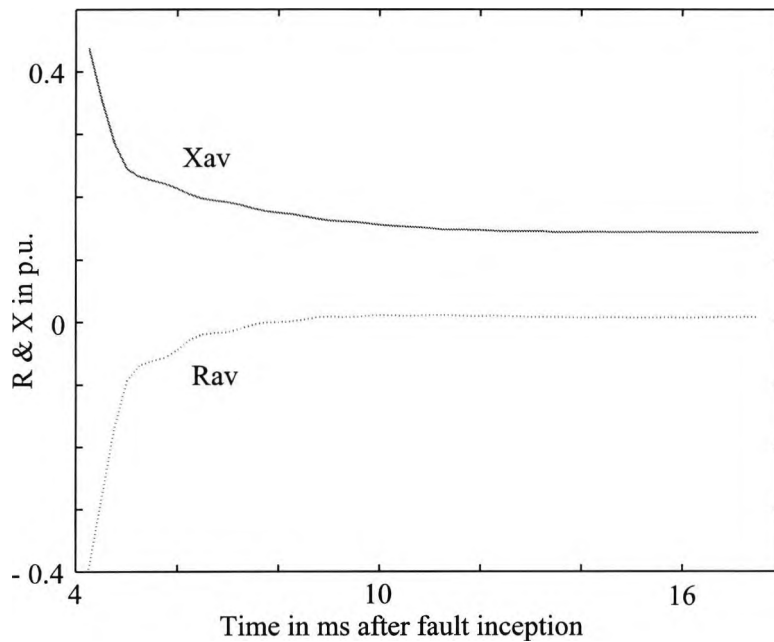


Fig. 3.16 Impedance measurement with fault inception angle = 90°

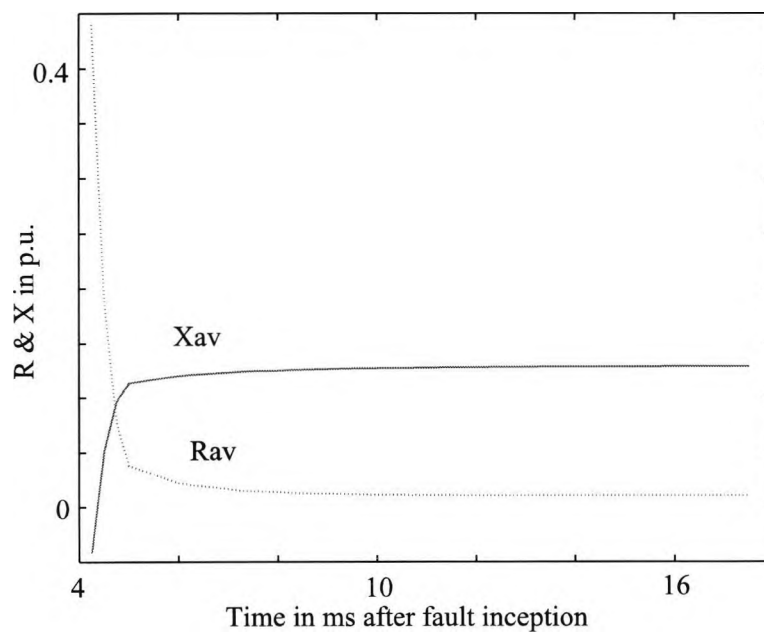


Fig. 3.17 Impedance measurement with fault inception angle = 0°

In Fig. 3.18 and 3.19, the fault is at 50% of line length. Local end SCL is 5 GVA and the power flow is 100 MW from the local end to the remote end.

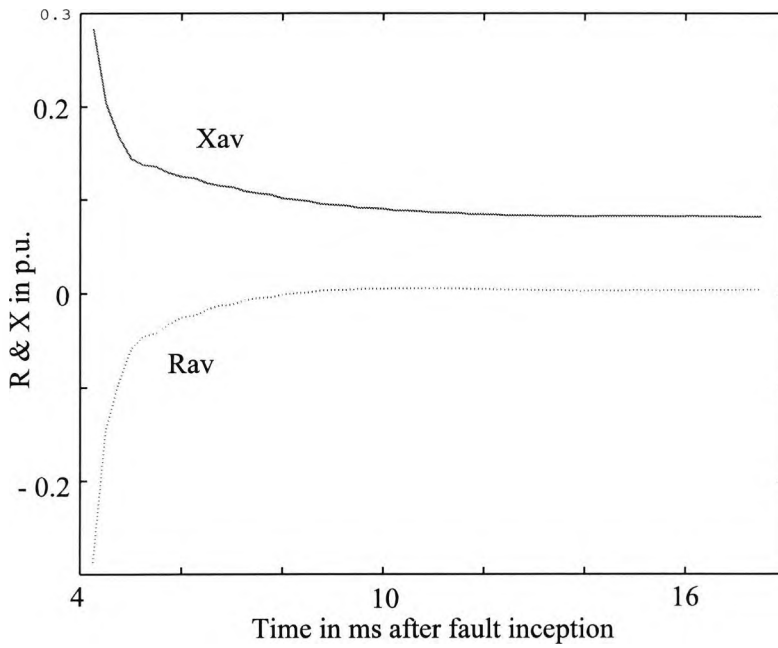


Fig. 3.18 Impedance measurement with fault inception angle = 90°

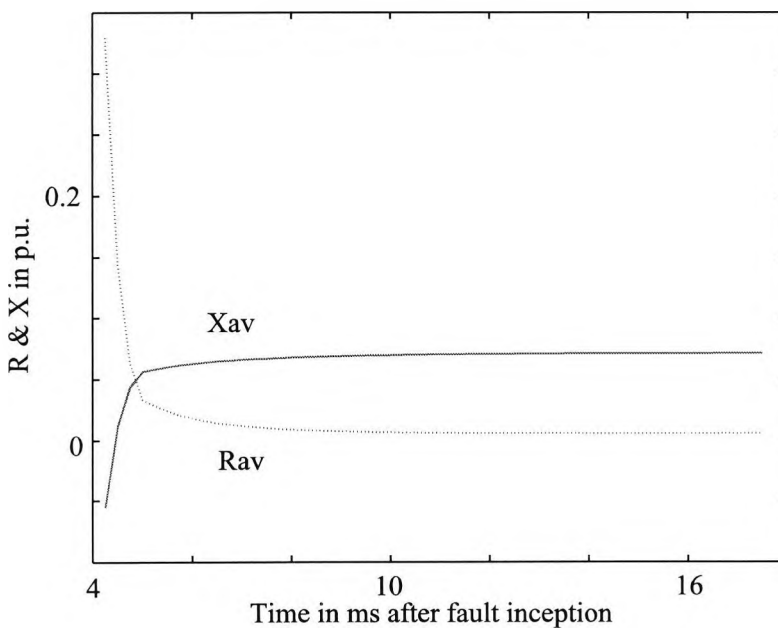


Fig. 3.19 Impedance measurement with fault inception angle = 0°

In Fig. 3.20 and 3.21, the fault is at 10% of line length. Local end SCL is 5 GVA and the power flow is 100 MW from the local end to the remote end.

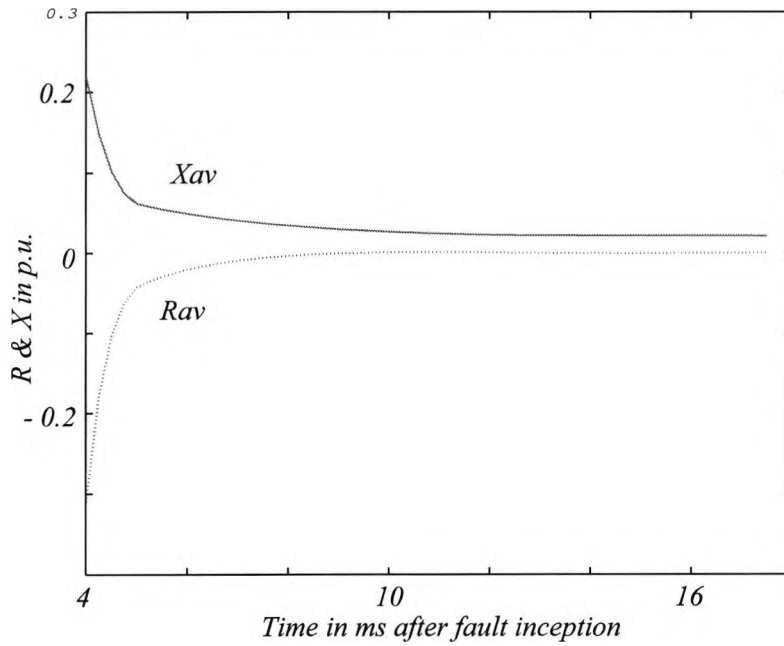


Fig. 3.20 Impedance measurement with fault inception angle = 90°

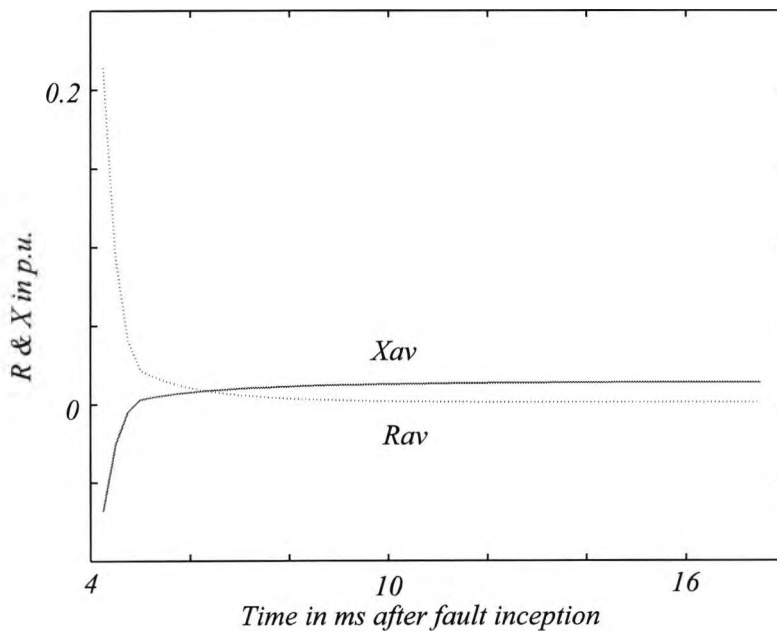


Fig. 3.21 Impedance measurement with fault inception angle = 0°

3.6.3 Three Phase Faults

In Fig. 3.22 to Fig. 3.25, local end SCL is 5 GVA and the power flow is 100 MW from the local end to the remote end. Fault inception angle is 45° in all cases.

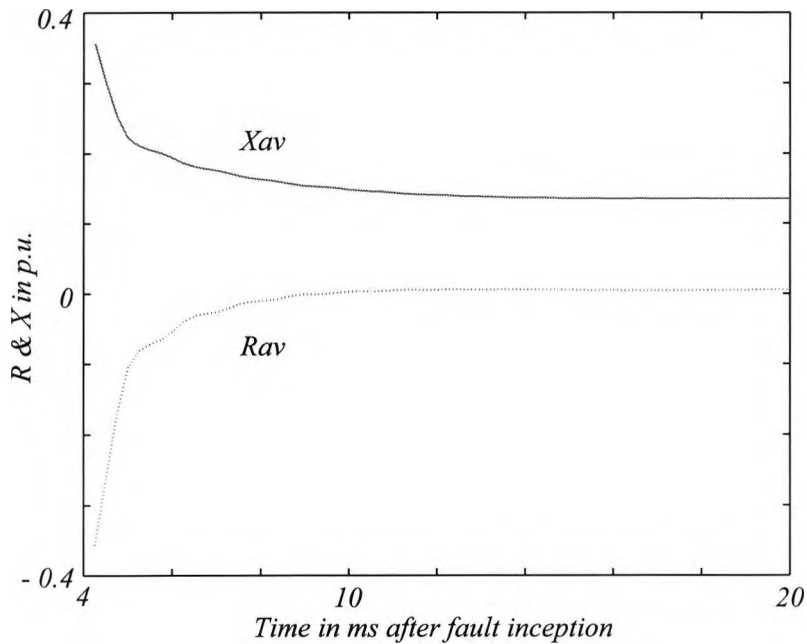


Fig. 3.22 Impedance measurement for fault at 90% of line length

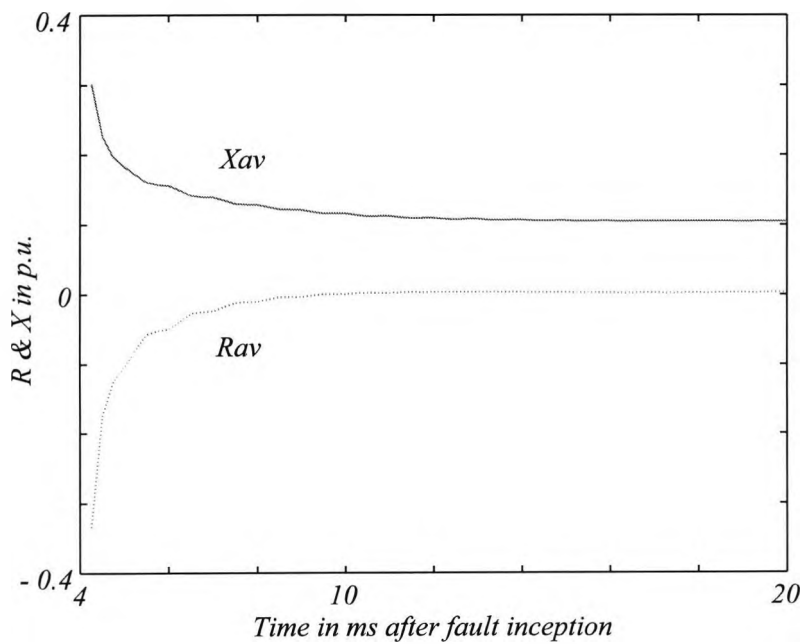


Fig. 3.23 Impedance measurement for fault at 70% of line length

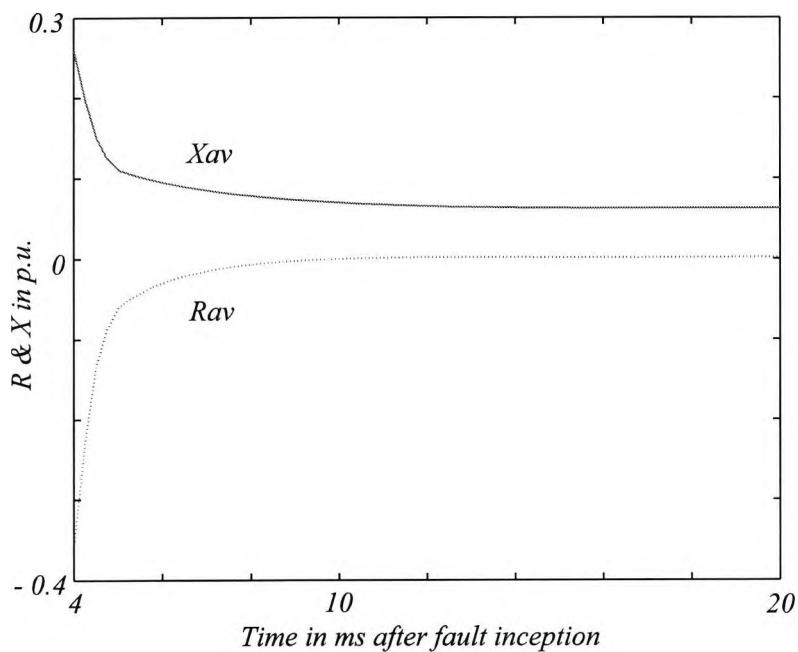


Fig. 3.24 Impedance measurement for fault at 40% of line length

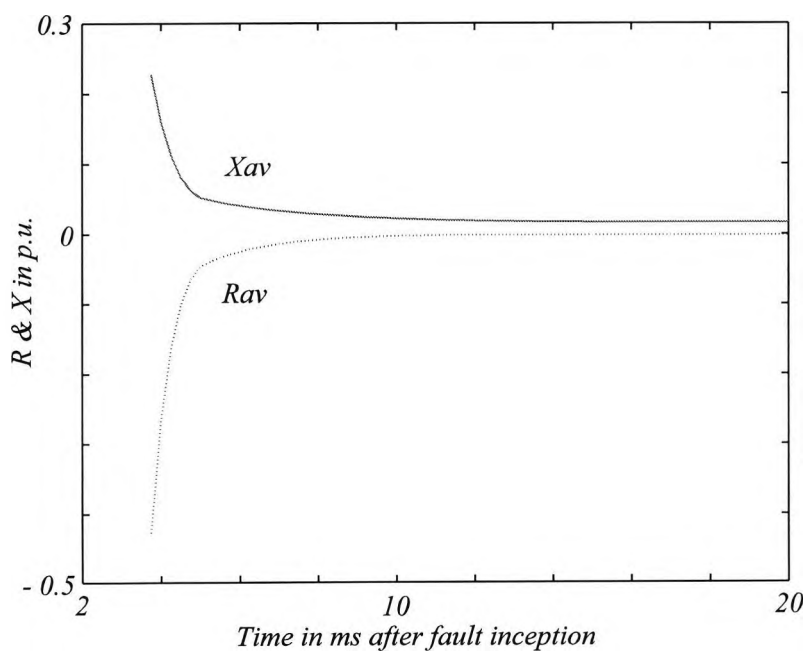


Fig. 3.25 Impedance measurement for fault at 10% of line length

3.7 ANALYSIS OF RESULTS

In general a fault inception angle of 90° will introduce maximum high frequency transients and reflection of travelling wave components. On the other hand, a fault inception angle of 0° will result in a maximum DC offset for fault currents. From the above results it is obvious that the algorithm handles both situations very well. Different fault types will not affect very much on the converging time of the algorithm. In all cases, the calculated impedances converged within 10 ms. Bear in mind that a very weak system is used for the simulations and in these cases normal protection will fail to work. The variable window algorithm is thus performing very well and half cycle detection has been achieved. In a normal system, the response of the algorithm would be better.

The modified variable window algorithm has solved the stability problems during the initial fault inception period. The modified algorithm is very stable under different system conditions and fault types. At the same time it gives a reliable and quick response while maintaining accurate measurements. The moving average technique can further improve the stability of the algorithm and it also helps in speeding up the convergence of the algorithm.

CHAPTER IV**DEVELOPMENT OF
THE ADAPTIVE WINDOW LENGTH ALGORITHM****4.1 THE NEED OF ADAPTIVE WINDOW LENGTH FOR RELAYING ALGORITHM**

Substantial research work towards better algorithms has been carried out for more than 20 years [9, 13]. The differential equation based algorithm [3] and Fourier Transform based algorithms [4], are widely accepted by the protective relaying industry because of their inherent advantages. However, disadvantages still remain to be overcome. The differential equation based algorithms exhibit poor high frequency characteristics so that filters with significant time delay are required. The Fourier Transform algorithm possesses good frequency characteristics, but the presence of DC component adversely affects the calculation accuracy.

Algorithms based on a differential equation combined with a Fourier transform [8, 12, 16, 17, 22] present a better solution for both DC and high frequency rejection. However problems still arise because of the utilisation of fixed data windows. A short data window does not satisfy the reach accuracy requirement, on the other hand, a long data window limits the operating speed.

A new variable data window length algorithm based on the first order differential equation and a finite transform has been developed [28]. The window size increases successively after a fault occurs until a preset desired length is reached. This algorithm is less affected by the decaying DC component and the high frequency characteristics depend on the window size. The only disadvantages of this algorithm is its instability during the initial period after fault inception and its response to different types of disturbances is different. A further development is therefore carried out by introducing a fixed pre-fault window length [32] to solve the initial stability

problem. The use of moving average technique [32] also helps to reduce transient oscillations during on-line measurements.

The use of a fixed window length algorithm will lead to various problems in speed, accuracy, and stability in measurement. In general the use of a short post-fault window length will lead to high speed operation but the measured output is sensitive to transient components in the power system and the output will have uncontrollable oscillations. Even the use of moving average technique cannot eliminate this completely. Using a long post-fault window length will of course give more accurate measurements and stable output, but the measured output needs more time to converge and will delay the relay operation. An algorithm whose post-fault window length is adaptive is thus required to be developed. In the developed adaptive window length algorithm which is an improved version of the fixed window length algorithm, a fixed data window length is used in the pre-fault period and the method has been discussed in detail in Chapter 3. A new fault detection technique which is superior than the present techniques is discussed in this chapter. On fault inception, the sampling window length will be increased automatically. The final post-fault window length is not constant but the most suitable one will be selected under different system conditions. The use of moving average technique further improves the performance.

4.2 THEORY OF THE ADAPTIVE WINDOW LENGTH ALGORITHM

The flow chart of the algorithm is shown in Fig. 4.1. During pre-fault period, a fixed short data window is used in the pre-fault period. In pre-fault conditions, only fundamental frequency components exist and DC and high frequency components are almost absent, a relatively short and fixed length data window is adequate to provide a stable output during the pre-fault period and during the initial period after fault inception. When a fault is detected, the window length will be increased in order to provide a stable output. For example, at the $(k)th$ sample, the window length is W_k . Then at the $(k+1)th$ sample, the window length will be increased to $(W_k + 1)$. As the data window length is steadily increased as new sets of sampled data become available, the filtering feature becomes more efficient. The most suitable window length depends on various factors and is affected by the local and remote source capacities, line length, fault

location, nature of fault, and the fault resistance. These will be discussed in the following sections.

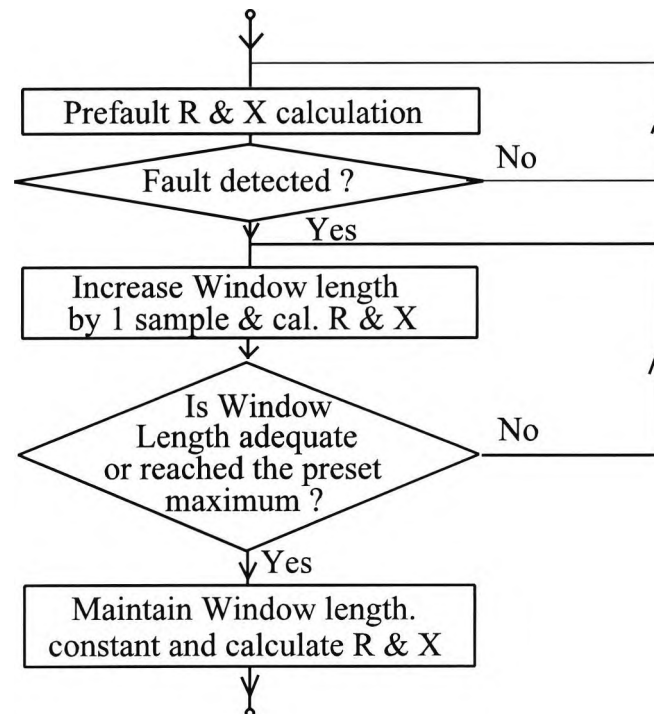


Fig. 4.1 Flow chart of the adaptive window length algorithm

4.3 FAULT DETECTION AND STARTING OF VARIABLE WINDOW ALGORITHM [33]

In conventional schemes, relay starting is carried out either by overcurrent or impedance starting. In EHV transmission lines, the fault current may be only slightly larger than full load current, especially under high resistance faults and overcurrent starting may fail. Impedance starting will face similar problems. In this study, an effective method is developed to start the variable window length algorithm.

The magnitude of the impedance at sample k can be calculated from

$$Z_{av}(k) = abs[R_{av}(k) + jX_{av}(k)] \quad 4.1$$

where Z_{av} is the average magnitude of measured impedance.

R_{av} is the average value of resistance measured over recent n_{av} samples.

X_{av} is the average value of reactance measured over recent n_{av} samples.

During the pre-fault period, the impedance calculated is very stable. On fault inception, owing to the DC offset and induced transient, the computed impedance will become unstable. Comparing a calculated magnitude of impedance with the value in the previous sample as shown in eqn. 4.2, a fault can be deemed to have occurred somewhere in the system if Z_{diff} exceeds a threshold limit $Z_{diff\ set}$. The moving average value is again used to smooth down transient fluctuations.

$$Z_{diff} = abs\left[\frac{Z_{av}(k-1) - Z_{av}(k)}{Z_{av}(k)}\right] \quad 4.2$$

Simulations were carried out under different system configurations and different load conditions. The results show that this method is very reliable in fault detection and is superior to conventional techniques.

4.4 VARIABLE WINDOW PROCESSING TECHNIQUE

When a fault is detected, the window length will be increased in order to provide a stable output. Again taking V_{r1} as an example, the $(k+1)th$ evaluation has been derived in eqn. 3.3 and is reproduced below

$$V_{r1}(k+1) = V_{r1}(k) + v(t_{k,1})C(k+1) \quad 4.3$$

As the data window length is steadily increased as new sets of sampled data become available, the filtering feature becomes more efficient.

4.5 FINAL WINDOW LENGTH

In the proposed method, the value of Z_{diff} is again used to determine the final window length. When the calculated impedance has converged, the difference of Z_{av} between successive samples will be reduced to a very small value. Thus, when Z_{diff} is less than the limit $Z_{diff\ lim}$, the window length will stop increasing and a constant window length mode is initiated. If Z_{diff} does not converge, the final post-fault window length will eventually stop at a pre-set maximum.

When the final window length has been reached, the four discrete integrals V_{r1} , V_{r2} , I_{r1} , and I_{r2} will be changed back to recursive evaluations. For example

$$V_{r1}(k+1) = V_{r1}(k) + v(t_{k+1})C(k+1) - v(t_{k+1-N_{fin}})C(k+1-N_{fin}) \quad 4.4$$

where N_{fin} is the number of samples in the post-fault final window length.

4.6 SIMULATION SYSTEM LAYOUT

Analysis has been carried out on a three-source 400 kV system shown in Fig. 4.2. The length of transmission line is 125 km between Local and Remote Systems. The total positive sequence impedance of the line (Z_{ll}) is $37.5 \angle 86^\circ \Omega$. The total zero sequence impedance of the line (Z_{0l}) is $136.6 \angle 69^\circ \Omega$. The length between Local to External and between Remote to External are both 200 km. The impedance parameters per kilometre for all 400 kV lines are the same.

E_L , E_R and E_E are the equivalent potentials at the local, remote and external ends respectively. $E_R/E_L = h_{RL} e^{j\delta_{RL}}$, $E_E/E_L = h_{EL} e^{j\delta_{EL}}$, and let Z_{SL} , Z_{SR} and Z_{SE} be the source impedances. Z_L is the line impedance, not referring to specific sequence component; p is the proportion of line length from the relaying point to the fault. R_f is the fault resistance. A fault is applied on the transmission line between local and remote ends.

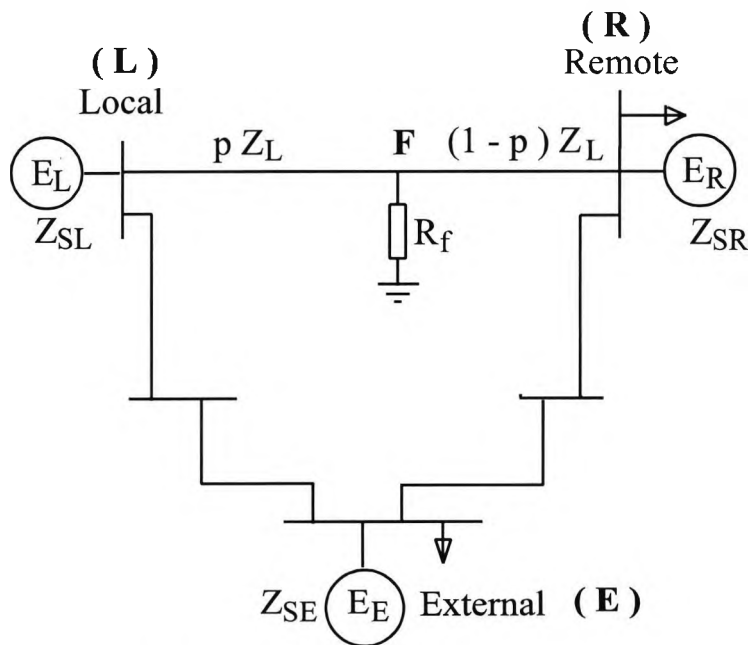


Fig. 4.2 Three source system model

4.7 SIMULATION RESULTS

Single-phase-to-earth faults and phase-to-phase faults are simulated by using the Electro-magnetic Transient Program (EMTP) at different locations on the line between local and remote ends with a maximum fault resistance of 200Ω . Different source capacities and fault inception angles are also considered. A sampling rate of 4 kHz is used. A pre-fault window length of 24 samples (6 ms) is used instead of 4 ms as mentioned in Chapter 3 as it will give more stable pre-fault calculations without increasing the amount of computations. The maximum post-fault window length is 80 samples (20 ms). In the figures shown in 4.7.1 to 4.7.5, 1 p.u. window length stands for 20 ms. The values of n_{av} and $Z_{diff\ set}$ used are 10 and 0.007 respectively. n_{av} is the number of samples to be averaged over and $Z_{diff\ set}$ is the threshold limit of Z_{diff} as defined in eqn. 4.2.

4.7.1 Single Phase Faults in a Strong System

The response of this algorithm under a strong local, remote and external source of 35 GVA short circuit level (SCL) is studied. Single-phase-to-earth faults are simulated at 10%, 50%, and 90% of line length to study the effects of close-in faults and remote faults. Three fault inception angles are considered, voltage peak (90°) which represents maximum reflected travelling wave components, voltage zero (0°) which represents maximum fault current offset and hence maximum DC components, and an inception angle of 45° which represents a combination of reflected travelling wave components and fault current offset. The scales used for v , i , R and X are different for different cases because of large difference between the cases but the same per unit scale is used for per unit window length, fault status and Z_{diff} .

- i) Single-phase-to-earth fault at 10% of line length, $R_f = 0\Omega$, and fault inception angle at 90° . Pre-fault power flow from local to remote is 731 MW.

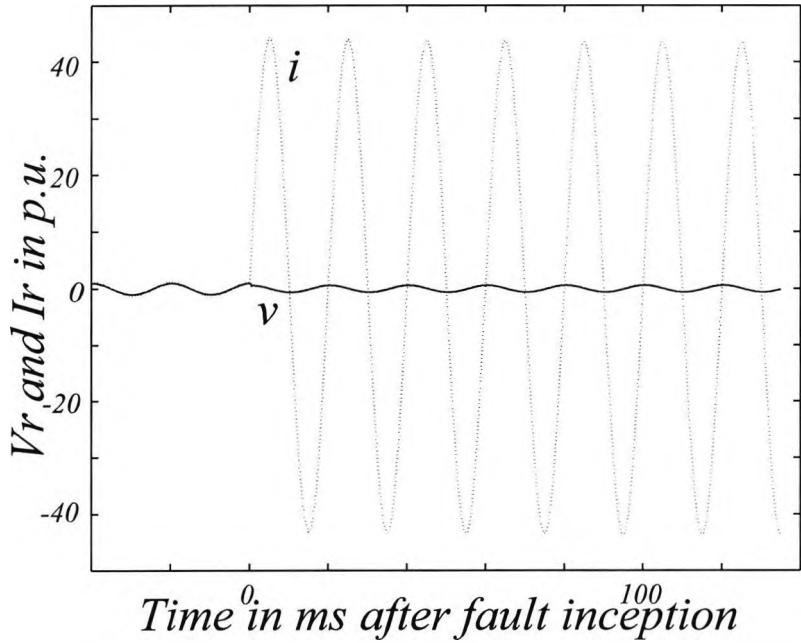


Fig. 4.3 Voltage & current at relaying point for case 4.7.1.i

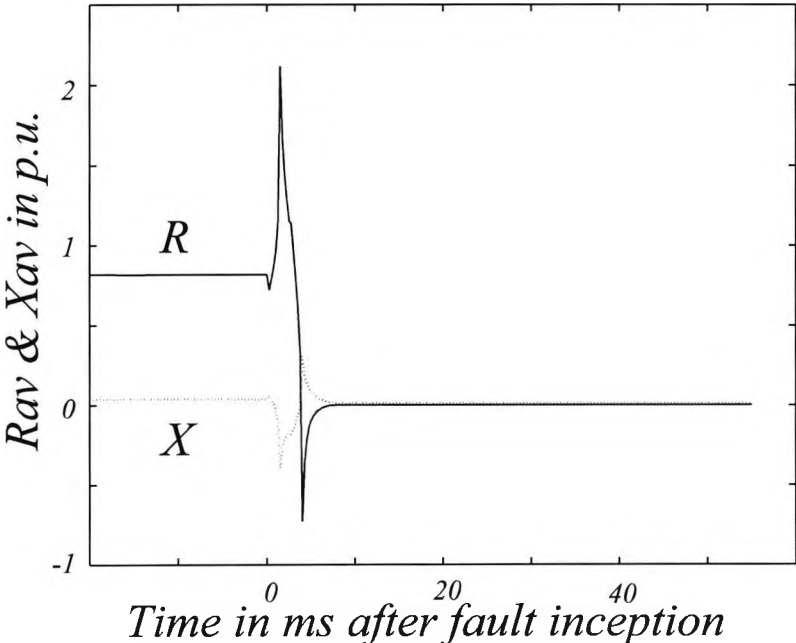


Fig. 4.4 Measured impedance for case 4.7.1.i

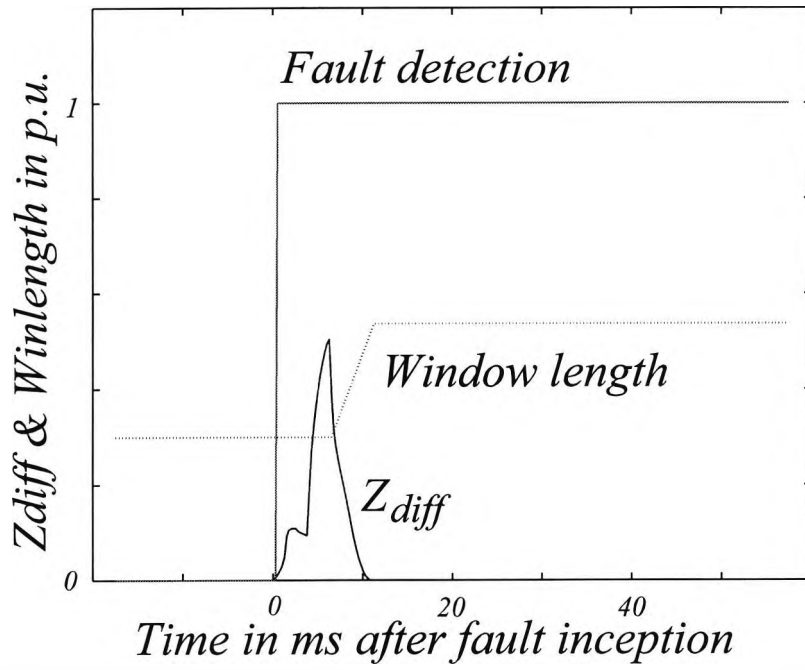


Fig. 4.5 Fault detection and changes of window length for case 4.7.1.i

- ii) Single-phase-to-earth fault at 10% of line length, $R_f = 0\Omega$, and fault inception angle at 0° . Pre-fault power flow from local to remote is 731 MW.

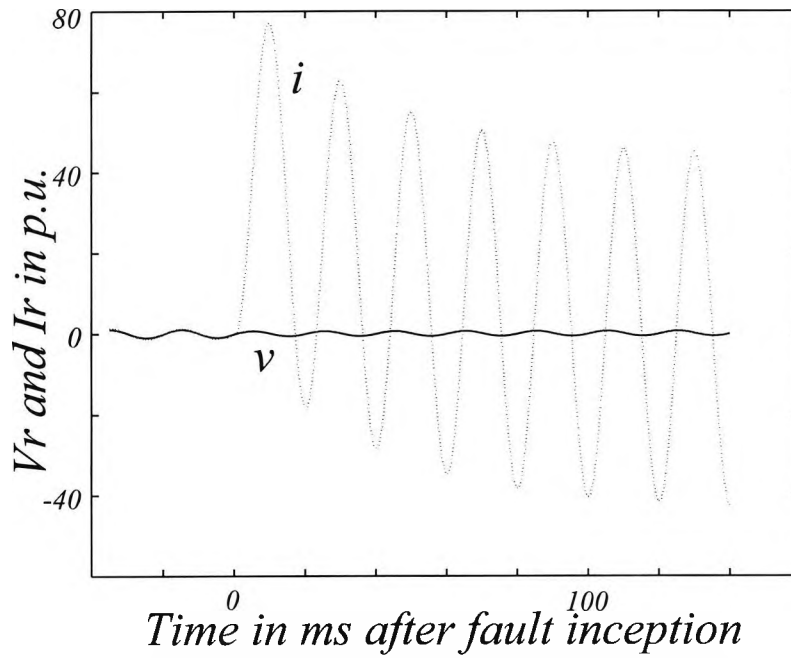


Fig. 4.6 Voltage & current at relaying point for case 4.7.1.ii

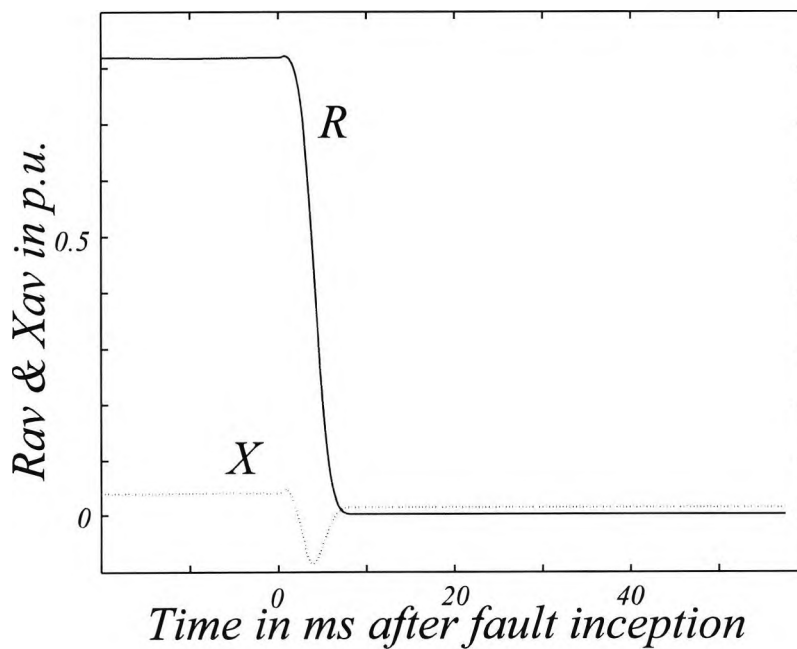


Fig. 4.7 Measured impedance for case 4.7.1.ii

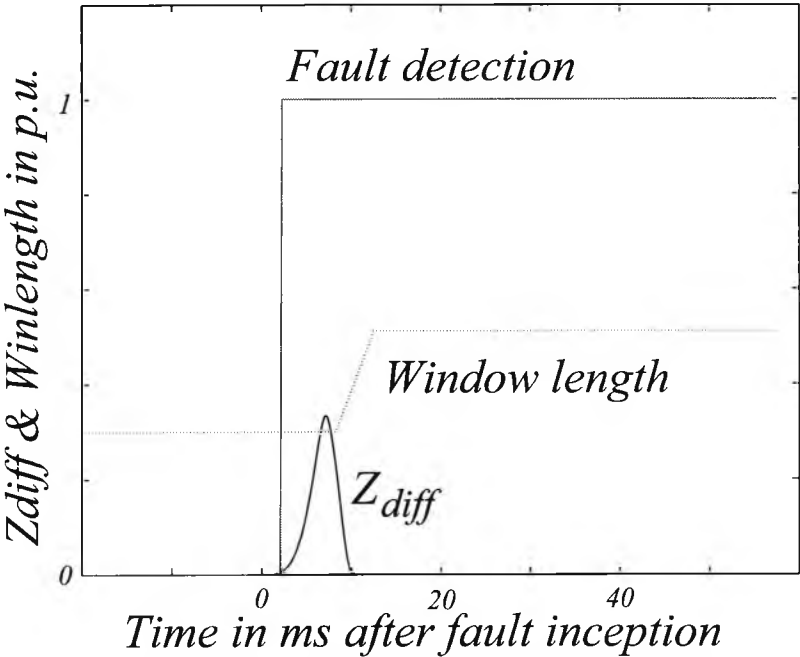


Fig. 4.8 Fault detection and changes of window length for case 4.7.1.ii

- iii) Single-phase-to-earth fault at 50% of line length, $R_f = 0\Omega$, and fault inception angle at 45° . Pre-fault power flow from local to remote is 1026 MW.

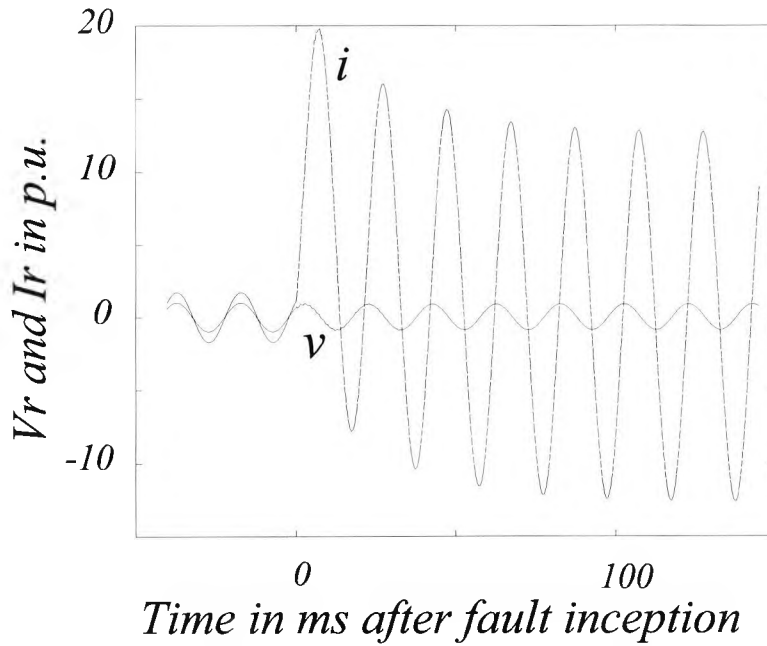


Fig. 4.9 Voltage & current at relaying point for case 4.7.1.iii

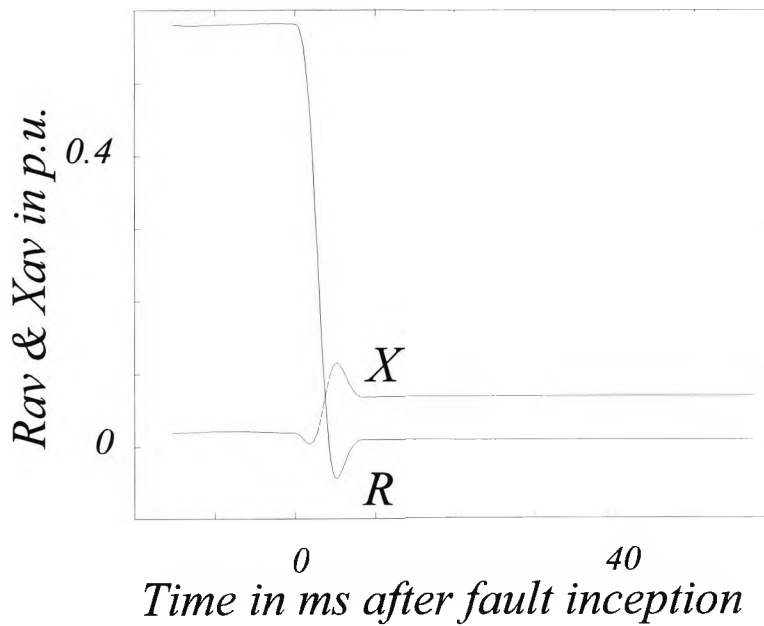


Fig. 4.10 Measured impedance for case 4.7.1.iii

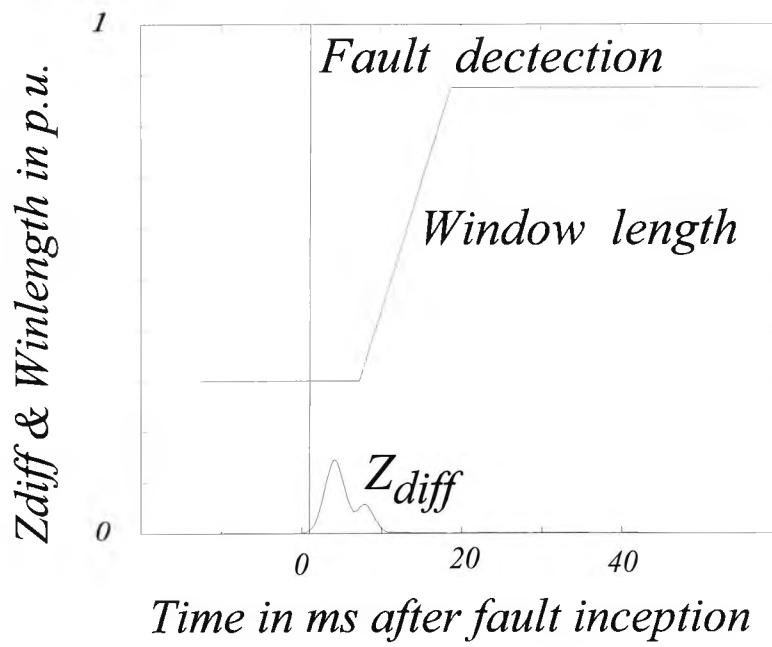


Fig. 4.11 Fault detection and changes of window length for case 4.7.1.iii

- iv) Single-phase-to-earth fault at 50% of line length, $R_f = 200\Omega$, and fault inception angle at 45° . Pre-fault power flow from local to remote is 1026 MW.

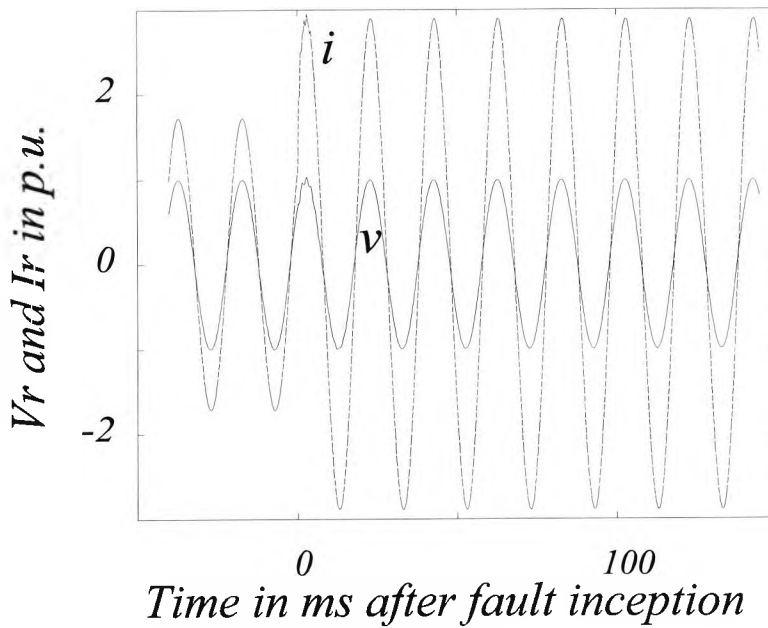


Fig. 4.12 Voltage & current at relaying point for case 4.7.1.iv

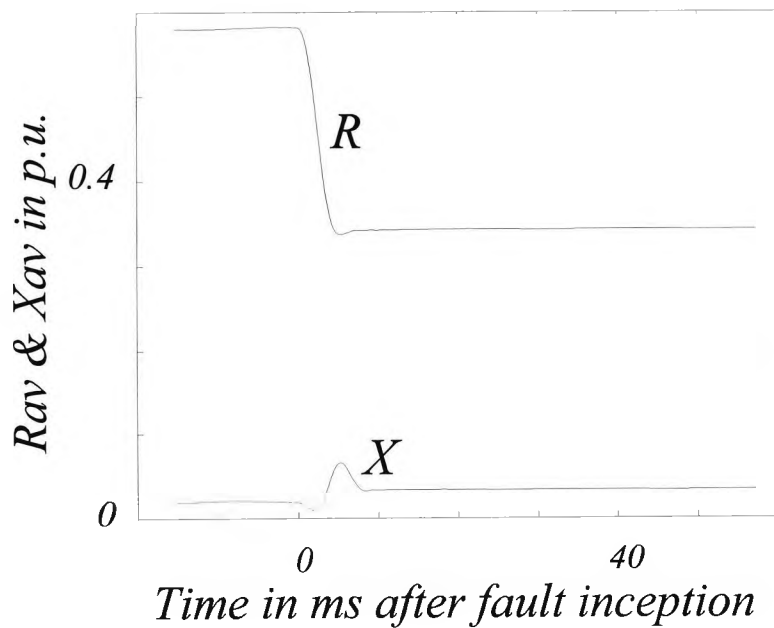


Fig. 4.13 Measured impedance for case 4.7.1.iv

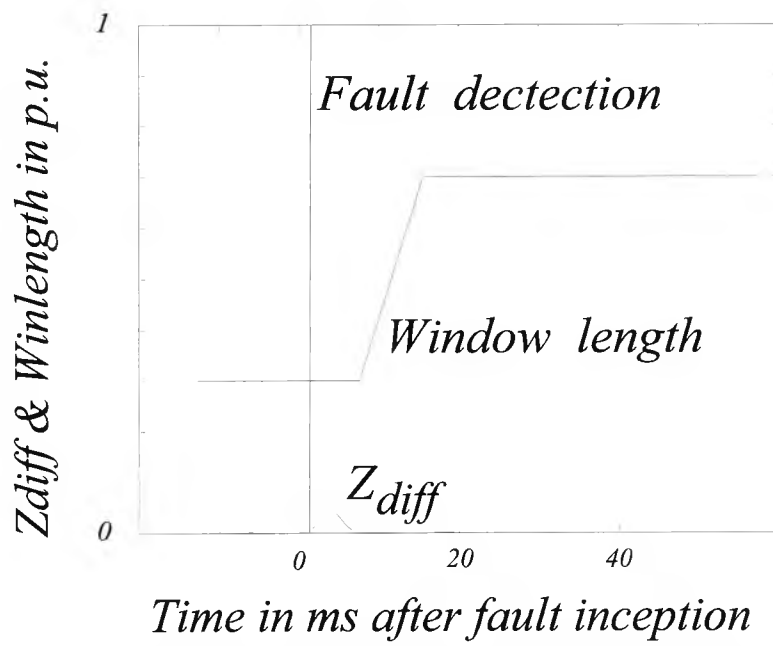


Fig. 4.14 Fault detection and changes of window length for case 4.7.1.iv

- v) Single-phase-to-earth fault at 90% of line length, $R_f = 0\Omega$, and fault inception angle at 90° . Pre-fault power flow from local to remote is 731 MW.

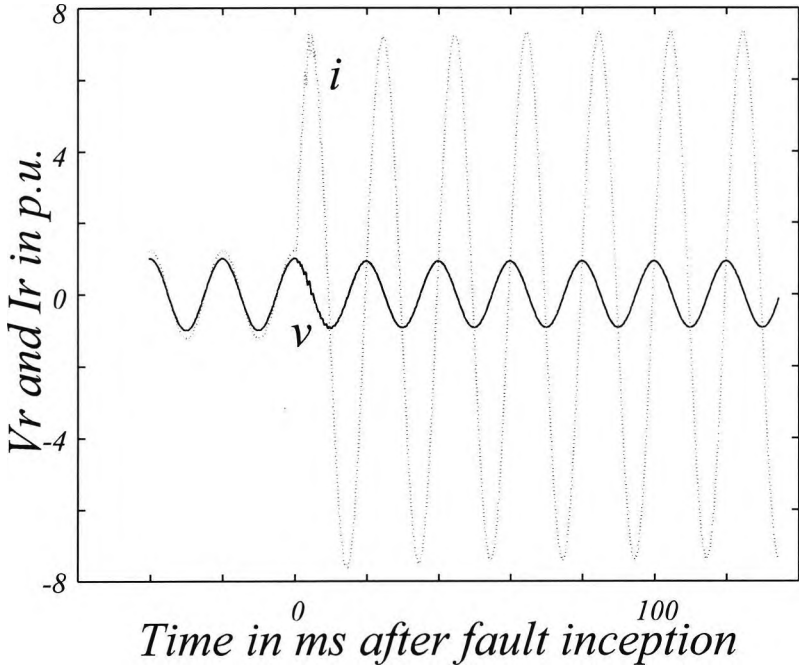


Fig. 4.15 Voltage & current at relaying point for case 4.7.1.v

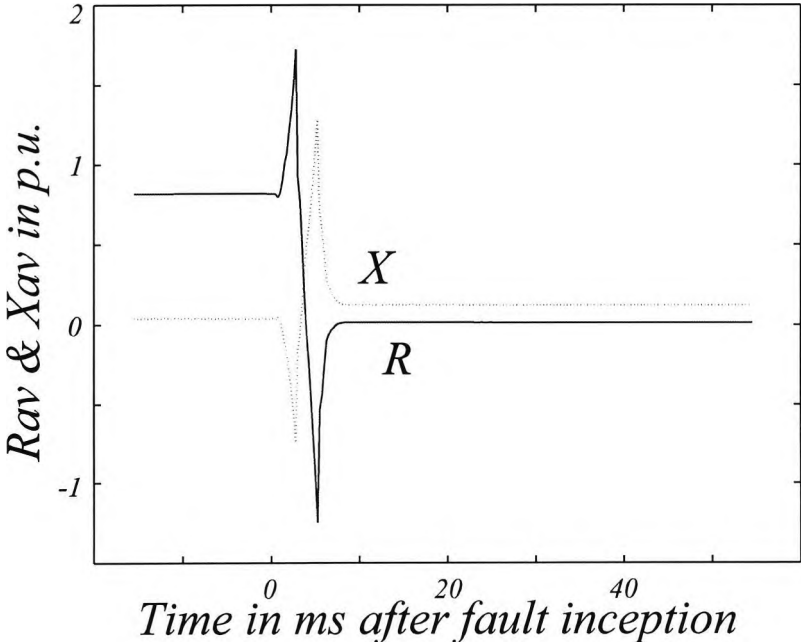


Fig. 4.16 Measured impedance for case 4.7.1.v

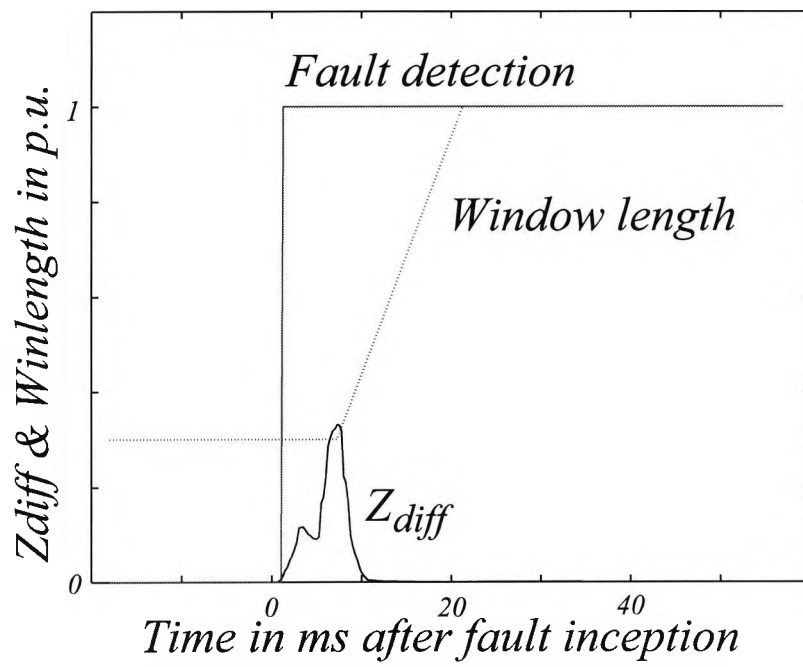


Fig. 4.17 Fault detection and changes of window length for case 4.7.1.v

- vi) Single-phase-to-earth fault at 90% of line length, $R_f = 0\Omega$, and fault inception angle at 0° . Pre-fault power flow from local to remote is 731 MW.

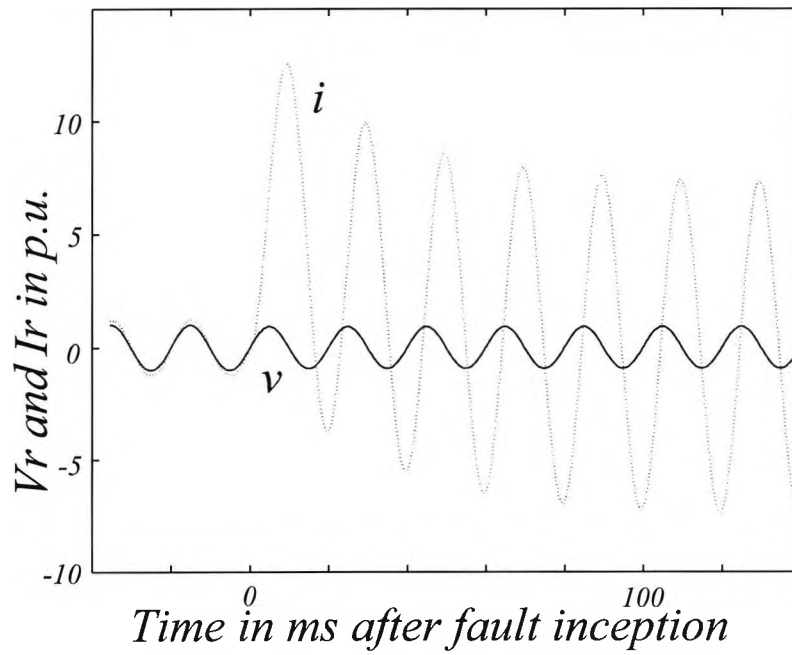


Fig. 4.18 Voltage & current at relaying point for case 4.7.1.vi

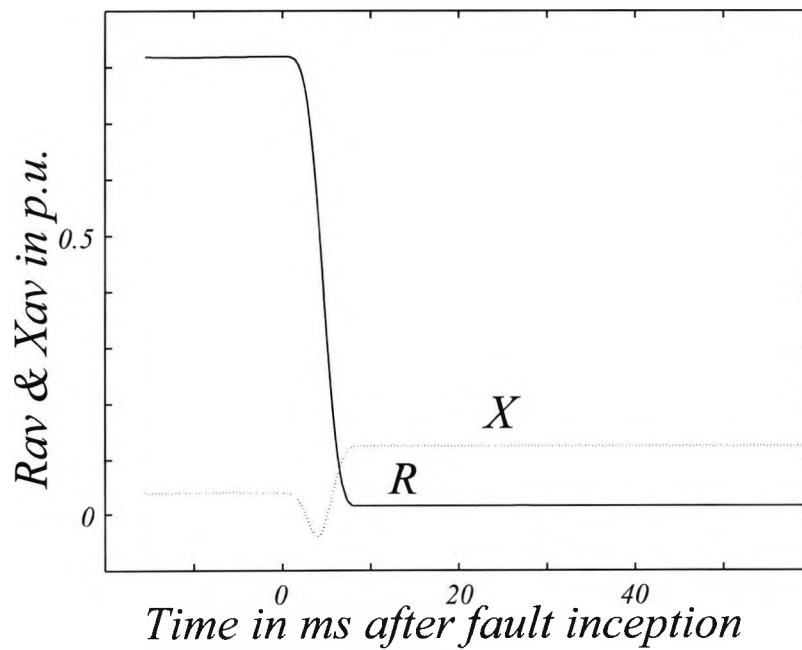


Fig. 4.19 Measured impedance for case 4.7.1.vi

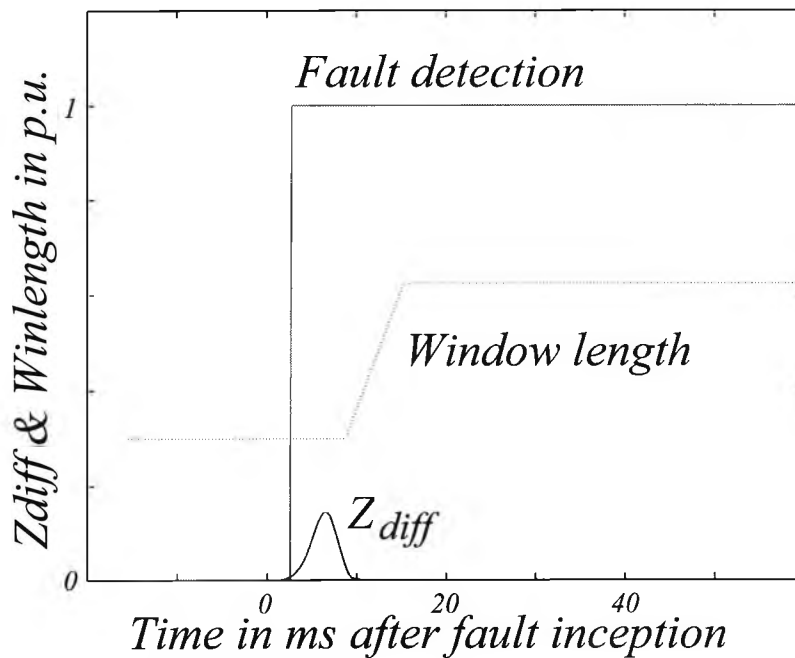


Fig. 4.20 Fault detection and changes of window length for case 4.7.1.vi

The value of Z_{diff} varies according to different conditions. In general it can be observed that there is a significant change of Z_{diff} for solid faults and the change of Z_{diff} is not so significant for high resistance faults, for example, Fig. 4.14. However it also shows that even under the most unfavourable situations, it is adequate to detect the occurrence of a fault. The above results show the fault detection works very well, all faults are detected within 3 ms of fault inception. The final post-fault window length, however, is related to the high frequency and reflected travelling wave components existing in the voltage and current waveforms and it varies between 0.5 to 1.0 p.u. The computed impedances in all cases converge in less than 10 ms.

4.7.2 Phase to Phase Faults in a Strong System

- i) Phase-to-earth fault at 10% of line length, $R_f = 0\Omega$, and fault inception angle at 45° . Pre-fault power flow from local to remote is 731 MW.

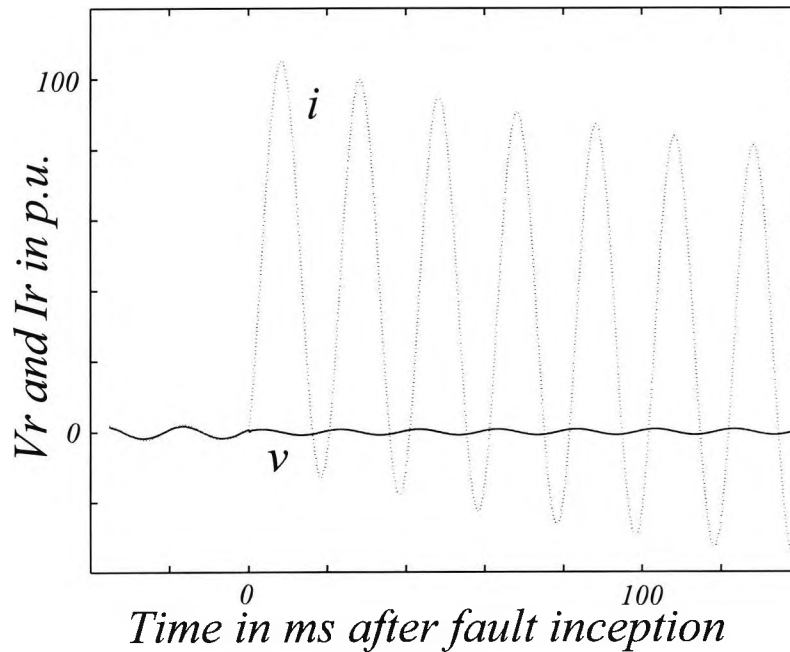


Fig. 4.21 Voltage & current at relaying point for case 4.7.2.i

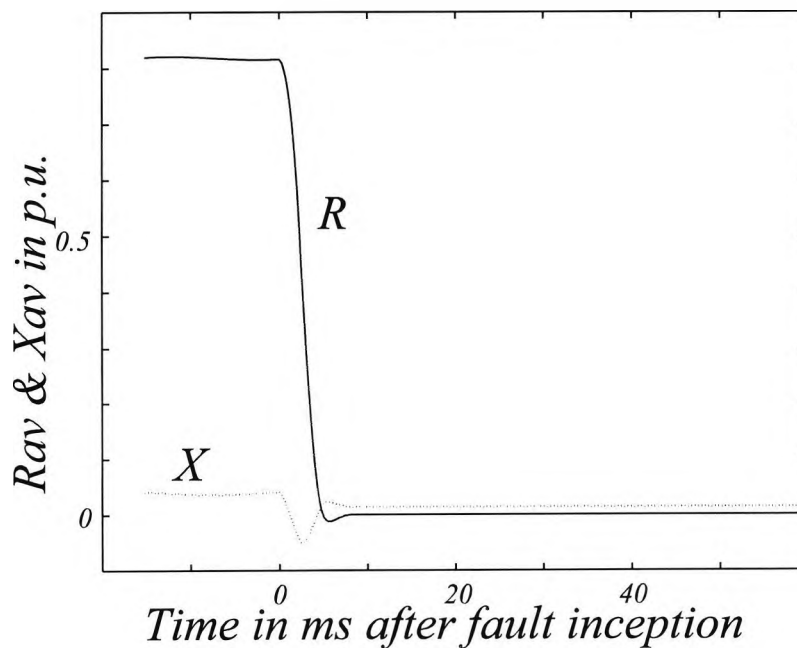


Fig. 4.22 Measured impedance for case 4.7.2.i

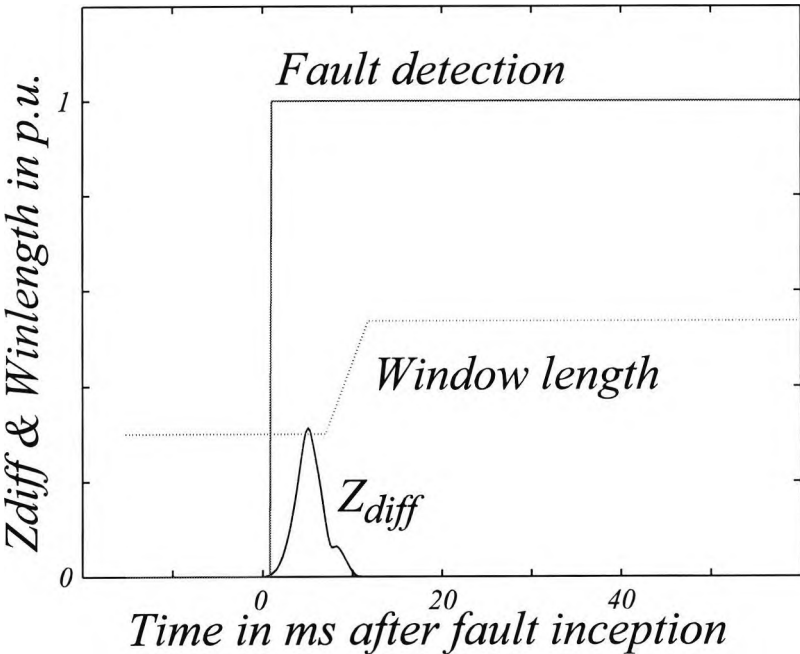


Fig. 4.23 Fault detection and changes of window length for case 4.7.2.i

- ii) Phase-to-earth fault at 90% of line length, $R_f = 0\Omega$, and fault inception angle at 45° . Pre-fault power flow from local to remote is 731 MW.

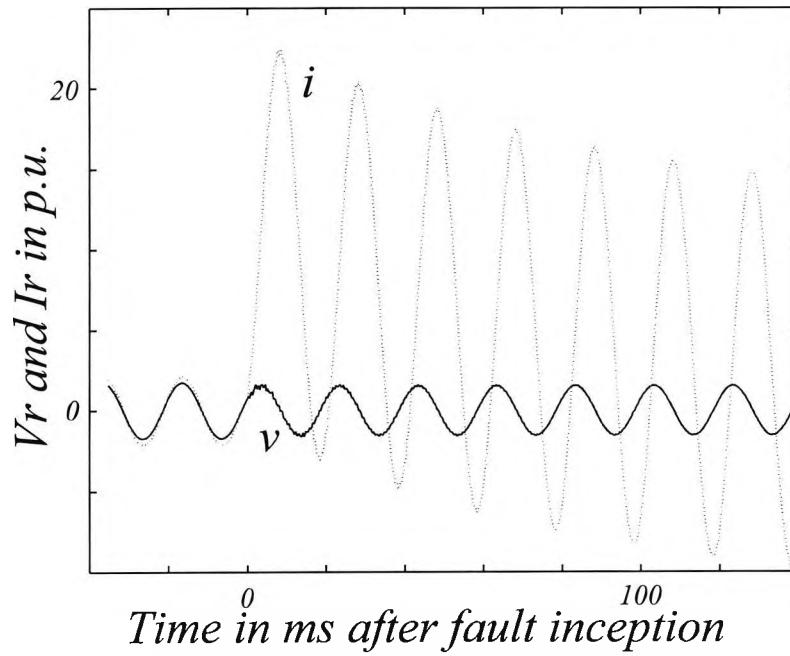


Fig. 4.24 Voltage & current at relaying point for case 4.7.2.ii

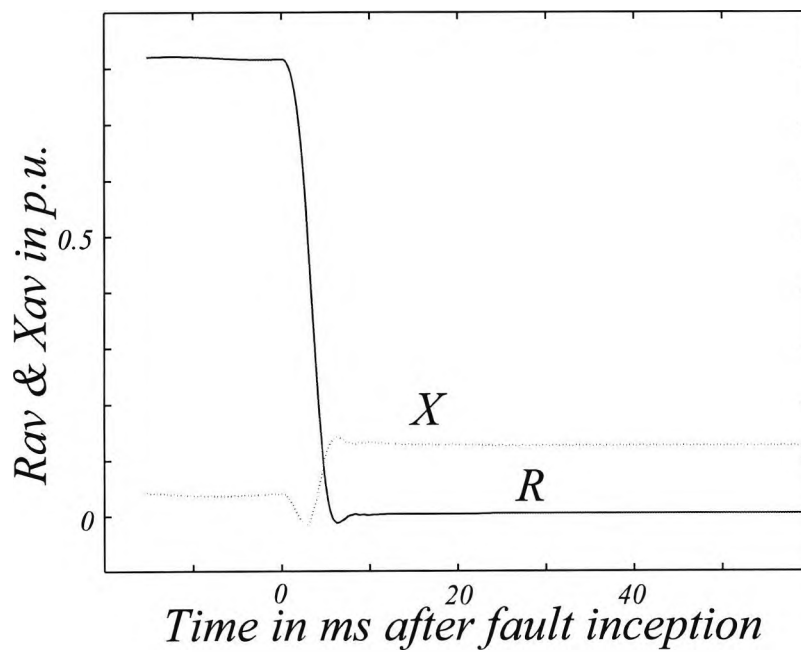


Fig. 4.25 Measured impedance for case 4.7.2.ii

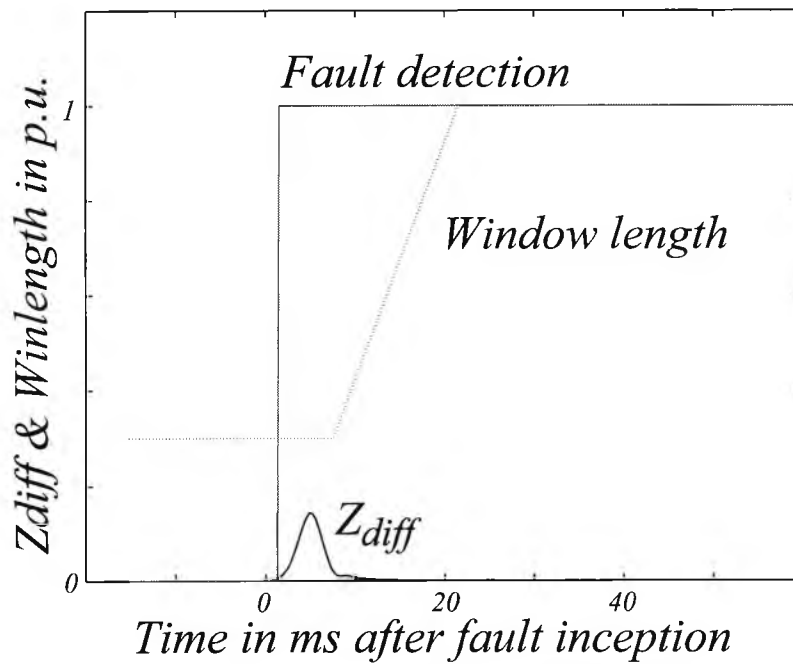


Fig. 4.26 Fault detection and changes of window length for case 4.7.2.ii

From Fig. 4.21 and 4.26, it can be seen that fault detection requires less than 3 ms. The final post-fault window length varies between 0.5 to 1.0 p.u. depending on the location of fault. In general, a longer window is needed for distant faults. In all cases, the computed impedances has converged in less than 10 ms.

4.7.3 Performance in a Weak Local System

Distance relays usually have difficulty in dealing with remote faults on a system with a weak local source and a strong remote source. In here a weak local source of 5 GVA SCL and a strong remote source of 35 GVA SCL is studied with fault applied at 90% of line length from the local end.

- i) Phase-to-earth fault at 90% of line length, $R_f = 0\Omega$, and fault inception angle at 90° . Pre-fault power flow from local to remote is 1026 MW.

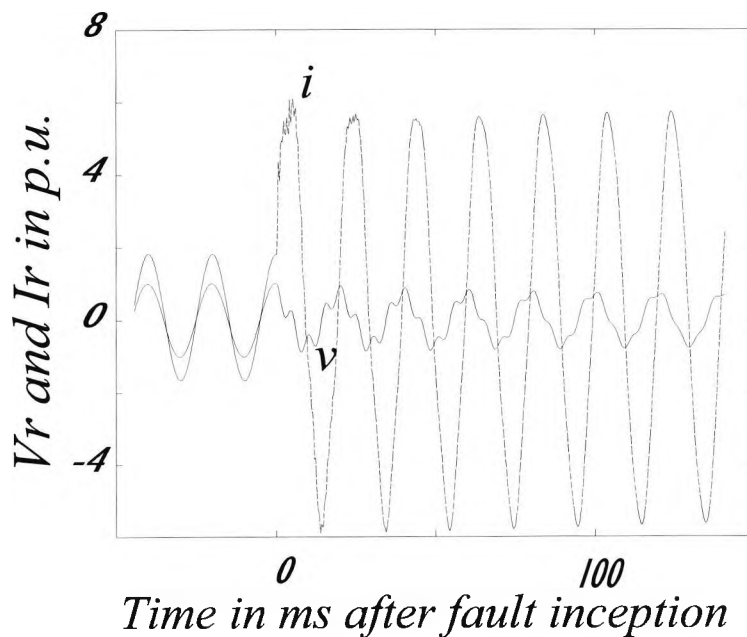


Fig. 4.27 Voltage & current at relaying point for case 4.7.3.i

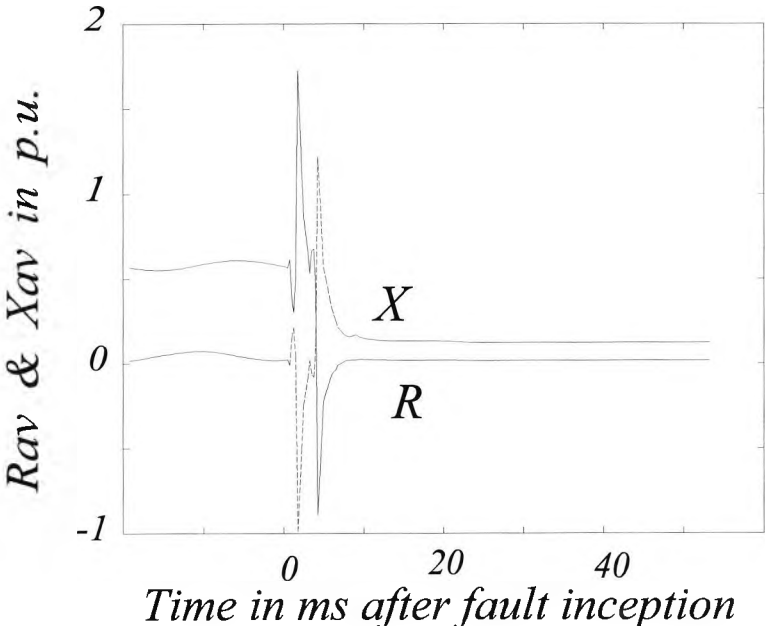


Fig. 4.28 Measured impedance for case 4.7.3.i

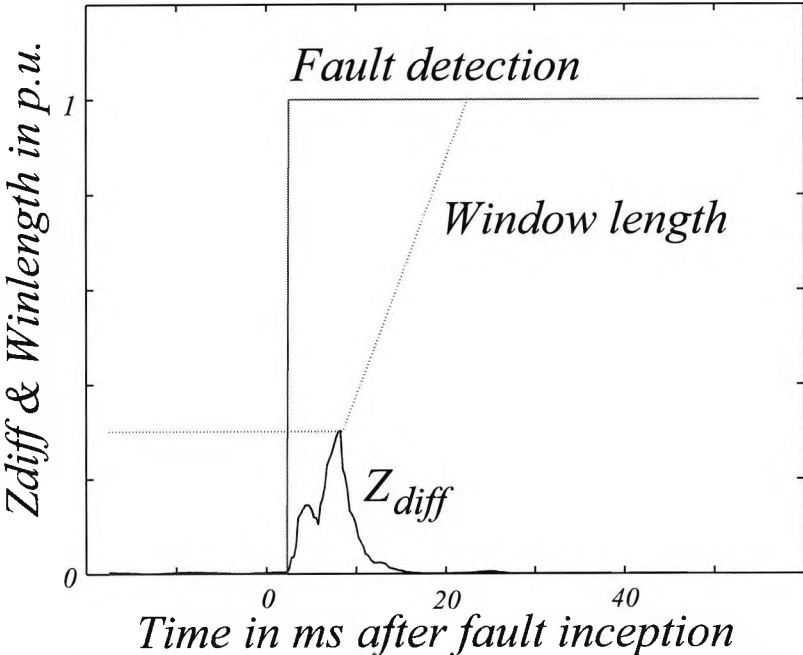


Fig. 4.29 Fault detection and changes of window length for case 4.7.3.i

- ii) Phase-to-earth fault at 90% of line length, $R_f = 0\Omega$, and fault inception angle at 0° . Pre-fault power flow from local to remote is 1026 MW.

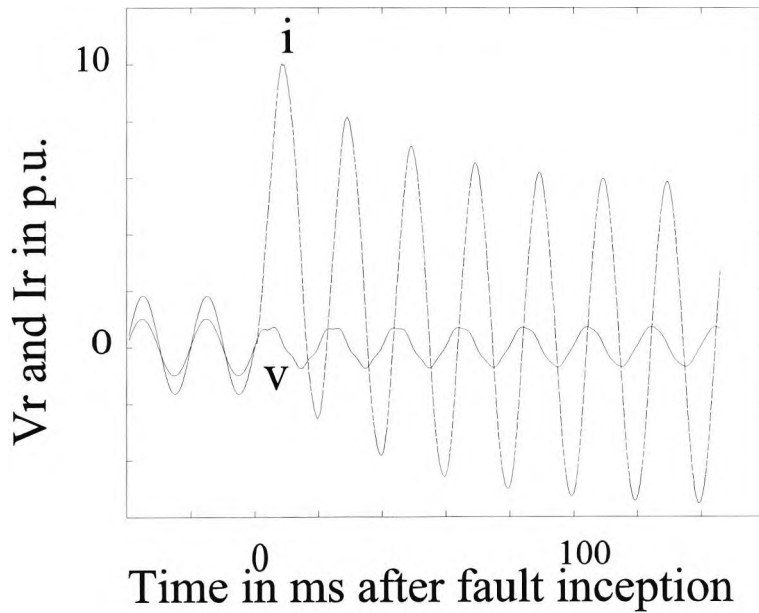


Fig. 4.30 Voltage & current at relaying point for case 4.7.3.ii

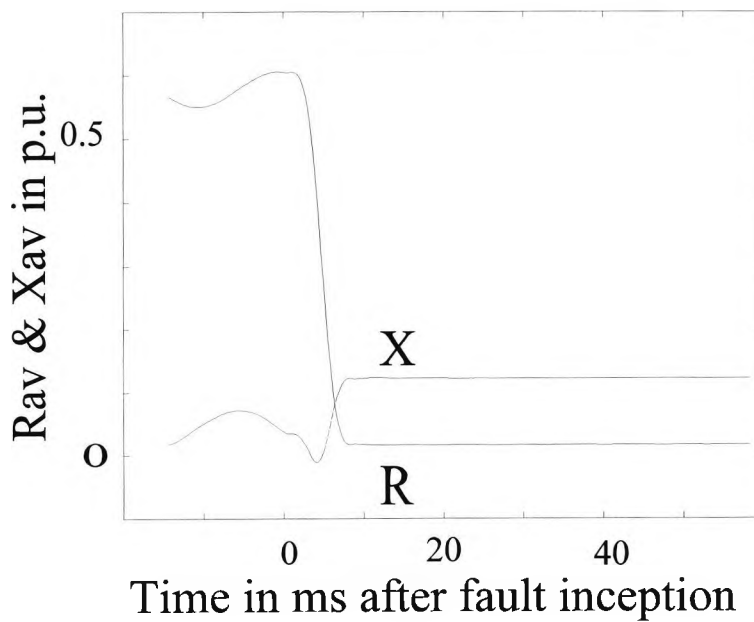


Fig. 4.31 Measured impedance for case 4.7.3.ii

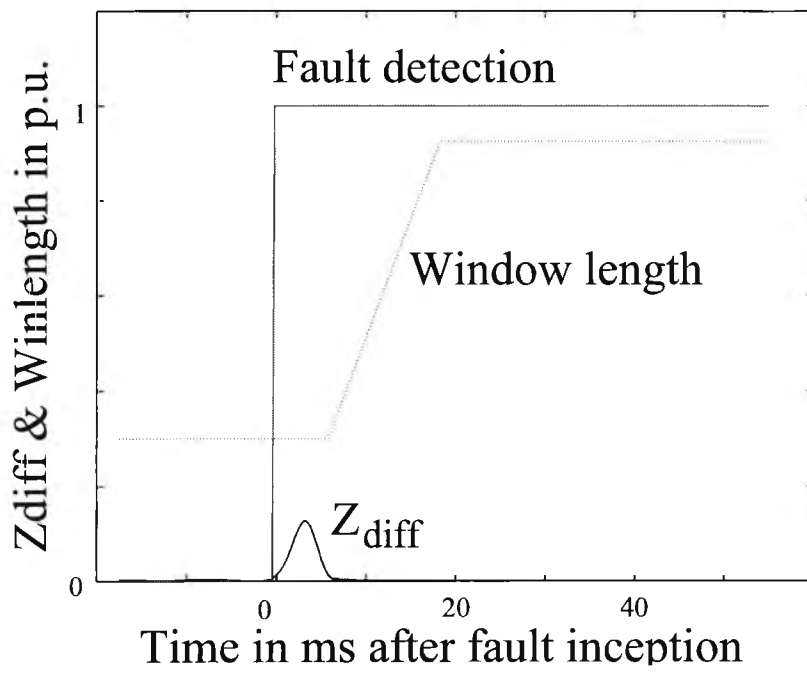


Fig. 4.32 Fault detection and changes of window length for case 4.7.3.ii

- iii) Phase-to-earth fault at 90% of line length, $R_f = 200\Omega$, and fault inception angle at 90° .
Pre-fault power flow from local to remote is 1026 MW.

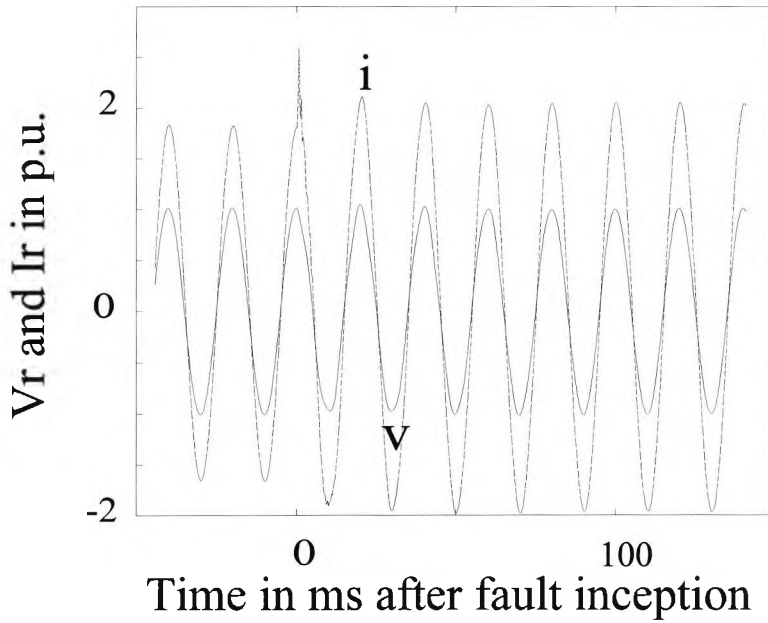


Fig. 4.33 Voltage & current at relaying point for case 4.7.3.iii

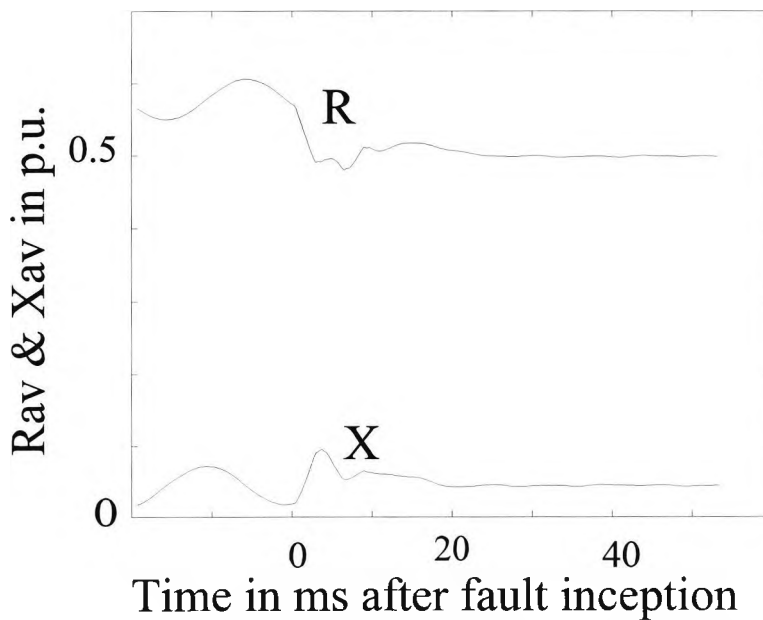


Fig. 4.34 Measured impedance for case 4.7.3.iii

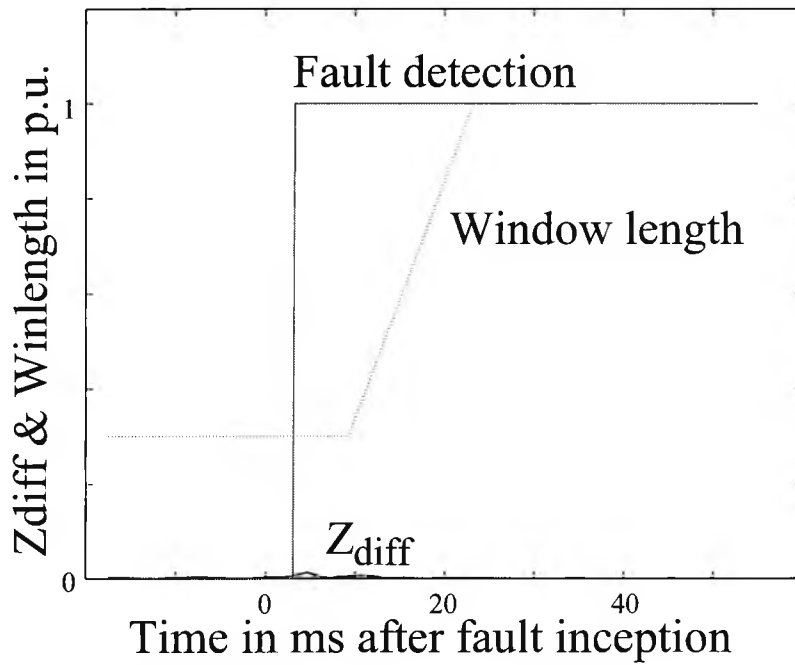


Fig. 4.35 Fault detection and changes of window length for case 4.7.3.iii

- iv) Phase-to-earth fault at 90% of line length, $R_f = 200\Omega$, and fault inception angle at 0° .
Pre-fault power flow from local to remote is 1026 MW.

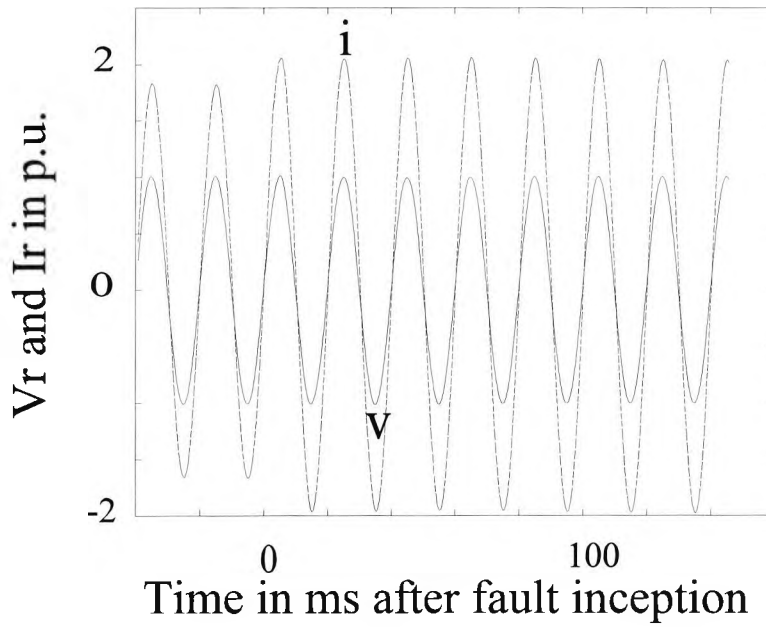


Fig. 4.36 Voltage & current at relaying point for case 4.7.3.iv

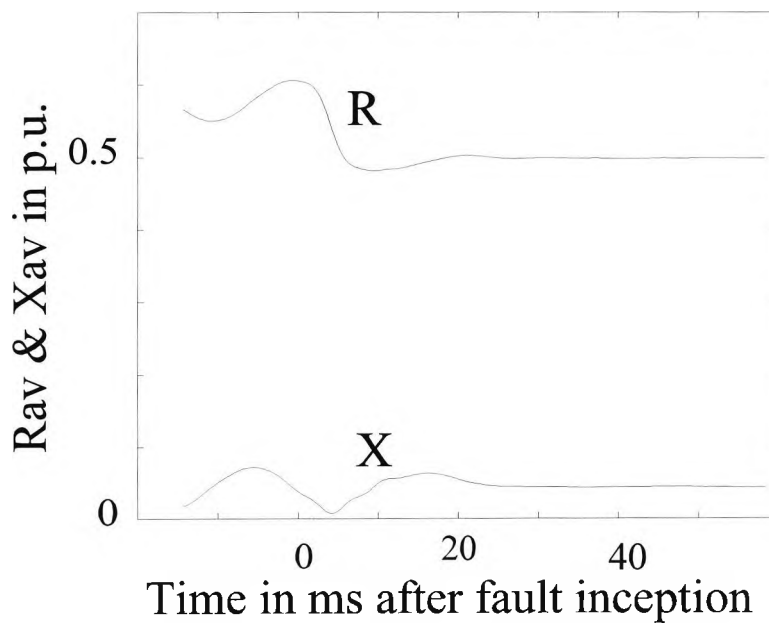


Fig. 4.37 Measured impedance for case 4.7.3.iv

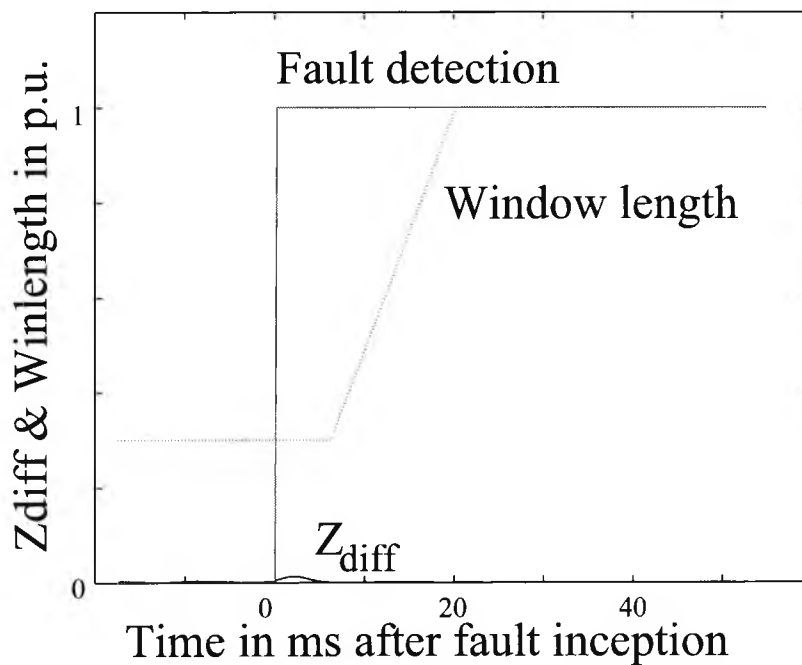


Fig. 4.38 Fault detection and changes of window length for case 4.7.3.iv

The results show that even under a high resistance fault at 90% from the local end as shown in Fig. 4.35, the fault is detected within 3 ms of fault inception. With a setting of $Z_{diff\ set}$ equal to 0.007, the value of Z_{diff} is adequate to detect the fault inception even for a high resistance earth fault at 90% of line length. As the relay for the cases in this section is handling an unfavourable condition, the final post-fault window length for each case is more than 0.9 p.u. For solid faults with zero fault resistance, the computed impedance has converged in less than 10 ms as shown in Fig. 4.28 and 4.31. For high resistance faults, the computed impedance has converged in less than 25 ms as shown in Fig. 4.34 and 4.37. Bearing in mind that a normal protection device will fail to operate under these unfavourable conditions, the performance of this algorithm is considered excellent.

4.7.4 Accuracy of the Algorithm

This algorithm, like other high speed algorithms, will be affected by errors caused by current and voltage transient distortions during the short window period. The error magnitude also depends on the current infeed from the far end and the fault resistance magnitude. In order to assess the accuracy, the impedance measured using the algorithm has been compared with calculated impedance values from steady state measurements of voltage and current at the relaying point under sustained fault conditions, (see Table 4.1).

Table 4.1
Accuracy of the adaptive variable window algorithm

Fault location	Inception angle (°)	$R_f \Omega$	Error %
90%	90°	0	-4.28
90%	0°	0	-4.24
90%	90°	200	0.77
90%	0°	200	1.54
50%	45°	0	-3.03
50%	45°	200	-0.01
10%	90°	0	-2.94
10%	0°	0	-3.01
10%	90°	200	1
10%	0°	200	1.07

4.8 PERFORMANCE OF THE ALGORITHM

The response time of the distance relay depends on the duration of the final post-fault window length. The adaptive window length algorithm gives the fastest fault detection possible for any prevailing condition. It has overcome the speed and stability problems which cannot be solved by a constant window length algorithm. The modified algorithm is very stable under different system conditions and fault types. At the same time it gives a reliable and quick response while maintaining accurate measurements for a wide range of system configurations and conditions.

The algorithm is very simple and easy to implement. The amount of computations is not excessive as most of it is of a recursive nature and only data updating is needed for every new sample obtained. Hardware implementation of this algorithm does not impose any constraint on the computational overheads as high speed microprocessors chips are available at a relatively low cost. The simulation results carried out on a 400 kV transmission line reveal that the adaptive window length algorithm is very suitable for EHV transmission line protection.

*CHAPTER V***USE OF ARTIFICIAL INTELLIGENCE TECHNIQUES
TO IDENTIFY HIGH RESISTANCE EARTH FAULTS****5.1 BACKGROUND**

In the light of recent developments in digital protection relaying techniques [10, 13], adaptive relaying concepts provide another opportunity for improved performance [14, 15, 23]; Rockfeller [14] conceptualized that maximum benefit from adaptive relaying will be achieved from integration with substation control and data acquisition (SCADA) functions and interfacing with the central energy management system (EMS).

Digital distance relays using microprocessor technology have indeed overcome some of the traditional problems in protective relaying. However, even with digital distance relaying, the practice has been to design the scheme on the basis of fixed relay settings. Changes would only be made when the configuration or system was significantly modified. Advantages of adaptive distance protection have been discussed and a practical scheme of adjusting the zone-1 boundary has been proposed [21]. Improved performance was obtained by using an algorithm to adjust the boundary angle. However, if the system conditions vary over a wide range and faults occur through high arc resistances the relay may lose selectivity.

In keeping with this trend adaptive protection achieves better performance from a protection system by allowing the settings to be made with consideration for fewer contingencies than is presently the case. Fewer constraints on a problem leads, in general, to a solution which is closer to the ideal. Sophisticated digital relays can be designed to adapt to varying conditions, that is, be free from the limitations imposed by the need to treat changing network conditions as unknown constraints. Adaptive schemes employing the neural network concept [41, 43] for

digital distance relay setting motivated by the desire to respond to the network conditions automatically is thus evolved.

5.2 ADVERSE EFFECT OF FAULT RESISTANCE

In the conventional distance relays, impedance measurement is made by using the A.C. quantities available at the local end only. It is impossible to determine the infeed current effect through the fault resistance. The remote-end infeed is dependent not only on fault location and fault resistance but also on source impedances of all power sources. The conventional safety margin used in zone 1 is not adequate to avoid maloperation. A large error results from high fault resistance and sometimes even zone 2 may not be able to provide coverage if the fault resistance is excessive. In E.H.V. transmission lines, a fault resistance up to 200 Ω is possible and therefore a solution to this problem is required.

Efforts have been made by various researchers trying to solve this problem. The method used in reference 41 does not consider high fault resistance. Reference 42 discusses a method which can detect high resistance earth fault and at the same time prevent the distance relay from overreach, but the relay still has underreach problems. Reference 43 proposes a method to solve this problem by using the artificial neural network, but a high speed carrier communication channel is needed. A device which can identify high resistance earth fault without the need of high speed communication channel is thus required.

System conditions external to the protected line influence relay performance. To demonstrate this effect and outline the adaptive relay setting scheme proposed, the same 400 kV three source system model as shown in Chapter 4 is used. (Fig. 4.2 is reproduced below.) A single-line-ground fault at F through a fault resistance R_f is examined and a digital distance relay installed at L is considered.

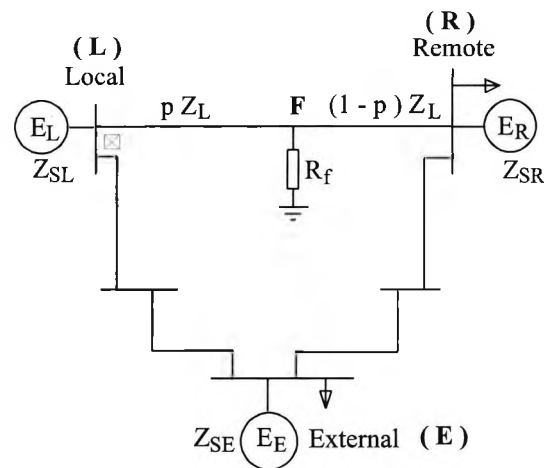


Fig. 4.2 Three source system model

For a fault at node F as shown in Fig. 4.2, the impedance measured by a distance relay at the local end [Appendix] can be expressed as

$$Z_R = p Z_{Ll} + \Delta Z \quad 5.1$$

ΔZ depends on a number of factors, say, the location of fault, the positive and zero sequence current distribution ratio, the fault resistance and the load current. The fault current again depends on the pre-fault voltage, the source capacities, the load current to a certain extent, and also the ratio of e.m.f.s and phase angles between different sources. The positive and zero sequence current distribution ratio also depends on the fault location, the fault resistance and the ratio of e.m.f.s and phase angles between different sources.

Therefore,

$$\Delta Z = f_L (Z_{SL}, Z_{SR}, Z_{SE}, h_{RL}, h_{EL}, h_{ER}, \delta_{RL}, \delta_{EL}, \delta_{ER}, p, Z_L, R_f) \quad 5.2$$

f_L is a non-linear function used to represent ΔZ in terms of the prefault and the postfault parameters.

The dependence of ΔZ on pre-fault and post-fault conditions as expressed in equation (5.2), introduces a significant difficulty for pilot-independent distance relaying, especially for high resistance faults. The measured impedance may be larger or smaller than the actual value depending on the value of the phasor ΔZ for different power system conditions. Simulation results for different values of R_f and fault location are given in Fig.5.1. The boundaries can be calculated in the local computer system through SCADA and EMS. Information from the remote and external end can be transferred through a computer link, rather than installing an expensive fast-response data channel exclusively for use during fault. If a maximum fault-resistance accommodation and relay reach are preset, an ideal trip region can be constituted prior to a fault or disturbance using equations 5.1 and 5.2. Setting patterns are renewed (that is f_L is recalculated) automatically to accord with changing network conditions.

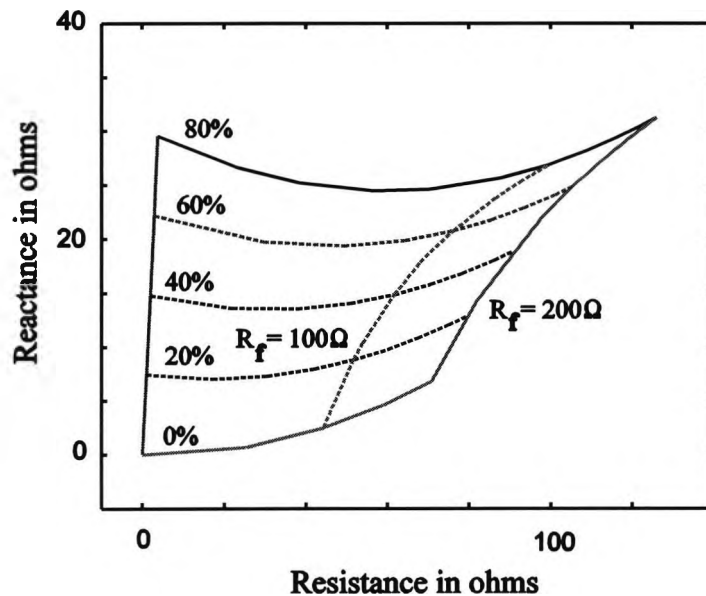


Fig. 5.1 Variation of measured impedance with fault resistance for different fault locations.

Fault Level of all sources = 30 GVA, $Z_{0SL}/Z_{1SL}=1$, $Z_{0SR}/Z_{1SR}=1$, $Z_{0SE}/Z_{1SE}=1$,
 $h_{RL}=1$, $\delta_{RL} = -13.5^\circ$, $h_{EL}=1$, $\delta_{EL} = -8.5^\circ$, $Z_{1L}=37.5\angle 86^\circ\Omega$, $Z_{0L}=136.6\angle 69^\circ\Omega$.
 $P_{L\ to\ R}=901\ MW$, $Q_{L\ to\ R}=200\ MVar$

5.3 IMPLEMENTATION OF ARTIFICIAL INTELLIGENCE TECHNIQUE TO DIGITAL DISTANCE RELAYING - METHOD 1

5.3.1 An Ideal Trip Characteristic

If system conditions are fixed, R_f and fault locations are varied, four boundary lines, defined below, can be obtained.

Boundary I: solid faults at different locations;

Boundary II: faults at a relay-reach end (80% of line length) with fault resistances of 0 to 200Ω ;

Boundary III: faults at different locations with a 200Ω fault resistance;

Boundary IV: faults at the relaying point with fault resistance of 0 to 200Ω ;

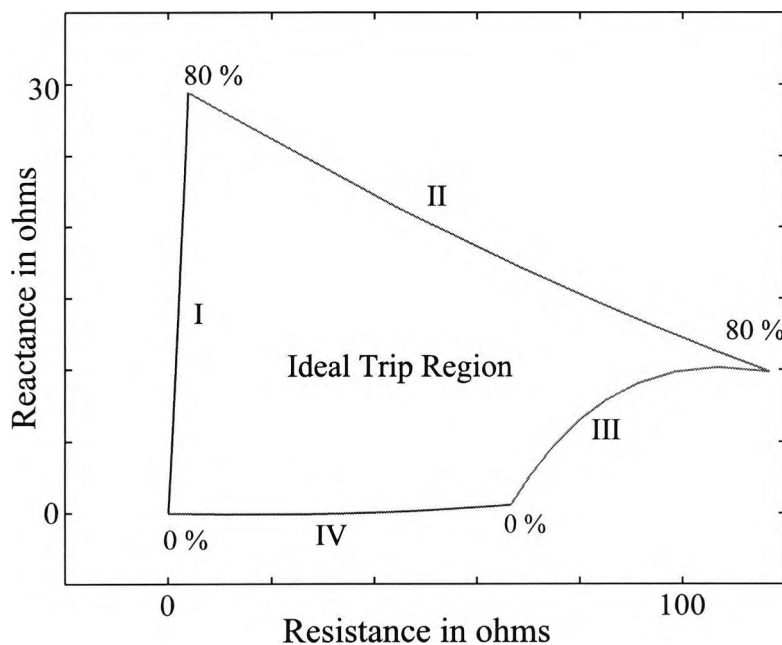


Fig. 5.2 An ideal trip region

The four lines and the included area constitute what may be designated an ideal trip region under the prevailing system conditions.

5.3.2 Application of Artificial Neural Network in Identifying Trip Region

Speed and accuracy are essential in relaying, but to achieve accuracy, a more complex software by the indicated accurate mathematical models derived previously has to be processed. This conflicts with speed requirements. In order to obtain both speed and accuracy, software pre-fault / during fault realizations have been designed and tested as described below.

5.3.3 Design of Artificial Neural Network

Four Artificial Neural Networks (ANN) have been designed for trip region identification for the four boundaries I, II, III, and IV as indicated in Fig. 3. Each of them has been tested with a parallel processing approach to adaptive distance relaying [31, 35]. The feedforward network with backpropagation training function is used. This method tends to give reasonable answers when presented with inputs that they have never seen. Better initial weights and biases are generated using Nguyen-Widrow initialization method[39]. Adaptive learning rate with momentum [39] is used to avoid a local minimum. Each ANN is designed with three layers, one input layer with two neurons, one output layer with one neuron and one hidden layer with a number of neurons. The logistic sigmoid transfer function is used between the input and hidden layers and the hypertangent sigmoid transfer function is used between the hidden and output layers. The measured value X_A and R_A are the inputs and, through the hidden layer, the trip decision is obtained as the output. The number of neurons in the hidden layer affects the accuracy of the nonlinear boundary and operating speed. Too few neurons can lead to underfitting, too many can contribute to overfitting, where all training points fit well, but the fitted curve makes wild oscillations between these points. In the present case, 5 neurons in the hidden layer is used. A more accurate boundary may be obtained by increasing this number but the training time and the during-fault calculation time will be longer.

5.3.4 Prefault Setting

The ideal boundary for a distance relay, as discussed previously, varies due to different pre-fault conditions. These conditions, however, can be obtained prior to a fault through the local on-line management computer system. A series of resistance and reactance values corresponding to different fault resistance for a pre-designed relay reach, say 80% of the line, can then be calculated. Calculated resistance and reactance pairs on, inside and outside the boundaries are used as training sets to obtain the weights and biases [31, 35]. The prefault training process ends when all weights and biases are converged. This NN constitutes the setting pattern which will be used during faults.

Stringent requirements of reliability for power system relays makes the application of ANN in the adaptive relaying very special in the sense that the trained neural network should be much more reliable in correct response to faults. Therefore, numerous training and testing patterns should be properly selected to represent different fault measurements [31, 35].

5.3.5 Trip Decision Making

As there are four boundaries, four different neural networks will be used, one for each boundary. Each network will be trained individually until satisfactory results are obtained. With well-trained weights in memory, the neural network of each boundary gives a decision output, Y , according to equation 5.3.

$$Y = f_{\tan} \left\{ |W_2| \cdot f_{\log} \left(|W_1| \cdot |Z|, |B_1| \right), |B_2| \right\} \quad 5.3$$

where f_{\tan} , f_{\log} are the hypertangent sigmoid and logistic sigmoid transfer functions respectively, $|W_1|$, $|W_2|$ are the weights of the trained network for layers 1 and 2 respectively, $|B_1|$, $|B_2|$ are the biases of the trained network for layers 1 and 2 respectively, and $|Z|$ is the impedance input to the neural network.

Each neural network is trained such that the output $Y > 0$ when the measured impedance is within the trip region. It therefore follows that when the output 'Y' from all four neural networks are all positive, the measured impedance is within the trip region. When the output $Y < 0$, even in only one of the four neural networks, the relay operation should be blocked. Performance depends on what has been "learnt" in the training process.

5.3.6 Training of Neural Network

Calculated reactances and resistances, $X_a(i)$ and $R_a(i)$, $i=1, 2, \dots, n$, constitute a reach boundary as shown in Figure 5.3. The required reach boundary (Z_a) and four curves (Z_a^+ , Z_a^{++}) and (Z_a^- , Z_a^{--}) just inside and just outside the boundary as shown in Fig. 5.3 are set up and used for training neural networks. It is desired that after training the output Y will reach the target - 0.2, - 0.1, 0, 0.1, 0.2 for Z_a^{--} , Z_a^- , Z_a , Z_a^+ , and Z_a^{++} respectively with a sum squared error less than 0.01. The network is trained using an established ANN back-propagation algorithm [31, 35].

The outer and inner curves are obtained by using a small impedance increase $|\Delta z|$ (1Ω or 2.6% of the protected line impedance in this case) and moving normal to the curve, inwards or outwards, from the base points on the boundary. They correspond to

$$\begin{aligned} X_a^+(i) &= X_a(i) + \Delta X(i) ; & X_a^-(i) &= X_a(i) - \Delta X(i) \\ R_a^+(i) &= R_a(i) + \Delta R(i) ; & R_a^-(i) &= R_a(i) - \Delta R(i) \end{aligned} \tag{5.4}$$

$$\begin{aligned} X_a^{++}(i) &= X_a(i) + 2\Delta X(i) ; & X_a^{--}(i) &= X_a(i) - 2\Delta X(i) \\ R_a^{++}(i) &= R_a(i) + 2\Delta R(i) ; & R_a^{--}(i) &= R_a(i) - 2\Delta R(i) \end{aligned} \tag{5.5}$$

where

$$\Delta X(i) = \frac{\Delta Z}{\sqrt{1 + k_a^2(i)}} ; \quad \Delta R(i) = - \frac{\Delta Z k_a(i)}{\sqrt{1 + k_a^2(i)}} \tag{5.6}$$

$$k_a(i) = \frac{X_a(i + 1) - X_a(i)}{R_a(i + 1) - R_a(i)} , \quad (i = 1, 2, \dots, n) \tag{5.7}$$

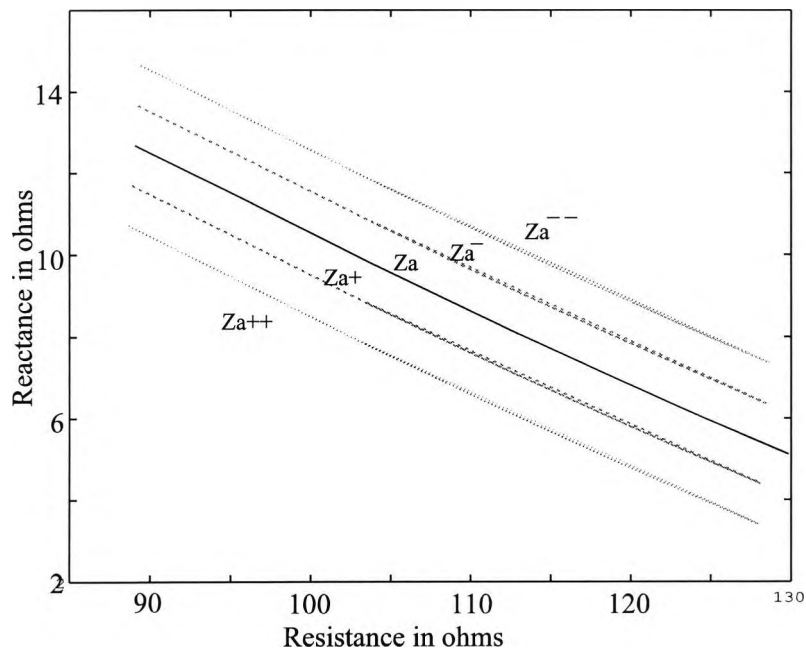


Fig. 5.3 Training pattern selection

More information provided to the ANN will help it to converge. For the ideal trip region as shown in Fig. 5.2, 14 and 15 points are selected on boundaries II and III respectively as they are the most non-linear and the most important. Nine and ten points are selected for boundaries IV and I respectively. The total number of training points for the outer and inner curves of Z_a^{--} , Z_a^- , Z_a , Z_a^+ , and $Z_{a^{++}}$ will produce a total of 46, 66, 71, and 41 training points for the boundaries I, II, III and IV respectively.

5.3.7 Testing Patterns and Results

Testing patterns should be properly selected to represent different fault measurements. Impedances which are different from the training patterns on the outer and inner curves of boundaries are chosen to test the neural network. A typical testing pattern for boundary II is shown in Fig. 5.4.

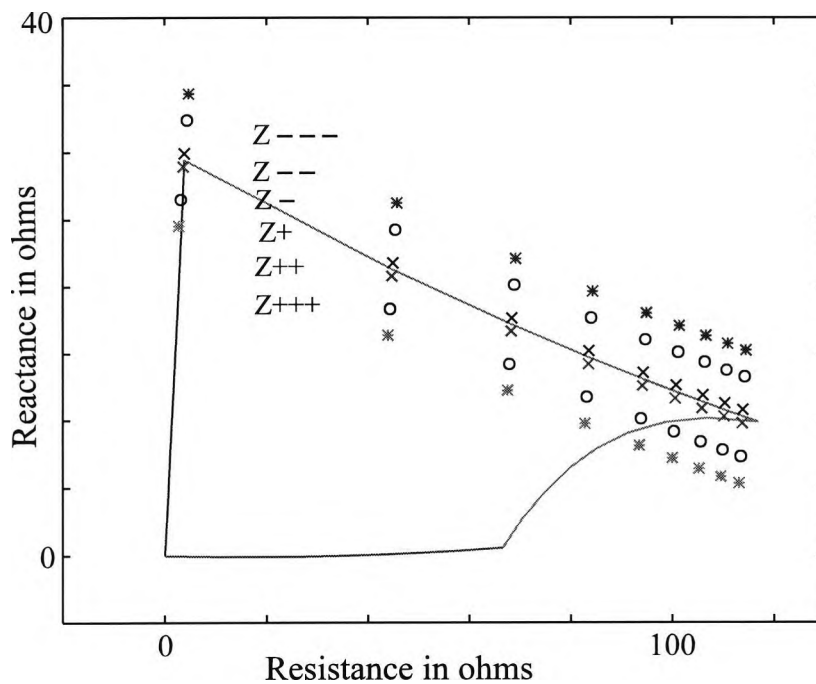


Fig. 5.4 Testing pattern

The test points are located at 0.5, 3 and 5 Ω normal to boundary II. Both in-zone and out-zone faults near the boundary, at different locations and/or with different fault resistance are represented. By presenting these testing patterns as inputs to the trained neural networks, we can obtain the corresponding outputs by processing equation 5.3 for each neural network. An internal fault will be identified if the output from all four neural networks are positive. The test result for the testing pattern as shown in Fig. 5.4 from top to bottom and from left to right is shown in Table 5.1.

Table 5.1 Output of Neural Network

Boundaries	Output of Neural Network								
Z ---	-0.73	-0.75	-0.75	-0.75	-0.76	-0.76	-0.76	-0.76	-0.76
Z --	-0.51	-0.53	-0.53	-0.53	-0.53	-0.53	-0.54	-0.54	-0.54
Z -	-0.02	-0.10	-0.10	-0.09	-0.09	-0.10	-0.10	-0.10	-0.11
Z +	-0.03	0.09	0.10	0.11	0.11	0.10	0.10	0.01	-0.08
Z ++	-0.06	0.53	0.54	0.54	0.15	-0.16	-0.34	-0.46	-0.54
Z +++	-0.08	0.75	0.76	0.44	-0.23	-0.51	-0.64	-0.72	-0.77

The result shows that the output is positive if the test points are inside the ideal operating zone and outside the operating zone if negative. The value of the output shows its distance from the boundary. Similar testing patterns for other boundaries are also selected. The results obtained are all correct. In some cases, however, if the result is not satisfactory for one or more testing patterns, the neural network should be re-trained including the failed patterns in the training set. The only drawback is the neural network output value is non-linear and it does not necessarily indicate the distance from the boundary in ohms. Another disadvantage is solid faults along the line may not be covered as these points are right on the boundary. This disadvantage can be covered by a conventional distance protection relay which can cover solid faults satisfactorily and will not cause mal-operation of the protection system.

5.3.8 Possible Sources of Error

A Slight Change in Power Flow

The ideal operating region should be updated whenever the system configuration or load pattern changes. Since the system load is always changing at a slow rate, one concern about the adaptive method is the possible error introduced if the ideal operating region was not updated for small load changes or if a fault occurs before the updating process is completed. This effect is illustrated in Fig. 5.5. Based on a initial power flow of 1000 MW, Fig. 5.5 shows the changes in

ideal trip region when the power flow changes by 100 MW. It can be seen that when the power flow decreases, the ideal trip region will expand slightly. This means that there is a slight reduction of maximum fault resistance to be detected. The error is higher for high resistance faults at the far end of the line. In general the percentage of line protected does not change. On the other hand, when power flow increases, there is a slight increase in maximum fault resistance detection and hence slightly higher error will also be expected for high resistance faults at far end of the line. Again the percentage of line protected does not change. It can be concluded that if load changes are not significant (± 100 MW in the case studied), re-training of the ANN is not necessary and it will not introduce significant errors.

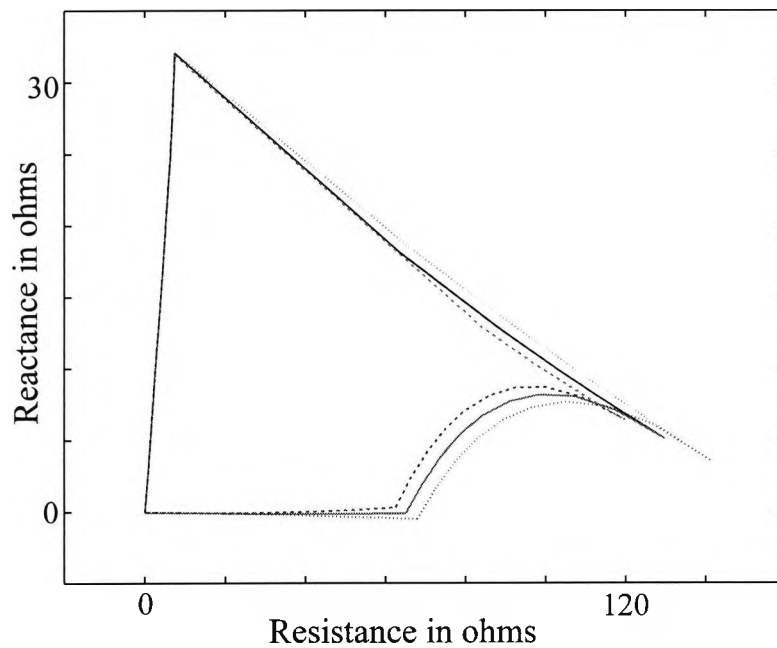


Fig. 5.5 Changes in ideal trip region

(———) $P = 1000$ MW (L to R), $\delta_{LR} = 14^\circ$.

(- - - - -) $P = 1100$ MW (L to R), $\delta_{LR} = 15.4^\circ$.

(.) $P = 900$ MW (L to R), $\delta_{LR} = 12.6^\circ$.

B Larger Change in Power Flow

Fig. 5.6 shows how the operating region is affected under a larger change in power flow conditions. The ideal operating region should be updated whenever the system configuration or load pattern changes. Since the system load is always changing at a slow rate, one concern about the adaptive method is the possible error introduced if the ideal operating region was not updated for small load changes or if a fault occurs before the updating process is completed. It can be seen from Fig. 5.6 that when the power flow decreases by about 20%, the ideal trip region will expand slightly. This means that there is a slight reduction of coverage. The error is higher for high resistance faults at the far end of the line. On the other hand, when power flow increases by about 20%, there is a slight increase in coverage and again slightly higher error will be expected for high resistance faults at the far end of the line. In general if load changes are less than $\pm 10\%$, re-training of the ANNs is not necessary [31, 35]. On a typical line such as the case studied, the daily minimum and peak loads are of the order of 600 MW and 1400 MW respectively, and the highest rate of rise of load which occurs before the morning peak is approximately 200 MW per hour. This means that the ANN probably need to be re-trained hourly in the morning before the morning peak, and then just a few times for the rest of the day. If the range of power flow is larger than this, there must be adequate ANN trainings to cover the entire range of power flow. Of course re-training is also necessary whenever there is any system configuration changes, such as system outages, switching of interconnectors, or change of generators.

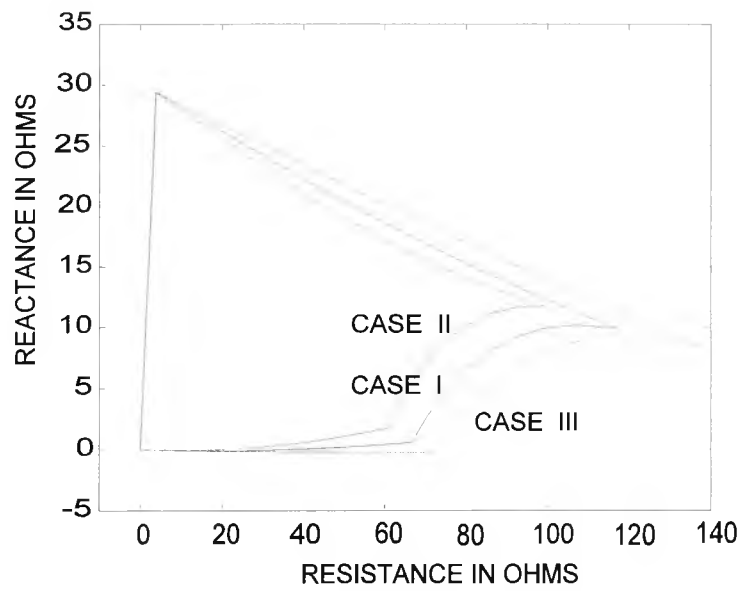


Fig. 5.6 Variation of measured impedance with fault resistance for different power flow conditions

Case I : $P_{L\text{ to }R}=1026$ MW, $h_{RL}=1$, $\delta_{RL}=15.1^\circ$,

Case II : $P_{L\text{ to }R}=1264$ MW, $h_{RL}=1$, $\delta_{RL}=23.4^\circ$,

Case III : $P_{L\text{ to }R}=829$ MW, $h_{RL}=1$, $\delta_{RL}=12^\circ$.

5.4 IMPLEMENTATION OF ARTIFICIAL INTELLIGENCE TECHNIQUE TO DIGITAL DISTANCE RELAYING - METHOD 2

5.4.1 A Practical Trip Characteristic

The trip characteristic is a little bit different from the one described in 5.3.1. In order to distinguish the difference in trip characteristic, a different lettering is used in this section. Under the effect of fault resistance R_f as mentioned before, four boundary lines, defined below, can be obtained.

Boundary A: faults at a relay-reach end (80% of line length) with fault resistances of 0 to 200Ω ;

Boundary B: faults at different locations with a 200Ω fault resistance;

Boundary C: faults at the relaying point with fault resistance of 0 to 200Ω ;

Boundary D: Constant resistance boundary set at -4Ω . This is to make sure that faults with zero fault resistance at different locations of the line are well inside the operating region.

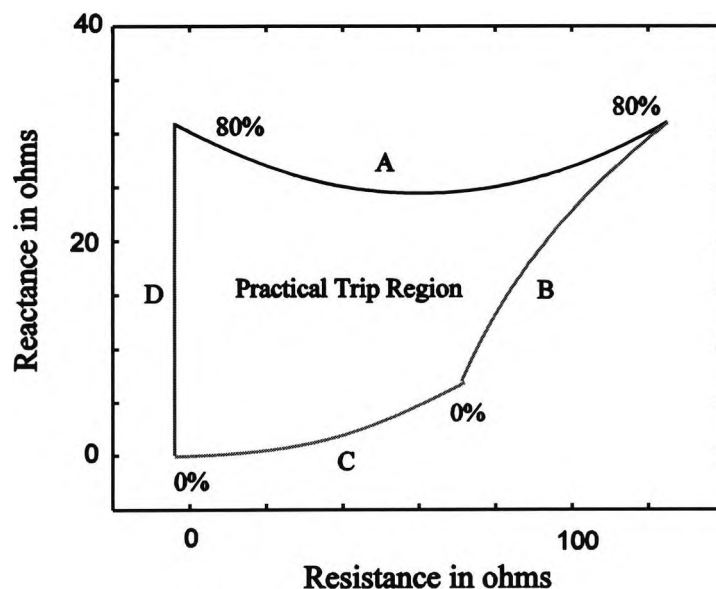


Fig. 5.7 A practical trip region

The four lines and the included area constitute what may be designated a trip region under the prevailing system conditions.

5.4.2 Design of Artificial Neural Network

Three Artificial Neural Networks (ANN) have been designed for trip region identification for the three non-linear boundaries A, B, and C shown in Fig. 5.7. Each of them has been tested using a parallel processing approach [26, 29, 31, 35]. The Nguyen-Widrow method is used to find the initial conditions of weights and biases. Use of the new Nguyen-Widrow initial conditions resulted in the network solving the problem quickly as stated in [39]. This speed up factor seems to prevail in a large variety of problems. This is a remarkable saving, considering that the time required to calculate Nguyen-Widrow initial conditions is negligible compared to the training time of the network.

The training performance is improved by using an approximation of Newton's method called Levenberg-Marquardt [39]. This optimization technique is more powerful than the gradient descent method used on ordinary back propagation training but needs more memory, however, this is no problem with modern computers. The method proved to be fast and accurate. It is found that the new training method is much faster than the adaptive learning rate method used in 5.3. Much less hidden nodes are required and can achieve a much higher accuracy.

Each ANN is designed with three layers, namely an input layer, an output layer, and a hidden layer. The logistic sigmoid transfer function is used between the input and hidden layers and the pure linear transfer function is used between the hidden and output layers.

The Levenberg-Marquardt update rule is

$$\Delta W = (J^T J + \mu I)^{-1} J^T e \quad 5.8$$

where J is the Jacobian matrix of derivatives of each error to each weight, μ is a scalar, and e is an error vector. If the scalar μ is very large, this expression approximates gradient descent, while if it is small it becomes the Gauss-Newton method. Because this second method is faster, but tends to be less accurate when near an error minima, the scalar μ is adjusted just like the adaptive learning rate [39].

5.4.3 Training of Artificial Neural Network

For training the ANN for boundary A, the resistance R_A at different points along boundary A are the inputs and the corresponding reactance X_A is obtained as the targeted output.

$$Y = f_{purelin} \{ [W_2] \cdot f_{log} ([W_1] \cdot [R], [B_1]), [B_2] \} \quad 5.9$$

where Y is the targeted output and equals to X_A for the training for Boundary A.

$f_{purelin}$, f_{log} are the pure linear sigmoid and logistic sigmoid transfer functions respectively,
 $|W_1|$, $|W_2|$ are the weights of the trained network for layers 1 and 2 respectively,
 $|B_1|$, $|B_2|$ are the biases of the trained network for layers 1 and 2 respectively.

For training the ANN for boundary B, the reactance X_B at different points along boundary B are the inputs and the corresponding resistance R_B is obtained as the output. Boundary C is trained in a similar manner as boundary A. No training is required for boundary D as it remains unchanged for all system configurations.

This training method is found to be more efficient and training time is faster than method 1. This is because the relay ideal boundary is non-linear in nature. The equal distance curves (Z_a^+ , Z_a^{++}) and (Z_a^- , Z_a^{--}) just inside and just outside the boundary do not provide a good environment for training the neural network.

5.4.4 Trip Decision Making

More information provided to the ANN will help it to converge. Training begins by presenting an input pattern vector (R_A, X_A) to the ANN, sweeping forward through the system using equation 5.9 to generate an output Y , and computing the error. The next step involves sweeping the effect of the error backward through the network to associate a "squared error derivative", with each neuron, computing a gradient from it and finally updating the weights based upon the corresponding gradient. A new pattern is then presented and the process is repeated until the network satisfies the target of all the training patterns.

Each network will be trained individually until satisfactory results are obtained. With well-trained weights in memory, the neural network of each boundary gives an output, Y , according to equation 5.9. Each neural network is trained to predict the corresponding boundary. The three ANNs can work together to estimate the required tripping region. Tripping decision can then be made based on the on-line measurement and the output from the ANNs. For example, in the ANN for Boundary A, the estimated boundary reactance X_A corresponding to the on-line measured resistance R_M is compared with the on-line measured reactance X_M to judge whether it is within the trip region of boundary A. If X_M is smaller than X_A , then it is inside the trip region. The distance of the measured impedance from Boundary A is then the difference between the ANN reactance output and the measured reactance. Similar reasoning is applied to Boundary B, C, and D. Based on this approach, a fault within the trip region and its distance from all boundaries in ohms can be identified.

5.4.5 Neural Network Training Result

The number of neurons in the hidden layer affects the accuracy of the nonlinear boundary and operating speed. Too few neurons can lead to underfitting, too many can contribute to overfitting, where all training points fit well, but the fitted curve makes wild oscillations between these points. In the present case, 2 neurons in the hidden layer is found adequate for the ANN for Boundary A and only 1 neuron in the hidden layer is needed for the ANN for Boundary B and

C. The training time varies according to the starting point and the acceptable error which can be tolerated. As the starting point is chosen at random, in some cases the training may not converge. In this case it is required to start again from a different starting point or try with a different number of neurons in the hidden layer. The tolerable sum square error chosen in this study is $1E-7$, $1E-6$, and $1E-5$ for Boundary A, B, and C respectively. The training converged in 53, 107 and 6 epochs for Boundary A, B, and C respectively. The predicted boundary produced by the neural network in comparison to the calculated ideal relay reach calculated for faults along the line in a similar way as in Fig. 5.2 is shown in Fig. 5.8. It can be seen that the neural network produces a trip region which can map the ideal relay reach smoothly. The neural network output can cover all earth faults with a maximum fault resistance of 200Ω from the relaying point up to 80% of the line length. The extra region at negative resistance region will ensure that solid faults along the line will also be covered. This can solve the protection black spot problem as discussed in 5.3.

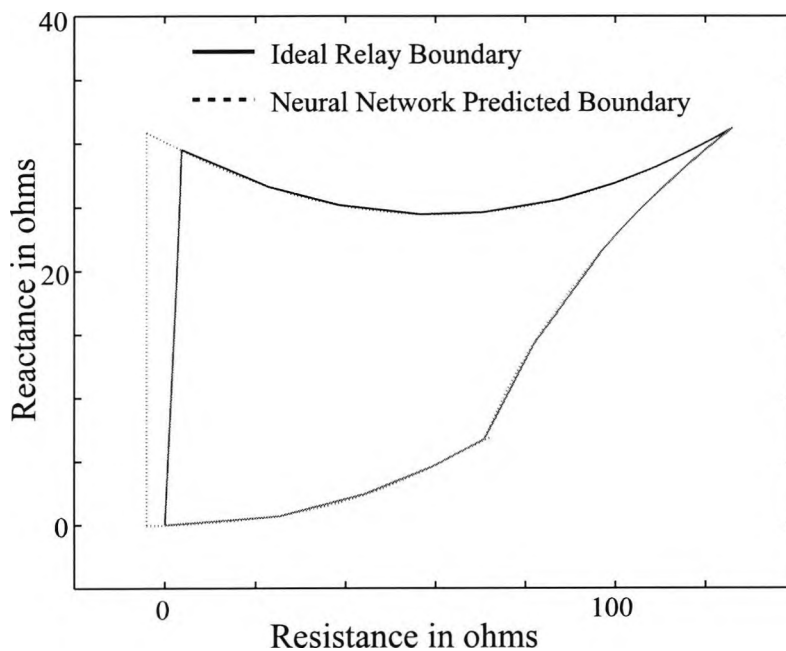


Fig. 5.8 ANN predicted boundary

5.4.6 Testing Patterns and Results

Testing patterns should be properly selected to represent different fault measurements. Impedances which are different from the training patterns on the outer and inner curves of boundaries are chosen to test the neural network. A typical testing pattern is shown in Fig. 5.9.

Testing points are generated by simulating single-phase to earth faults located at 20%, 40%, 60%, 70%, 75%, 85%, and 90% of the line length from the relaying point with fault resistance R_f ranging from 0 to 220 Ω . Both in-zone and out-zone faults at different locations and with different fault resistance are represented. By presenting these testing patterns as inputs to the trained neural networks, we can obtain the corresponding outputs by processing equation 5.9 for each ANN. The distance of the measured impedance from all boundaries can be identified based on the output from all neural networks. The test result for the testing pattern as shown in Fig. 5.9 is shown in Table 5.2. Each row corresponds to faults with different fault resistance at different locations of the line from the relaying point. The top row shows the corresponding fault resistance for that column. The test results show that the Neural Network gives a correct prediction for all in-zone faults. The value shown in Table 5.2 is positive if the test points are inside the tripping zone and negative if it is outside the operating zone. The value of the output shows its distance from the nearest boundary in ohms.

Table 5.2 Output of neural network

R_f	0	25	50	75	100	125	150	180	220
90%	-3.8	-2.2	-1.6	-1.2	-1.0	-0.8	-0.8	-0.7	-0.7
85%	-1.9	-1.2	-0.9		-0.6		-0.5		
75%	1.9	1.4	1.1	1.0	0.8		0.6	0.6	-1.0
70%	3.7	2.9	2.4	2.0	1.8	1.6	1.4	1.3	-1.3
60%	6.9	6.2	5.3	4.6	4.1	3.7	3.3	2.3	-1.7
40%	6.0	11.9	11.7	10.5	9.6	8.8	8.1	2.8	-2.4
20%	5.0	6.5	6.8	7.3	8.1	8.9	8.8	3.1	-2.9

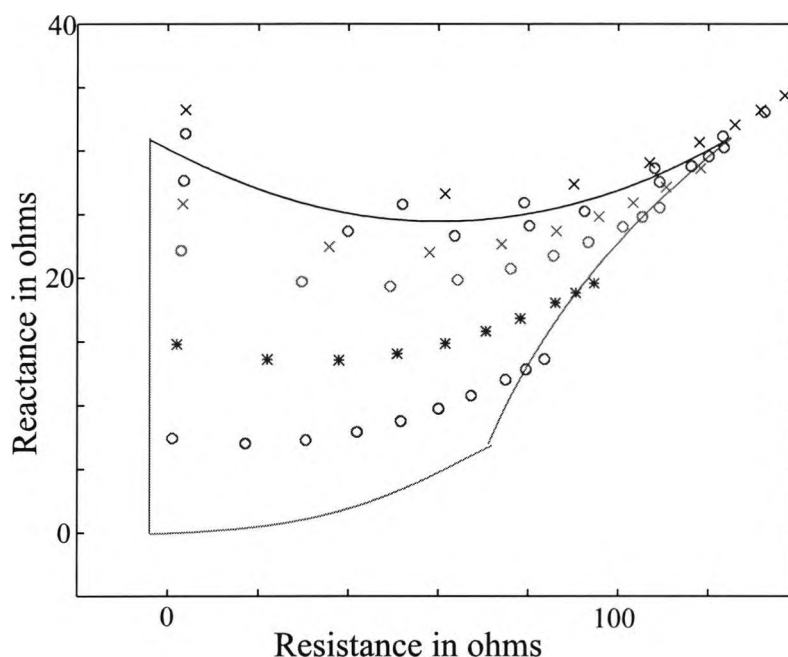


Fig. 5.9 Testing pattern for the neural network

5.4.7 Effect of Load Flow Changes on the Output of Neural Network

A Decrease in Power Flow

It is interesting to find out how the neural network is affected by changes in power flow. Fig. 5.10 shows how the operating region is affected when the power flow in the line is decreased to 800 MW from 900 MW but the reactive power flow remains unchanged. The same system configurations as in Fig. 5.1 is used. The operating region should be updated whenever the system configuration or load pattern changes. Since the system load is always changing at a slow rate, one concern about the adaptive method is the possible error introduced if the ideal operating region was not updated for small load changes or if a fault occurs before the updating process is completed. It can be seen from Fig. 5.10 that the ideal trip region expands slightly for a decrease of power flow. This means that there is a slight reduction of coverage and the relay will underreach in certain circumstances. The error is higher for high resistance faults at the far end of the line near the preset boundary. A similar testing pattern as mentioned in 5.4.6 is generated

to test the error caused. The test result is shown in Table 5.3. It can be seen that the relay will underreach and the reach error is mainly in the line section between just under 70% to 80% of the line length from the relaying point and the error is larger for fault resistance above 100Ω.

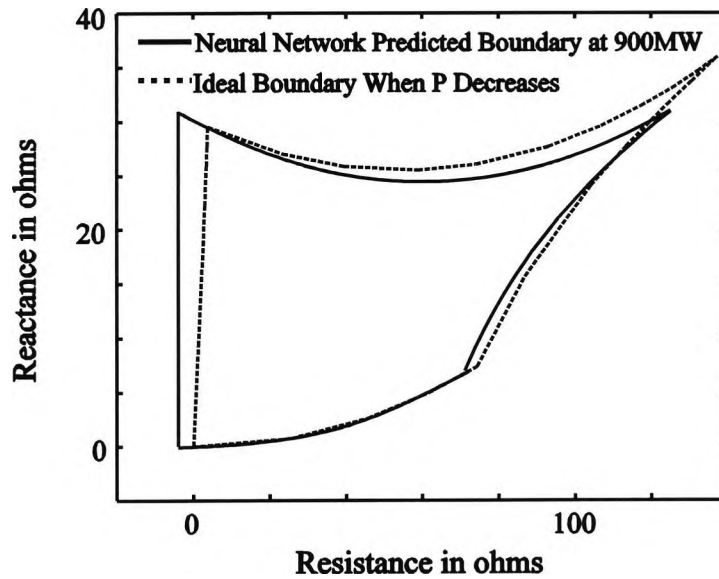


Fig. 5.10 Changes in relay coverage due to decrease in the power flow of the line

Table 5.3 Output of neural network for decrease in power flow

R_f	0	25	50	75	100	125	150	180	220
90%	-3.8	-3.4	-3.3	-3.1	-3.0	-3.1	-3.2	-3.4	-3.7
85%	-1.9	-2.3	-2.4		-2.5		-2.6		
75%	1.8	0.7	-0.02	-0.5	-0.8		-1.2	-1.4	-1.6
70%	3.7	2.3	1.4	0.8	0.3	-0.03	-0.3	-0.5	-0.8
60%	6.9	5.7	4.5	3.6	2.9	2.3	1.9	1.4	-0.5
40%	6.0	12.0	11.2	9.9	8.8	7.9	6.5	1.1	-4.0
20%	5.0	6.6	6.9	7.6	8.4	9.3	9.7	0.6	-5.7

B Increase in Power Flow

On the other hand, when the power flow increases to 1000 MW from 900 MW while the reactive power flow remains approximately constant, there is a increase in coverage and again the error is higher for high resistance faults. A similar testing pattern is used to test the resultant error. The test result is shown in Table 5.4. It can be seen from Table 5.4 that the relay will overreach for fault resistance higher than 50Ω .

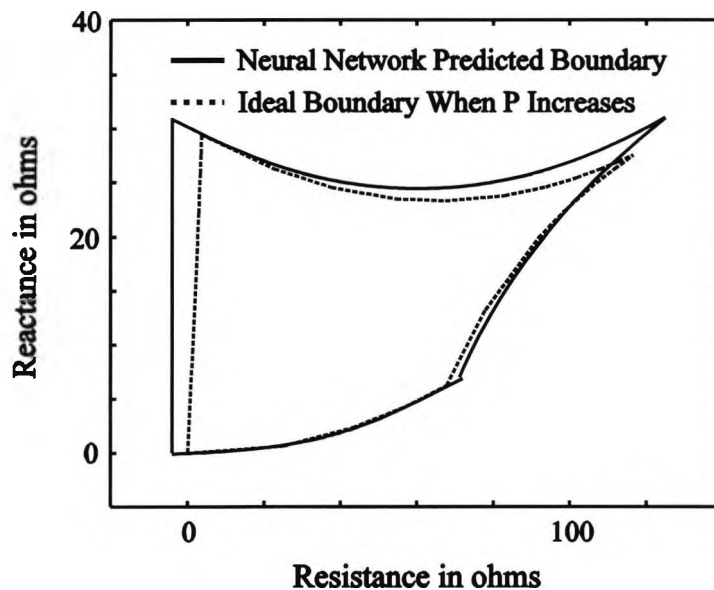


Fig. 5.11 Changes in relay coverage due to increase in the power flow of the line

Table 5.4 Output of neural network for increase in power flow

R_f	0	25	50	75	100	125	150	180	220
90%	-3.7	-1.1	-0.04	0.5	0.9	-0.5	-3.0	-4.9	-6.5
85%	-1.8	-0.3	-0.4		-1.1		-0.5		
75%	1.9	2.1	2.2	2.3	2.3		2.3	-0.1	-3.4
70%	3.8	3.5	3.4	3.2	3.1	3.0	3.0	1.0	-2.7
60%	6.9	6.6	6.0	5.6	5.2	4.9	4.7	2.8	-1.6
40%	6.0	11.7	11.5	11.1	10.3	9.7	9.1	4.5	-0.7
20%	5.0	6.5	6.6	7.1	7.7	8.4	9.2	5.2	-0.5

C Slight Increase in P and Q Flow in the Line

When both the active and reactive power flow in the line are increased to 951 MW and 225 MVar respectively from 900MW and 200MVar, there is a slight underreach for resistance faults above 100Ω near the setting limit (that is, near boundary A). There is also a slight overreach in boundary B and fault resistance coverage is extended to between 250 and 300Ω. A similar testing pattern is generated to test the resultant error. The test result is shown in Table 5.5.

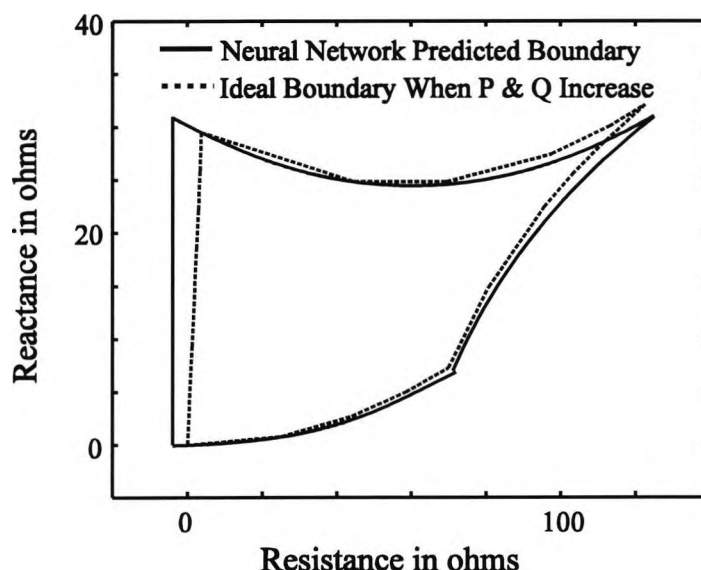


Fig. 5.12 Changes in relay coverage due to increase in the active and reactive power flow of the line

Table 5.5 Output of neural network for slight increase in P and Q flow in the line

R_f	0	25	50	100	150	180	220	250	300
90%		-2.3	-2.1	-2.3		-2.6		-2.9	
85%		-1.3	-1.3	-1.6		-2.1		-2.4	
75%		1.4	1.0	0.1	-0.4	-0.7	-1.0	-1.2	
70%	3.8	3.0	2.3	1.2	0.5	0.1	-0.2	-0.5	-0.8
60%	6.9		5.2	3.7	2.6	2.1	1.6	1.2	0.1
50%	6.4		8.3	6.4		4.3	1.8	-0.2	-2.3
25%	5.3		8.2	9.5	10.2	5.0	-0.3	-3.3	-6.9

D *Slight Increase in P Flow and Larger Increase in Q Flow in the Line*

When there is a slight increase in the active power flow in the line from 900 MW to 950 MW and a larger increase of line reactive power flow from 200 MVar to 275 MVar, it can be observed that the ideal operating region has drifted upwards. The test result shown in Table 5.6 shows that the relay is basically underreaching and the measurement for high resistance faults is not very reliable. The relay can only maintain a reasonable accuracy for low fault resistance.

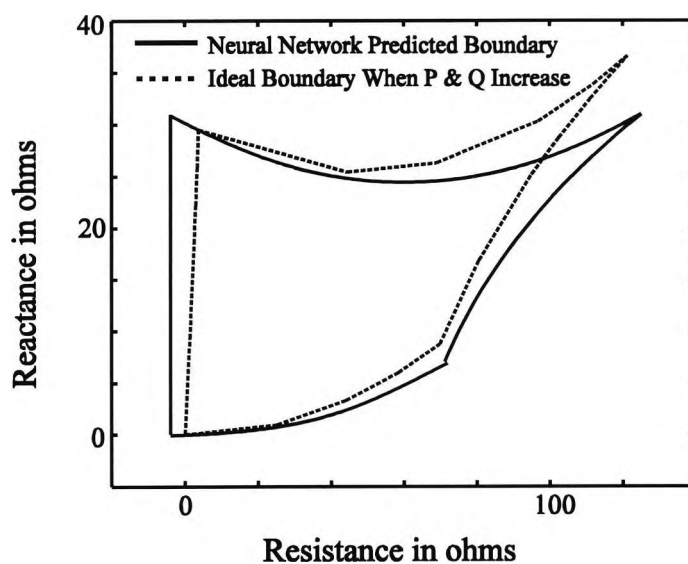


Fig. 5.13 Changes in relay coverage due to increase in the active and reactive power flow of the line

Table 5.6 Output of neural network for slight increase in P flow and larger increase in Q flow

R_f	0	25	50	100	150	180	220	250	300
90%		-3.5	-4.6	-6.4		-8.2		-9.2	
85%		-2.1	-3.2	-5.1		-7.1		-8.1	
75%		0.9	-0.3	-2.4	-4.0	-4.7	-5.5	-6.1	
70%	3.8	2.6	1.3	-1.0	-2.7	-3.5	-4.4	-5.0	-5.8
60%	6.9		4.4	2.0	0.01	-0.9	-2.0	-2.7	-3.6
50%	6.4		7.8	5.0		1.8	0.6	-0.2	-1.3
25%	5.3		8.5	10.2	10.4	8.4	4.3	2.2	0.2

5.4.8 Effect of Remote End Load Switching

One may have the query about the effect of heavy load switching at the remote end to the distance relay. Simulations for a heavy load switching at the remote busbar are carried out for the system configuration as in Fig. 5.1. A three phase balanced load of load resistance from 200 to 500 Ω are switched onto the remote busbar. This is equivalent to switching a load ranging from a equivalent value of 740 MW to 300 MW. The impedance measured at the relaying end is shown in Fig. 5.14. It can be seen that the load impedances measured are well away from the ideal operating region and the relay will not be sensitive to heavy load switching.

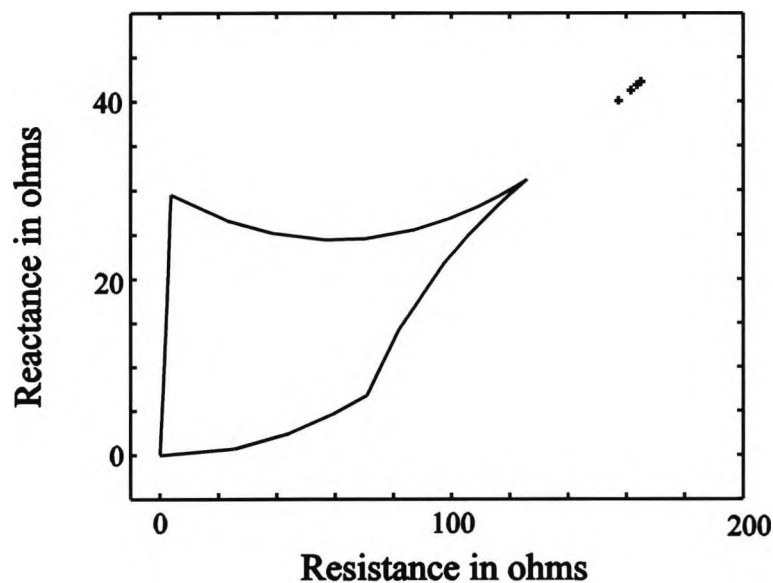


Fig. 5.14 Effect of Load Switching

5.5 ANALYSIS OF RESULTS

From the results obtained in Section 5.3 and 5.4, it can be seen that the Neural Network gives a very accurate prediction at the specified active and reactive power (P and Q) flow in the line. In general, an increase of power flow in the line will result in overreach of the relay and decrease in power flow will result in underreach. An increase of reactive power flow will enable the relay to cover fault resistance higher than the setting value. Consequently a decrease in reactive power flow will have the opposite effect. If the P and Q flow in the protected line is drifted to within 100 MW and 25 MVAR respectively in the present case, the error of the relay is still within the acceptable limit. In this case the reach of the relay will change for an order of 10% of line length. If the change of active and reactive power flow in the line is beyond this range, the error becomes intolerable. However, in all cases, the relay operation for low fault resistance are all correct. The relay will not be sensitive to heavy load switching.

CHAPTER VI**IDEAL OPERATING REGION OF DIGITAL DISTANCE RELAY
UNDER HIGH RESISTANCE EARTH FAULT****6.1 INTRODUCTION**

From the results obtained in Chapter 5, it can be observed that the ideal operating region of distance relays will change in different system configurations and conditions. The neural network approach, although gives a very accurate prediction at the specified system condition, has limitations in actual application and the system and line active and reactive power (P and Q) flow is continuously changing. In order to carry out further research on the application of artificial intelligent techniques to digital relaying, it is therefore necessary to investigate the main factors which affects the ideal operating region.

The sections below discuss the findings on the main factors which affect the ideal operating region under different conditions. This method does not need real time computation and thus can overcome the restrictions in [31, 35]. The effect caused by changes in power system configurations will also be discussed.

6.2 SYSTEM MODEL FOR DISTANCE RELAY STUDIES

System conditions external to the protected line influence relay performance. To demonstrate this effect several 400 kV system models were considered. Fig. 6.1 shows a simple two-source system model with a 400 kV line of length 125 km between the sources. A more complicated system layout is shown in Fig. 6.2 where the fault is all fed from two additional sources. The system layout shown in Fig. 6.2 can obviously be simplified into a two-source model as shown in Fig. 6.1 by adjusting the equivalent terminal short circuit levels. The effect of fault infeed by parallel

lines can be considered by adding a parallel line to the two-source system model as shown in Fig. 6.3 where the length of parallel line can be adjusted according to the system layout. The length and impedance of the parallel line will of course affect the fault current infeed ratio at both ends of the protected line. A more general system layout is shown in Fig. 6.4 where a third external source is added. The length and impedance of line from both ends of the protected line to the external source, the short circuit capacity of the external source and the load demand at the external source which affect the fault infeed ratio can all be varied in Fig. 6.4. The circuit of Fig. 6.4 also incorporates Fig. 6.3, parallel line feed which is one of the factors which makes infeed ratio more complex. Therefore the system layout as shown in Fig. 6.4 has been chosen because in effect it incorporates all of the essential elements of the systems in Fig. 6.1 to Fig. 6.3.

The length of the transmission line between Local and Remote Systems in Fig. 6.4 is 125 km. The total positive sequence impedance of the protected line (Z_{1l}) is $37.5/86^\circ \Omega$ and the total zero sequence impedance (Z_{0l}) is $136.6/69^\circ \Omega$. The length between Local to External and between Remote to External are both 200 km but they may be varied to simulate changes in external system configuration. The same line constants are used for all 400 kV lines. Short circuit level (SCL) of sources may be set according to different requirements. A single-line-ground fault at F through a fault resistance R_f is examined. A digital distance relay, employing the adaptive variable window length algorithm [6], installed at L is considered.

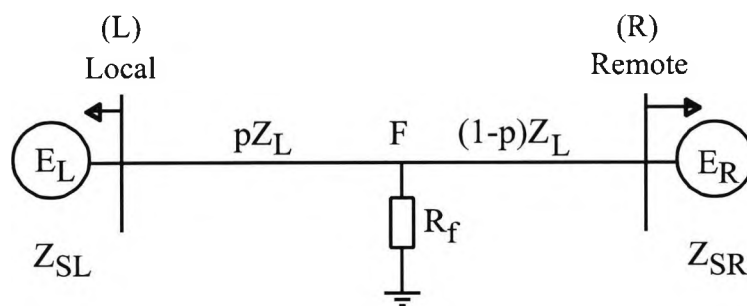


Fig. 6.1 Two-source system model

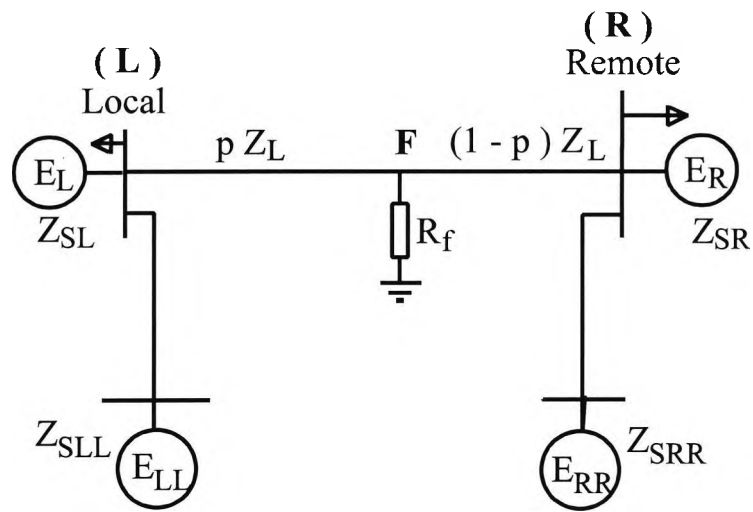


Fig. 6.2 Extended two-source system model

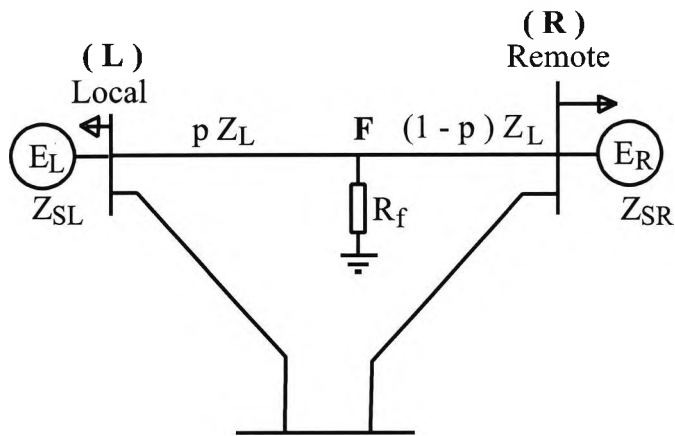


Fig. 6.3 Two-source system model with parallel line

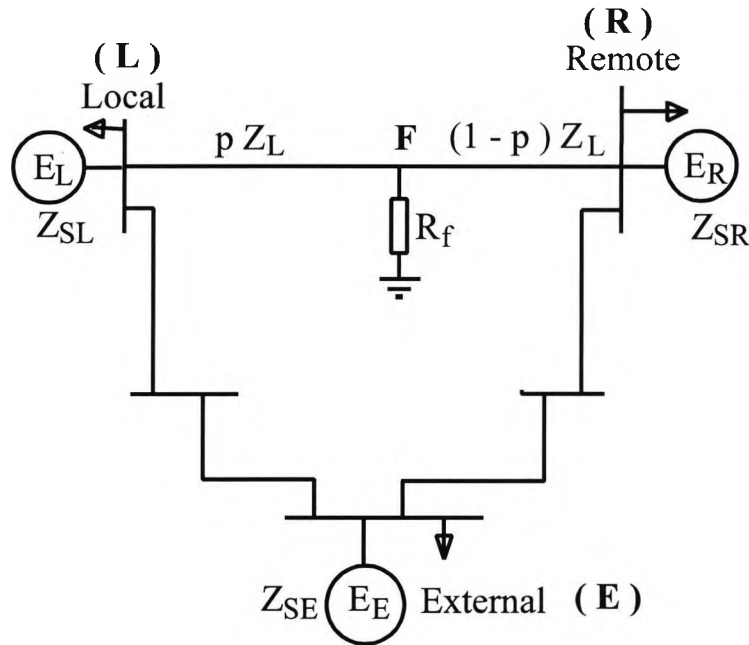


Fig. 6.4 Three-source system model

E_L , E_R and E_E are the equivalent potentials at the local, remote and external ends respectively. $E_R/E_L = h_{RL} e^{j\delta_{RL}}$, $E_E/E_L = h_{EL} e^{j\delta_{EL}}$. h_{RL} , h_{EL} are the ratio of source potentials. $-\delta_{RL}$, $-\delta_{EL}$ are the phase angle between corresponding sources. Z_{SR} , Z_{SL} , Z_{SR} and Z_{SE} are the source impedances. Z_L is the line impedance, not referring to any specific sequence component; p is the proportion of line length from the relaying point to the fault.

As mentioned in Chapter 5.2, impedance measurement at the local end can be expressed as

$$Z_a = pZ_{1L} + \Delta Z \tag{5.1}$$

where

$$\Delta Z = f_L (Z_{SL}, Z_{SR}, Z_{SE}, h_{RL}, h_{EL}, h_{ER}, \delta_{RL}, \delta_{EL}, \delta_{ER}, p, Z_L, R_f) \tag{5.2}$$

f_L is a non-linear function used to represent ΔZ in terms of the pre-fault and the postfault parameters as discussed in Chapter 5

6.3 IDEAL OPERATING REGION OF DISTANCE RELAY

6.3.1 The Influence of Active and Reactive Power Flow in the Line.

In order to study the influence on the ideal distance relay coverage under different conditions, the ideal relay coverage for six different cases are carried out. In these cases the length of lines are the same as shown in Fig. 6.4 but the active and reactive power (P and Q) flow in MW in the line between L and R and the Short Circuit Level (SCL) in GVA of different sources can be different. The system configurations and load conditions for these cases are shown in Table 6.1, 6.2 and Appendix C respectively. The ideal operating region of these cases are shown in Fig. 6.5, 6.6, and 6.7.

Table 6.1 System Configurations for Cases 1 to 6

Case	$SCL(L)$	$SCL(R)$	$SCL(E)$	$L-R$	$L-E$	$R-E$
1	15 GVA	15 GVA	35 GVA	125 km	200 km	200 km
2	35 GVA	20 GVA	35 GVA	125 km	200 km	200 km
3	15 GVA	15 GVA	35 GVA	125 km	200 km	200 km
4	35 GVA	20 GVA	35 GVA	125 km	200 km	200 km
5	15 GVA	15 GVA	35 GVA	125 km	200 km	200 km
6	15 GVA	35 GVA	35 GVA	125 km	200 km	200 km

Table 6.2 Load Conditions for Cases 1 to 6 (contd.) (in MVA)

Case	$P+jQ (L-R)$	$P+jQ (L-E)$	$P+jQ (R-E)$	$P+jQ (L)$	$P+jQ (R)$	$P+jQ (E)$
1	1000+j0.64	570-j48	-60-j59	-j30	1542-j100	1000
2	999.8+j0.63	1079+j67	462-j67	0	2000-j77	2000-j270
3	1000+j215.8	1105+j84	437-j178	-j450	2024+j850	2000-j400
4	1000+j215.7	584-j45	-74-j178	-j200	2055+j760	1400-j140
5	750.3+j100.1	1015+j51	523-j128	-j250	1697+j543	2000-j350
6	750.4+j100.1	1015+j53	524-j126	-j250	1697+j850	2000-j320

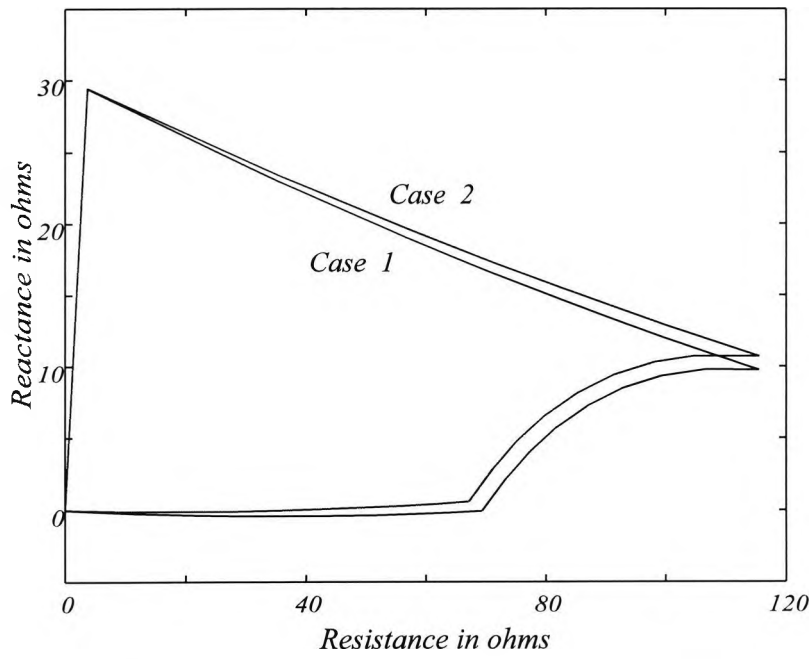


Fig. 6.5 Ideal operating region of cases 1 and 2

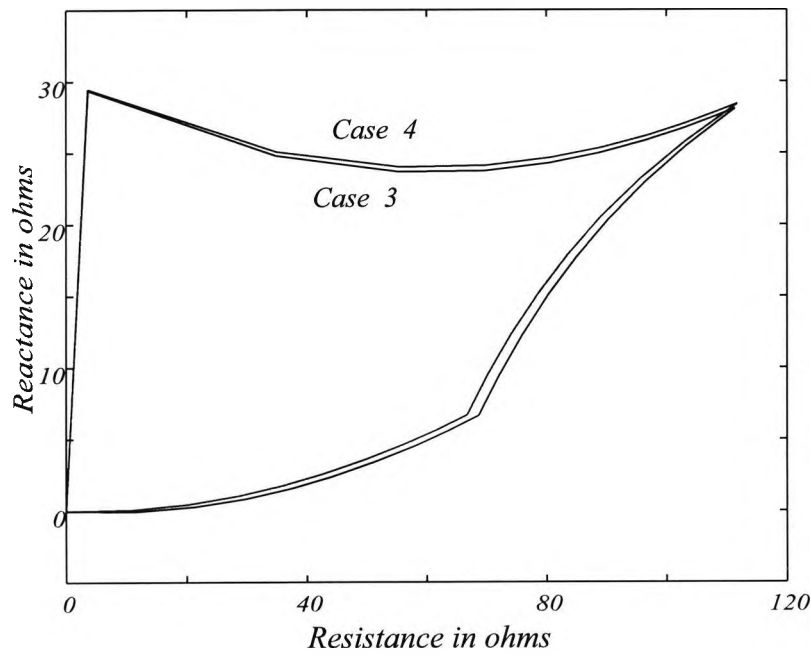


Fig. 6.6 Ideal operating region of cases 3 and 4

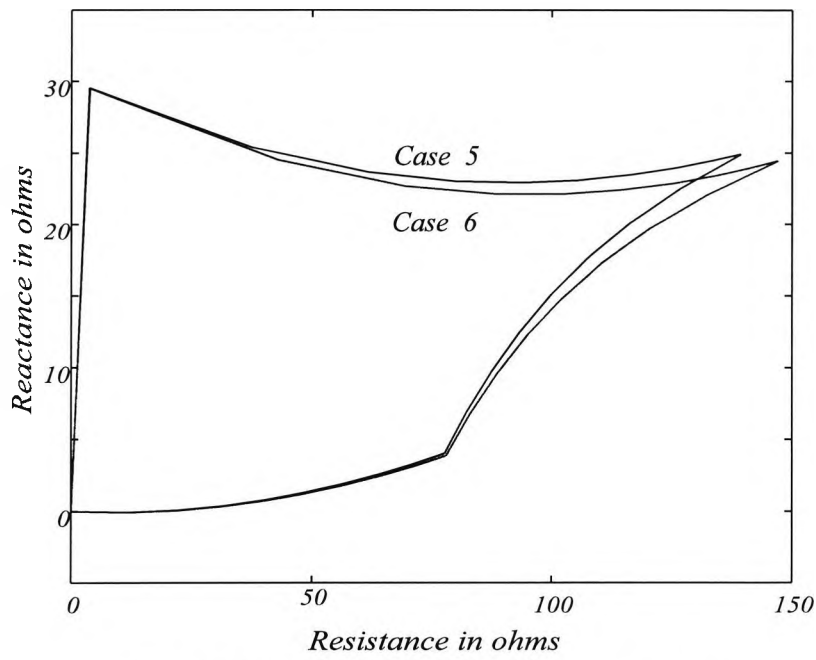


Fig. 6.7 Ideal operating region of cases 5 and 6

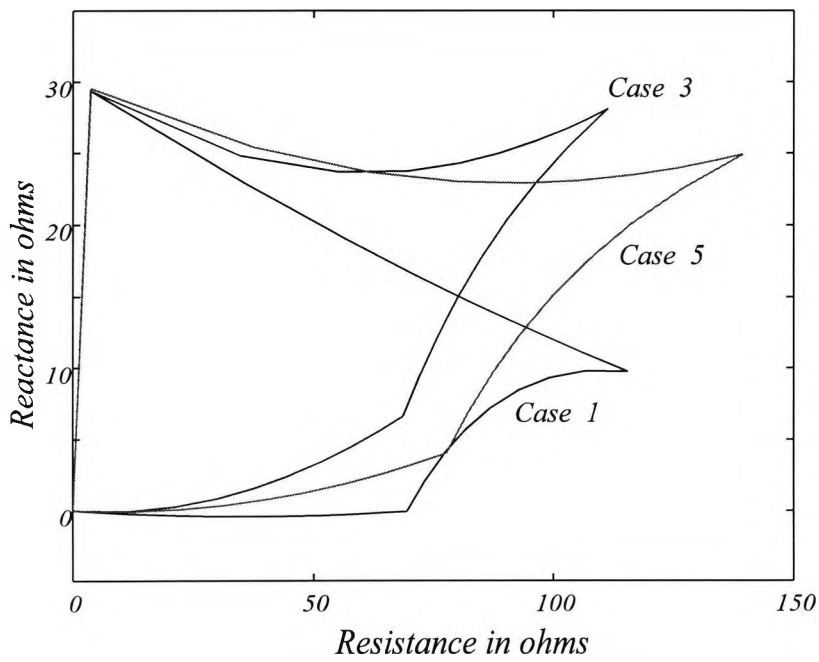


Fig. 6.8 Variations in ideal operating region of cases 1, 3, and 5

The six cases shown in Table 1 are divided into three groups. They are cases 1 and 2, cases 3 and 4, and cases 5 and 6. The active and reactive power flow in the protected line in each group are approximately the same. From Fig. 6.5 to 6.7, it can be seen that if there are not much change in the active and reactive power flow in the protected line between L and R, the ideal operating region of the distance relay is almost identical. It is also noticed that changes in P and Q flow will result in a major change of the ideal operating region. Fig. 6.8 shows the variation of ideal operating region for Cases 1, 3, and 5.

6.3.2 Influence of External System Connections

In order to investigate the influence of external network to the ideal operating region, the ideal operating region of 4 different system configurations (Cases 7, 8, 9, and 10) with different line lengths from L to E and R to E are studied. The parameters and length of the protected line remain unchanged. In these cases, the P and Q flow in the protected line is approximately the same as that in Case 3. The configurations and load conditions of these cases are shown in Tables 6.3, 6.4 and Appendix C. The ideal operating regions as compared with Case 3 are shown in Fig. 6.9 to 6.12.

Table 6.3 System Configurations for Cases 3, 7, 8, 9 and 10

Case	$SCL(L)$	$SCL(R)$	$SCL(E)$	$L-R$	$L-E$	$R-E$
3	15 MVA	15 MVA	35 MVA	125 km	200 km	200 km
7	20 MVA	20 MVA	35 MVA	125 km	100 km	200 km
8	20 MVA	20 MVA	35 MVA	125 km	200 km	100 km
9	20 MVA	15 MVA	35 MVA	125 km	100 km	100 km
10	20 MVA	15 MVA	35 MVA	125 km	50 km	50 km

Table 6.4 Load Conditions for Cases 3, 7, 8, 9 and 10 (contd.) (in MVA)

Case	$P+jQ (L-R)$	$P+jQ (L-E)$	$P+jQ (R-E)$	$P+jQ (L)$	$P+jQ (R)$	$P+jQ (E)$
3	1000+j215.8	1105+j84	437-j178	-j450	2024+j850	2000-j400
7	1000+j215.5	773.1-j59	-262-j161	-j150	2723+j970	1000-j200
8	999.9+j215.5	960.9+j21	573.5-j324	-j150	1807+j1412	2000-j500
9	1000+j215.4	1165+j4.8	-144-j269	-j350	2125+j975	2000-j450
10	1000+j215.7	1543+j46	-1016-j324	-j400	2497+j1080	1500-j300

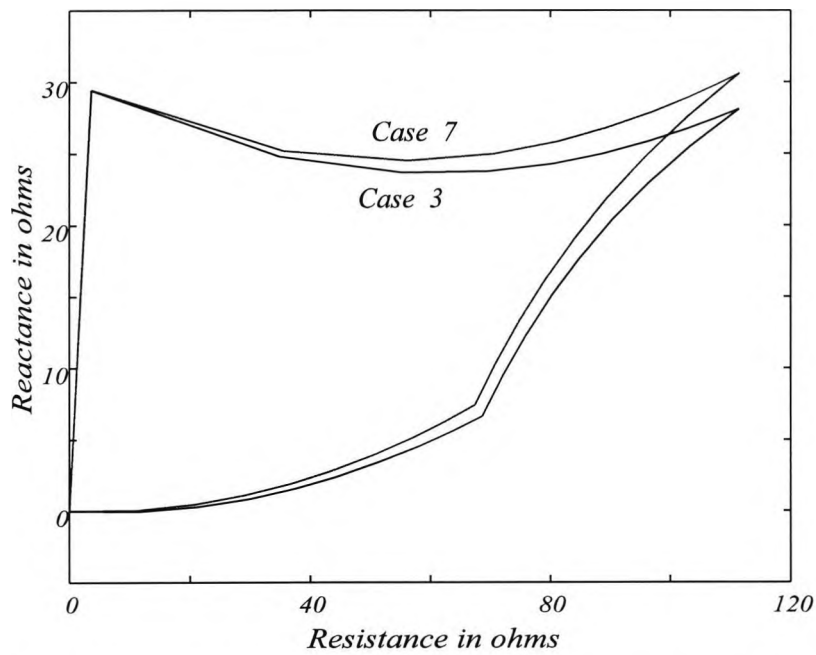


Fig. 6.9 Ideal operating region of case 7 as compared with case 3

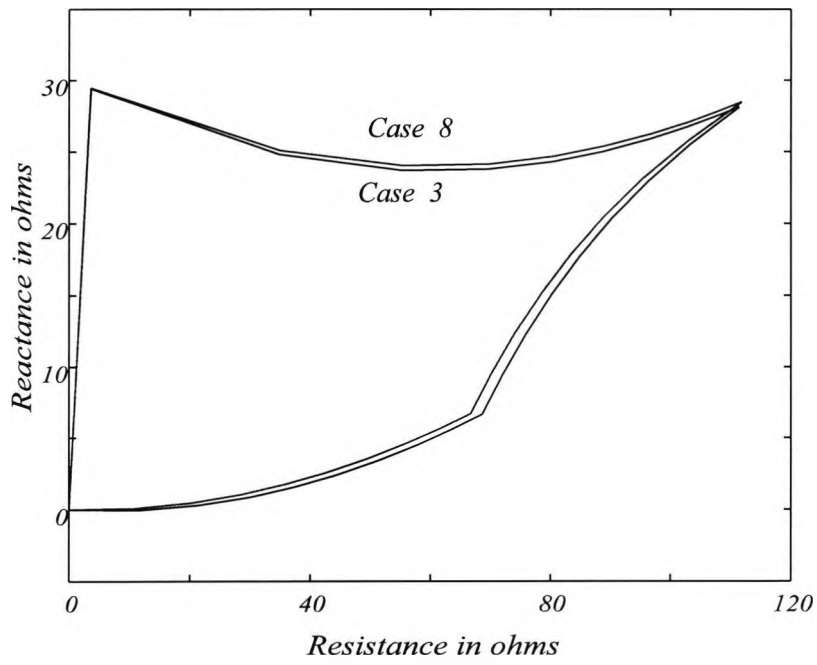


Fig. 6.10 Ideal operating region of case 8 as compared with case 3

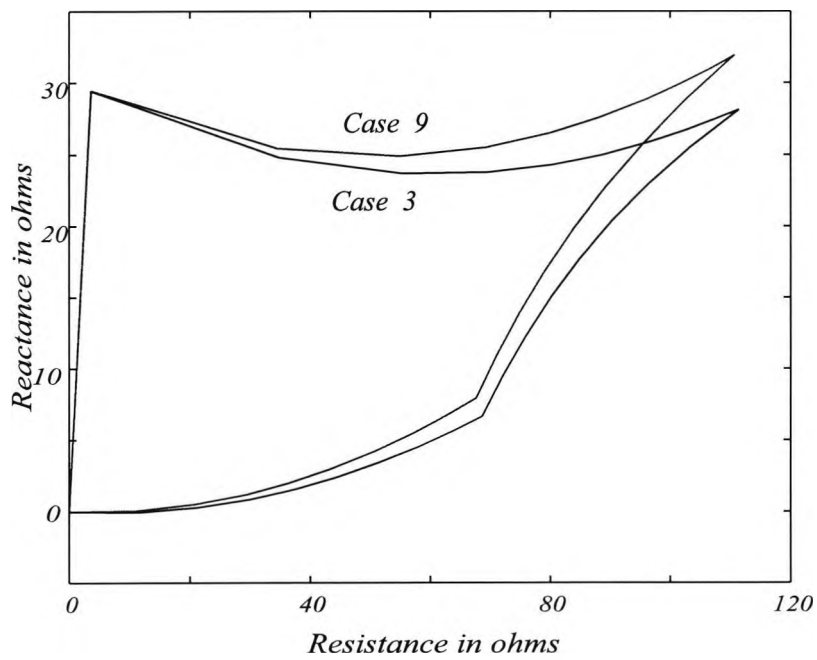


Fig. 6.11 Ideal operating region of case 9 as compared with case 3

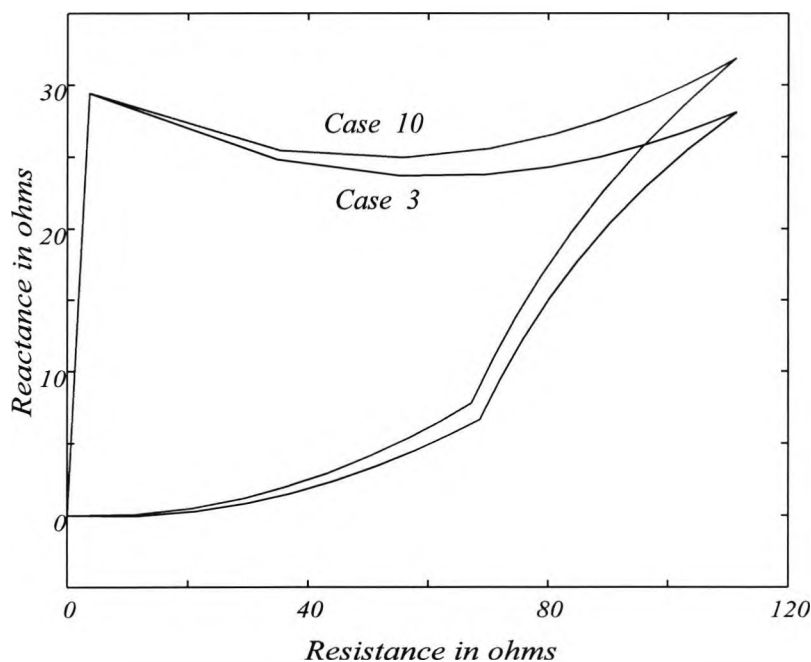


Fig. 6.12 Ideal operating region of case 10 as compared with case 3

The very significant observation from case 1 to 6 (Fig. 6.9 to 6.12) show that if the active and reactive power (P and Q) flow in the protected line remains virtually constant over a wide range of external system changes, the ideal operating region changes very little. It further verifies that the ideal operating region of distance relay is mainly governed by the active and reactive power flow in the protected line. The external system configuration only causes a minor change in the coverage. Comparison of Case 3 with Case 7 and 8 verifies that large changes in the length of the external lines only causes a small change in the coverage. In case 8 for example the combined length of the two external lines is less than 125 km, the length of the protected line.

6.4 ACCURACY OF THE IDEAL OPERATING REGION

From Fig. 6.5 to 6.7, it can be observed that if the P and Q flow in the protected line remain approximately constant, and if there is no big change in the system configurations such as switching of major interconnectors, the ideal operating region is not affected too much simply by changes in generation or load demand in the system. The accuracy of the coverage is estimated

to be better than 5% of line length even for high resistance earth faults. Where fault resistance is low, the change is negligible. On the other hand, changes in system configuration (Fig. 6.9 to 6.12), such as switching of major interconnector does cause a slightly larger change in the ideal operating region. However, even under these cases, the accuracy of distance relay coverage is still roughly within 10% of line length under a high resistance earth fault. Again the accuracy will be better when the fault resistance is low.

6.5 APPLICATION FOR ADAPTIVE DISTANCE RELAY

Based on the above concept, the ideal operating region of distance relay within the normal range of active and reactive power flow can thus be calculated offline based on the usual system configuration. Real time data transfer is not necessary. The only disadvantage is the slight increase of error which is within the tolerable range under high resistance earth fault. If a higher tolerance to error can be accepted, the same region can be applied even under a major change in system configuration. To produce better accuracy, different sets of calculated ideal operating regions can be pre-calculated for each of the major system configurations. Bear in mind that even if these are not available, the relay characteristic will not change substantially and its major function can be retained.

It has been shown that the main factor affecting the ideal operating region of a digital distance relay is the active and reactive power flow in the line. The error in ideal operating region caused by changes in system configuration is within the tolerable range. The relay can still retain its main function even under a major change in system configuration. It is believed that the finding will be important for developing a simple and practical intelligent digital relay which does not require an expensive communicating link in the future.

CHAPTER VII**STAND ALONE INTELLIGENT DIGITAL DISTANCE RELAY****7.1 INTRODUCTION**

The advance in microprocessor technology and communication systems and the low cost of digital devices are making digital distance relaying attractive. The digital technique provides major benefits as compared to the old technology such as the possibility of implementing adaptive methods. Advantages derived from adaptive relaying are well known [21], however, if system operating conditions vary significantly, and for high impedance faults, relay selectivity will be in question. In order to provide coverage for high resistance faults, an ideal relay coverage was proposed in [26] which relied on pre-fault information from the remote end. The ideal distance relay coverage is calculated on-line based on this information and slow-speed communication channel.

It has been shown in Chapter 6 that the main factors affecting the ideal operating region of a digital distance relay is the active and reactive power flow in the line and this finding is once again confirmed in section 7.3 of this chapter. The relay can retain its main function even under a major change in system configuration. This finding is important for developing a simple and practical intelligent digital relay which does not require an expensive communicating link. A typical case study in the application of ANN for high resistance fault identification is included in Appendix B to provide more detailed information.

7.2 APPLICATION OF ARTIFICIAL NEURAL NETWORK IN ADAPTIVE DISTANCE RELAY

These findings motivated an investigation of the hypothesis that the ideal operating region of distance relay within the normal range of active and reactive power flow can be calculated off-line based on the usual system configuration. Real time data transfer is not necessary. It has been shown in [31] that Artificial Neural Networks (ANN) can be used to identify the trip region of the non-linear boundaries. However the boundary needs to be updated regularly as the load in the line changes.

7.2.1 Design of Artificial Neural Network

The same practical relay trip characteristic as defined in 5.4 is used and is reproduced below:

Boundary A: faults at a relay-reach end (80% of line length) with fault resistances of 0 to 200 Ω ;

Boundary B: faults at different locations with a 200 Ω fault resistance;

Boundary C: faults at the relaying point with fault resistance of 0 to 200 Ω ;

Boundary D: Constant resistance boundary set at - 4 Ω to make sure that faults with zero fault resistance along the protected line are well inside the operating region.

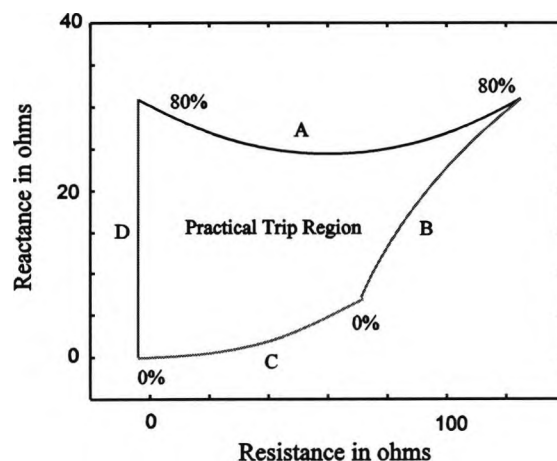


Fig. 5.7 A practical trip region

Three Artificial Neural Networks (ANN) have been designed for trip region identification for the three non-linear boundaries A, B, and C as indicated in Fig. 5.7. Each of them has been tested using with a parallel processing approach [26, 29, 31, 35]. Nguyen-Widrow method is used to find the initial conditions of weights and biases. The new Nguyen-Widrow initial conditions is used for the reason explained in 5.4. The Levenberg-Marquardt training technique [39] is used for fast and accurate performance.

Each ANN is designed with three layers, namely an input layer, an output layer, and a hidden layer. The hypertangent sigmoid transfer function is used between the input and hidden layers and the pure linear transfer function is used between the hidden and output layers.

To incorporate the effect of active and reactive power flow in the line, the changes of active and reactive power flow (ΔP , ΔQ) in the line from fixed reference values is used in training the ANN so as to improve the dynamic performance of the ANN. For training the ANN for boundary A, ΔP , ΔQ , and the resistance R_A at different points along boundary A are the inputs and the corresponding reactance X_A is obtained as the output. For boundary B, ΔP , ΔQ , and the reactance X_B at different points along the boundary are the inputs and the corresponding resistance R_B is obtained as the output. Boundary C is trained in a similar manner to boundary A. No training is required for boundary D as it remains unchanged for all configurations.

The Levenberg-Marquardt training method is proved to be more superior in the present case study. For the problem under study, training was successfully completed in less than 40 epochs and reached a sum square error goal of $2 \text{ E-}8$ when using the Levenberg-Marquardt method. When the adaptive learning rate with momentum was used, the number of epochs exceeded one million with the same network architecture and sum square error goal.

7.2.2 Trip Boundary Prediction

Each network was trained individually until satisfactory results were obtained. Based on the P and Q flow in the line, the three ANNs can work together to estimate the required tripping region for that particular load condition. A tripping decision can then be made based on the on-line measurement and the output from the ANNs. For example, the neural network of Boundary A gives the reactance output X, according to equation (7.1).

$$X = f_{purelin} \left([W_2] \cdot f_{tan} \left([W_1] \cdot \begin{bmatrix} \Delta P \\ \Delta Q \\ R \end{bmatrix}, [B_1] \right), [B_2] \right) \quad 7.1$$

where $f_{purelin}$, f_{tan} are the pure linear sigmoid and hypertangent sigmoid transfer functions respectively,

$|W_1|$, $|W_2|$ are the weights of the trained network for layers 1 and 2 respectively,

$|B_1|$, $|B_2|$ are the biases of the trained network for layers 1 and 2 respectively.

The measured reactance is thus compared with the predicted output from the three ANN to judge whether it is an internal fault.

7.3 TRAINING DATA

The system configurations and line parameters are the same as in Fig. 6.4. Short circuit level of all sources are 30 GVA. The reference values of active and reactive power chosen for the study are 950MW and 250 MVar respectively. ΔP , ΔQ , two of the inputs to the ANN, are therefore defined as the difference in P and Q flow in that particular load condition from these reference values. The ANN is trained for a range of P from 800 to 1000 MW in 100 MW steps, and a range of Q from 200 to 300 MVar in 50 MVar steps. There are altogether a total of 9 cases used for training and the corresponding system information and P and Q flow in the line are listed in Tables 7.1, 7.2, and Appendix C. Fault simulations are carried out by using the EMTP and the

corresponding impedance seen by the relay is calculated by applying the adaptive variable window length algorithm [33]. The ideal operating region of 4 cases, Case 1, 3, 7, and 9, where the P and Q flow are of the extreme points of the range are shown in Fig. 7.1. The boundary information of all 9 cases are supplied to the ANN.

Table 7.1 System Information of the Training Cases (in MVA)

Case	$P+jQ (L-R)$	$P+jQ (L-E)$	$P+jQ (R-E)$	$P+jQ (L)$	$P+jQ (R)$	$P+jQ (E)$
1	800+j200	306-j22	-202-j125	-j800	1490+j1200	600
2	801+j250	306+j3.3	-202-j130	-j1200	1490+j1280	600
3	801+j300	306+j22	-201-j140	-j1500	1489+j1445	600
4	901+j200	340-j34	-235-j126	-j600	1620+j1255	600
5	900+j250	338-j2.6	-233-j124	-j1100	1618+j1249	600
6	900+j300	338+j16	-233-j135	-j1400	1617+j1417	600
7	1000+j200	321-j43	-315-j110	-j500	1796+j1182	500
8	1000+j250	319-j11	-313-j109	-j1000	1794+j1182	500
9	1000+j300	318+j7.9	-312-j119	-j1300	1793+j1350	500

Table 7.2 System Information of the Training Cases (contd.)

Case	$V_L (p.u.)$	$V_R (p.u.)$	$V_E (p.u.)$
1	1.02∠-2.1	0.967∠-12.7	1.001∠-8.4
2	1.03∠-2.1	0.966∠-12.6	1.002∠-8.3
3	1.04∠-2.0	0.962∠-12.5	1.002∠-7.2
4	1.01∠-2.3	0.964∠-14.5	1.001∠-9.4
5	1.03∠-2.3	0.965∠-14.2	1.002∠-9.2
6	1.03∠-2.3	0.961∠-14.1	1.002∠-9.1
7	1.01∠-2.5	0.964∠-16.1	1.000∠-9.2
8	1.02∠-2.5	0.966∠-15.8	1.002∠-8.0
9	1.03∠-2.4	0.962∠-15.7	1.002∠-8.9

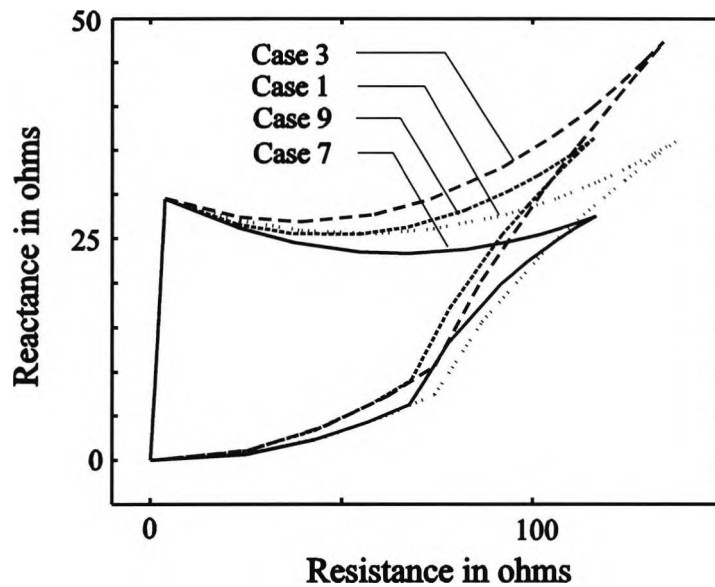


Fig. 7.1 Relay ideal boundaries of case 1, 3, 7 & 9

7.4 TRAINING THE ARTIFICIAL NEURAL NETWORK

The number of neurons in the hidden layer affects the accuracy of the nonlinear boundary and operating speed. Too few neurons can lead to underfitting. Too many can contribute to overfitting, where all training points fit well, but the fitted curve makes wild oscillations between these points. It was found that 15 neurons in the hidden layer were required for all the boundaries. The training time varies according to the starting point and the acceptable error. As the starting point is chosen at random, in some cases the training may not converge. In this case it was necessary to start again from a different point or try with a different number of neurons in the hidden layer. In this study, the tolerable sum square error chosen is $2E-8$, $1.5E-8$, and $2E-8$, and the training converged in 20, 34 and 15 epochs for boundaries A, B, and C respectively.

7.5 NEURAL NETWORK TRAINING RESULT

Four test cases within the P and Q range of the training set are produced for testing the accuracy of the ANN. As the system configurations will not change during normal circumstances, the system configuration of the test cases are the same as those used for training. However, the P and Q flow in the protected line in the test cases are different from those used for training. The system information of the test cases are shown in Tables 7.3, 7.4, and Appendix C.

Table 7.3 System Information of the Test Cases

Test	P+jQ (L-R)	P+jQ (L-E)	P+jQ (R-E)	P+jQ (L)	P+jQ (R)	P+jQ (E)
A	951+j225	352-j1.7	-247-j104	-j1100	1681+j964	600
B	851+j226	321+j4.1	-216-j111	-j1200	1553+j1010	600
C	950+j275	354+j10.5	-248-j121	-j1300	1681+j1222	600
D	851+j275	321-j16.3	-217-j127	-j1400	1553+j1265	600

Table 7.4 System Information of the Test Cases (contd.)

Test	V_L	V_R	V_E
A	1.03∠-2.4	0.973∠-15.0	1.002∠-9.6
B	1.03∠-2.2	0.966∠-13.3	1.002∠-8.7
C	1.03∠-2.4	0.962∠-14.9	1.002∠-9.6
D	1.04∠-2.2	0.964∠-13.3	1.001∠-8.6

Again EMTP is used for fault simulation studies for the test cases and the ideal boundaries seen by the relay are generated by applying adaptive variable window length algorithm. The predicted boundary produced by the neural network is compared with the ideal one. Fig. 7.2 to 7.5 show the comparison of the predicted and ideal boundaries of the test cases. It can be seen that the neural network can adapt to power flow changes in the line and produces a trip region which can

map the ideal relay reach very closely and smoothly. The neural network output can cover all earth faults with a maximum fault resistance of 200Ω from the relaying point up to 80% of the line length. Since the test cases are generated separately and are independent of the trained cases, this further supports the notion that the ideal operating region of distance relay is mainly affected by the pre-fault P and Q flow in the line.

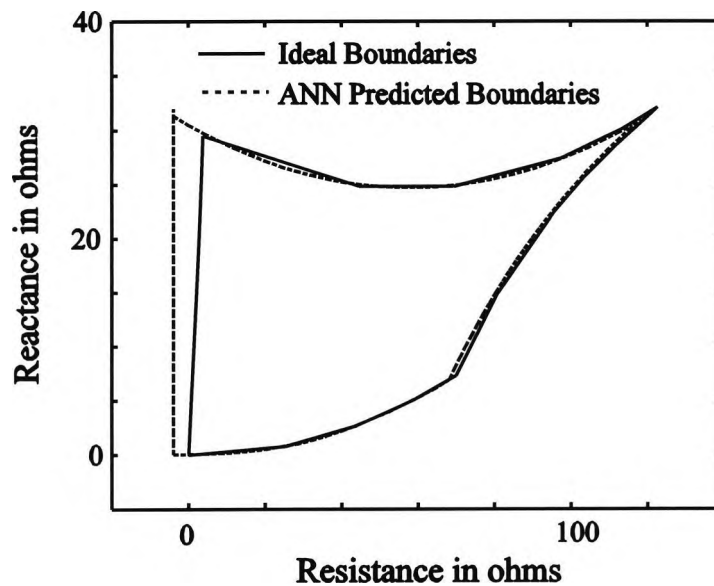


Fig. 7.2 ANN predicted relay boundary for test case A

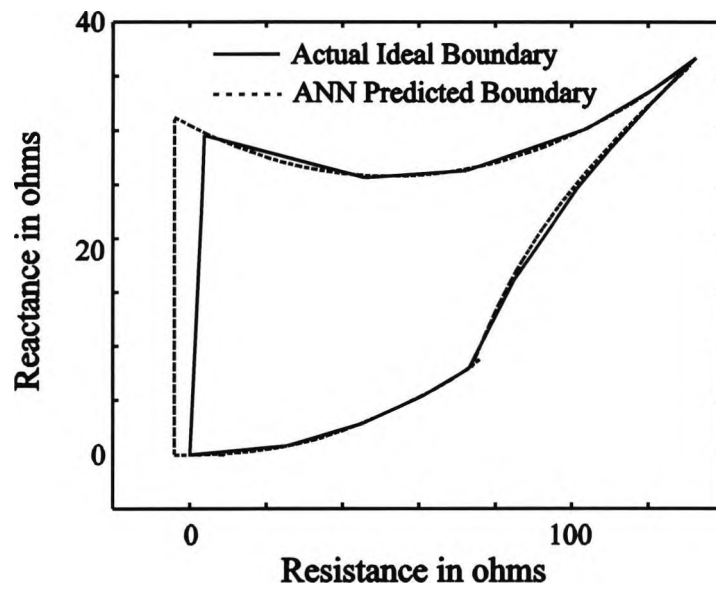


Fig. 7.3 ANN predicted relay boundary for test case B

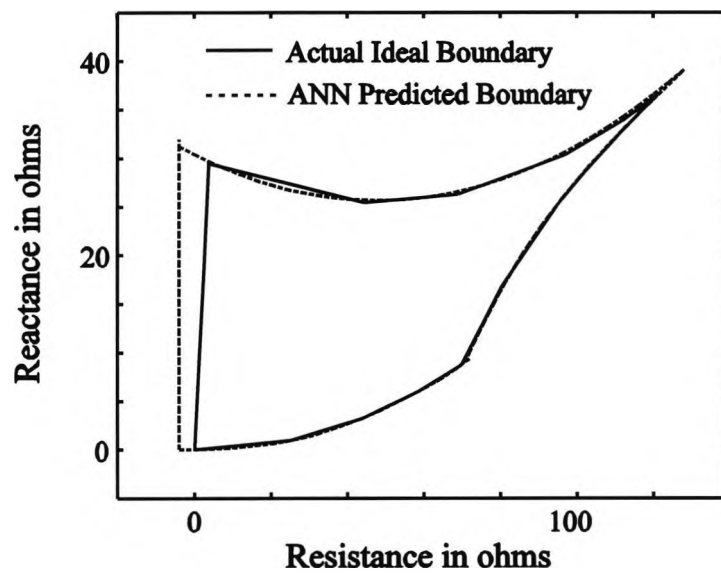


Fig. 7.4 ANN predicted relay boundary for test case C

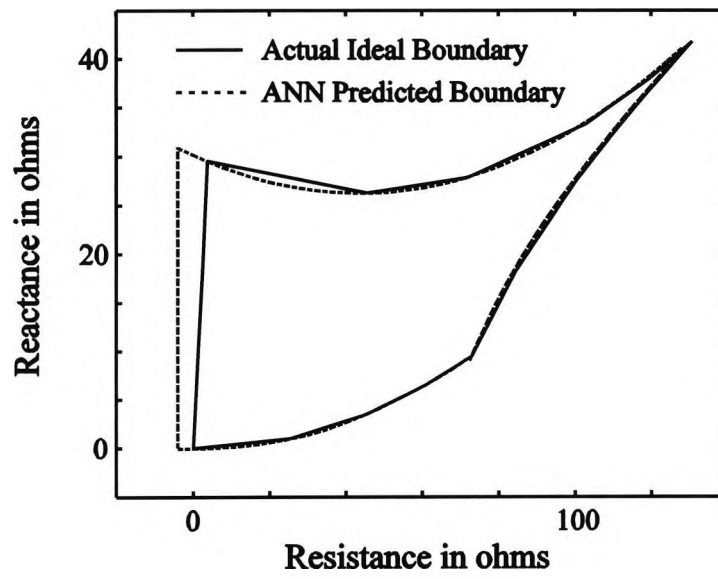


Fig. 7.5 ANN predicted relay boundary for test case D

7.6 TESTING PATTERNS AND RESULTS

7.6.1 Testing Pattern

Testing patterns should be properly selected to represent different fault measurements. Impedances in the test cases on the outer and inner curves of boundaries are chosen to test the neural network. A typical testing pattern is shown in Fig. 7.6.

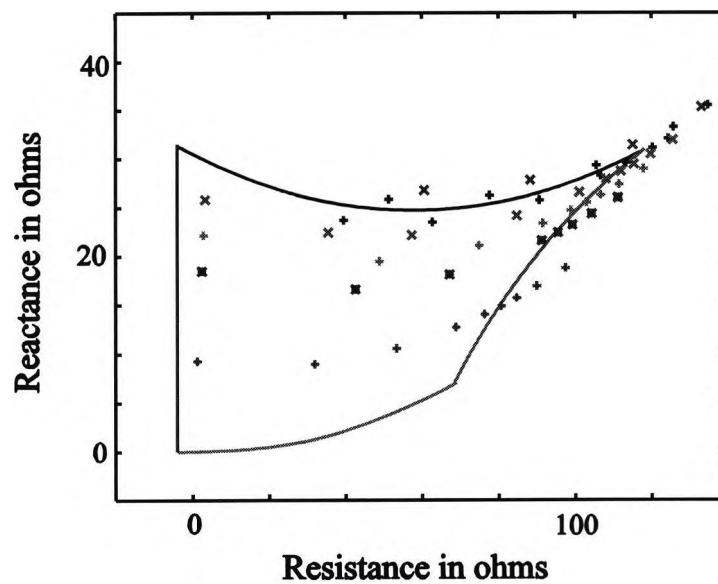


Fig. 7.6 Testing patterns

7.6.2 Testing Results

Testing points are generated by simulating single-phase to earth faults located at 25%, 50%, 60%, 70%, 75%, 85%, and 90% of the line length from the relaying point with fault resistance R_f ranging from 0 to 300 Ω by using EMTP. Both in-zone and out-zone faults at different locations and with different fault resistances are represented. By presenting these testing patterns as inputs to the trained neural networks, we can ascertain the accuracy of the trained ANN. The distance of the measured impedance from all boundaries can be identified based on the output from all neural networks. The distance of the measured impedance from the nearest boundary can thus be obtained and the corresponding test results for test cases A to D are shown in Table 7.5 to 7.8.

Each row corresponds to faults with different fault resistance at different locations of the line from the relaying point. The top row shows the corresponding fault resistance for that column in ohms. In Tables 7.5 to 7.8, the value shown is the impedance from the nearest relay boundary. Positive means that it is within the tripping region and negative means that the relay will restrain. The results show that the ANN can adapt to load changes and gives a correct trip decision.

Table 7.5 Output of Neural Network for Test Case A

$R_f(\Omega)$	0	25	50	100	150	180	220	250	300
90%		-2.0	-1.5	-1.1		-0.3		-0.6	
85%		-1.1	-0.8	-0.7		-0.2		-0.6	
75%		1.6	1.3	0.8	0.5	0.4	-1.8	-2.7	
70%	4.0	3.1	2.5	1.8	1.3	0.7	-2.0	-3.2	-4.3
60%	6.9		5.4	4.1	3.3	1.3	-2.3	-4.2	-6.0
50%	6.4		8.5	6.7		1.9	-2.6	-4.9	-7.5
25%	5.3		7.6	6.5	5.6	2.3	-3.1	-6.3	-10.2

Table 7.6 Output of Neural Network for Test Case B

$R_s(\Omega)$	0	25	50	100	150	180	220	250	300
90%		-2.1	-1.5	-1.0		-0.7		-0.6	
85%		-1.1	-0.8	-0.6		-0.5		-0.4	
75%		1.7	1.4	0.9	0.7	0.6	-0.5	-1.2	
70%	4.0	3.2	2.7	2.0	1.5	1.2	-1.1	-2.0	-2.7
60%	6.9		5.6	4.4	3.6	1.1	-2.2	-3.7	-5.1
50%	6.4		8.8	7.1		1.3	-3.1	-5.2	-7.4
25%	5.3		7.8	6.6	5.9	2.6	-3.6	-7.1	-11.4

Table 7.7 Output of Neural Network for Test Case C

$R_s(\Omega)$	0	25	50	100	150	180	220	250	300
90%		-1.9	-1.2	-0.7		-0.3		-0.2	
85%		-1.0	-0.6	-0.3		-0.1		-0.01	
75%		1.6	1.4	1.1	1.0	0.9	-0.5	-1.2	
70%	4.0	3.2	2.6	2.1	1.7	1.2	-0.9	-1.8	-2.5
60%	6.9		5.5	4.3	3.6	1.6	-1.5	-2.9	-4.2
50%	6.4		8.6	6.9		2.0	-1.9	-3.8	-5.8
25%	5.3		7.7	6.5	5.7	3.2	-2.0	-5.0	-8.6

Table 7.8 Output of Neural Network for Test Case D

$R_s(\Omega)$	0	25	50	100	150	180	220	250	300
90%		-2.3	-1.5	-0.8		-0.4		-0.2	
85%		-1.3	-0.9	-0.5		-0.2		-0.04	
75%		1.4	1.2	1.0	0.9	0.4	-1.3	-2.0	
70%	3.7	3.0	2.5	2.0	1.7	0.7	-1.5	-2.4	-3.3
60%	6.9		5.4	4.3	3.7	1.2	-1.9	-3.3	-4.7
50%	6.4		8.5	7.0		1.6	-2.3	-4.2	-6.2
25%	5.3		7.9	6.7	5.9	2.4	-3.1	-6.2	-9.7

7.7 PROPOSED TRIPPING SCHEME

The output from the artificial neural network indicates the distance of the measured impedance from the nearest boundary. The case studies have shown that if this value is less than 1Ω , the fault is very near to the boundary. If the neural network measurement is more than 2Ω , the fault is well within the trip region and tripping should be triggered without delay. Therefore, for neural network output from zero to less than 2Ω , a time delay which is inversely proportional to the measured impedance can be adopted. This will also avoid unnecessary tripping.

7.8 IMPLEMENTATION OF THE NEURAL NETWORK THEORY TO DIGITAL DISTANCE PROTECTION RELAY

A crucial finding is that a change of protected line load condition can give rise to a different ideal trip region while other variables have a much smaller or negligible effect. To cater for the training requirements for different line loading conditions, families of hypothetical prefault conditions and ideal trip boundaries have to be supplied in advance for the range of active and reactive power flow in the line. In the present case study, adequate data must be available for every 100 MW and 50 MVar interval within the load range of 800 to 1000MW and 200 to 300 MVar. The relay can then be trained initially, off-line, before it is put into use. Then, whenever a fault occurs within the trained range, the ANN is able identify internal faults within 0 to 80% of line length with a fault resistance up to 200Ω .

The adoption of relay operating region to system changing condition has been addressed. The concept of using neural networks as a digital distance relay has been proven to be feasible. Although a simple model has only been considered, it contains some necessary information for a practical study, for example, the effect due to changes of extended system configurations and variations in load of remote end. The positive results show a high potential for the proposed relay to be applied in real life system in future.

The concern for the time being is with economics, due to the requirement of high performance microprocessor chips. However, by virtue of the fact that electronic engineering is rapidly developing and analog and digital VLSI techniques for neural network are available [30], the cost of implementation will decline in the future. If the price becomes acceptable this approach could improve the performance of protective relaying and application specific IC chips should be considered for these applications.

CHAPTER VIII**CONCLUSION AND FURTHER WORKS****8.1 CONCLUSION****8.1.1 Development of the Adaptive Window Length Algorithm**

An adaptive window length algorithm has been developed. The simulation results in Chapter 4 show that it gives the fastest fault detection possible for any prevailing condition. It has overcome the speed and stability problems which cannot be solved by a constant window length algorithm. The algorithm is very stable under different system conditions and fault types. At the same time it gives a reliable and quick response while maintaining accurate measurements for a wide range of system configurations and conditions.

The algorithm is very simple and easy to implement. The amount of computations is not excessive as most are of a recursive nature and only data updating is needed for every new sample obtained. Hardware implementation of this algorithm does not impose any constraint on the computational overheads as high speed microprocessors chip are available at a relatively low cost. This algorithm forms the backbone of the work carried out in this thesis.

8.1.2 Relationship between the Distance Relay Ideal Operating Region and the Active and Reactive Power Flow in the Protected Line

One very significant observation of this project is the discovery of the relationship between the active and reactive power (P and Q) flow in the protected line and the ideal operating region of distance relay for the same line. It shows that (Chapter 6) if the active and reactive power (P and Q) flow in the protected line remains virtually constant, the ideal operating region changes very little over a wide range of external system changes. The external system configuration only

causes a minor change in the coverage. In a practical system, the system configuration will not deviate from the normal system configuration drastically and switching operation does not happen frequently. In this case the only factors which affects the ideal operating region of distance relay are the P and Q flow in the line. This finding is important for developing a simple and practical intelligent digital relay which does not require an expensive communicating link.

Based on this concept, the ideal operating region of distance relay within the normal range of active and reactive power flow in the line can thus be calculated offline based on the usual system configuration. Real time data transfer is not necessary. The only disadvantage is the slight increase of error which is within the tolerable range under high resistance earth fault. If a higher tolerance to error can be accepted, the same region can be applied even under a major change in system configuration. To produce better accuracy, different sets of calculated ideal operating region can be pre-calculated for each of the major system configuration. Bear in mind that even if these are not available, the relay characteristic will not change substantially and its major function can be retained.

8.1.3 Development of the Stand Alone Intelligent Digital Distance Relay

A crucial finding in this thesis is that a change of protected line load condition can give rise to a different ideal trip region while other variables have a much smaller or negligible effect. A stand alone intelligent digital distance relay based on artificial neural network concept can thus be developed. Families of hypothetical prefault conditions and ideal trip boundaries can be supplied in advance for the range of active and reactive power flow in the line. Artificial neural networks using backpropagation theory is used for the training requirements for different line loading conditions. The relay can then be trained initially, off-line, before it is put into use. Then, whenever a fault occurs within the trained range, the ANN is able to identify internal faults within its protected range (0 to 80% in this case) and up to the designed maximum fault resistance (200 Ω in this case).

The concept of using neural networks as a digital distance relay has been proven to be feasible. Although a simple model has only been considered, it contains some necessary information for a practical study, for example, the effect due to changes of extended system configurations and variations in load of remote end. The positive results show a high potential for the proposed relay to be applied in real life system in future.

8.2 FURTHER WORKS

8.2.1 Development of the Mathematical Relationship for the Line Flow and Ideal Operating Region

One of the main work is to develop the mathematical relationship between the active and reactive power (P and Q) flow in the protected line and the ideal operating region of distance relay for the protected line.

During pre-fault condition,

$$P_{LR} + jQ_{LR} = V_L I_{LR}^* \quad 8.1$$

where

$$I_{LR} = \frac{V_L \angle \delta_L - V_R \angle \delta_R}{Z_L} \quad 8.2$$

where Z_L is the impedance of the line

Therefore

$$P_{LR} + jQ_{LR} = f(V_L, V_R, \delta_L, \delta_R, Z_L) \quad 8.3$$

To work out the mathematical relationship between the line flow and ideal operating region, a general expression for unbalance fault analysis must be carried out. The most efficient method to carry out unbalance fault analysis for a multi-node network is by using impedance matrix

method [40]. The impedance matrix, although more difficult to derive, has certain advantages for fault computations. This is primarily due to the impedance matrix being an "open circuit" network description, and this coincides with the open circuit approximation usually in fault studies. In the impedance matrix, the diagonal impedance element Z_{ff} may be thought of as the impedance seen looking into the network at node f with all nodes except the f node open.

Then the sequence voltage and current at node l (the relaying point) contributing to the fault may be computed as shown in eqn. 8.4 and 8.5

$$V_{s-l} = -Z_{s-lf} \frac{V_f}{Z_T} \tag{8.4}$$

$$\begin{aligned} I_{s-lf} &= \frac{V_{s-l} - V_{s-f}}{z_{s-lf}} \\ &= \frac{V_f (Z_{s-ff} - Z_{s-lf})}{z_{s-lf} Z_T} \end{aligned} \tag{8.5}$$

where

V_{s-l} = corresponding sequence fault voltage at relaying point

V_{s-f} = corresponding sequence fault voltage at fault location

z_{s-lf} = corresponding sequence line impedance between node l and f

I_{s-lf} = corresponding sequence fault current in the line from node l to node f

V_f = pre-fault voltage at fault location

Z_{s-lf} = corresponding sequence transfer impedance between node l and f

Z_{s-ff} = corresponding sequence diagonal impedance for node f

Z_T = driving point impedance at node f

$$= Z_{0-ff} + Z_{1-ff} + Z_{2-ff} + 3R_f$$

The A phase voltage and current at relaying point are:

$$V_R = V_{1-l} + V_{2-l} + V_{0-l} \tag{8.6}$$

$$I_a = I_{1-l} + I_{2-l} + I_{0-l} \tag{8.7}$$

As shown in Chapter 5,

$$I_R = I_a + I_{0-l} \frac{Z_{0L} - Z_{1L}}{Z_{1L}} \quad 8.8$$

where Z_{0L} and Z_{1L} are the zero sequence and positive sequence impedance of the protected line.

The impedance seen by the relay is

$$Z_R = \frac{V_R}{I_R} \quad 8.9$$

The impedance measured by a distance relay at the local end can be expressed as

$$\begin{aligned} Z_R &= z_{1lf} + \Delta Z \\ &= pZ_{1L} + \Delta Z \end{aligned} \quad 8.10$$

Examining eqn. 8.4 to 8.10, it can be seen that the impedance measured at the relaying point depends on V_f , Z_{s-lf} , Z_{s-ff} , and Z_T . Z_{s-lf} , Z_{s-ff} , and Z_T depends on the distance of fault from the relaying point, the system configurations, and the fault resistance. ΔZ can therefore be expressed as

$$\Delta Z = f(V_f, p, Z_L, R_f, Z_{s-lf}, Z_{s-ff}, Z_T) \quad 8.11$$

where Z_L is the impedance of the protected line.

V_f is the pre-fault voltage at fault location

Z_{s-lf} = corresponding sequence transfer impedance between node l and f

Z_{s-ff} = corresponding sequence diagonal impedance for node f

Z_T = Driving point impedance at node f

$$= Z_{0-ff} + Z_{1-ff} + Z_{2-ff} + 3R_f$$

Since the line impedance is constant and we consider a high resistance earth fault of known fault resistance at a known position, p , Z_L and R_f are all known. Therefore

$$\Delta Z = f(V_f, Z_{s-lf}, Z_{s-ff}, Z_T) \quad 8.12$$

If P and Q flow in the line remains approximately constant, V_L , and the phasor difference between V_L and V_R has to remain approximately the same. In other words, V_f would remain constant. The next step is to prove that the changes in the transfer impedance Z_{s-lf} Z_{s-ff} and therefore the driving point impedance Z_T is relatively small if there is only minor changes in system configuration and conditions provided the flow in the line and hence V_f is constant, for example, changes in generation and/or switching of lines apart from the protected line. If this can be proved, then it follows that ΔZ will remains constant.

Further work can be done to verify this phenomena mathematically.

8.2.2 The Possibility of Using Fuzzy Neural Network for Operating Region Identification

As the ideal operating region only remains roughly constant for a constant P and Q flow in the line, the system configuration and conditions does have a slight effect on the ideal operating region. High resistance faults at the far end of the line will be affected most and they are very difficult to be identified as an internal or external fault. Fuzzy logic and hence fuzzy neural network will be useful to solve problems in this nature. Further studies will be carried out in this direction.

8.2.3 Practical Range of P and Q Flow for ANN Training

As the ideal operating region does not change linearly with the change of P and Q flow in the line, there exists a limit of loading range where ANN can be applied to predict operation. At the present case study the range of P and Q flow in the line is from 800 to 1000 MW and 200 to 300 MVar. This range can be extended further. The practical limit depends on the resultant error produced by the ANN. It may be necessary to divide the whole range of P and Q flow in the line into different zones and several individual ANNs are used for each zone. The P and Q flow in the line can be used as an indicator for which ANNs should be used.

8.2.4 Development of a Comprehensive High Impedance Fault Detection Relay

Based on the above mentioned concept, a comprehensive high impedance fault detection relay can be developed. Fault detection can be divided into several classes:

(i) Solid fault - This needs immediate attention and high speed tripping is necessary. A quadrilateral tripping zone and a tripping logic as suggested by A.T. Johns [8, 12] can be employed to identify faults of this nature and high speed tripping can be achieved. The adaptive window length algorithm can be applied here as it fulfills the speed and stability requirement of impedance calculation.

(ii) High resistance fault - Different types of fault would cause different fault resistance. Thus high resistance faults are again classified into: (a) fault resistance less than 50 Ω , (b) fault resistance between 50 to 200 Ω , and (c) fault resistance between 200 to 400 Ω . Adaptive time delay can be used according to their fault class and distance from the boundary. In general faults with a fault resistance between 50 to 200 Ω should be given a longer time delay than faults with fault resistance less than 50 Ω in order to verify that it is a genuine fault. The damaging effect of high resistance fault is not excessive and bear in mind that this type of fault cannot be identified by normal distance relays, a slightly longer delay in tripping can be tolerated. For fault

resistance above 400Ω , an alarm will be initiated to warn the operator to carry out further investigation and decision making.

A comprehensive high impedance fault detection relay is thus developed. The flow chart of the relay for different classes of fault is shown in Fig. 8.1.

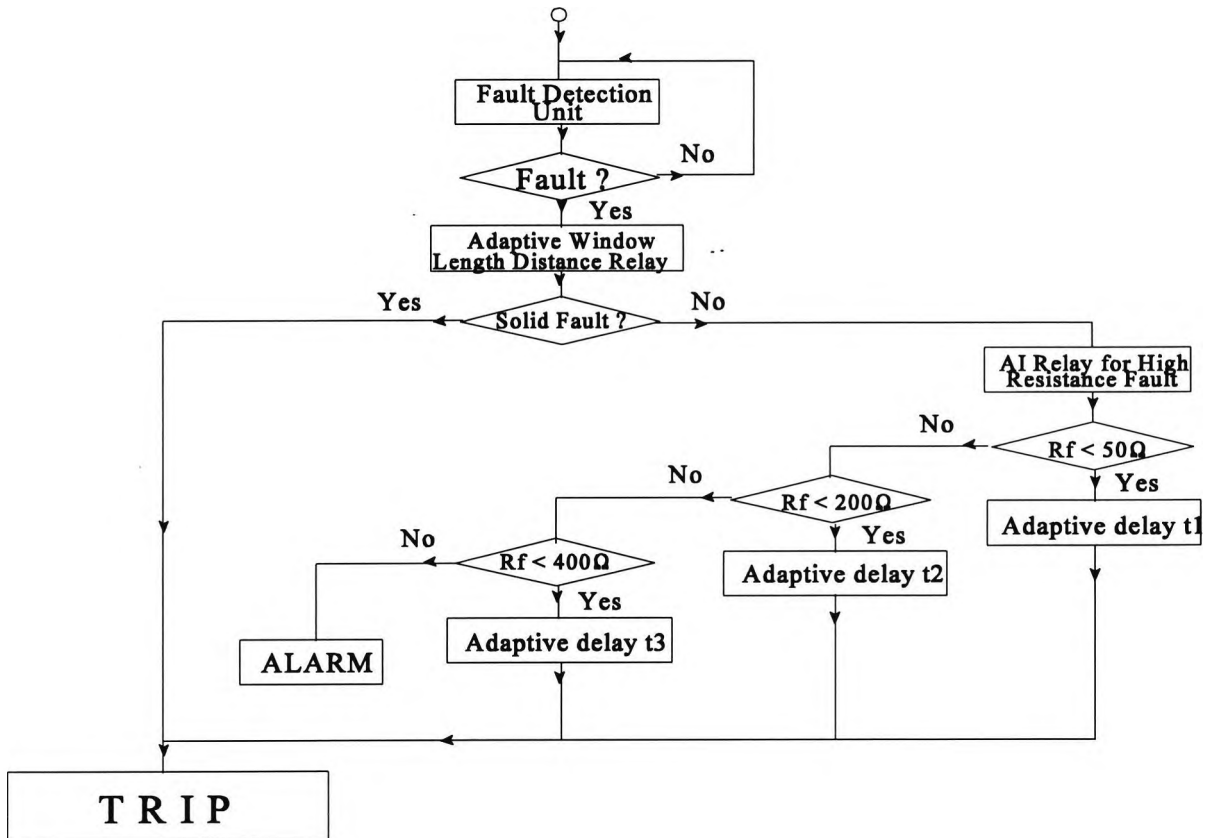


Fig. 8.1

Flow chart of digital distance relay for high resistance fault detection

REFERENCE

1. G.D. Rockefeller : "Fault Protection with a Digital Computer", *IEEE Trans. on Power Apparatus and Systems*, 1969, PAS-88, pp. 438-464.
2. B.J. Mann and I.F. Morrison : "Digital Calculation of Impedances for Transmission Line Protection", *IEEE Trans. on Power Apparatus and Systems*, 1971, PAS-90, pp. 270-279.
3. B.E. McInnes and I.F. Morrison : "Real Time Calculation of Resistance and Reactance for Transmission Line Protection by Digital Computer", *EE Trans., Inst. of Engrs., Australia*, Vol. EE7, No. 1, 1970, pp. 16-23.
4. M. Ramamoorthy : "Application of Digital Computers to Power System Protection", *J. Inst. Eng. India*, 1972, 52(10), pp.235-238.
5. J.A. Sykes and I.F. Morrison, "A Proposed Method of Harmonic Restraint Differential Protection of Transformers by Digital Computer", *IEEE Trans. on Power Apparatus and Systems*, Vol. PAS 91, No. 3, May/June 1972, pp. 1266-72.
6. J.G. Gilbert and R.J. Shovlin, "High Speed Transmission Line Fault Impedance Calculation Using a Dedicated Minicomputer", *IEEE Trans. on Power Apparatus and Systems*, Vol. 94, No. 3, May/June 1975, pp. 872-883.
7. A.T. Johns and R.K. Aggarwal : "Digital Simulation of Faulted e.h.v. Transmission lines with Particular Reference to Very-High-Speed Protection", *IEE Proceeding*, Vol. 123, No. 4, April 1976.
8. A.T. Johns and M.A. Martin : "Fundamental Digital Approach to the Distance Protection of e.h.v. Transmission Lines", *IEE Proceeding*, Vol. 125, No. 5, May 1978, pp. 377-384.
9. M. S. Sachdev, etc, "Computer Relaying", *IEEE Tutorial Course*, Text No. 79 EH0148-7-PWR, Piscataway, NJ, 1979.
10. *IEEE Power System Relaying Committee Working Group Report*, "EHV Protection Problem", *IEEE Transactions on Power Apparatus and Systems*, Vol. PAS-100, No. 5, May 1981, pp. 2399-2406.
11. A.G. Phadke, T. Hlibka, and etc, "A Microcomputer Based Ultra-High-Speed Distance Relay: Field Tests", *IEEE Trans. on Power Apparatus and Systems*, Vol. PAS-100, No.4, pp.2026-2033, 1981.
12. A.T. Johns and M.A. Martin : "New Ultra-high-speed Distance Protection using Finite Transform Techniques", *IEE Proceeding*, Vol. 130, Pt. C, No. 3, May 1983, pp. 127-138.

Reference

13. M. S. Sachdev, etc, "Microprocessor Relays and Protection Systems", *IEEE Tutorial Course*, Text No. 88 EH0269-1-PWR, Piscataway, NJ, 1988.
14. G. D. Rockefeller, C. L. Wagner, J. R. Linders, "Adaptive Transmission Relaying Concepts for Improved Performance", *IEEE Transactions on Power Delivery*, Vol.3, No.4, October 1988, pp.1446-1458.
15. S. H. Horowitz, A. G. Phadke, J. S. Thorp, "Adaptive Transmission System Relaying", *IEEE Transactions on Power Delivery*, Vol.3, No.4, October 1988, pp.1436-1445.
16. K.K. Li, C. Cheung, Y.Q. Xia, : 'Processing Power System Signals for Digital Distance Protection', *IEEE, IREE, and IE(Aust) International Symposium on Signal Processing and Its Applications*, Gold Coast, Australia, August 27-31, 1990, Vol. 2, pp. 806-809.
17. K.K. Li, C. Cheung, Y.Q. Xia, : 'A Modified Finite Transform Algorithm for Digital Distance Protection Relay', *8th CEPSTI*, Singapore, November 5-9, 1990, Paper 4-41.
18. Bernard Widrow, M.A. Lehr, "30 Years of Adaptive Neural Networks: Perceptron, Madaline, and Back-propagation", *Proceeding of the IEEE*, Vol. 78, No. 9, September 1990, pp. 1415-1442.
19. A. Wiszniewski, "Digital High Speed Calculation of the Distorted Signal Fundamental Component", *IEE Proceeding*, Part C, 1990, Vol. 137, No. 1, pp. 19-24.
20. A.F. Sultan, G.W. Swift, D.J. Fedirchuk, "Detection of High Impedance Arcing Faults Using a Multi-Layer Perceptron", *IEEE Transactions on Power Delivery*, Vol. 7, No. 4, October 1992, pp. 1871-1877.
21. Z. Zhang, D. Chen "An Adaptive Approach in Digital Distance Protection", *IEEE Transactions on Power Delivery*, Vol.6, No.1, January 1991, pp. 135-142.
22. K.K. Li, C. Cheung, Y.Q. Xia, : 'High Speed Digital Distance Protection - Real Time Simulation and Hardware Development', *1st IEE International Conference in Advances in Power System Control, Operation, and Management (APSCOM-91)*, Hong Kong, November 5-8, 1991, pp. 95-100.
23. IEEE Power System Relaying Committee, "Feasibility of Adaptive Protection and Control", *IEEE Transactions on Power Delivery*, Vol. 8., No. 3, July 1993, pp. 975-983.
24. K.K. Li, Y.Q. Xia, : 'Operating Speed and Reach Accuracy Study for a Digital Distance Relaying Algorithm', *1993 IEEE Region 10 Conference on Computer, Communication, Control and Power Engineering (TENCON-93/BEJING)*, October 19-21, 1993, Beijing, Vol. 5, pp. 284-287.

Reference

25. K.K. Li, Y.Q. Xia, : 'Considerations for Adaptive Distance Relaying', *2nd IEE International Conference in Advances in Power System Control, Operation, and Management (APSCOM-93)*, Hong Kong, December 7-10, 1993, Vol. 1, pp. 379-384.
26. Y.Q. Xia, K.K. Li, A.K. David : 'Adaptive Relay Setting for Stand-Alone Digital Distance Protection', *IEEE Transactions on Power Delivery*, Vol. 9, No. 1, January 1994, pp. 480-491.
27. Y.Q. Xia, A.K. David, K.K. Li : 'High-Resistance Faults on a Multi-Terminal Line : Analysis, Simulated Studies and an Adaptive Distance Relaying Scheme', *IEEE Transactions on Power Delivery*, Vol. 9, No. 1, January 1994, pp. 492-500.
28. Y.Q. Xia, K.K. Li : 'Development and Implementation of a Variable Window Alogorithm for High Speed and Accurate Digital Distance Protection', *IEE Proceeding, Generation Transmission and Distribution*, Vol. 141, No. 4, July 1994, pp.383-389.
29. K.K. Li. Y.Q. Xia, : 'Application of Artificial Neural Network in Adaptive Distance Relaying', *Electrical Engineering Congress 94 (EEC-94)*, Sydney, November 24-30, 1994, Vol. 1, pp. 3-8.
30. E. M. Georges, L.L. Lai, F. Ndeh-Che, and H. Braun, 'Neural Networks Implementation with VLSI', Proceeding, *IEE Fourth International Conference on Artificial Neural Networks*, Cambridge, U.K. June 1995, pp. 489-494.
31. K.K. Li, A.K. David, L.L. Lai, Y.Q. Xia, : 'An Adaptive Digital Distance Relay for EHV Transmission Lines", Preprints, *International Federation of Automatic Control (IFAC-95) Symposium on Large Scale Systems*, London, July 1995, Vol. 1, pp. 433-438.
32. K.K. Li, L.L. Lai, Y.Q. Xia, : 'Development in Variable Window Algorithm for High Speed and Accurate Digital Distance Protection', *3rd IEE International Conference in Advances in Power System Control, Operation, and Management (APSCOM-95)*, Hong Kong, November 1995, Vol. 1, pp.271-276.
33. K.K. Li : 'An Adaptive Window Length Algorithm for Accurate High Speed Digital Distance Protection', *The International Journal of Electrical Power & Energy Systems*, Volume 19, No. 6, August 1997, pp. 375-383.
34. K.K. Li, L.L. Lai : 'Ideal Operating Region of Digital Distance Relay Under High Resistance Earth Fault', *International Journal of Electric Power System Research*, Elsevier Science Ltd., Vol. 43, No.3, Dec. 1997, pp. 215-219.
35. K.K. Li, L.L. Lai, A.K. David : 'Intelligent Digital Distance Relay', *The International Conference on Intelligent Systems - Applications to Power Systems (ISAP'97)*, The Korean Institute of Electrical Engineers, Seoul, Korea, July 6-10, 1997, pp. 279-283.

Reference

36. K.K. Li, L.L. Lai : 'An Adaptive Variable Window Algorithm for Digital Distance Protection', *4th IEE International Conference in Advances in Power System Control, Operation, and Management (APSCOM-97)*, Hong Kong, November 11-14, 1997, Vol. 1, pp. 83-88.
37. K.K. Li, L.L. Lai, A.K. David : 'High Speed and Stable Adaptive Variable Window Algorithm for Digital Distance Protection', *Australian Universities Power Engineering Conference / IEAust Energy Conference (AUPEC/EEC 97)*, Sydney, 29 September - 1 October, 1997, Vol. 2, pp. 383-388.
38. K.K. Li, L.L. Lai, A.K. David : 'Stand Alone Intelligent Digital Distance Relay', *IEEE Transactions on Power Systems*, paper submitted for consideration.
39. "Neural Network Toolbox User's Guide for Use with MATLAB", Howard Demuth, Mark Beale, The Math Works Inc., 1994.
40. "Analysis of Faulted Power Systems", Paul M. Anderson, IEEE Press Power Systems Engineering Series, 1995.
41. W. Qi, G.W. Swift, P.G. McLaren, A.V. Castro : 'An Artificial Neural Network Application to Distance Protection', *The International Conference on Intelligent Systems - Applications to Power Systems (ISAP'96)*, January 28 - February 2, 1996, Florida, U.S.A., pp. 226-230.
42. P. Ye, D.S. Chen, K.K. Li, A.K. David : 'A Novel Algorithm for High Resistance Earth Fault Distance Protection', 1996 IEEE/PES T & D Conference and Exposition, Los Angeles, Sept. 1996, pp.475-480.
43. P. Ye, D.S. Chen, K.K. Li, A.K. David : 'Intelligent Phase Comparison Carrier Protection', *IEE 6th International Conference on Developments in Power System Protection*, Nottingham, U.K., March 25-27, 1997, pp. 295-298.

APPENDIX A

**IMPEDANCE MEASURED AT THE RELAYING POINT
WITH THE PRESENCE OF FAULT RESISTANCE**

Referring to the same 400 kV three source system model as shown in Chapter 4 (Fig. 4.2 is reproduced below.), a single-line-ground fault at F through a fault resistance R_f is examined and a digital distance relay installed at L is considered.

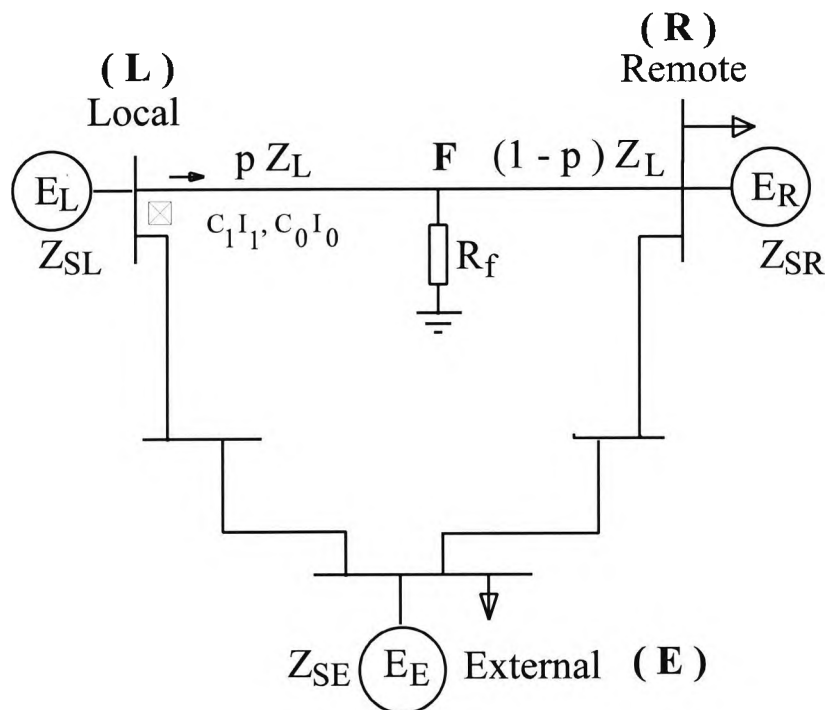


Fig. 4.2 Three source system model

For a fault at node F as shown in Fig. 4.2,

$$I_{a0-f} = I_{a1-f} = I_{a2-f} = \frac{V_f}{Z_T} \quad \text{A.1}$$

where

V_f = pre-fault voltage at fault location

I_{a0-f} = total zero sequence fault current at F .

I_{a1-f} = total positive sequence fault current at F .

I_{a2-f} = total negative sequence fault current at F .

Z_T = driving point impedance at node F

$$= Z_{0-ff} + Z_{1-ff} + Z_{2-ff} + 3R_f$$

Z_{0-ff} = total zero sequence impedance for a fault at F .

Z_{1-ff} = total positive sequence impedance for a fault at F .

Z_{2-ff} = total negative sequence impedance for a fault at F .

R_f = fault resistance.

At relaying point, the faulted phase current I_a is given by

$$\begin{aligned} I_a &= C_1 I_1 + C_2 I_2 + C_0 I_0 + I_L \\ &= 2 C_1 I_1 + C_0 I_0 + I_L \end{aligned} \quad \text{A.2}$$

where C_1 , C_2 , and C_0 are the current distribution ratio at the relaying point comparing to the total positive, negative and zero sequence fault current respectively.

The relaying current I_R is given by

$$\begin{aligned} I_R &= I_a + C_0 I_0 \frac{Z_{0L} - Z_{1L}}{Z_{1L}} \\ &= 2 C_1 I_1 + C_0 I_0 \frac{Z_{0L}}{Z_{1L}} + I_L \end{aligned} \quad \text{A.3}$$

The relaying voltage V_R is

$$\begin{aligned} V_R &= 2 C_1 I_1 Z_{1L} + C_0 I_0 Z_{0L} + I_L Z_{1L} + 3 I_0 R_f \\ &= \left(2 C_1 I_1 + C_0 I_0 \frac{Z_{0L}}{Z_{1L}} + I_L \right) Z_{1L} + 3 I_0 R_f \\ &= I_R Z_{1L} + 3 I_0 R_f \end{aligned} \quad \text{A.4}$$

Therefore the impedance seen by the relay Z_R is

$$\begin{aligned} Z_R &= \frac{V_R}{I_R} = Z_{1L} + \frac{3 I_0 R_f}{I_R} \\ &= Z_{1L} + \frac{3 I_0 R_f}{2 C_1 I_1 + C_0 I_0 \frac{Z_{0L}}{Z_{1L}} + I_L} \end{aligned} \quad \text{A.5}$$

Based on eqn. A.5, the impedance measured by a distance relay at the local end can be expressed as

$$Z_R = p Z_{1L} + \Delta Z \quad \text{A.6}$$

ΔZ depends on a number of factors, say, the location of fault, the positive and zero sequence current distribution ratio, the fault resistance and the load current. The fault current again depends on the pre-fault voltage, the source capacities, the load current to a certain extent, and also the ratio of e.m.f.s and phase angles between different sources. The positive and zero sequence current distribution ratio also depends on the fault location, the fault resistance and the ratio of e.m.f.s and phase angles between different sources.

Therefore,

$$\Delta Z = f_L (Z_{SL}, Z_{SR}, Z_{SE}, h_{RL}, h_{EL}, h_{ER}, \delta_{RL}, \delta_{EL}, \delta_{ER}, p, Z_L, R_f) \quad \text{A.7}$$

f_L is a non-linear function used to represent ΔZ in terms of the prefault and the postfault parameters.

APPENDIX B**CASE STUDY ON THE APPLICATION OF
ARTIFICIAL NEURAL NETWORK IN
ADAPTIVE DISTANCE RELAY FOR
HIGH RESISTANCE FAULT IDENTIFICATION****B.1 SYSTEM CONFIGURATION**

A 400 kV three source system model as shown in Fig. B.1 is chosen for the case study. In the chosen system, the short circuit level (SCL) of all sources are 30 GVA. The magnitude of e.m.f.s of all sources both equal to 1.0 p.u. The length of the 400 kV line between Local to Remote end is 125 km and the length between Local to External and between Remote to External are both 200 km. The impedance parameters per kilometre for all 400 kV lines are the same. The total positive sequence impedance of the 125 km line (Z_{1L}) is $37.5 \angle 86^\circ \Omega$ whereas its zero sequence impedance (Z_{0L}) is $136.6 \angle 69^\circ \Omega$. The total positive sequence impedance of the 200 km line (Z_{1L}) is $60 \angle 86^\circ \Omega$ whereas its zero sequence impedance (Z_{0L}) is $218.6 \angle 69^\circ \Omega$.

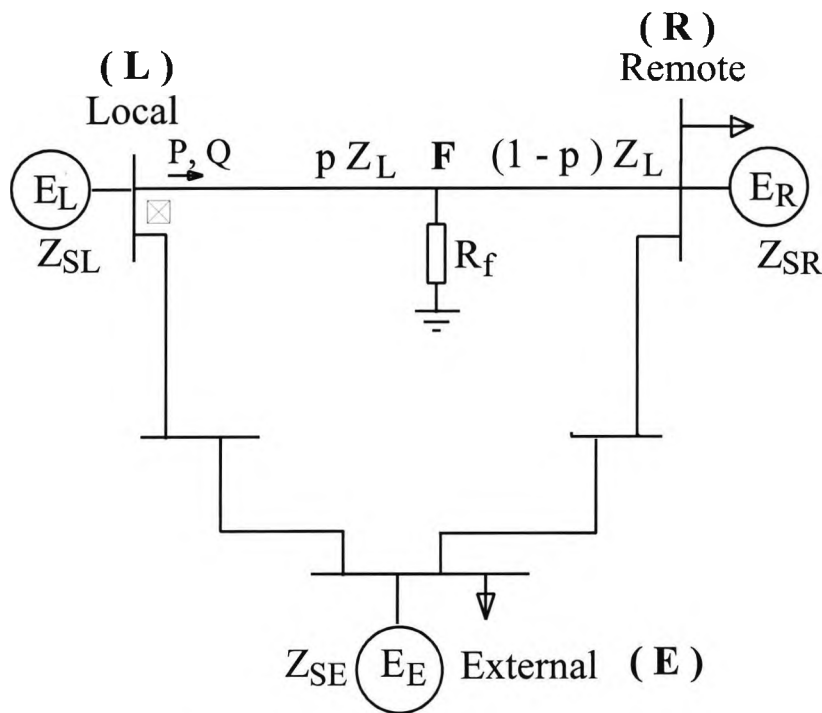


Fig. B.1 Three source system model

B.2 SELECTION OF TRAINING CASES FOR THE TRAINING OF THE ANN

In the present case study the range of active and reactive power flow from local to remote end is assumed changing from 800 to 1000 MW and from 200 to 300 MVAR respectively. Under normal operating conditions the system configuration would not change too much and hence the SCL and e.m.f. of all sources remain unchanged while the P and Q flow in the line changes. Nine cases are selected within this range of active and reactive power flow to prepare for the training data and four cases are selected for the test data. The distribution of training cases and testing cases are shown in Fig. B.2. The training cases are numbered from 1 to 9 and the testing cases are marked from A to D.

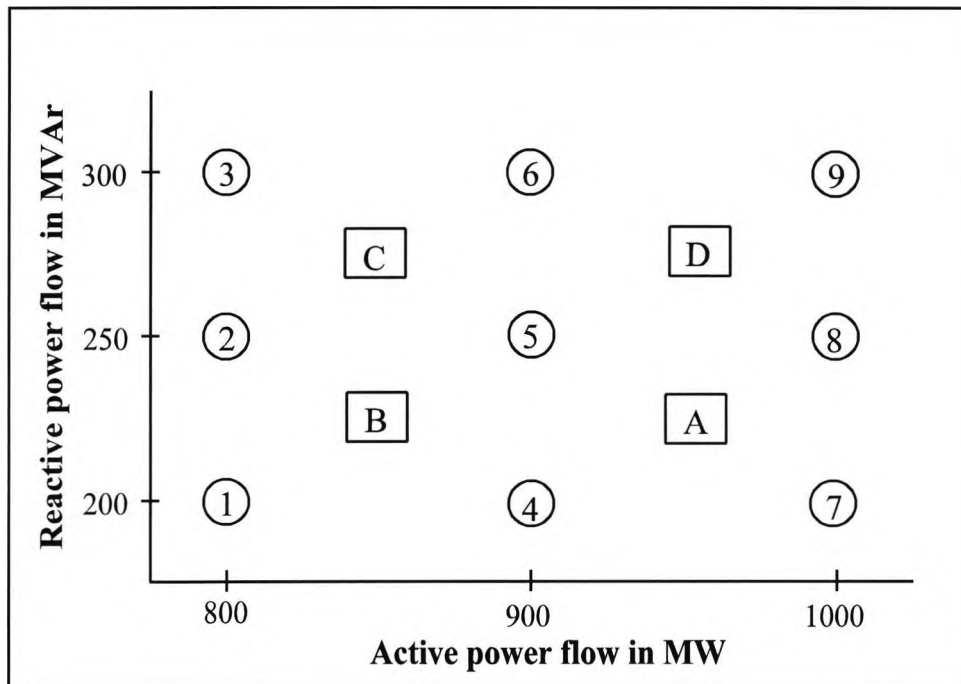


Fig. B.2 Distribution of training and testing cases

B.3 LOAD FLOW STUDIES ON THE SELECTED CASES

Load flow studies are carried out on all selected cases to compute the magnitude and phase angle relationships between all sources and the load required to be applied on all busbars. The local source is used as the slack bus. This information is essential for the transient analysis to be carried out in the next step. The 'ERACS' load flow software developed by ERA Technology Ltd., England is used for this purpose. The result of the load flow studies on all training and testing cases are shown in Appendix C.

B.4 TRANSIENT ANALYSIS

On each selected case, transient analysis is carried out with a single phase to earth fault applied on various locations of the line with fault resistance R_f ranging from 0 to 200 Ω . The EMTP program is used to generate the transient voltage and current signals at the relaying point. A typical EMTP program listing for the simulation of a single phase to earth fault at 60% of line

length with a fault resistance of 25 Ω for training case 1 is shown in Table B.1. The relaying voltage and current waveform simulated under this condition is shown in Fig. B.3. Similar transient analysis are carried out for all other training and testing cases.

Table B.1 EMTP Program for Fault Transient Simulation

```

BEGIN NEW DATA CASE
C
C Three source system fault transient simulation
C Flow N40 L30 R30 E30 P800.0 Q200.2
C El=1.0 Er=1.0 Ee=1.0
C
$WIDTH, 80
C 345678901234567890123456789012345678901234567890123456789012345678901
C DELTAT| TMAX | XOPT | COPT | EPSILN| TOLMAT| TSTART|
  2.5E-5  .7000      1.E-15
C IOUT | I PLOT | IDOUBL| KSSOUT| MAXOUT| IPUN | MEMSAV| ICAT | NERERG| IPRSUP|
  10      10      1      1      1      1      0      2
TACS HYBRID
BLANK
C
C NETWORK DESCRIPTION
C
C Three sources system with five interconnectors
C R in ohms, L in mH, and C in uF.
C Source sequence impedance
C Local Source
C 345678901234567890123456789012345678901234567890123456789012345678901
C | BUS1| BUS2| BUS3| BUS4|R OHM| L in mH |
C Zero sequence impedance of the source
51BUS1A BUS2A 16.97652726
C Positive sequence impedance of the source
52BUS1B BUS2B 16.97652726
C Third card to be left blank
53BUS1C BUS2C
C Remote Source
51BUS7A BUS6A 16.97652726
52BUS7B BUS6B 16.97652726
53BUS7C BUS6C
C External Source
51BUS12ABUS11A 16.97652726
52BUS12BBUS11B 16.97652726
53BUS12CBUS11C
C
C Current measurement by inserting a very small resistance
C
BUS2A BUS3A 1.E-9 1
BUS2B BUS3B BUS2A BUS3A 1
BUS2C BUS3C BUS2A BUS3A 1
BUS6A BUS5A BUS2A BUS3A
BUS6B BUS5B BUS2A BUS3A
BUS6C BUS5C BUS2A BUS3A
C
C Voltage measurement by connecting a very large resistance to bus
C
BUS2A 1.0E9 2
BUS2B BUS2A 2
BUS2C BUS2A 2
BUS6A BUS2A
BUS6B BUS2A
BUS6C BUS2A
C
C Line impedance using distributed parameters
C Use double precision
C
$VINTAGE, 1
C 345678901234567890123456789012345678901234567890123456789012345678901

```

Appendix B

```

C | BUS1| BUS2|          | R OHM/km | L mH/km | C uF/km | Length km | | |
C Zero sequence impedance
-1BUS3A BUS4A          0.38848  3.2508352 0.008454708      75.00  0 10
C Positive sequence impedance
-2BUS3B BUS4B          0.02336  0.951025057 0.012379469      75.00  0 10
C Leave blank
-3BUS3C BUS4C
-1BUS5A BUS4A          0.38848  3.2508352 0.008454708      50.00  0 10
-2BUS5B BUS4B          0.02336  0.951025057 0.012379469      50.00  0 10
-3BUS5C BUS4C
C
C Line impedance using lumped sequence parameters
C
$VINTAGE, 0
C 345678901234567890123456789012345678901234567890123456789012345678901234567890123456789012345678901
51BUS2A BUS9A          38.848      325.1
52BUS2B BUS9B          2.336      95.10
53BUS2C BUS9C
51BUS9A BUS11A         38.848      325.1
52BUS9B BUS11B         2.336      95.10
53BUS9C BUS11C
51BUS6A BUS10A         38.848      325.1
52BUS6B BUS10B         2.336      95.10
53BUS6C BUS10C
51BUS10ABUS11A        38.848      325.1
52BUS10BBUS11B        2.336      95.10
53BUS10CBUS11C
C
C Load impedance
C
$VINTAGE, 1
C 345678901234567890123456789012345678901234567890123456789012345678901234567890123456789012345678901
C | BUS1| BUS2| BUS3| BUS4|   R in ohm |   L in mH   |   C in uF   |
  BUS2A
  BUS2B      BUS2A
  BUS2C      BUS2A
  BUS6A          100.4122416
  BUS6A          396.8640975
  BUS6B          100.4122416
  BUS6B          396.8640975
  BUS6C          100.4122416
  BUS6C          396.8640975
  BUS11A         267.20026670
  BUS11B      BUS11A
  BUS11C      BUS11A
C
C Fault resistance
C
C 345678901234567890123456789012345678901234567890123456789012345678901234567890123456789012345678901
C | BUS1| BUS2| BUS3| BUS4|   R in ohm |   L in mH   |   C in uF   |
  BUS8A          25.0
C
$VINTAGE, 0
C
BLANK CARD ENDING ALL NETWORK CARDS
C
C SWITCH CARDS
C
C 345678901234567890123456789012345678901234567890123456789012345678901234567890123456789012345678901
C | BUS1| BUS2| T close | T open |
  0BUS4A BUS8A    0.48575  0.640
C
BLANK CARD ENDING ALL SWITCH CARDS
C
C SOURCE CARDS
C
C 345678901234567890123456789012345678901234567890123456789012345678901234567890123456789012345678901
C | NAME| |AMPLITUDE| FREQ | PHASE |
14BUS1A 3.265986E5 50. -90.
14BUS1B 3.265986E5 50. 150.
14BUS1C 3.265986E5 50. 30.
14BUS7A 3.265986E5 50. -101.74
14BUS7B 3.265986E5 50. 138.26
14BUS7C 3.265986E5 50. 18.26
14BUS12A 3.265986E5 50. -97.442

```

```

14BUS12B 3.265986E5      50.  142.558
14BUS12C 3.265986E5      50.   22.558
C
BLANK CARD ENDING ALL SOURCE CARDS
BLANK
C CALCOMP PLOT
C 1830.1 0.0 1.0          BUS2A      BUS2B
C 1930.1 0.0 1.0          BUS2A BUS3A BUS2B BUS3B
BLANK card ending all plot cards
BEGIN NEW DATA CASE
BLANK
    
```

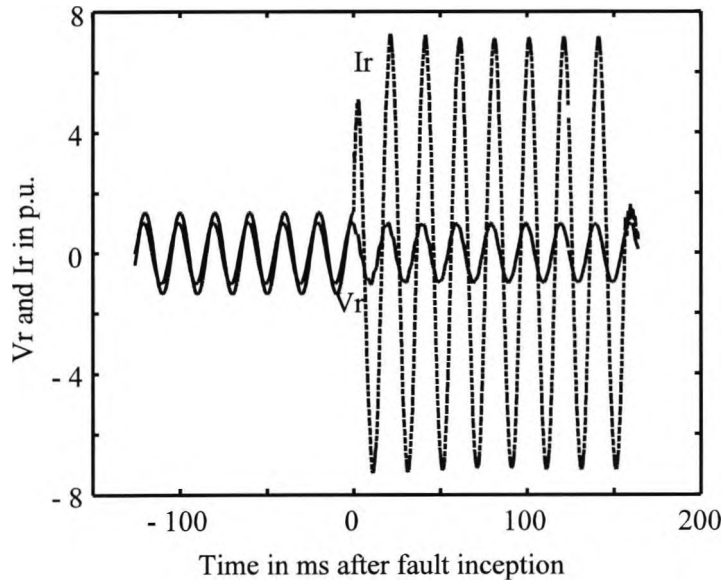


Fig. B.3 Voltage and current waveform at relaying point for L-E fault at 60% of line length with $R_f = 25 \Omega$

B.5 COMPUTATION OF THE IDEAL OPERATING REGIONS

Based on the result obtained from B.4, the converged impedance seen by the distance relay using the adaptive window length algorithm is then computed for each of the transient analysis carried out along the line with different values of fault resistance. This will then form the ideal operating region of the distance relay covering 80% of line length to a maximum fault resistance of 200Ω for that particular load flow condition. The ideal operating region of 4 cases, Case 1, 3, 7, and 9, where the P and Q flow are of the extreme points of the range are shown in Fig. B.4. Similar computations are carried out for the other load flow conditions.

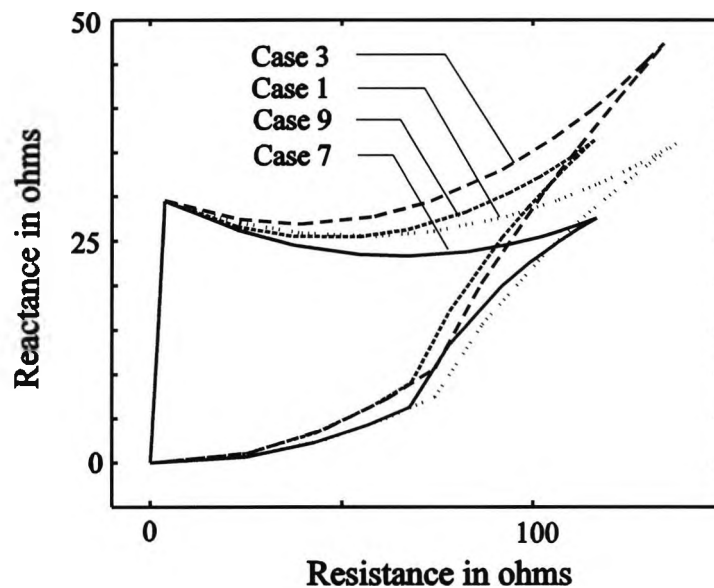


Fig. B.4 Relay ideal boundaries of case 1, 3, 7 & 9

B.6 INPUTS AND TARGETS OF ANN

Each ANN is designed with three layers, namely an input layer, an output layer, and a hidden layer. The hypertangent sigmoid transfer function is used between the input and hidden layers and the pure linear transfer function is used between the hidden and output layers. To incorporate the effect of active and reactive power flow in the line, the changes of active and reactive power flow (ΔP , ΔQ) in the line from fixed reference values is used in training the ANN so as to

improve the dynamic performance of the ANN. For training the ANN for boundary A, ΔP , ΔQ , (in MW and MVar) and the resistance R_A (in ohms) at different points along boundary A are the inputs and the corresponding reactance X_A (in ohms) is obtained as the output. For boundary B, ΔP , ΔQ , and the reactance X_B at different points along the boundary are the inputs and the corresponding resistance R_B is obtained as the output. Boundary C is trained in a similar manner to boundary A. No training is required for boundary D as it remains unchanged for all configurations. The reference values of active and reactive power chosen for the study are 950MW and 250 MVar respectively. In order to assist the ANN to converge and achieve a better accuracy, the inputs and targets should map into both the linear and non-linear region of the transfer function between ANN layers. For example, for the ANN of boundary A, the inputs ΔP , ΔQ and R_A are normalized by a constant of 150, 75 and 170 respectively. The targets X_A are normalized by a constant of 60. There are altogether a total of 99 sets of training points for boundary A. The input and target of the ANN for boundary A is shown in Table B.2. Input and targets for the ANN of other boundaries are produced in a similar way.

Table B.2 Inputs and Outputs to the ANN on Boundary A

Inputs	ΔP	0.6733	0.6733	0.6733	0.6733	0.6733	0.6733	0.6733
	ΔQ	-0.6507	-0.6507	-0.6507	-0.6507	-0.6507	-0.6507	-0.6507
	R_A	0.0215	0.1330	0.2206	0.3211	0.3964	0.4872	0.5509
Targets	X_A	0.4910	0.4374	0.4091	0.3915	0.3886	0.3967	0.4100
Inputs	ΔP	0.6733	0.6733	0.6733	0.6733	0.6667	0.6667	0.6667
	ΔQ	-0.6507	-0.6507	-0.6507	-0.6507	0	0	0
	R_A	0.5980	0.6342	0.6629	0.6861	0.0215	0.1326	0.2203
Targets	X_A	0.4239	0.4370	0.4489	0.4595	0.4913	0.4412	0.4180
Inputs	ΔP	0.6667	0.6667	0.6667	0.6667	0.6667	0.6667	0.6667
	ΔQ	0	0	0	0	0	0	0
	R_A	0.3213	0.3972	0.4885	0.5526	0.5999	0.5999	0.6649
Targets	X_A	0.4091	0.4147	0.4357	0.4596	0.4824	0.4824	0.5207

Table B.2 Inputs and Outputs to the ANN on Boundary A (contd.)

Inputs	ΔP	0.6667	0.6667	0.6667	0.6667	0.6667	0.6667	0.6667
	ΔQ	0	0.6667	0.6667	0.6667	0.6667	0.6667	0.6667
	R_A	0.6882	0.0215	0.1320	0.2194	0.3201	0.3957	0.4864
Targets	X_A	0.5365	0.4912	0.4439	0.4254	0.4246	0.4383	0.4712
Inputs	ΔP	0.6667	0.6667	0.6667	0.6667	0.6667	0.0047	0.0047
	ΔQ	0.6667	0.6667	0.6667	0.6667	0.6667	-0.6560	-0.6560
	R_A	0.5497	0.5963	0.6319	0.6600	0.6827	0.0215	0.1351
Targets	X_A	0.5050	0.5327	0.5627	0.5860	0.6064	0.4919	0.4439
Inputs	ΔP	0.0047	0.0047	0.0047	0.0047	0.0047	0.0047	0.0047
	ΔQ	-0.6560	-0.6560	-0.6560	-0.6560	-0.6560	-0.6560	-0.6560
	R_A	0.2262	0.3329	0.4146	0.5146	0.5860	0.6394	0.6808
Targets	X_A	0.4199	0.4077	0.4100	0.4266	0.4478	0.4688	0.4882
Inputs	ΔP	0.0047	0.0047	0.0033	0.0033	0.0033	0.0033	0.0033
	ΔQ	-0.6560	-0.6560	0.0120	0.0120	0.0120	0.0120	0.0120
	R_A	0.7139	0.7408	0.0216	0.1347	0.2258	0.3328	0.4148
Targets	X_A	0.5056	0.5210	0.4920	0.4474	0.4286	0.4257	0.4376
Inputs	ΔP	0.0033	0.0033	0.0033	0.0033	0.0033	0.0033	0.0013
	ΔQ	0.0120	0.0120	0.0120	0.0120	0.0120	0.0120	0.6720
	R_A	0.5151	0.5866	0.6399	0.6812	0.7140	0.7407	0.0215
Targets	X_A	0.4688	0.5025	0.5339	0.5621	0.5868	0.6086	0.4925
Inputs	ΔP	0.0013	0.0013	0.0013	0.0013	0.0013	0.0013	0.0013
	ΔQ	0.6720	0.6720	0.6720	0.6720	0.6720	0.6720	0.6720
	R_A	0.1339	0.2247	0.3313	0.4128	0.5122	0.5825	0.6348
Targets	X_A	0.4509	0.4371	0.4431	0.4640	0.5088	0.5539	0.5948
Inputs	ΔP	0.0013	0.0013	0.0013	-0.6667	-0.6667	-0.6667	-0.6667
	ΔQ	0.6720	0.6720	0.6720	-0.6640	-0.6640	-0.6640	-0.6640
	R_A	0.6750	0.7069	0.7327	0.0217	0.1373	0.2323	0.3462
Targets	X_A	0.6307	0.6620	0.6892	0.4927	0.4508	0.4313	0.4255

Table B.2 Inputs and Outputs to the ANN on Boundary A (contd.)

Inputs	ΔP	-0.6667	-0.6667	-0.6667	-0.6667	-0.6667	-0.6667	-0.6667
	ΔQ	-0.6640	-0.6640	-0.6640	-0.6640	-0.6640	-0.6640	-0.6640
	R_A	0.4352	0.5466	0.6276	0.6891	0.7372	0.7759	0.8076
Targets	X_A	0.4342	0.4616	0.4933	0.5239	0.5520	0.5772	0.5996
Inputs	ΔP	-0.6613	-0.6613	-0.6613	-0.6613	-0.6613	-0.6613	-0.6613
	ΔQ	0.0040	0.0040	0.0040	0.0040	0.0040	0.0040	0.0040
	R_A	0.0216	0.1367	0.2315	0.3451	0.4339	0.5446	0.6247
Targets	X_A	0.4933	0.4547	0.4406	0.4447	0.4639	0.5076	0.5534
Inputs	ΔP	-0.6613	-0.6613	-0.6613	-0.6613	-0.6627	-0.6627	-0.6627
	ΔQ	0.0040	0.0040	0.0040	0.0040	0.6707	0.6707	0.6707
	R_A	0.6852	0.7324	0.7702	0.8010	0.0216	0.1360	0.2304
Targets	X_A	0.5960	0.6343	0.6682	0.6980	0.4932	0.4575	0.4486
Inputs	ΔP	-0.6627	-0.6627	-0.6627	-0.6627	-0.6627	-0.6627	-0.6627
	ΔQ	0.6707	0.6707	0.6707	0.6707	0.6707	0.6707	0.6707
	R_A	0.3435	0.4315	0.5408	0.6194	0.6783	0.7240	0.7604
Targets	X_A	0.4622	0.4913	0.5506	0.6097	0.6635	0.7110	0.7527
Inputs	ΔP	-0.6627						
	ΔQ	0.6707						
	R_A	0.7900						
Targets	X_A	0.7892						

B.7 TRAINING THE ARTIFICIAL NEURAL NETWORK

The number of neurons in the hidden layer affects the accuracy of the nonlinear boundary and operating speed. Too few neurons can lead to underfitting. Too many can contribute to overfitting, where all training points fit well, but the fitted curve makes wild oscillations between these points. It was found that 15 neurons in the hidden layer were required for all the boundaries. The training time varies according to the starting point and the acceptable error. As the starting

point is chosen at random, in some cases the training may not converge. In this case it was necessary to start again from a different point or try with a different number of neurons in the hidden layer. In this study, three ANNs are used for the boundaries A, B, and C. The tolerable sum square error chosen is $2E-8$, $1.5E-8$, and $2E-8$, and the training converged in 20, 34 and 15 epochs for boundaries A, B, and C respectively. The neural network toolbox of the MATLAB software [39] is used for the training and testing of the ANNs mentioned in this thesis.

B.8 TESTING OF ANN

Four testing sets (A, B, C, and D) are generated within the same range of P and Q flow in the protected line. Their distribution are shown in Fig. B.2. When the ANN is successfully trained, it can predict the practical trip region simply based on the current P and Q flow in the protected line. A typical prediction by the ANN compared with the corresponding ideal operating region calculated by simulation based on test case A is shown in Fig. B.5.

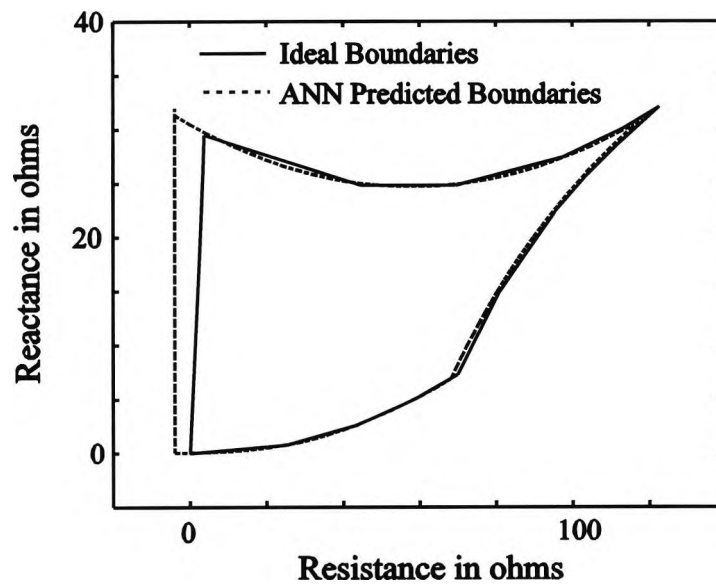


Fig. B.5 ANN predicted relay boundary for test case A

In order to test the ability of the ANN in identifying in-zone and out-zone faults, L-E faults with different fault resistance are simulated to generate a testing pattern as shown in Fig. B.6.

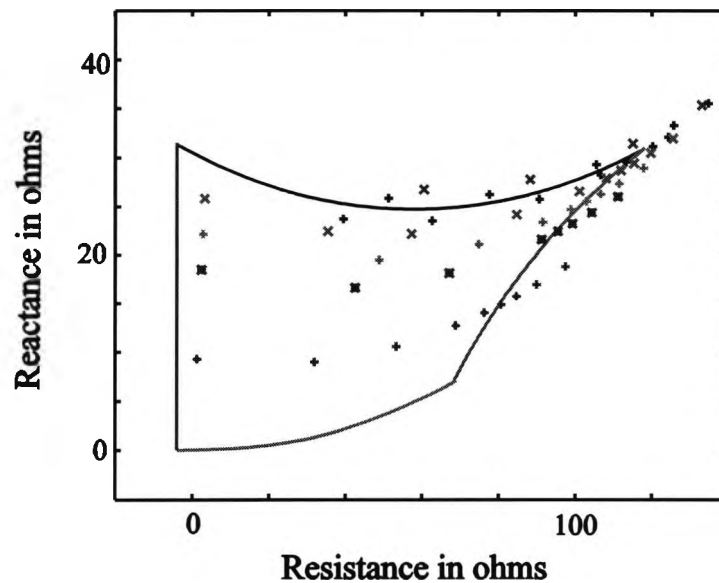


Fig. B.6 Testing patterns

The impedance measurement of the relay together with the pre-fault P and Q is fed into the ANN. The measured values compared with the ANN prediction can deduce a conclusion on whether the fault is in-zone or out-zone. A corresponding tripping decision can then be made based on this. Part of the ANN testing results along boundary A compared with actual impedance calculated based on simulations for the same case is shown in Table B.3. The output of neural network for test case A is shown in Table B.4. Each row in the table corresponds to faults with different fault resistance at different locations of the line from the relaying point. The top row shows the corresponding fault resistance for that column in ohms. The value shown is the impedance from the nearest relay boundary. Positive means that it is within the tripping region and negative means that the relay will restraint.

Table B.3 Part of ANN Testing Results Compared with Actual Impedance Values

- Boundary A of Case A (Values shown are normalized)

Inputs	ΔP	0.3367	0.3367	0.3367	0.3367	0.3367	0.3367
	ΔQ	-0.3333	-0.3333	-0.3333	-0.3333	-0.3333	-0.3333
	R_A	0.0216	0.2623	0.4081	0.5737	0.6644	0.7213
ANN Output	X_{ANN}	0.4966	0.4170	0.4158	0.4562	0.4980	0.5316
Actual Value	X_{ACT}	0.4916	0.4138	0.4139	0.4573	0.5008	0.5355
Error converted to ohmic values	$X_{ANN} - X_{ACT}$	0.3Ω	0.19Ω	0.11Ω	-0.06Ω	-0.17Ω	-0.23Ω

Table B.4 Output of Neural Network for Test Case A

$R_A(\Omega)$	0	25	50	100	150	180	220	250	300
90%		-2.0	-1.5	-1.1		-0.3		-0.6	
85%		-1.1	-0.8	-0.7		-0.2		-0.6	
75%		1.6	1.3	0.8	0.5	0.4	-1.8	-2.7	
70%	4.0	3.1	2.5	1.8	1.3	0.7	-2.0	-3.2	-4.3
60%	6.9		5.4	4.1	3.3	1.3	-2.3	-4.2	-6.0
50%	6.4		8.5	6.7		1.9	-2.6	-4.9	-7.5
25%	5.3		7.6	6.5	5.6	2.3	-3.1	-6.3	-10.2

APPENDIX C

LOAD FLOW RESULTS

C.1 LOAD FLOW FOR CASE STUDIES IN CHAPTER 6

C.1.1 Case 1

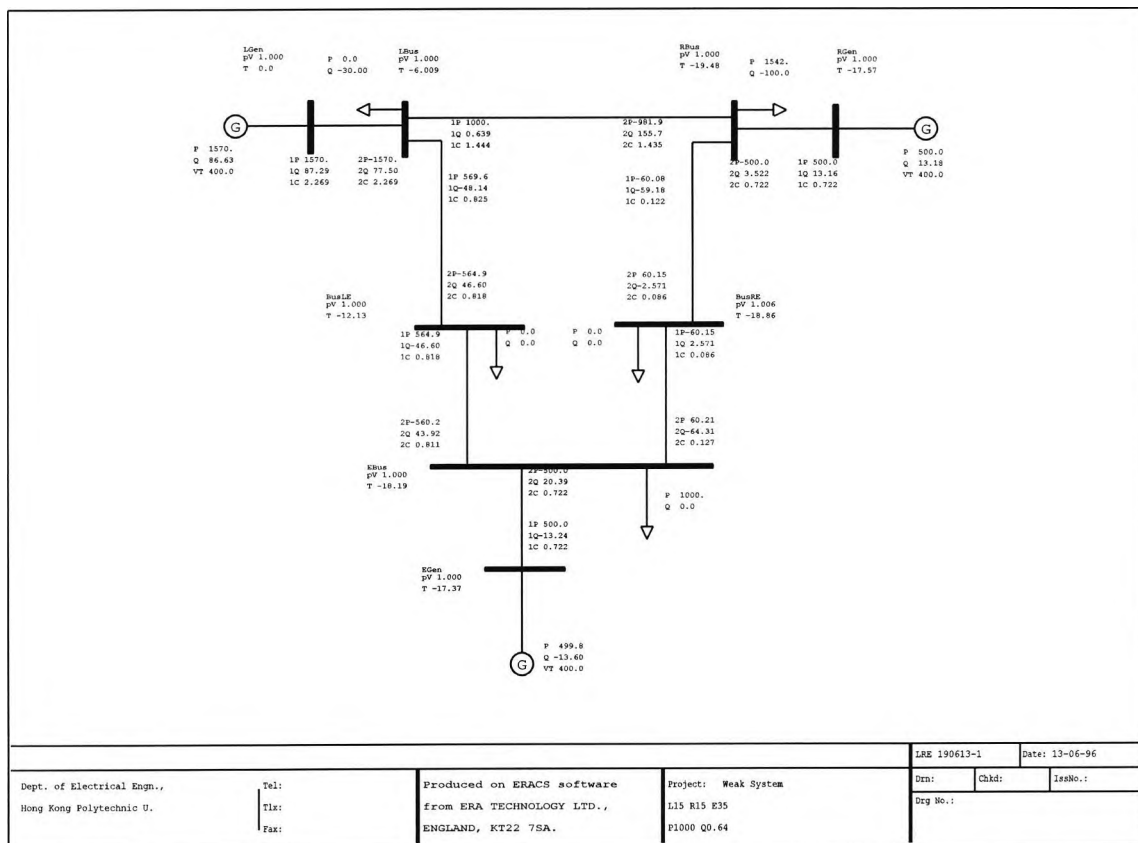


Fig. C.1 Load flow for case 1 in Chapter 6

C.1.2 Case 2

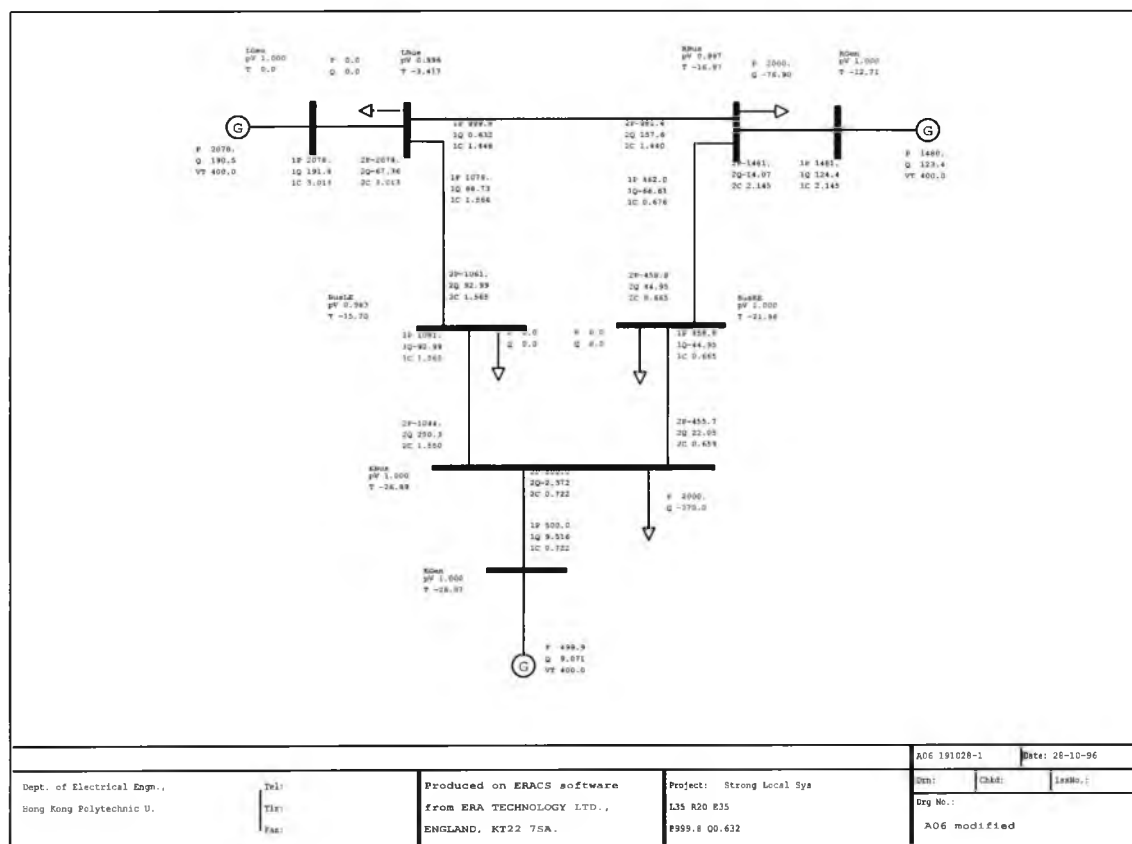


Fig. C.2 Load flow for case 2 in Chapter 6

C.1.4 Case 4

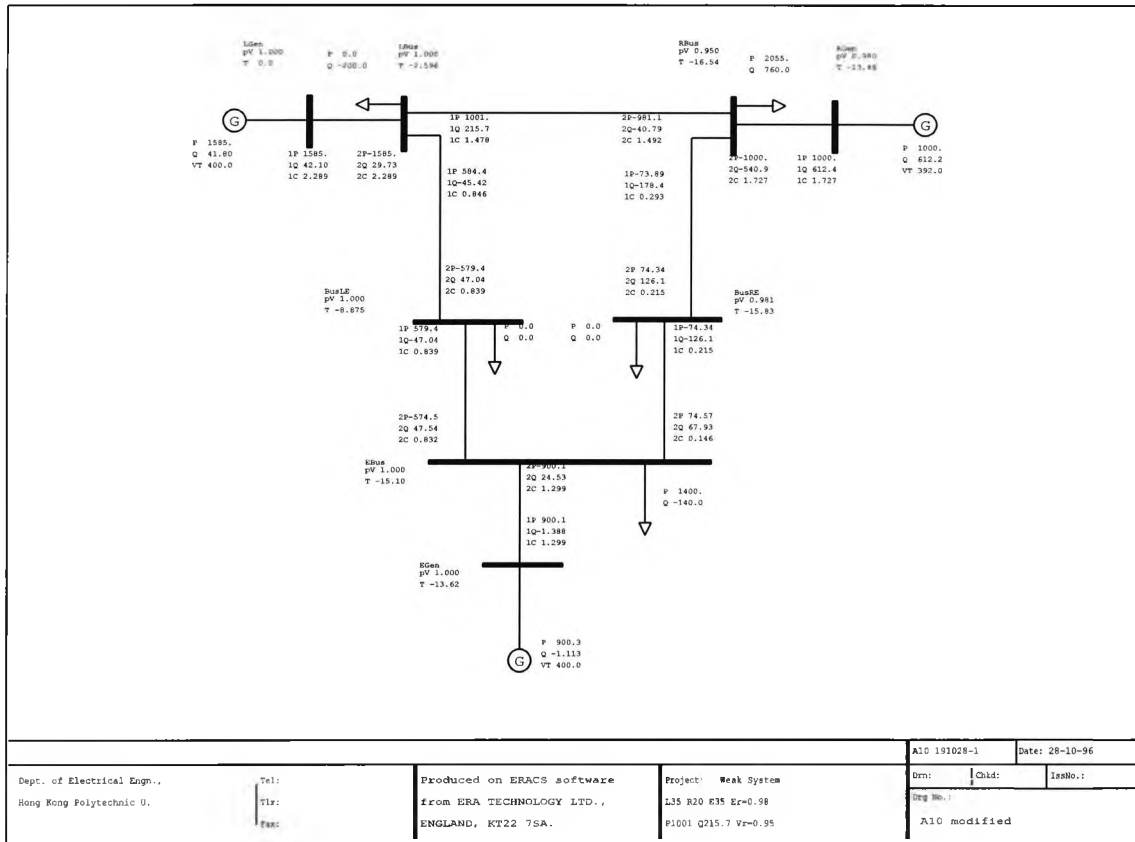


Fig. C.4 Load flow for case 4 in Chapter 6

C.1.6 Case 6

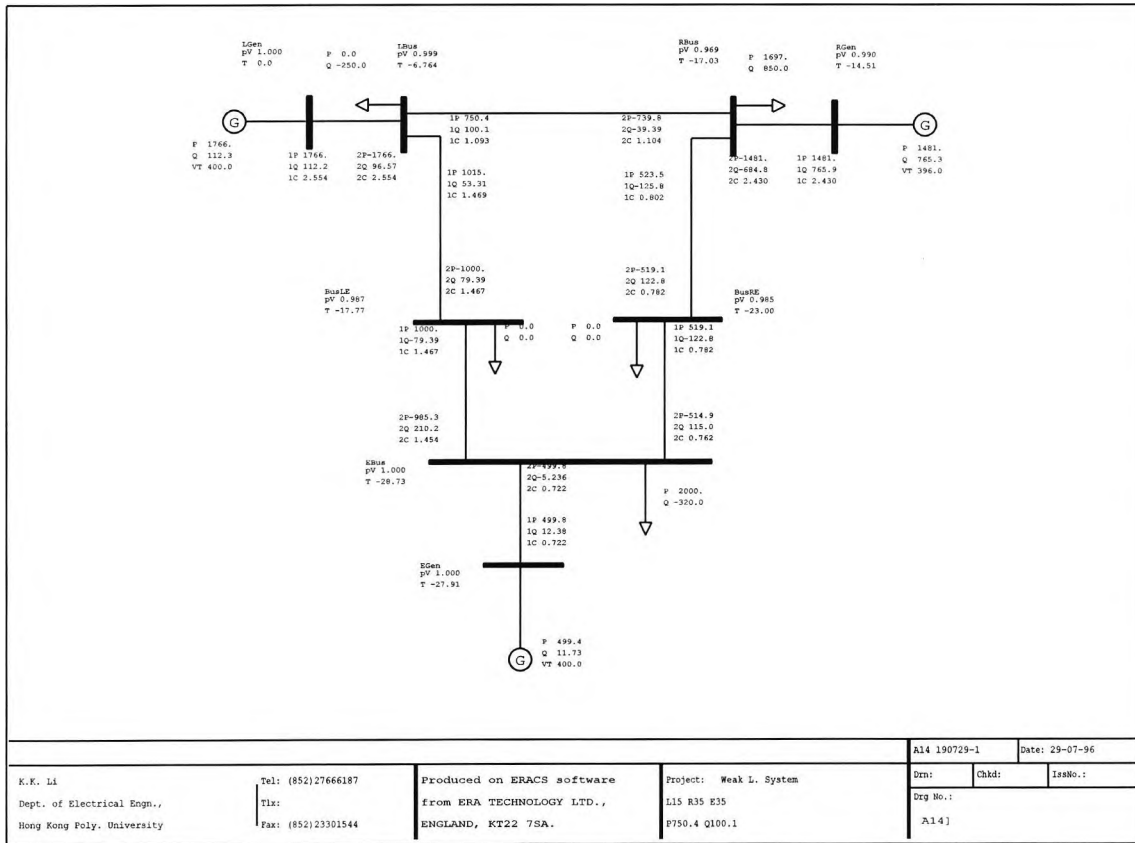


Fig. C.6 Load flow for case 6 in Chapter 6

C.1.7 Case 7

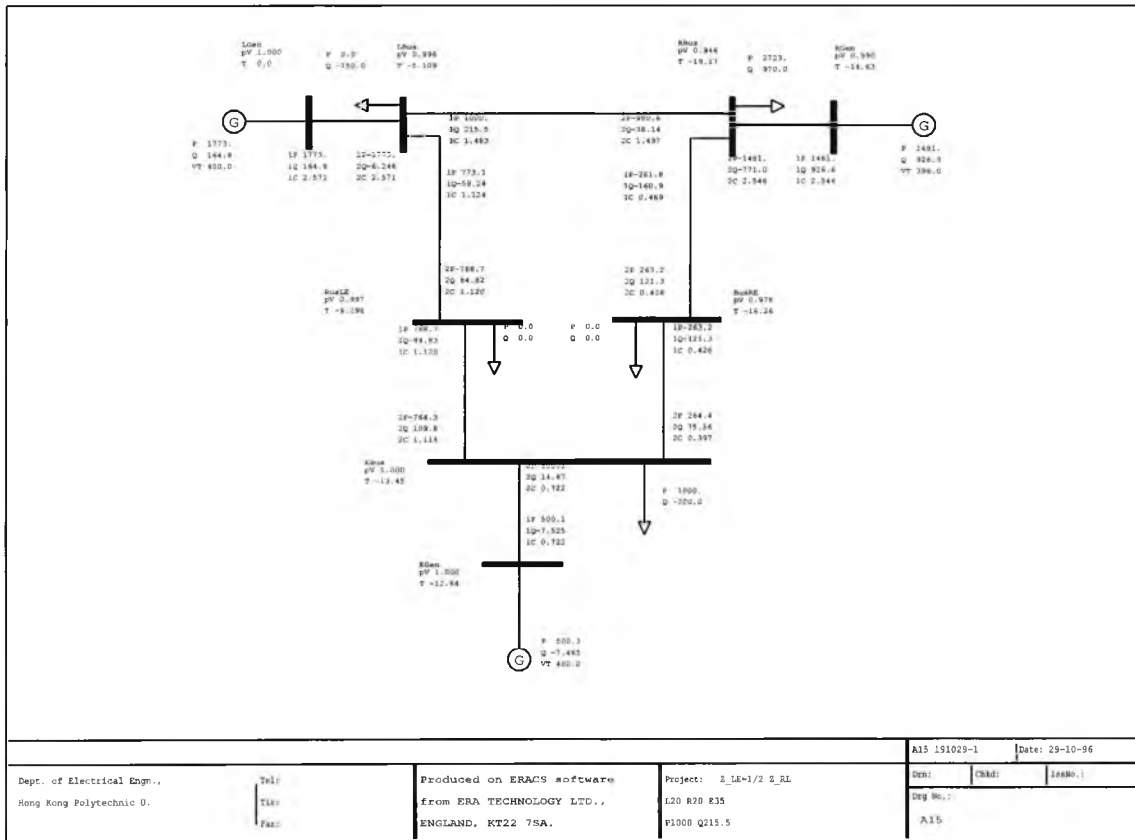


Fig. C.7 Load flow for case 7 in Chapter 6

C.1.8 Case 8

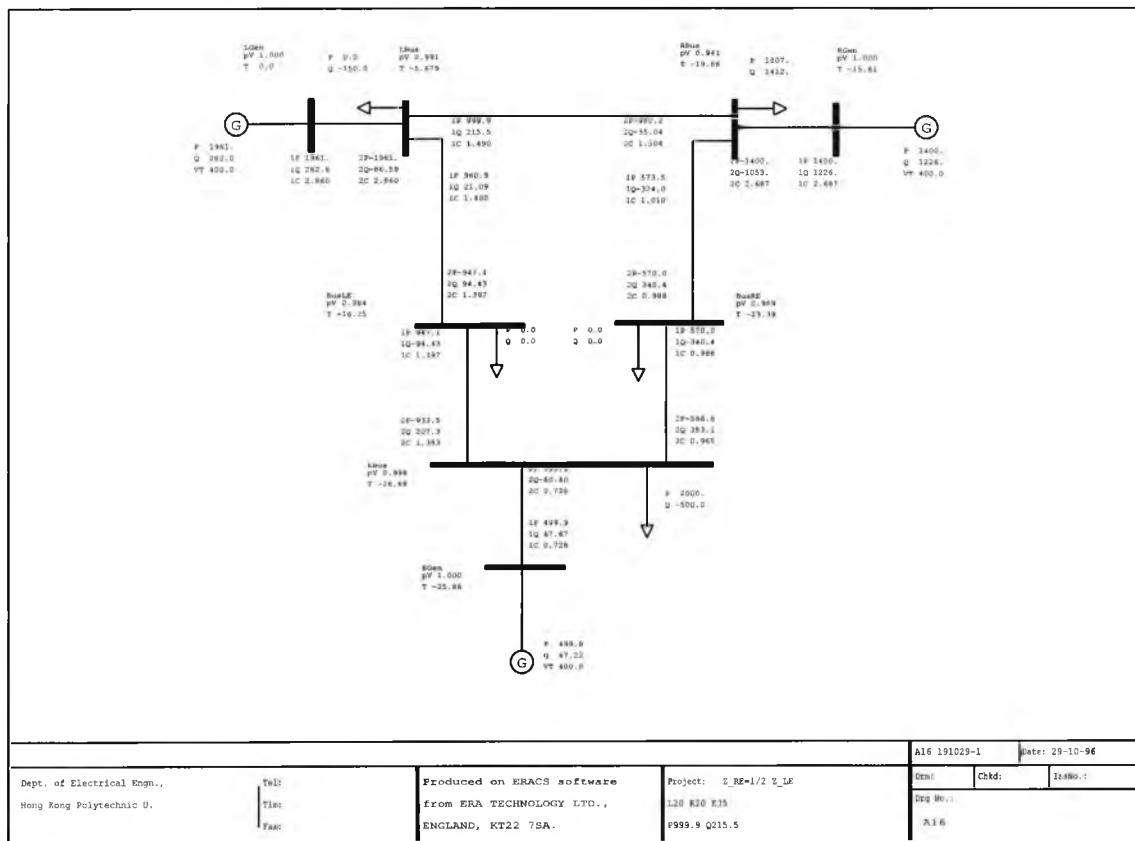


Fig. C.8 Load flow for case 8 in Chapter 6

C.1.9 Case 9

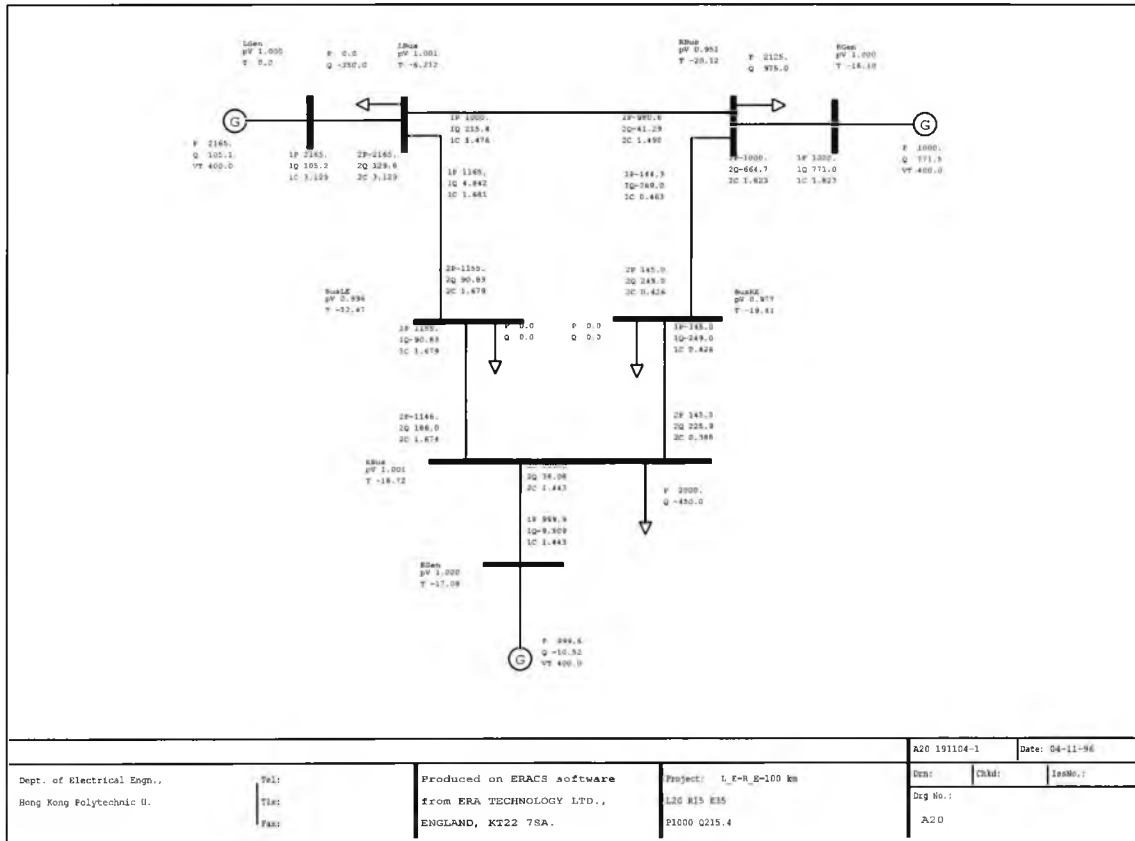


Fig. C.9 Load flow for case 9 in Chapter 6

C.1.10 Case 10

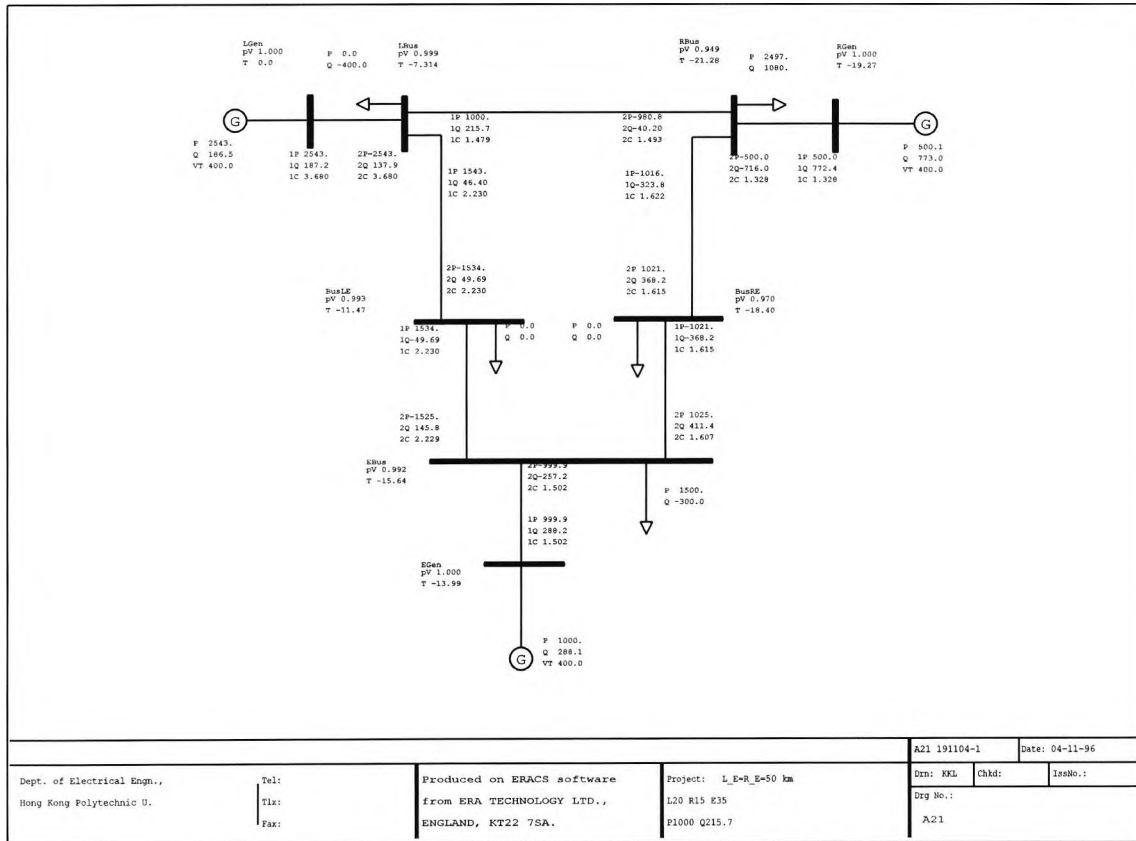


Fig. C.10 Load flow for case 10 in Chapter 6

C.2 LOAD FLOW FOR CASE STUDIES IN CHAPTER 7

C.2.1 Case 1

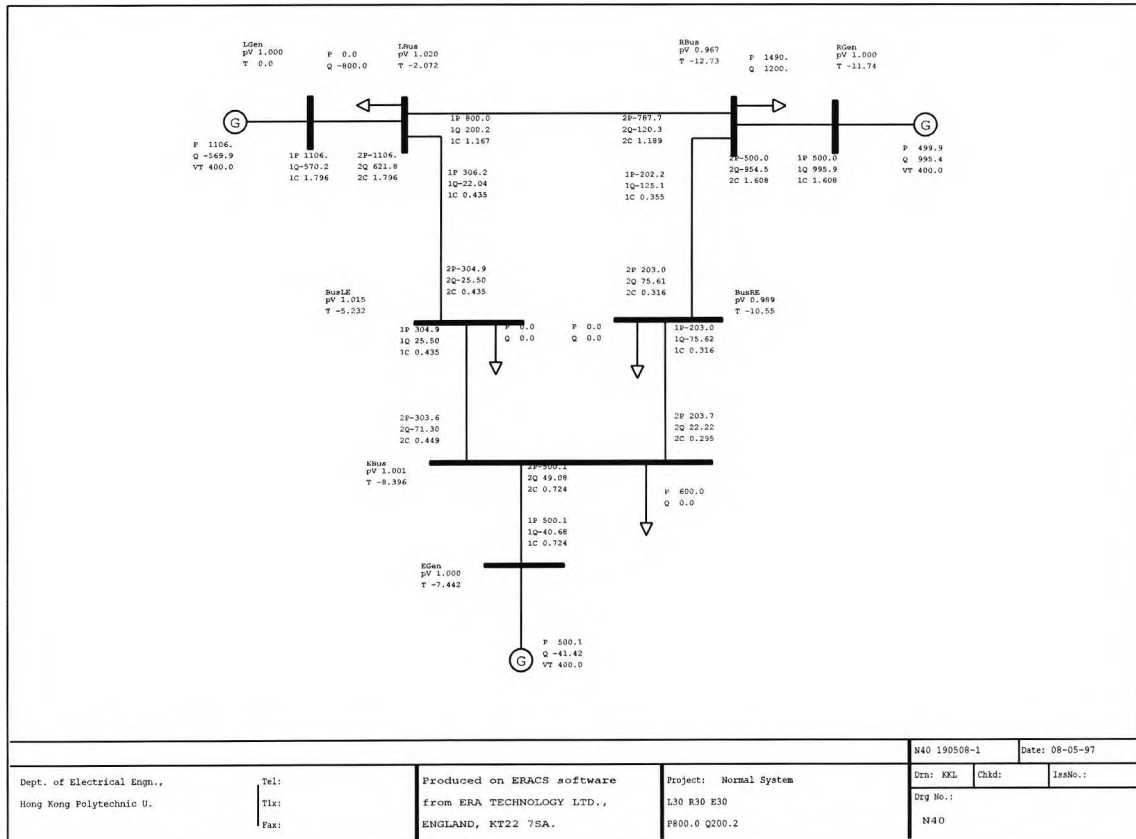


Fig. C.11 Load flow for case 1 in Chapter 7

C.2.2 Case 2

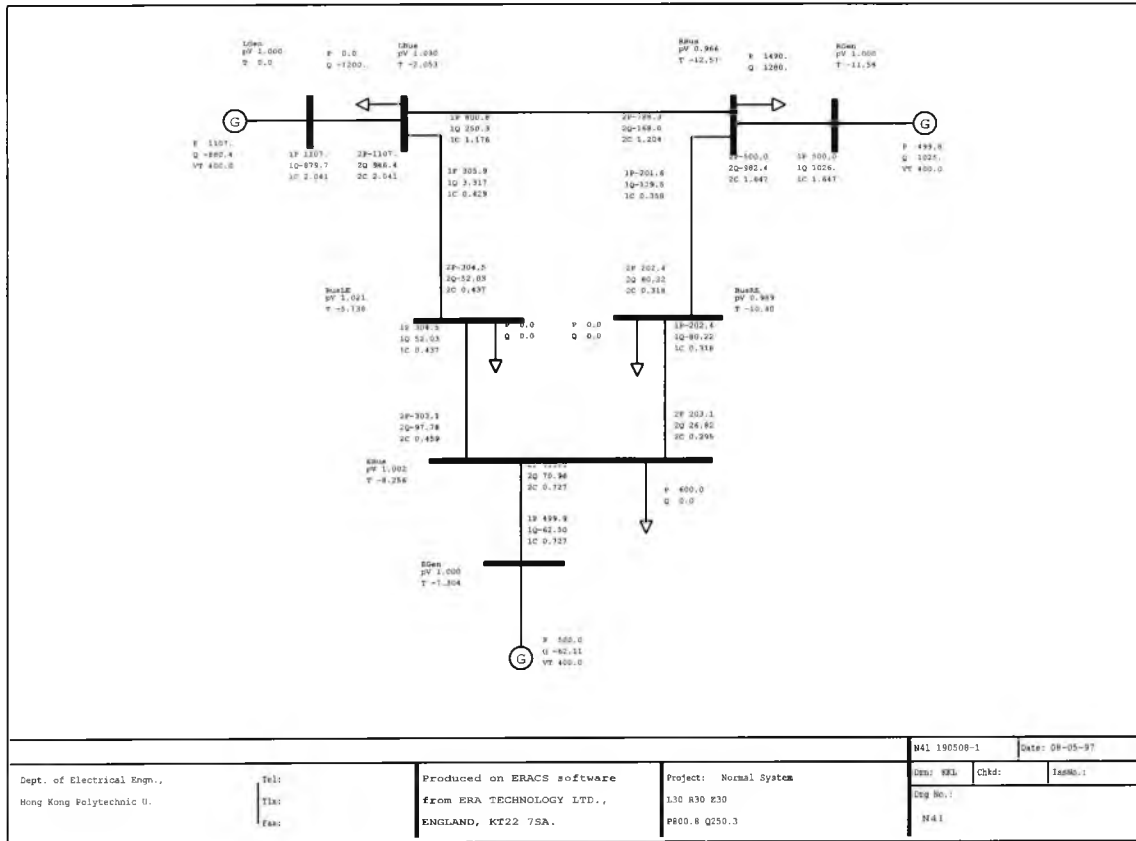


Fig. C.12 Load flow for case 2 in Chapter 7

C.2.3 Case 3

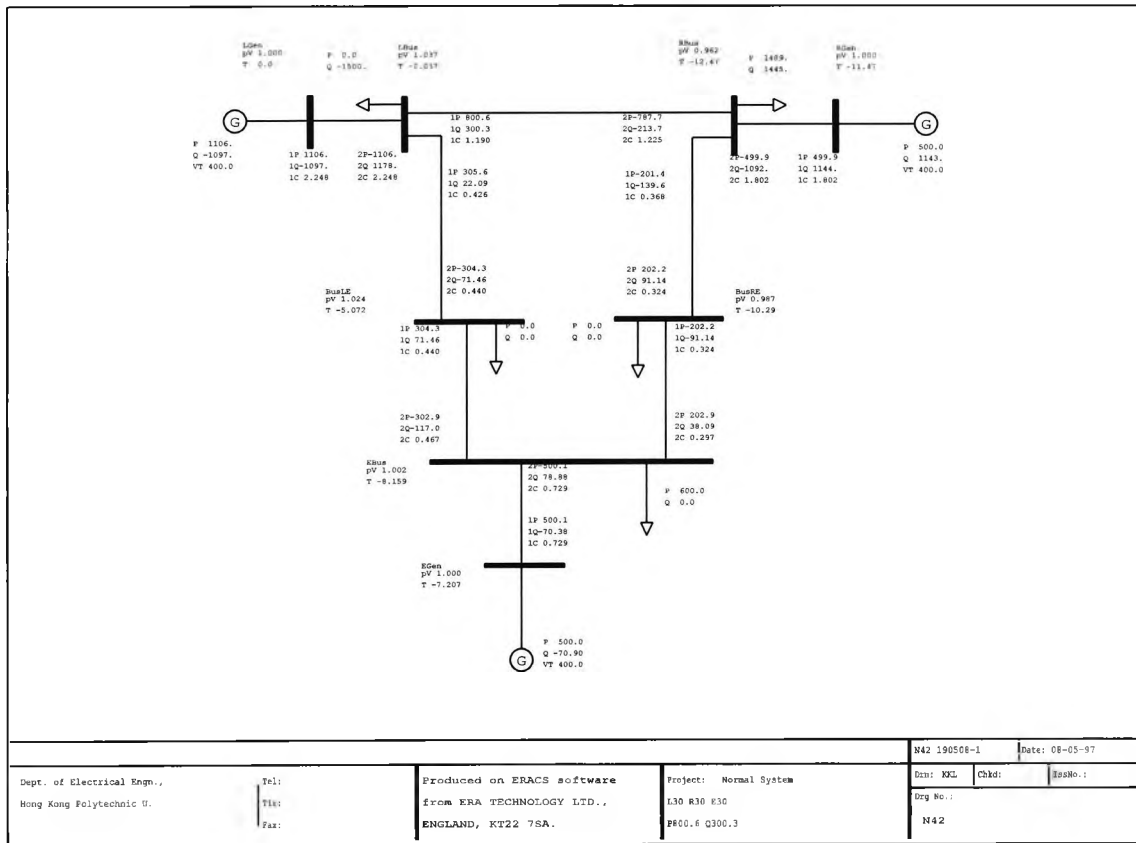


Fig. C.13 Load flow for case 3 in Chapter 7

C.2.5 Case 5

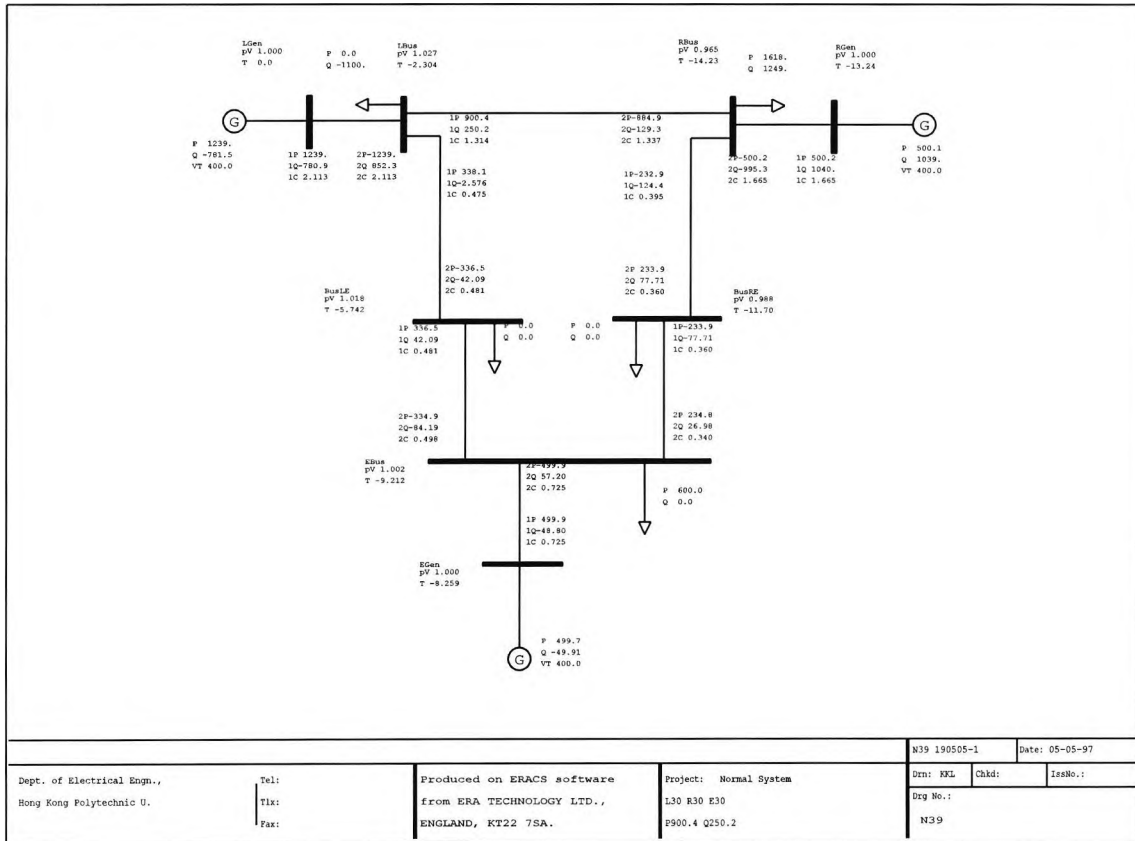


Fig. C.15 Load flow for case 5 in Chapter 7

C.2.6 Case 6

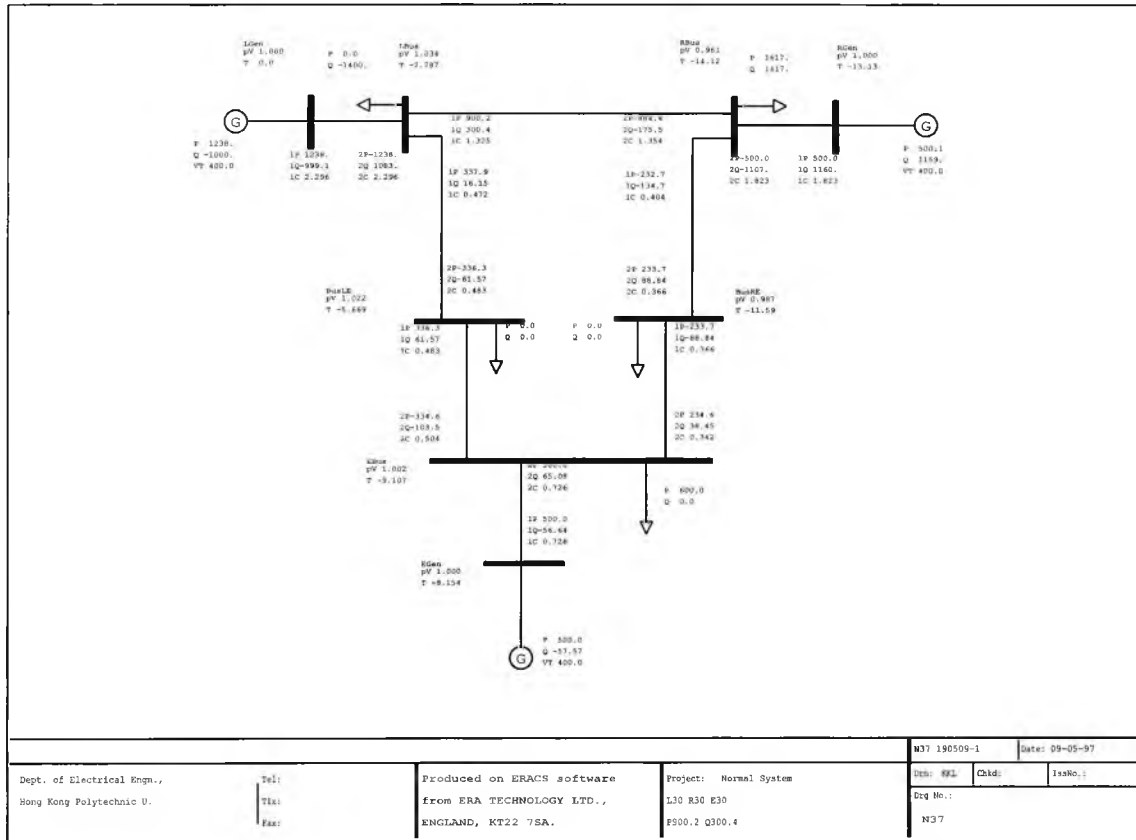


Fig. C.16 Load flow for case 6 in Chapter 7

C.2.7 Case 7

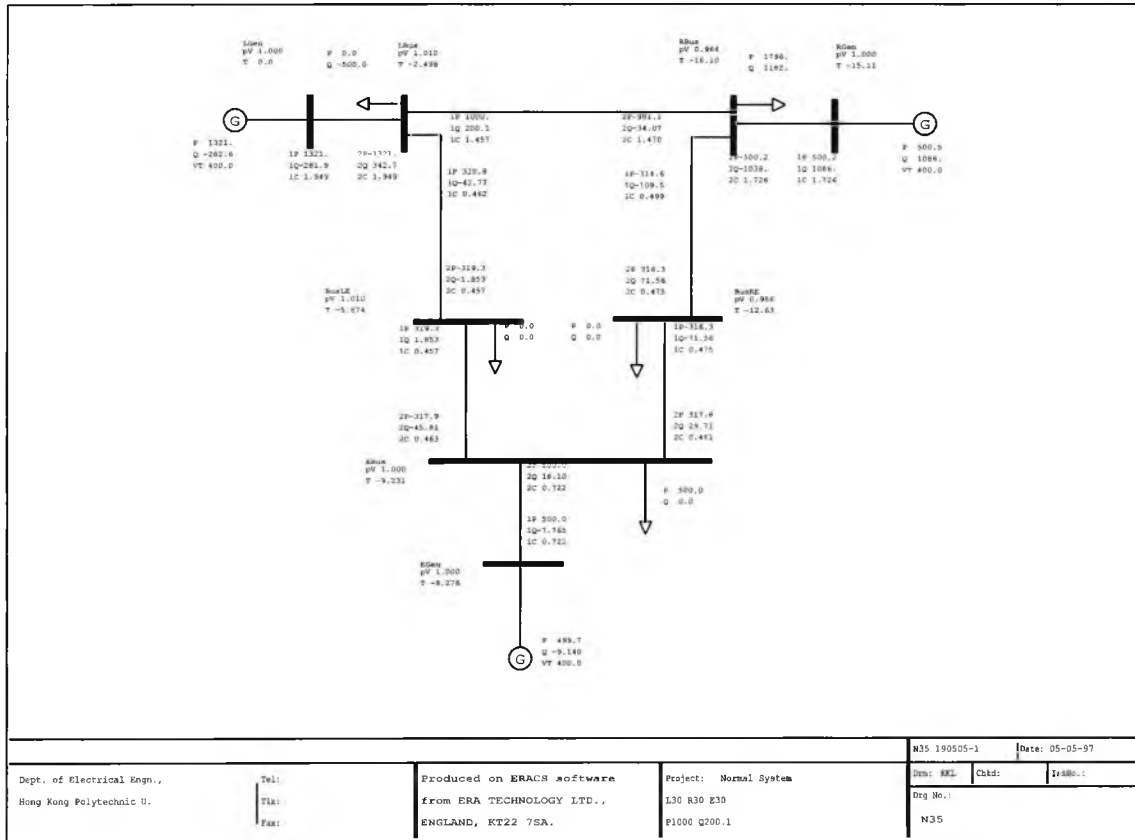


Fig. C.17 Load flow for case 7 in Chapter 7

C.2.8 Case 8

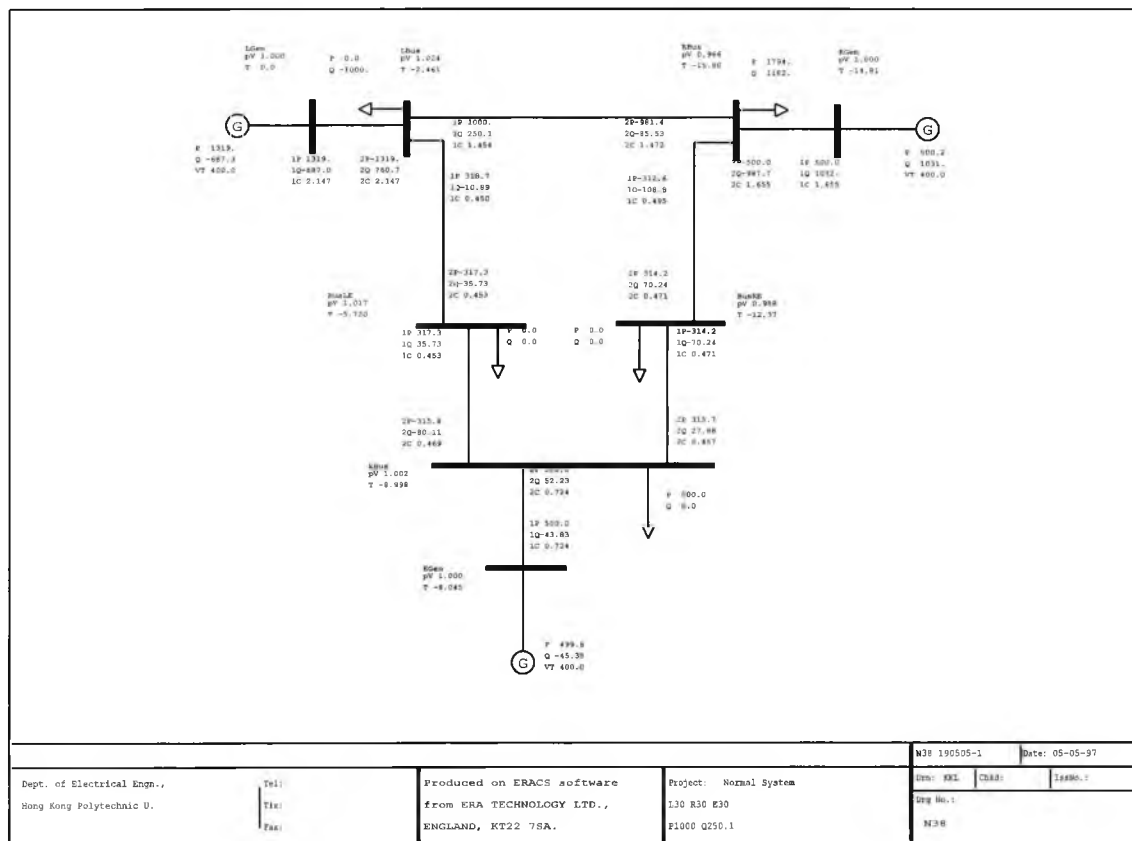


Fig. C.18 Load flow for case 8 in Chapter 7

C.2.9 Case 9

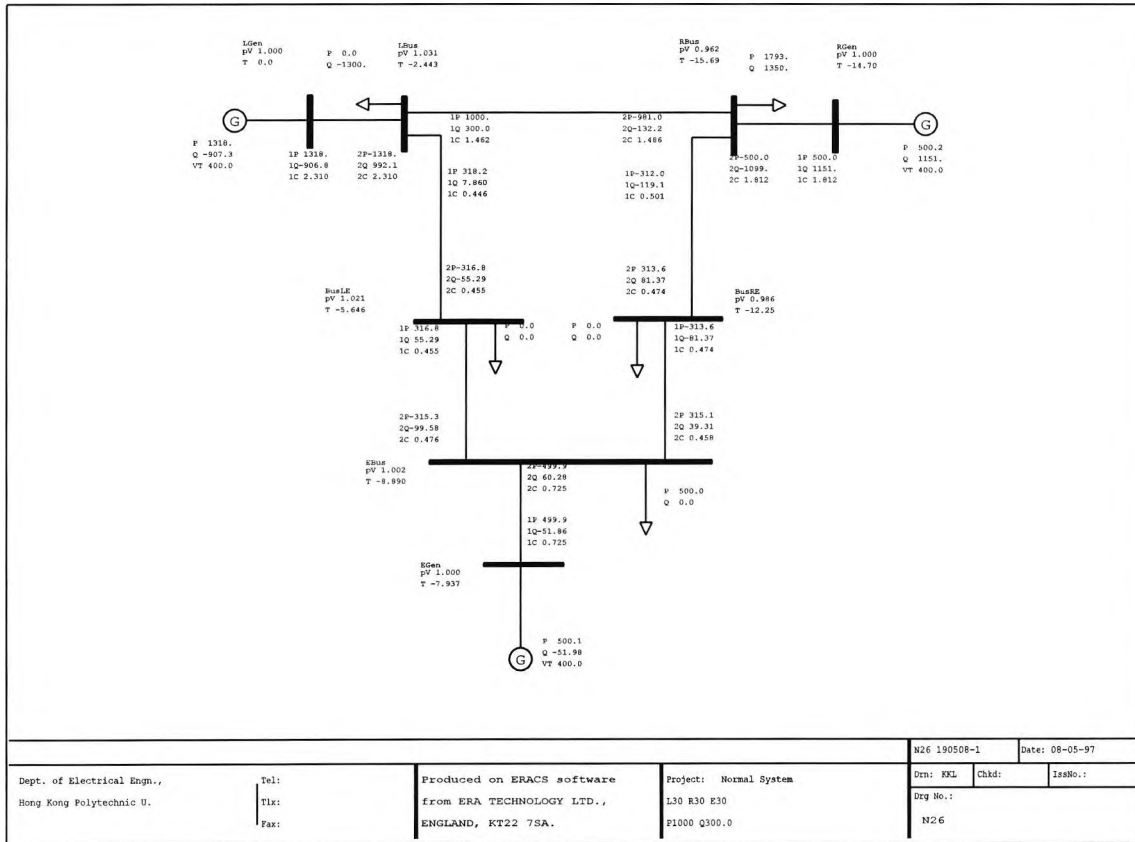


Fig. C.19 Load flow for case 9 in Chapter 7

C.2.10 Test Case A

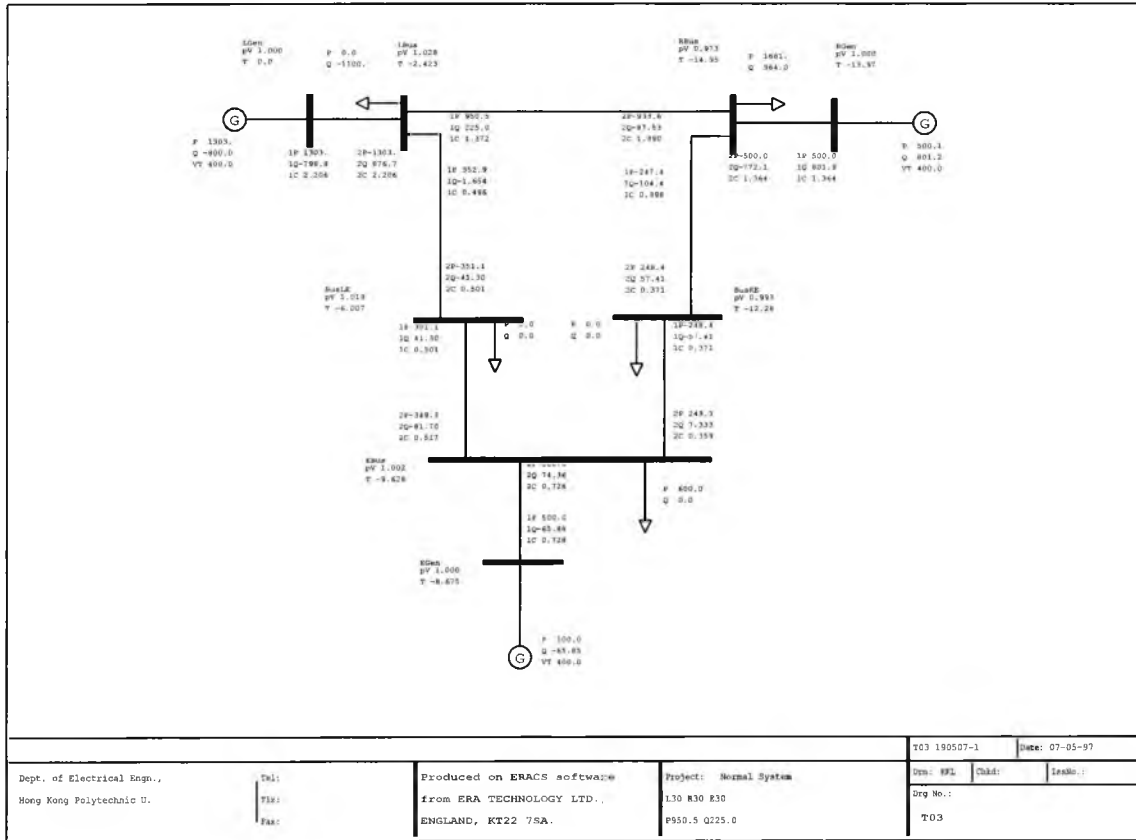


Fig. C.20 Load flow for test case A in Chapter 7

C.2.11 Test Case B

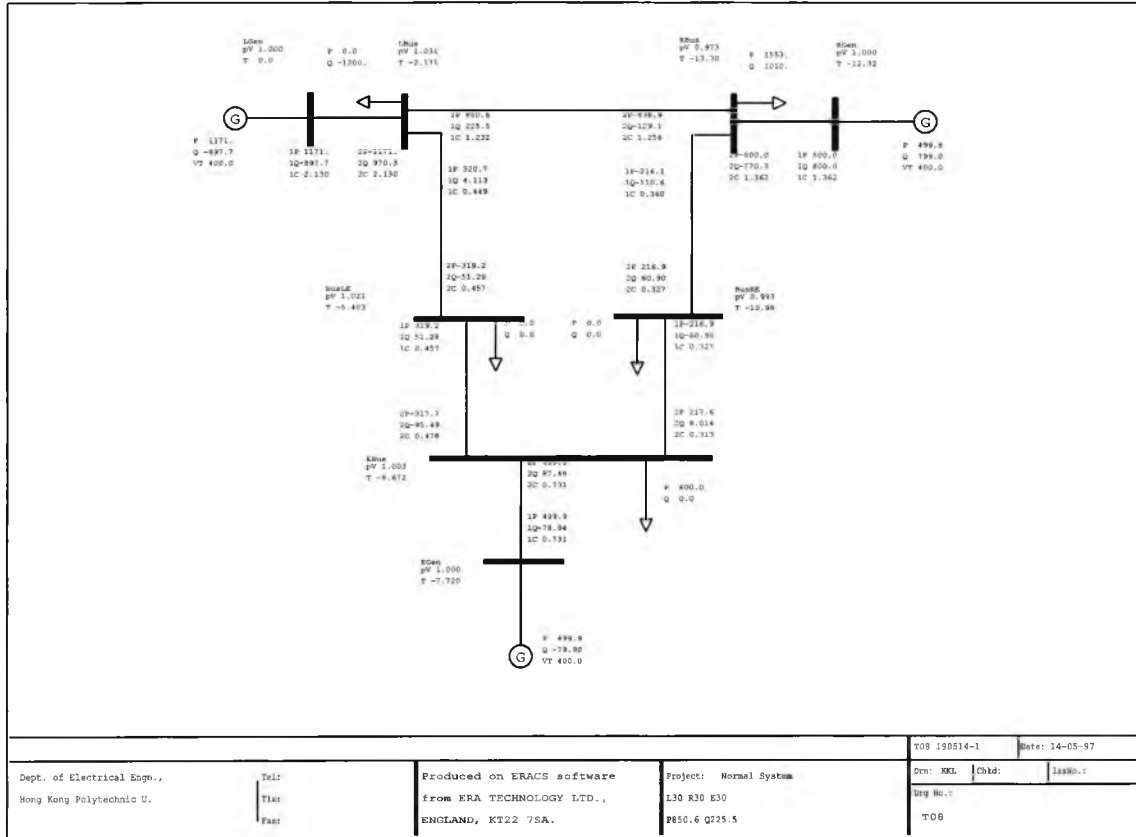


Fig. C.21 Load flow for test case B in Chapter 7

C.2.12 Test Case C

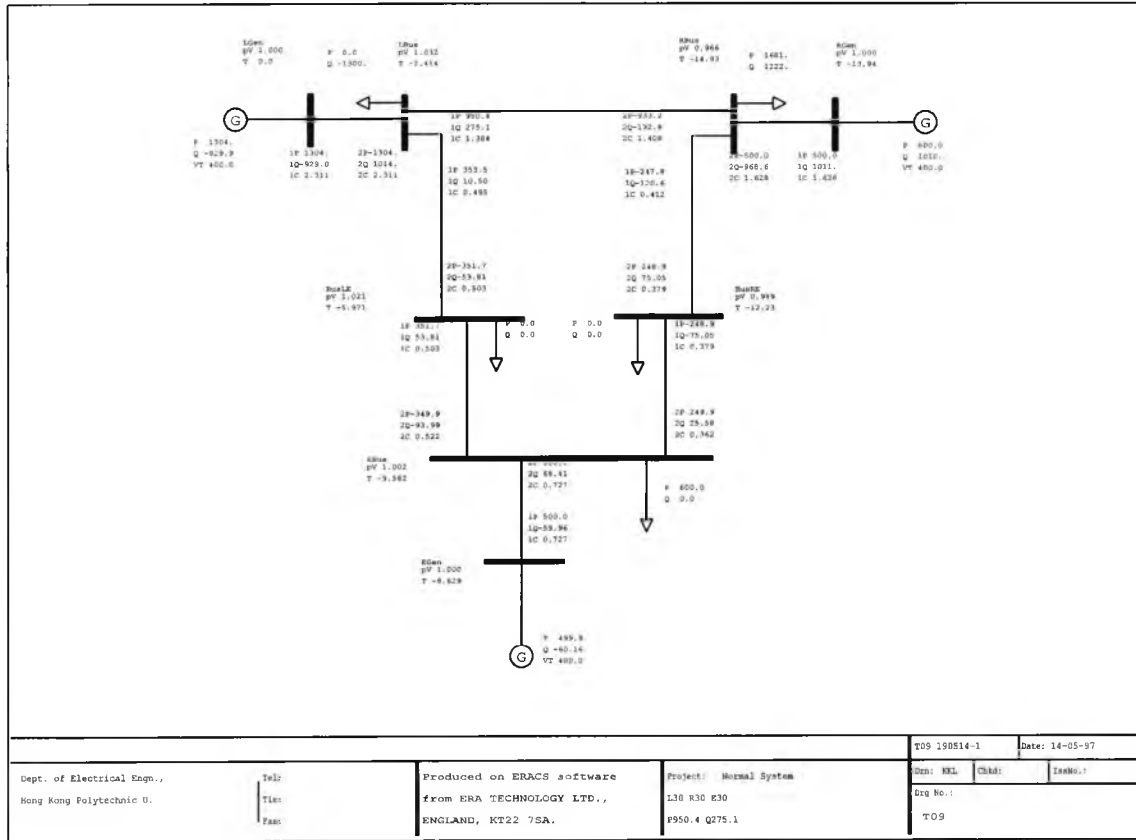


Fig. C.22 Load flow for test case C in Chapter 7

C.2.13 Test Case D

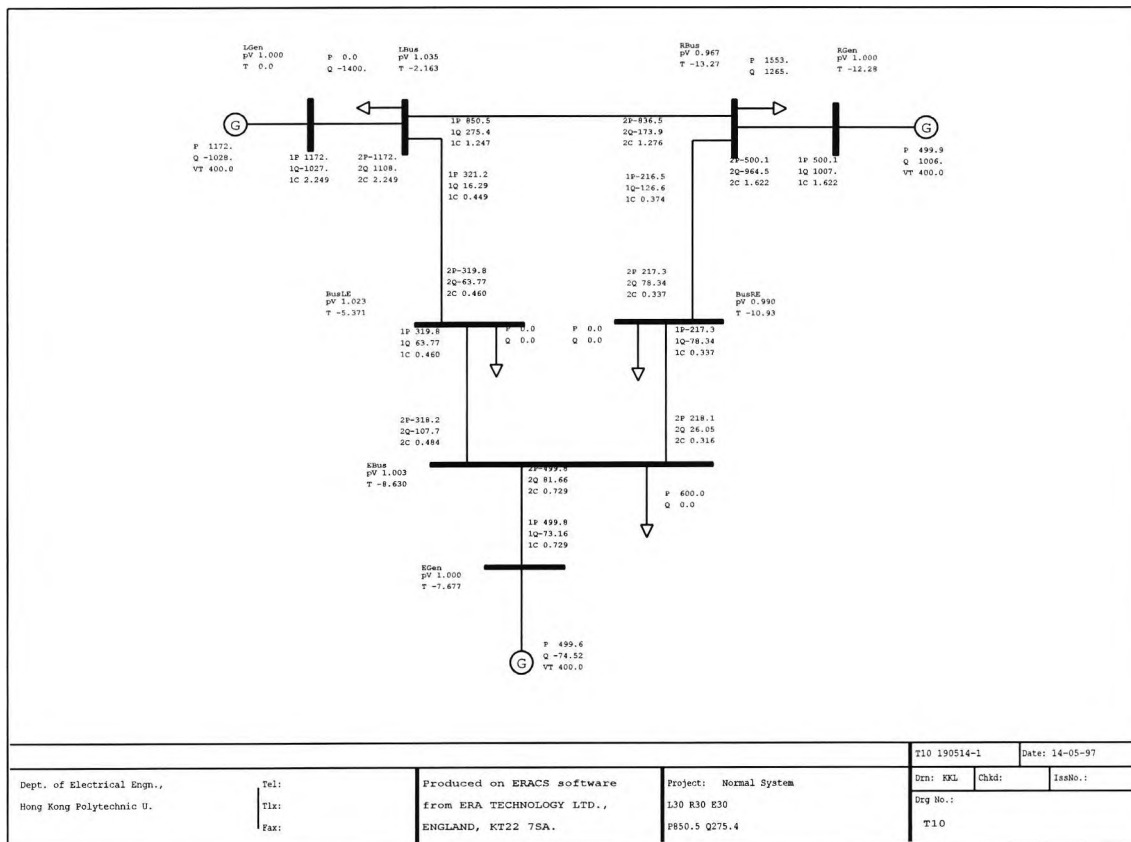


Fig. C.23 Load flow for test case D in Chapter 7